INAUGURAL - DISSERTATION

submitted to the

Combined Faculties for the Natural Sciences and for Mathematics

of the Ruperto-Carola University of Heidelberg, Germany

for the degree of

Doctor of Natural Sciences

Put forward by

M.Sc. Paul Faßl

Born in Gießen, Germany

Oral examination: 12.12.2018

Exploration of Properties, Stability and Reproducibility of Perovskite Solar Cells

Referees: **Prof. Dr. Yana Vaynzof**

                    Prof. Dr. Annemarie Pucci

Erforschung der Eigenschaften, Stabilität und Reproduzierbarkeit von Perowskit-Solarzellen

Der erste Teil dieser Arbeit zielte auf das Verständnis der Rolle der Mikrostruktur in der Degradationsrate von polykristallinen Methylammonium-Bleiiodid-Perowskit (MAPbI$_3$)-Schichten unter kontrollierter Exposition gegenüber Sauerstoff und simuliertem Sonnenlicht ab. Es wurde festgestellt, dass MAPbI$_3$ Filme, die aus kleinen und unregelmäßig geordneten Kristallkörnern bestehen, viel schneller degradieren als Filme, die aus großen, regelmäßig geordneten Körnern bestehen. Die Mikrostrukturanalyse ergab, dass die Degradationsrate auf einem Film stark variiert und an den Korngrenzen beginnt, was darauf hindeutet, dass die Degradation in MAPbI$_3$ Filmen auf eine räumlich unterschiedliche Defektdichte zurückzuführen ist. Der zweite Teil dieser Arbeit zielte auf das Verständnis von Fragen der Reproduzierbarkeit durch die Untersuchung der Wirkung von minimalen Variationen in der Precursorlösungs-Stöchiometrie, die für die MAPbI$_3$ Filmherstellung verwendet wird. Trotz nur geringfügiger Veränderungen in der Mikrostruktur zeigten solche Variationen einen starken Einfluss auf die Oberflächenzusammensetzung und Energetik von MAPbI$_3$ Schichten sowie auf die photovoltaischen Parameter und die Stabilität von Solarzellenbauelementen. Stationäre und zeitaufgelöste Photolumineszenzmessungen unter verschiedenen Atmosphären zeigten starke Heterogenitäten in den Materialeigenschaften in Abhängigkeit von der genauen Stöchiometrie. Zusammengenommen zeigen diese Ergebnisse die geringe Toleranz von Perowskitmaterialien gegenüber Sauerstoffbelastung sowie gegenüber kleinen Schwankungen in der Precursorlösungs-Stöchiometrie und erklären teilweise die Diskrepanzen und die Irreproduzierbarkeiten, die in der Perowskitforschung häufig auftreten.

Exploration of Properties, Stability and Reproducibility of Perovskite Solar Cells

The first part of this thesis was aimed at understanding the role of microstructure in the material degradation rate of polycrystalline methylammonium lead iodide perovskite (MAPbI$_3$) films under controlled exposure to oxygen and simulated sunlight. It was ascertained that MAPbI$_3$ films consisting of small and irregularly ordered crystal grains degrade much more rapidly when compared to films consisting of large, regularly ordered grains. Microstructural analysis revealed that the degradation rate varies widely across a film and commences at the grain boundaries, which suggests that degradation in MAPbI$_3$ films stems from a spatially varying density of defects. The second part of this thesis aimed at understanding reproducibility issues by exploring the effect of fractional variations in the precursor solution stoichiometry, which is used for MAPbI$_3$ film fabrication. Despite only minor changes in microstructure, such variations showed a strong effect on the surface composition and energetics of MAPbI$_3$ films, as well as the photovoltaic parameters and stability of solar cell devices. Steady-state and time-resolved photoluminescence measurements under various atmospheres revealed strong heterogeneities in the material properties depending on the exact stoichiometry. Taken together, these results reveal the low tolerance of perovskite materials towards oxygen exposure, as well as towards small variations in precursor stoichiometry, and partly explain the discrepancies and irreproducibility commonly encountered in perovskite research.

Contents

Abbreviations

AFM	atomic force microscopy
BCP	bathocuproine
CB	conduction band
CBM	conduction band minimum
DMF	*N,N*-dimethylformamide
DMSO	dimethyl sulfoxide
ETL	electron transport layer
FAI	formamidinium iodide, $HC(NH_2)_2I$
FF	fill factor
FTO	fluorine-doped tin oxide
GB	grain boundaries
GBL	γ-butyrolactone
HBL	Hole blocking layer
HOMO	highest occupied molecular orbital
HPA	hypophosporous acid solution
HTL	hole transport layer
IPA	2-Propanol
ITO	indium tin oxide
J$_{SC}$	short-circuit current density
Li-TFSI	lithium bis(trifluoromethylsulfonyl)imide
LUMO	lowest unoccupied molecular orbital
MAI	methylammonium iodide, CH_3NH_3I
P3HT	poly(3-hexylthiophene)
PC$_{60}$BM	[6,6]-Phenyl-C61-butyric acid methyl ester
PCE	power conversion efficiency
PDS	photothermal deflection spectroscopy

PFN	poly[(9,9-bis(3′-(N,N-dimethylamino)propyl)-2,7-fluorene)-alt-2,7-(9,9–dioctylfluorene)]
PL	photoluminescence
PTAA	Poly[bis(4-phenyl)(2,4,6-trimethylphenyl)amine
poly-TPD	poly[N,N′-bis(4-butylphenyl)-N,N′-bis(phenyl)benzidine]
PV	photovoltaic
rms	root mean square
SEM	scanning electron microscopy
Spiro-OMeTAD	2,2′,7,7′-Tetrakis[N,N-di(4-methoxyphenyl)amino]-9,9′-spirobi-fluorene
SOC	spin-orbit coupling
tBP	4-tert-Butylpyridine
UPS	ultraviolett photoemission spectroscopy
UV	ultra violett
VBM	valance band maximum
VB	valance band
V_{OC}	open-circuit voltage
w.r.t.	with respect to
XPS	X-ray photoemission spectroscopy
XRD	X-ray diffraction

1. Introduction

Due to industrialization and increasing wealth in emerging markets, particularly in China and India, there is a rapidly growing demand for energy. To date, the standard choice to satisfy these demands is fossil fuels, which are a finite source of energy. Furthermore, by producing greenhouse gases, the use of fossil fuels has a negative impact on the world's climate which has already resulted in an increase of the atmospheric CO_2 concentration from around 320 ppm in 1960 to above 400 ppm in 2017 [1]. This rise in CO_2 can be directly related to the ~0.8 °C increase of Earth's average surface temperature since 1980 [2]. The goal of the Paris agreement in 2015 has been set to avoid a rise of temperature that exceeds 2 °C above pre-industrial levels and thus to combat the causes of climate change [3]. Despite this globally accepted need for change, in 2017 fossil fuels still accounted for ~85% of total primary energy consumption, with a decline of only ~2-3% in the last decade [4], leading to an ongoing increase of CO_2 levels [1].

In order to solve what many think of as one of the biggest challenges facing mankind in the 21st century, the use of new technologies based on renewable energies seems inevitable. While in Germany the share of renewable energies in electricity generation reached a stunning 40% in 2018 [5], it was only 24% worldwide in 2017 [6]. At present, most of it is provided by hydro power (16%), a clean and effective technique which, however, has a limited scale-up potential. Fusion reactors, another promising emission free technique, will not be ready for application before ~2050 [7]. Because of these shortcomings, one of the most promising renewable energy sources for the near future is solar power.

The sun is an inexhaustible source of energy with an annual average irradiance of 2500 kWh/m^2 hitting the Earth's surface close to the equator. As an example, a 800x800 km^2 area covered with 10% efficient solar cells situated in the African desert would be sufficient to cover the world's total energy consumption of ~157 000 TWh in 2017 [4]. As a result of raised investments in renewable energies and significantly reduced production costs for silicon (Si) based solar cells, the globally installed photovoltaic power capacity has increased from below 100 GW in 2012 to 400 GW in 2017 and is estimated to surpass 1 TW in 2022 [8]. While this development is very promising, the estimated demand for newly installed power capacity by 2050 is on a ~8 TW scale [9]. Furthermore, the currently established Si solar cells, which make up more than 90% of the market share, are rigid and have a rather long energy payback time of ~1-2 years. Therefore, other cheap, scalable and flexible technologies for a variety of applications are strongly needed.

While organic solar cells were thought of as a promising option a decade ago, they were found to lack in efficiency to become a real alternative on a large scale. In this context, metal halide perovskites have emerged as a new promising class of mate-
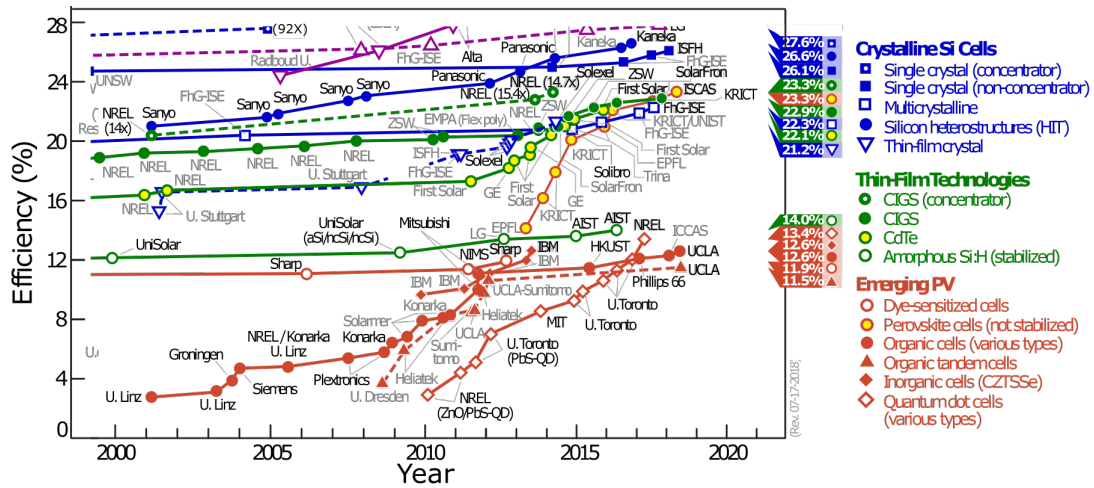
Figure 1.1: Details from the NREL efficiency chart with the development of record efficiency for the common photovoltaic (PV) technologies since 2000: Crystalline Si (blue), thin film (green) and emerging PV (orange). Perovskite solar cells are shown as orange points with yellow fill. Adapted from [14] and modified.

rial, combining the advantages of organic (low-cost, light-weight and flexible) and Si (high-efficiency) solar cells.

In 2009, Kojima and coworkers were the first to report the use of methylammonium lead triiodide ($MAPbI_3$) and methylammonium lead tribromide ($MAPbBr_3$) in a liquid dye-sensitized solar cell (DSSC) (introduced by Grätzel and coworkers in 1991 [10]), which yielded a power conversion efficiency of 3.8% [11]. However, the corrosive liquid in this kind of cell quickly degraded the perovskite structure, resulting in a loss of interest in the material. It was not until 2012, when Kim and coworkers reported the use of $MAPbI_3$ perovskite as sensitizer in an all solid-state heterojunction solar cell [12] with efficiencies up to 9.7% and a strongly enhanced stability, that the interest in this material was revived. In the same year, Lee and coworkers discovered that $MAPbI_3$ is able to conduct both electrons and holes, and demonstrated an efficiency of 10.9% [13].

These two reports led to an incredible growth of research conducted with focus on perovskite materials, especially for application in solar cells. While in 2012 and 2013 only 70 scientific papers were published on this topic, nearly 10000 publications (WebofScience) have been published since, with an average of eight new scientific articles published every day during the last three years. Because of this immense research effort, the power conversion efficiency of perovskite solar cells has skyrocketed, with certified efficiencies of 22.1% in 2016 [15] and 23.3% in 2018 [14]. Such a fast development has not been reached before by any other photovoltaic technology, such as organic, Si or CdTe solar cells. As a result of this tremendous effort, perovskite solar cells can already compete with the most efficient technologies after just six years of intense research (Figure 1.1).

Undoubtedly, the success of this technology stems from the numerous fascinating properties that perovskite materials possess, including a high defect tolerance, a long charge carrier lifetime, a high absorption coefficient as well as a direct and tunable bandgap [16, 17]. Most importantly, it offers the possibility to be processed by solution at low temperatures (~100 °C), making it suitable for scalable techniques such as printing [18]. The most promising applications are in flexible technologies [19] and as the second absorber in perovskite/Si tandem solar cells [20]. In addition, perovskite materials also have the potential to be used in applications as light-emitting diodes [21–23], photodetectors [24, 25], lasers [25, 26], transistors [27, 28] or even memristors [29]. In response to the promising research findings from the last few years and the material's diverse applicability, the first companies trying to commercialize perovskite products are emerging. For example, *Oxford Photoltaics Ltd* demonstrated a perovskite-silicon tandem solar cell with efficiencies over 27% for a $1\,cm^2$ cell in August 2018 and is part of a new consortium, funded by the German Federal Ministry of Economics and Energy with 2.8 million €, with the goal to bring the technology to the market within the next decade [30].

However, in spite of all its advantages, perovskite materials also possess properties hampering direct industrial success [31, 32]. The first issue is that perovskite materials are mixed ionic-electronic conductors, implying mobile charged defects in the crystal lattice if an electric field is applied [33, 34]. This leads to the so-called hysteresis effect, describing a phenomenon during which the measured power conversion efficiency depends on the scanning direction of the applied voltage and might not be stable over time [35–37]. The second issue is the relatively low stability of perovskite materials. For a solar cell to penetrate the market, lifetimes of ~20 years are required [38, 39]. Perovskite materials, however, degrade under extrinsic factors such as thermal stress [40], humidity [41], the combination of oxygen and light [42], or even UV illumination [43]. The third issue is related to reproducibility, as the reported properties of perovskite materials and devices show a large variation when examined by different researchers [31, 44]. This is due to the complicated solution chemistry [45] and sensitivity of perovskite crystallization to various parameters during the low temperature fabrication process. Even though increased efforts have been made to understand and address these issues, they hamper a clear understanding of some fundamental properties of the material and an easy upscaling of its fabrication [17, 18].

This work was aimed at studying two of the fundamental issues – stability and reproducibility. While, for example, early research focused on studying the degradation of $MAPbI_3$ in humid atmospheres, little attention has been paid to the degradation caused by the combined effect of oxygen and light. Therefore, this work aimed to advance the understanding of this degradation pathway by studying the influence of the perovskite microstructure on oxygen induced photodegradation. Furthermore, understanding and improving reproducibility is a major challenge for researchers

and industry to make perovskite materials a viable option for future energy generation. By studying the effect of fractional variations in precursor stoichiometry on the properties of MAPbI$_3$ films and devices using various characterization methods, this work is aimed at helping to understand and resolve some of the mentioned issues. The detailed literature review and novel research findings attempt to explain some of the problems facing perovskite materials and fundamentally improve the understanding of the sensitive properties of this material class.

To accomplish this, we will first discuss the fundamental physics of solar cells in Chapter 2, followed by a detailed discussion of the intrinsic properties of metal halide perovskite semiconductors. An overview of perovskite solar cell architectures as well as common deposition protocols is presented and the chapter concludes by reviewing the current state of research with the focus on environmental stability and the influence of precursor stoichiometry. Chapter 3 provides detailed information on the materials and methods for film preparation and introduces the analytical methods. In Chapter 4 we study and discuss the influence of microstructure on oxygen induced photodegradation of MAPbI$_3$ films. In Chapter 5 the impact of fractional variations in precursor stoichiometry on perovskite film properties and the efficiency and stability of perovskite devices is studied in detail. Chapter 6 discusses the effect of such variations on the steady-state and spatially resolved photoluminescence properties of MAPbI$_3$. Chapter 7 summarizes the results presented in this thesis and provides ideas for further possible studies building on the conclusions of this thesis.

2. Theoretical Background

In this chapter the basic physics of solar cells is introduced, followed by a detailed discussion of the intrinsic properties of metal halide perovskite semiconductors. Common perovskite solar cell architectures as well as fabrication routines are introduced. Finally, the current state of research regarding environmental effects on perovskite material stability as well as effects of variations in precursor stoichiometry on the properties of perovskite materials is reviewed.

2.1 Physics of Solar Cells

2.1.1 Interfaces

In general, the conversion of solar to electrical power is based upon three steps: (i) The generation of an electron-hole pair (exciton) upon absorption of photons by the active material, (ii) its dissociation into free charge carriers (electrons and holes) and (iii) charge transport and extraction of the carriers within an external circuit. To build an efficient solar cell, selective contacts are required to split the charge carriers and transport them to the contacts. In solar cells employing inorganic semiconductors, different regions of the absorber layer are typically doped to yield a pn-junction. Generated holes are transported to and *via* the p-doped region, and electrons to and *via* the n-doped region. In solar cells employing organic materials typically a bulk heterojunction, a randomly intermixed region of donor (p-type) and acceptor (n-type) organic compounds, is employed for efficient dissociation of excitons into free charge carriers.

Metal halide perovskites show ambipolar charge carrier transport properties and exhibit a very low exciton binding energy, as will be described in Section 2.2, and hence act as an 'intrinsic' layer in a solar cell. Excitons efficiently dissociate into free charge carriers, which are transported towards the contacts within the perovskite absorber layer. When sandwiched between two doped selective contacts, the structure is called a p-i-n solar cell and the energy levels in equilibrium, in the dark, are schematically depicted in Figure 2.1 (a). Electrons occupy energetic states with the probability governed by the Fermi distribution and the Fermi level E_F as chemical potential. Due to the difference in work function - the minimum energy required to remove an electron from the material surface to a point in the vacuum - of the doped contact layers, there is an intrinsic built-in field (V_{bi}) across the active layer, which is the driving force for charge carrier extraction. Upon light illumination, the electron population relaxes into a new equilibrium whose chemical potential is termed the quasi-Fermi level. The difference in the quasi-Fermi levels for electrons and holes determines the maximum potential difference of a photovoltaic device. Under il-
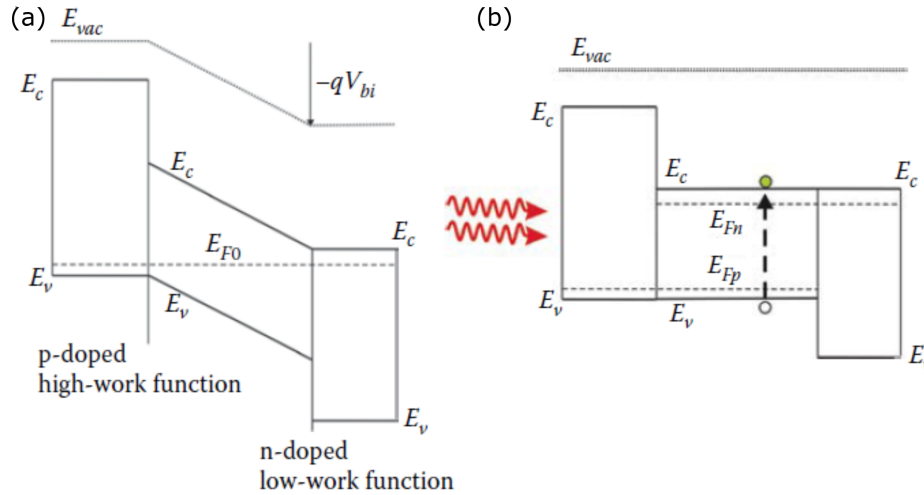
Figure 2.1: Schematic model of a p-i-n solar cell: (a) The system is in equilibrium, with Fermi level E_{F0} and a built-in field (V_{bi}) due to the different work functions of the selective contacts. (b) Under illumination and no charge extraction, generated charge carriers compensate for V_{bi} until flat band conditions are present (open-circuit conditions). Adapted from [46].

lumination and open-circuit conditions (no external load being connected), charge carriers will compensate for the internal electric field and the bands will shift until an equilibrium is reached (flat bands) (Figure 2.1 (b)). An example of a typical solar cell structure for perovskite solar cells (inverted structure) and the corresponding energy levels of the materials are shown in Figure 2.2. Typical device architectures of perovskite solar cells will be discussed in more detail in Section 2.3.1.
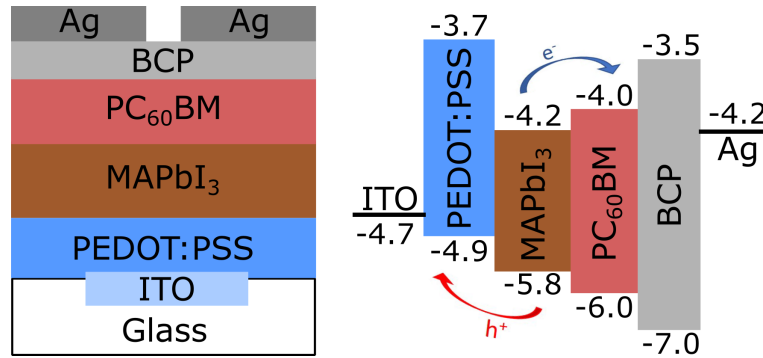
Figure 2.2: Schematic representation of an inverted perovskite solar cell and the corresponding energy levels of the materials.

2.1.2 Electrical Properties and Characteristic Parameters

The current of a solar cell can be divided into three parts: the dark current (I_D), which is determined by the diode properties of the solar cell, the photo-current (I_L), which is determined by charge carriers generated upon light absorption, and a shunt current (I_{sh}), which is determined by device imperfections [46]. The equivalent circuit
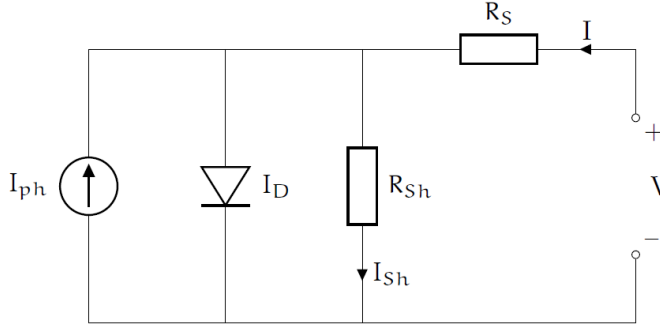
Figure 2.3: Equivalent circuit of a solar cell: Such a minimal model comprises a diode and a photocurrent source that generates I. A serial and shunt resistance, R_s and R_{sh}, account for loss mechanisms. [46].

comprising these contributions is shown in Figure 2.3, with the series resistance R_s being determined by the electrical resistance of the whole solar cell, and the shunt resistance R_{sh} modeling alternative current pathways. The current through a solar cell is typically divided by its active area A, to yield the current density $J = I/A$ Hence, the total current density in a solar cell can be written as:

$$J = J_D + J_{sh} + J_L \tag{2.1}$$

The dark current density is described by the Shockley Diode equation

$$J_D = J_0 \left[exp\left(\frac{q(V + IR_s)}{mk_B T} \right) - 1 \right], \tag{2.2}$$

with m being the diode ideality factor describing the diode properties of a device. The shunt current density is determined by Ohm's law and hence, the total current density through a solar cell can be written as:

$$J = J_0 \left[exp\left(\frac{q(V + IR_s)}{mk_B T} \right) - 1 \right] + \frac{V + J \cdot R_s}{R_{sh}} + J_L \tag{2.3}$$

A typical current density curve (JV curve), together with the generated power is plotted in Figure 2.4. When the applied voltage is zero, no power is generated and the current flowing through the device (caused by V_{bi}), is called short-circuit current density:

$$J_{SC} = J(V = 0) \approx J_L \tag{2.4}$$

Under the assumption that R_s and R_{sh} are negligible, that means $R_s \to 0$ and $R_{sh} \to \infty$, the open-circuit voltage (no current flowing through the device) can be approximated by:

$$V_{OC} = V(J = 0) \approx \frac{mk_B T}{q} \cdot \ln\left(\frac{J_L}{J_0} + 1 \right) \tag{2.5}$$

The shape of a JV-curve is mainly governed by the values of R_s and R_{sh}. The influence of these two parameters is schematically shown in Figure 2.5. Hence, the so-called fill factor (FF) can serve as a measure for imperfections in a solar cell and is defined by the ratio of the dark blue and light blue rectangles in Figure 2.4:
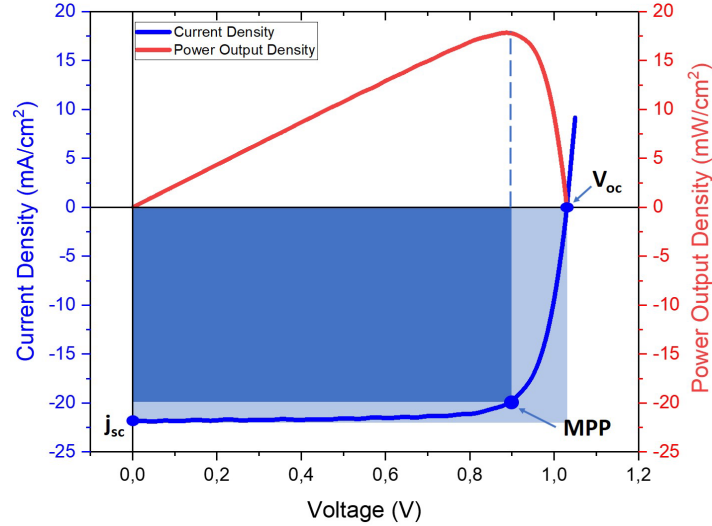
Figure 2.4: Typical current density-voltage curve (JV curve) and corresponding electrical power output density from a solar cell. Denoted are the short-circuit current density (J_{SC}), the open-circuit voltage (V_{OC}), and the maximum power point at (V_{MPP}), which generates the maximum power output P_{MPP}. Adapted from [47].

$$\text{FF} = \frac{V_{MPP} \cdot J_{MPP}}{V_{OC} \cdot J_{SC}} = \frac{P_{MPP}}{V_{OC} \cdot J_{SC}} < 1 \tag{2.6}$$

Finally, the most important parameter of a solar is the power conversion efficiency (PCE), generated at the maximum power point (MPP), and is defined as the ratio of generated to incident power:

$$\text{PCE} = \frac{P_{MPP}}{P_{\text{incident}}} = \frac{\text{FF} \cdot V_{OC} \cdot I_{SC}}{\phi_E^{AM1.5G} \cdot A}, \tag{2.7}$$

with $\phi_E^{AM1.5G}$ being the suns power density on the Earth's surface.

2.1.3 Efficiency Limits

The light absorption properties of a solar cell should be optimized to the properties of solar radiation. The sun, with an average temperature of 5800 K, is approximately a black body radiator (thermal electromagnetic radiation), and the spectrum of the sun just above Earth's atmosphere is called AM0 and has an integrated power density of $\phi_E^{AM0} = 136.6\,\text{mW/cm}^2$. When the light passes the atmosphere, a part of the spectrum becomes filtered. The total surface irradiation depends on the length the light traveled through the atmosphere and is determined by a coefficient called air mass (AM) [46]. The spectrum and intensity reaching Earth's surface depends on the season and varies over the year, however, for convenience the AM1.5G spectrum, with the sun at 48° above the horizon, was defined (see Figure 2.6 (a)). The AM1.5G spectrum, with an integrated power density of $\phi_E^{AM1.5G} = 100\,\text{mW/cm}^2$, defines the

Figure 2.5: Current-voltage characteristics of a solar cell with different values of R_s and R_{sh}. (a) The valu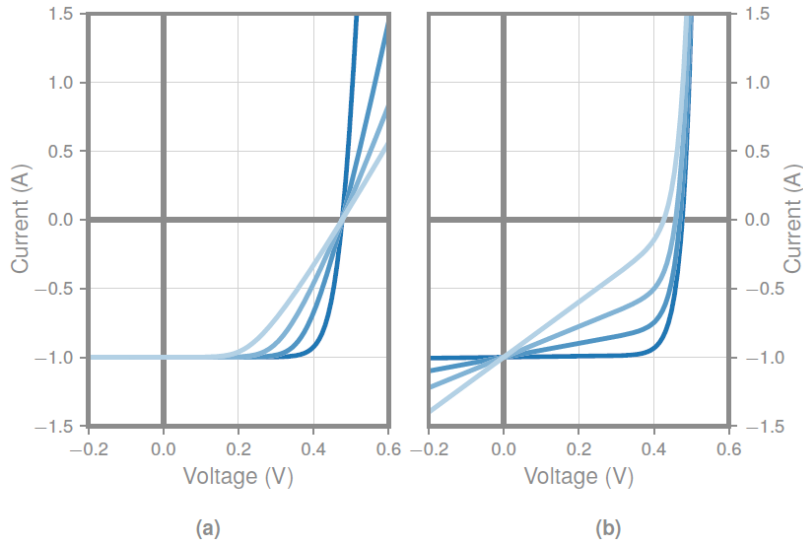es for R_s increase form dark blue ($R_s \ll 1\,\Omega$) to light blue.The values for R_{sh} decrease from dark blue ($R_{sh} \to \infty$) to light blue. Adapted from [48].

achievable power conversion efficiency of solar cells after accounting for fundamental intrinsic losses: thermalization, Boltzmann and Carnot losses reduce the maximum achievable voltage, while below bandgap radiation and emission losses reduce the maximum current of a solar cell [46, 49]).

The maximum achievable efficiency for a given bandgap is called Shockley-Queisser limit, and is shown in Figure 2.6 (b), together with the maximum achievable J_{SC} (c) and V_{OC} (d). The figure also provides experimental record values for the most common PV technologies, Si, GaAs and metal halide perovskite. As can be seen, the J_{SC} experimentally obtained is already close to its theoretical maximum for all technologies. The main cause for the PCE being below its theoretical limit, in particular for metal halide perovskite materials, is due to losses in V_{OC}. Such losses are mainly caused by defect states in the material, which result in non-radiative recombination. Typically, there are three recombination pathways in semiconductor materials: radiative band-to-band, non-radiative Shockley-Read-Hall Recombination (SRH) and Auger recombination ([46]; Figure 2.7). SRH recombination occurs due to defect states, which are energetically situated within the bandgap, and this recombination pathways dominates at low charge carrier densities. For example, an electron can become trapped at a defect, and subsequently recombine non-radiatively with a hole. Such a single-particle recombination process is termed monomolecular. Auger recombination describes a process in which the excess energy upon recombination is passed to a third particle, typically an electron or a hole. Auger recombination involves three-particles, and is thus a trimolecular process. Direct band-to-band radiative recombination always involves two charge carriers and is thus a bimolecular process. In perovskite materials, all these recombination pathways are present, and
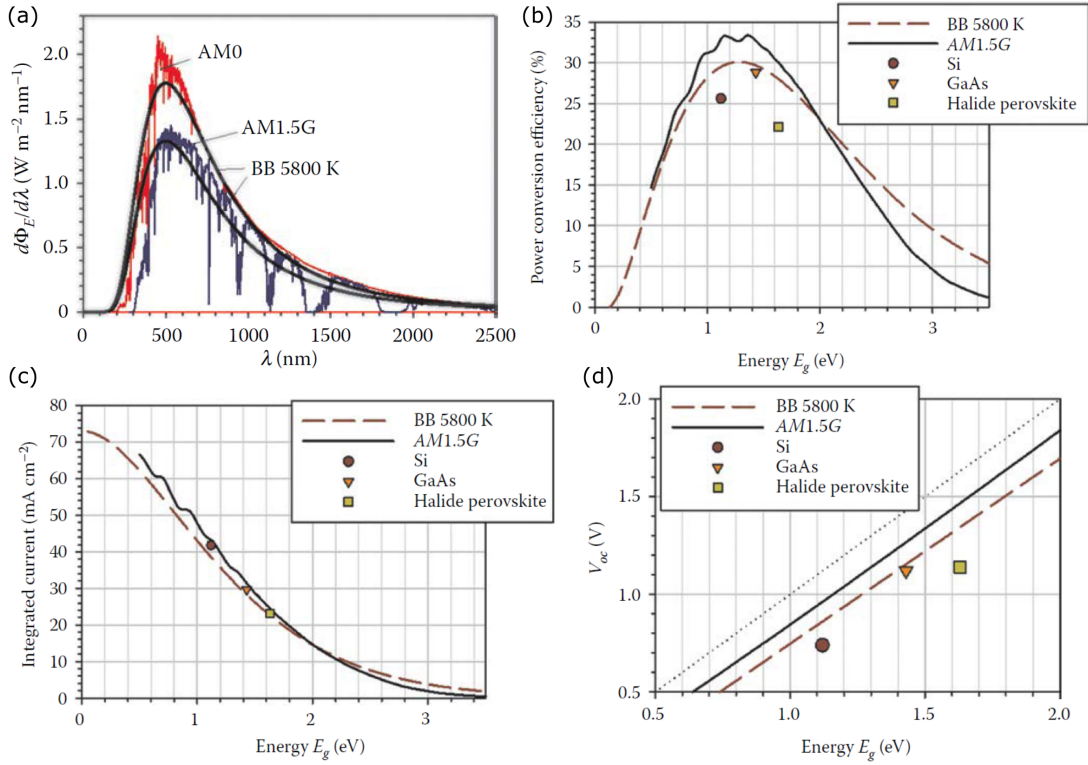
Figure 2.6: (a) The spectral irradiance from the sun just outside the atmosphere (AM0 spectrum) and (AM1.5G) terrestrial solar spectrum, together with spectra of a blackbody at T = 5800 K, normalized to the total power density of $\phi_E^{AM0} = 136.6 \, \mathrm{mW/cm^2}$ and $\phi_E^{AM1.5G} = 100 \, \mathrm{mW/cm^2}$ (b) Maximum Shockley-Queisser efficiency limits for the given bandgaps in case of black body radiation (dotted) and AM1.5G solar irradiance. The points depic the current records for Si, GaAs and metal halide perovskite solar ceolls. (c)+(d) The corresponding maximum achievable J_{SC} and V_{OC} for a given bandgap. Adapted from [46].

will be discussed more closely in Section 2.2.6.

2.2   Metal Halide Perovskite Semiconductors

The word "perovskite" originates from the discovery of $CaTiO_3$ in 1839 by Gustav Rose, who named the new mineral after the Russian count Lev Alekseyevich Perovski. Later, all compounds with the general composition ABX_3 were termed as perovskites and they cover a wide range of ternary oxides, nitrides, halides and other compositions [50]. Amongst others,they have been investigated as field-effect transistors [51] and high temperature superconductors [52].

As introduced in Chapter 1, it was not until in 2012 that metal halide perovskites incorporating organic cations were investigated in more detail for application in photovoltaic devices. In this section, the most important properties of this intriguing class of materials are summarized with focus on the typically employed $MAPbI_3$ composition, and recent findings in literature are presented.

Figure 2.7: From left to right: Band-to-band radiative recombination, trap-assisted non-radiative Shockley-Read-Hall Recombination (SRH) and Auger recombination. Adapted from [46].

2.2.1 Structural Properties

The Goldschmidt tolerance factor t can be used to estimate whether a combination of materials (A, B and X) is able to form a stable 3D ABX$_3$ perovskite crystal structure [53, 54],

$$t = \frac{r_A + r_X}{\sqrt{2}\,(r_B + r_X)},$$ (2.8)
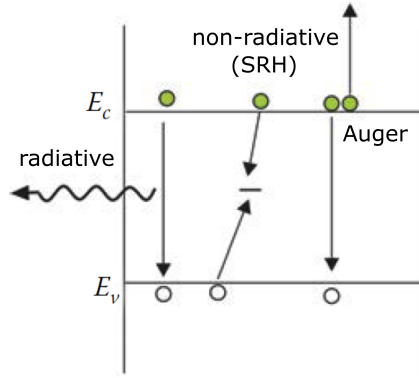
with r_A, r_B and r_X being the ionic radii of the respective atoms. In addition, the so-called octahedral factor $\mu = r_B/r_X$ must be taken into account. Empirically, t and μ are suggested to be in the range of $0.8 \leq t \leq 1.0$ and $0.44 \leq \mu \leq 0.9$ for a stable perovskite structure [55]. However, these values only serve as an estimate. For the non-spherical shaped and fast rotating organic cations incorporated in metal halide perovskites, additional corrections must be applied for the effective atomic radii [54, 56]. Travis *et al.* have recently suggested that for hybrid metal halide perovskites, the values should be around $0.8 \leq t \leq 1.06$ and $0.41 > \mu$ [56]. This applies only to a limited number of material combinations. While the organic component mainly determines the structural stability of a given composition, the metal cation and halogen anion will determine whether the properties of the resulting perovskite (bandgap and electronic properties) will be beneficial for photovoltaic applications ([55, 56], Sec. 2.2.2).

The metal halide ABX$_3$ structure employed in photovoltaics is based on corner sharing anionic BX$_6$ octahedra, with A being an monovalent cation (A = methylammonium (MA$^+$), formamidinium (FA$^+$), Cs$^+$), B a divalent cation (B = Pb^{2+}, Sn^{2+}) and X a halogen ion (X = I$^-$, Br$^-$, Cl$^-$). The corresponding idealized cubic perovskite crystal structure is shown in Figure 2.8. For the A cation also inorganic Cs can be used to yield purely inorganic CsBX$_3$, however, due to its slightly too small ionic radius and hence low tolerance factor of $t < 0.8$, the 3D perovskite phase of this composition is not stable at room temperature. However, Cs can be mixed with MA/FA to "tune" the tolerance factor and electronic properties of the resulting perovskite, as will be explained later.

Taking the composition MAPbI$_3$ as an example, it's 3D structure has three solid perovskite phases (α, β and γ). The high temperature α phase (T~330 K) has a cubic
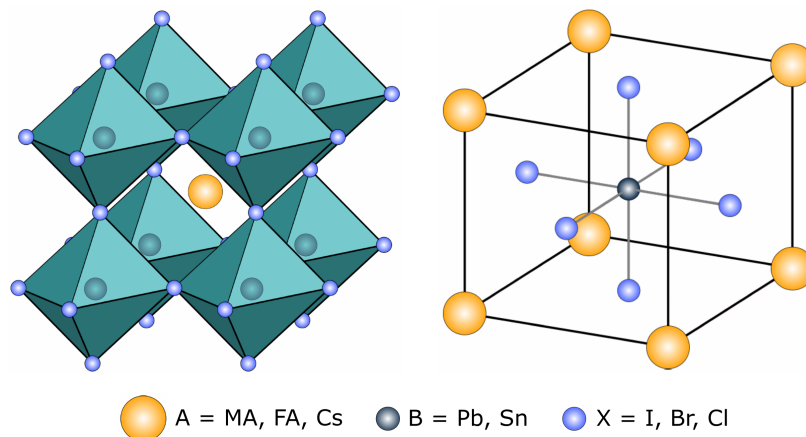
Figure 2.8: Idealized cubic crystal structure of ABX$_3$ perovskite: BX6 octahedra with A in the interstices (left). Unitcell with A at the corner positions, metal B at the body-centerposition and halides X at the face-center positions (right). Adapted from [57].

crystal structure. At lower temperatures the PbI$_6$ cage becomes distorted and tilted, resulting in structural disorder and a change in crystal packing [58, 59]. Hence, the β phase at temperatures between $162\,\mathrm{K} \leq T \leq 330\,\mathrm{K}$ is tetragonal, while the low temperature γ phase ($T < 162\,\mathrm{K}$) shows an orthorhombic crystal structure [60, 61]. However, a slight Pb-I-Pb bond angle distortion does not significantly change the basic electronic structure of MAPbI$_3$. Hence, the optical bandgap is only slightly changing throughout all three phases [62–64]. The MA molecules in the α and β phase are strongly disordered, while their motion is frozen in the γ phase. The disordered rotational dynamics of the cations have several effects on the properties of perovskite materials, recently summarized by Gallop *et al.* ([65]; Sec. 2.2.4).

The composition FAPbI$_3$, in contrast, only exists in a yellow hexagonal non--perovskite phase (δ-phase) at room temperature, due to the slightly too large size of the A cation ($t > 1$) (see Figure 2.9 (b)). Annealing at temperatures above $150\,°\mathrm{C}$ leads to the formation of a black 3D α phase, which is maintained upon cooling [68, 69]. However with progressing time, the δ-phase reappears, which limits the performance and stability of this composition at room temperature. As already mentioned, Cs can be used as cation at the A side and be mixed with MA/FA to tune the tolerance factor. Lee *et al.* as well as Li *et al.* have been the first groups to demonstrate this possibility by stabilizing a FA$_{1-x}$Cs$_x$PbI$_3$ composition in the cubic phase at room temperature by introducing a small amount of Cs ($\approx$ 0.1) [67, 69] (Figure 2.9). The possibility of tuning the structural properties motivated researchers to search for further stable multi-cation compositions, and they will be discussed in more detail later on. Table 2.1 summarizes typical 3D perovskite compositions and their relevant crystal structures and properties.

Larger organic cations than MA or FA (e.g. PEA or BA) (with $t > 1$) result in the formation of layered structures with the general formula (RNH$_3$)$_2$MA$_{n-1}$B$_n$X$_{3n-1}$ with insulating organic layers between n inorganic BX$_6$ octahedron sheets. These are

termed 2D ($n = 1$) or quasi-2D ($n > 2$) structures and have received interest due to their enhanced temperature and moisture stability compared to 3D perovskite structures [70, 71]. However, the electronic and optical properties of the layered structures become highly anisotropic, resulting in lower efficiencies compared to their 3D counterparts.

2.2.2 Optical and Electronic Properties

The perovskite bandgap is predominantly determined by the halide p-orbitals interacting with the metal's s- or p-orbitals and is only weakly depending on the A cation. In case of $MAPbI_3$, a direct bandgap is formed between the antibonding valance band maximum (VBM) originating from the Pb 6s – I 5p interactions and the antibonding conduction band minimum (CBM) originating from the Pb 6p – I 5p interaction [72] (Figure 2.10 (a)). Most studies agree that free carriers dominate the electronic dynamics in metal halide perovskite materials and the exciton contribution is negligible. This effect arises due to the very low exciton binding energy in metal halide perovskite materials which allows excitons to freely dissociate into free charge carriers [73].

The exciton binding energy of $MAPbI_3$ has been recently determined to be 16 meV in its orthorhombic phase and below 13 meV in its tetragonal phase using magneto-reflectivity at very high magnetic field [75, 76]. These energies are lower than the thermal energy at room temperature (≈ 25 meV). In addition, a correlation between the exciton binding energy and the perovskite grain size, as suggested previously [77], was excluded in these studies. An even lower value of 7.4 meV was determined by Ziffer *et al.* from electroabsorption spectroscopy measurements [78]. Recent ab ini-

Table 2.1: 3D metal halide perovskite compounds commonly employed in photovoltaic devices. Data adapted from [66–68].

Composition	Tolerance factor	RT phase	E_g [eV]	Relevant phase transition
$MAPbI_3$	0.89	Tetragonal	1.55	cubic above 60 °C
$MAPbBr_3$	0.93	Cubic	2.3	
$FAPbI_3$	1.02	Hexagonal	1.49	cubic above 150 °C
$CsPbI_3$	0.79	Orthorhombic	1.72	cubic above 300 °C
$FA_{0.9}Cs_{0.1}PbI_3$	0.95	Cubic	1.52	
$CsPb(I_{0.67}Br_{0.33})_2$	0.81	Orthorhombic	1.9	cubic above 250 °C
$FA_{0.85}MA_{0.15}Pb(I_{0.85}Br_{0.15})_3$	1.01	Cubic	1.62	
$FA_{0.85}Cs_{0.15}Pb(I_{0.83}Br_{0.17})_3$	1.01	Tetragonal	1.74	

(a)

(b)

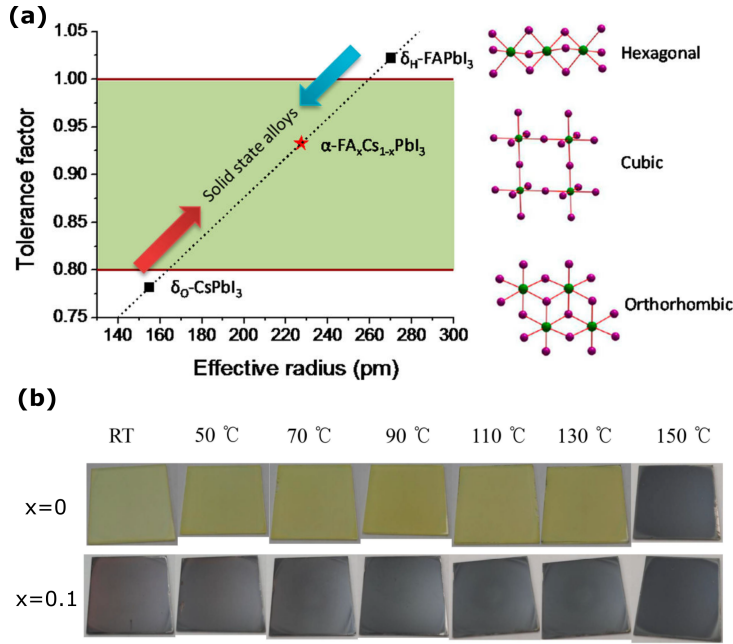**Figure 2.9:** (a) Correlations between tolerance factor and crystal structure of perovskite materials for the case of $FA_{1-x}Cs_xPbI_3$. Reproduced with perimission from [67]. Copyright 2015, American Chemical Society. (b) Photograph of $FA_{1-x}Cs_xPbI_3$ films heated at the stated temperatures for 5 min with $x = 0$ (top row) and $x = 0.1$ (bottom row). Reproduced with permission from [69]. Copyright 2015, Wiley-VCH.

tio calculations by De Angelis and coworkers suggest that the exciton binding energy is significantly lowered by dynamical dielectric screening from low energy phonons [79]. Their results also suggest that dynamic disorder and roatation of the organic cations plays only a minor role in this process. The value for the effective mass of the exciton was independently determined in various studies to be $\mu \approx 0.1m_0$ with m_0 being the bare-electron mass [75, 80, 81]. The correlation between the effective masses of excitons, electrons (m_e) and holes (m_he) is given by $1/\mu = 1/m_e + 1/m_h$ [82]. The experimental values suggest that m_e and m_h are a bit higher than determined from GW calculations ($m_e = 0.12m_0$ and $m_h = 0.15m_0$), which would yield $\mu = 0.067$ [83].

The low exciton binding energy and effective mass and the direct bandgap of perovskite materials result in very high absorption coefficients of above $\sim1 \cdot 10^{-4}$ for wavelengths below 700 nm [84] as well as high mobilities of $\mu \approx 100\,cm^2/V/s$ [85]. These properties are crucial for reaching high efficiencies [59]. The absorption coefficient is even higher compared to other direct bandgap semiconductors, such as mono-crystalline GaAs, and much higher than that of indirect bandgap c-Si ([84]; Figure 2.11). Very thin perovskite layers in the range of 300-500 nm are sufficient to absorb most of the visible light and yield high efficiencies, allowing e.g. semi-transparent and flexible devices. The slope of the exponential part of the absorption onset is the so-called Urbach energy and is representative of absorption tail states of semiconductor films and hence their electronic quality ([84]; Figure 2.11). The Urbach energy of high-quality $MAPbI_3$ films can be very low [86] with values similar to GaAs which possesses high electronic quality [87]. In contrast, due to the indirect bandgap of c-Si, the absorption onset occurs at much lower absolute values (not visible in Figure 2.11) and shows signatures related to phonon-assisted absorption [84].
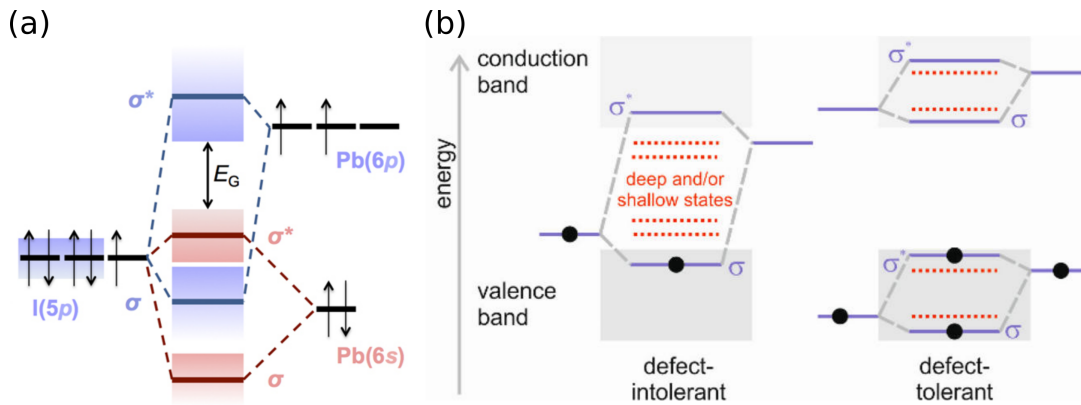
Figure 2.10: (a) Bonding and antibonding orbitals of MAPbI$_3$ perovskites, showing the formation of the valence and conduction band structure. Reproduced with permission from [72]. Copyright 2015, Materials Research Society. (b) Schematics of the limiting cases of a defect intolerant, and defect tolerant semiconductor. Reproduced with permission from [74]. Copyright 2017, American Chemical Society.

As mentioned before, it is possible to tune the structural stability of perovskites by partly substituting MA with FA or Cs. Similarly, a tuning of the bandgap is also possible by substituting I with Br/Cl or Pb with Sn. For example, Noh *et al*. demonstrated in 2013 that the perovskite bandgap of MAPb(I$_{1-x}$Br$_x$)$_3$ can be tuned from 1.57 eV up to 2.29 eV upon substitution of I with Br ([88]; Figure 2.12). Jacobsson *et al*. performed a similar study for more complicated compositions of (FA$_{1-x}$MA$_x$)-Pb(I$_{1-y}$Br$_y$)$_3$, where combinations of FA/MA and I/Br were tested over the entire parameter space [89]. Upon substitution of Pb with Sn, Prasanna *et al*. tuned the bandgap of a FA$_{1-x}$Cs$_x$Pb$_{1-y}$Sn$_y$I$_3$ composition between 1.24 eV and 1.56 eV [90].

Recently, Xiao *et al*. proposed that in addition to the structural dimensionality the electronic dimensionality also plays an important role in determining suitable perovskite structures for photovoltaics. They suggested that the electronic dimensionality depends on the connectivity of the atomic orbitals which comprise the VBM and CBM. For some metal halide perovskite compositions - while structurally being 3D perovskites - the electronic dimensionality can be 1D or even 0D and these compositions thus do not yield good device performance [91].

2.2.3 Defect Physics

The outstanding electronic properties of perovskite materials result, for example, in very long charge carrier diffusion length with reported values above 1 μm in thin films [92, 93] and several hundreds of μm in single crystals [93, 94]. These properties stem from the peculiar defect physics of perovskite materials [95, 96]. The relatively fast rate of crystal growth from solution at low temperatures makes the presence of defects unavoidable [95, 97]. Generally, there are three kinds of intrinsic point defect that can be formed in a crystalline structure of a semiconductor - vacancies, interstitials and antisites [82, 98]. For crystalline Si employed in solar cells, a low defect
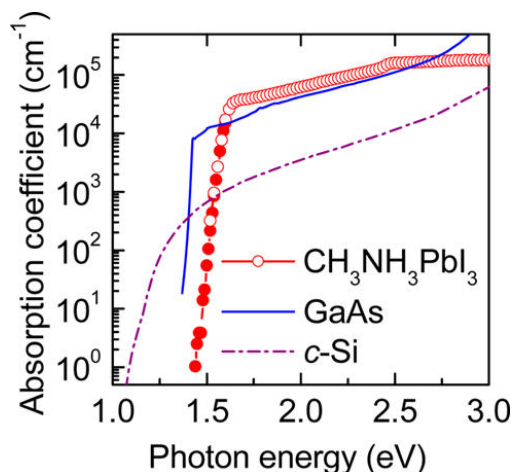
Figure 2.11: Absorption coefficients for the direct bandgap absorbers MAPbI₃ and GaAs as well as for the indirect bandgap absorber c-Si. Reproduced with permission from [84]. Copyright 2014, American Chemical Society.
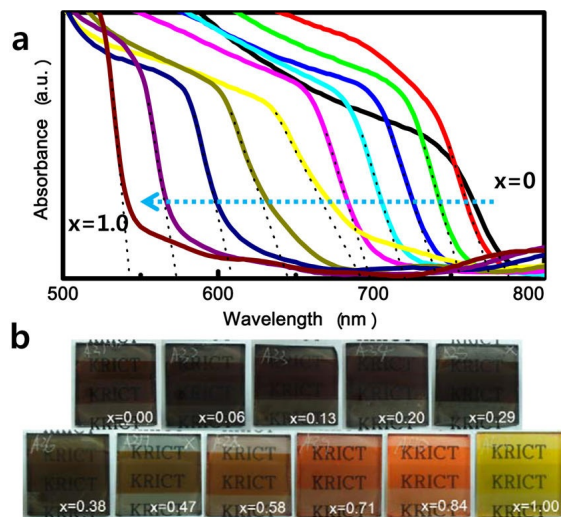
Figure 2.12: (a) UV-vis absorption spectra of FTO/TiO$_2$/meso-TiO$_2$/MAPb(I$_{1-x}$Br$_x$)$_3$/Au cells measured using an integrating sphere. (b) Photographs of 3D TiO$_2$/MAPb(I$_{1-x}$Br$_x$)$_3$ bilayer nanocomposites on FTO glass substrates. Reproduced with permission from [88]. Copyright 2013, American Chemical Society.

concentration - depending on the type of defect on the order of 10^{-15}–10^{-16} cm^{-3} (i.e. 10^{-2}–10^{-1} ppm) - is required for decent semiconducting properties, which makes the purification process very expensive [99, 100]. In contrast, the optoelectronic properties of perovskite materials do not seem to be hampered by incorporating a high number of defects in its structure, on the order of 10^{19}–10^{20} cm^{-3} (i.e. ~0.1%) [101]. Only few of these defects act as electronic traps resulting in non-radiative recombination (Sec. 2.2.6).

Such a behavior is termed defect-tolerant and is schematically depicted in Figure 2.10 (b) for the extreme cases of a defect intolerant (most commonly observed for semiconductors) and completely defect tolerant system. If the VBM is formed by a bonding orbital, most defects in the crystal structure have their energy deep within the electronic bandgap. In the case that the VBM is formed by an antibonding orbital, and the CBM from a bonding orbital, all defects are situated within the bands leaving the energetic landscape within the bandgap free of defects [72, 74]. For perovskites, a mixture between these two limiting cases is present, with the electronic bands formed between two antibonding orbitals.

Yin *et al.* were the first to provide DFT calculations suggesting that there are various defects with a low formation energy in MAPbI₃ perovskite, most of which, however, only form shallow trap states situated close to or within the MAPbI₃ bands. In contrast, deep level defects within the bandgap exhibited a very high formation energy [95, 103]. Such early calculations did not take into account corrections due to

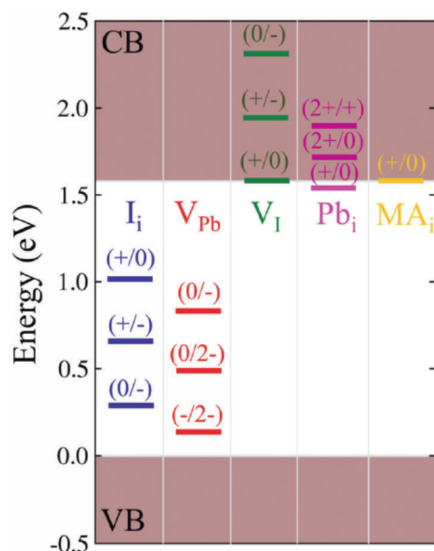**Figure 2.13:** Thermodynamic ionization levels for the most stable defects in MAPbI$_3$ as calculated by Meggiolare *et al.* for *iodine medium* conditions. Adapted with permission from [102]. Copyright 2018, Royal Society of Chemistry.

spin-orbit coupling (SOC) caused by the high mass of the Pb atom. Mao-Hua Du was the first to report such a calculation and proposed that only iodine interstitials and its complexes introduce deep defect levels within the MAPbI$_3$ bandgap [104]. All other defects either were situated in the bands or formed shallow defects.

The same conclusion was drawn recently by Meggiolaro, De Angelis and co workers employing up-to-date DFT calculations taking SOC the growth conditions of the films into account [102]. The growth conditions are influenced by factors such as the precursor composition and the surrounding atmosphere during the crystallization process and are termed as *I-rich/I-medium/I-poor* in their calculations. They define the chemical potentials of the MAPbI$_3$ constituents and with it the native Fermi level of the perovskite film. The importance of the growth conditions had already been proposed by Buin *et al.* , who decreased the number of defects in their films by employing iodide poor growth conditions ([105], Sec. 2.3.2.1). Wang *et al.* had revealed that the perovskite can be either n- or p-doped depending on the surface composition of the films [106]. As an example, the defects predicted to exhibit the lowest formation energies in *I-medium* conditions are iodide interstitals/vacancies, MA interstitials and Pb vacancies. The calculated energetic position within the perovskite band structure is shown in Figure 2.13 [102]. Despite iodide interstitials forming potentially detrimental deep traps, the authors proposed that these iodine hole traps can be converted into kinetically inactive electron traps by exposing the samples to mild oxidizing conditions during or even after the crystal growth [102, 107].

While the iodine redox chemistry in MAPbI$_3$ perovskite might be one of the pillars to explain the high defect tolerance of metal halide perovskites, it can only serve as one explanation amongst others. A certain density of deep traps in perovskite materials can, for example, also be formed by Pb$_I$ or I$_{Pb}$ antisite defects despite their rather high formation energy[108, 109]. These can not be healed by the iodine redox chemistry theory and other explanations then must serve to explain the sustained

defect tolerance. For example, Tan *et al.* very recently revealed by DFT calculations that while the incorporation of a small amount of MA into $Cs_xFA_{1-x}PbI_3$ does not necessarily reduce the density of defects, its higher dipole moment compared to FA heals deep traps and thus results in a more defect tolerant material [110].

2.2.4 Phonons and Polarons

Another very important aspect defining the defect tolerance of perovskite materials is their polaronic nature. Because metal halide perovskites semiconductors are soft polar materials with low phonon energies compared to conventional semiconductors [80], electron–phonon interactions might set an intrinsic limit to the achievable charge-carrier mobilities at room temperature if they are dominated by polar-optical phonon modes [111].

Wright *et al.* reported on electron-phonon coupling in metal halide perovskites and derived frequencies for the longitudinal optical (LO) phonons indirectly via temperature dependent photoluminescence measurements. They established that the interaction between charge carriers and LO phonons is dominant and the contribution from acoustic phonons is negligible at room temperature [112]. Leguy *et al.* employed Raman and terahertz absorption spectroscopy and found high dynamic disorder and short phonon lifetimes for LO optical phonons. They also concluded that optical phonon scattering is dominating at room temperature in perovskite materials and thus determines the achievable mobility [113]. Sendner *et al.* experimentally determined frequencies of the transversal and longitudinal optical phonons by far-infrared spectroscopy measurements [80]. The authors derived values for the polaron mass and radii, and calculated upper limits for the mobilites of all three $MAPbX_3$ perovskite compositions. The authors concluded that large polarons form in $MAPbX_3$ perovskite materials.

It had already been hypothesized that large polarons could explain the existence of very long charge carrier lifetimes and yet only moderate charge carrier mobilities in perovskite thin films and single crystals [93, 114]. Miyata *et al.* employed time-resolved optical Kerr-effect spectroscopy and revealed that deformation of the PbX_3-sublatice and the fact that charge carriers are partially located in the PbX_3 phonon environment, creates large polarons on a sub-ps-timescale [115]. The screened Coulomb potential of these charge carriers reduces their scattering with charged point defects and other charge carriers, and thus contributes to the long charge carrier lifetimes in perovskite materials. The authors proposed a "crystal-liquid" duality in $MAPbI_3$, implying that lead halide perovskites can be classified as phonon-glass electron crystals [116]. This picture was recently confirmed by ab initio molecular dynamics calculations, which suggest that the separate localization of the electrons and holes are induced by the structural disorder of the PbI_3 sublattice [117]. Recently, Miyata *et al.* also discussed a possible dynamic transient ferroelectric-like dielectric response of perovskite materials in the THz region, which could lead to the formation of polar nanodomains surrounding a charge carrier. The authors suggested that such ferro-

electric large polarons would screen the charge carriers even stronger than conventional large polarons [118].

Anusca *et al.* [119] proposed that the material response of MAPbI$_3$ can be split into three frequency ranges: below 1 MHz the slow response of ionic species dominates which was termed the "static" part of dielectric properties. The frequency range around 1 THz is dominated by relaxation of the inorganic sublattice, which is relevant for the formation of the large polaron and exciton breakup. The lattice dynamics in the intermediate GHz range was assigned to disordered rotations of the MA cation. Specifically, the authors pointed out that the MA rotation provides more than 50% of the dielectric response below the GHz range and thus might further improve screening effects. However, it was pointed out that additional screening effects of MA cations could further slow down the polaron movement, thus further reducing the achievable mobility in perovskite materials [116].
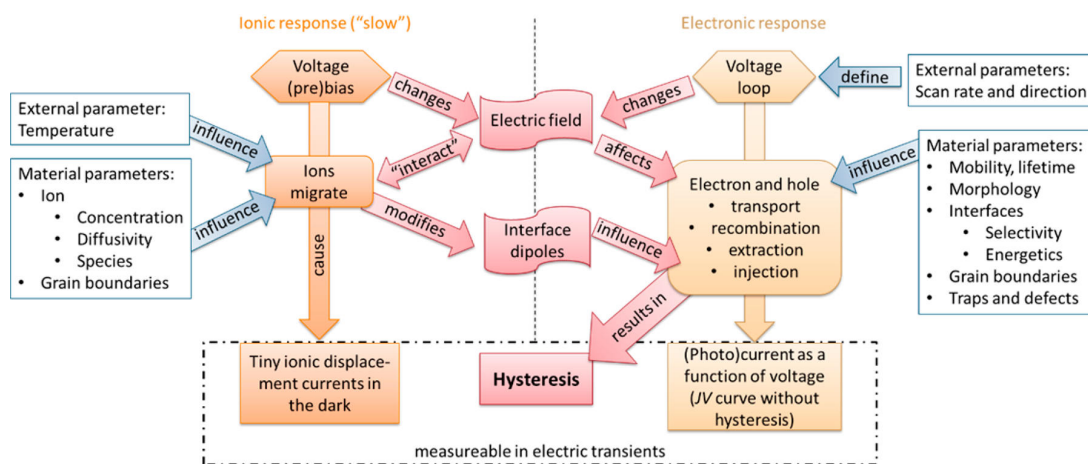
Figure 2.14: Schematic summary of the complex processes due to interactions between the ionic and electronic response upon applying an external voltage, which all together determine the severity of current-voltage scan hysteresis. Reprinted with permission from [37]. Copyright 2017, American Chemical Society.

In addition to the before mentioned effects, charge-carrier cooling processes following above bandgap absorption are also governed by interactions between charges and phonons, in which the organic cations play a major role [120]. For example, acoustic-optical phonon up-conversion resulting in a hot-phonon bottleneck at high excitation densities has recently been discovered in perovskite materials [121, 122]. Frost *et al.* proposed that this effect could be closely related to the ultralow thermal conductivity of perovskite materials [123]. For lower excitation densities, trap-free hot carrier relaxation accompanied with above bandgap photoluminescence has been observed experimentally [124]. The effects of the disordered rotational nature of the organic cations on perovskite properties have recently been summarized by Gallop *et al.* [65].

2.2.5 Ionic Transport and Hysteresis

While most of the charged point defects in the perovskite structure only result in shallow trap states, they might still be able to move within the crystal lattice. For example, oxygen vacancy diffusion is a common and well-characterized process in perovskite metal oxides [125]. The defect population is determined by equilibrium thermodynamics, which for metal halide perovskite semiconductors can be influenced by the history of the sample, such as annealing temperature, solvent environment, chemical treatments, light illumination or electric fields [126, 127]. For vacancies or interstitials to be able to move in a crystal lattice, they must overcome a certain energy barrier, denoted as activation energy ΔG_{ion}. The diffusion coefficient of ionic point defects is then described by

$$D_{\mathrm{ion}} = D_0 \exp\left(\frac{-\Delta G_{\mathrm{ion}}}{k_{\mathrm{B}}T}\right), \tag{2.9}$$

with the temperature independent factor $D_0 = \alpha a^2 \nu_0$ which includes the lattice constant a and an attempt frequency ν_0 related to lattice vibrations and the constant α which is 1/6 for a cubic lattice [82]. There is now compelling evidence that ions migrate in a perovskite film, e.g. from the observation of current-voltage hysteresis [35], an electric-field-switchable reversible photovoltaic effect (p-i-n to n-i-p) [128], light-induced halide redistribution [129] or light induced phase separation of I/Br mixed-halide compounds [130]. The possible diffusion mechanisms for ionic defects in the perovskite structure are through the A and B vacancy sites or the X vacancy/interstitial site ([127]; Figure 2.15).

Eames *et al.* provided a combined experimental and computational (employing DFT calculations) study on ionic transport in MAPbI$_3$ perovskites. They reported facile vacancy-assisted diffusion of iodide ions with an activation energy of 0.58 eV, being in good agreement with the activation energies determined from temperature dependent current relaxation measurements on MAPbI$_3$ solar cells [131]. For methylammonium and lead vacancies the authors derived activation energies of 0.84 eV and 2.31 eV respectively. Azpiroz *et al.*, also employing DFT, calculated even lower activation energies of 0.1 eV for iodine vacancies and interstitals, 0.5 eV for MA and 0.8 eV for Pb vacancies [132]. Many experimental and theoretical studies followed, trying to determine which defects are the most abundant and which have the lowest activation energy, with some conflicting reports. Analyzing most recent literature reports - summarized in a work by Aaron Walsh and Samuel Stranks [127] - yields the following picture of ionic transport in metal halide perovskites:

- Iodide vacancies exhibit the lowest activation energies (~0.1 eV; [133–135]) and are now generally accepted to be the main cause for the reported hysteresis effects in photovoltaic devices. Their diffusion constants are estimated to be on the order of $D_{\mathrm{I}} \approx 10^{-7}\,\mathrm{cm}^2\,\mathrm{s}^{-1}$ at room temperature [135, 136].
- It has been measured by several groups that the iodide (vacancy) mobility is enhanced by several orders of magnitude upon light illumination. This effect
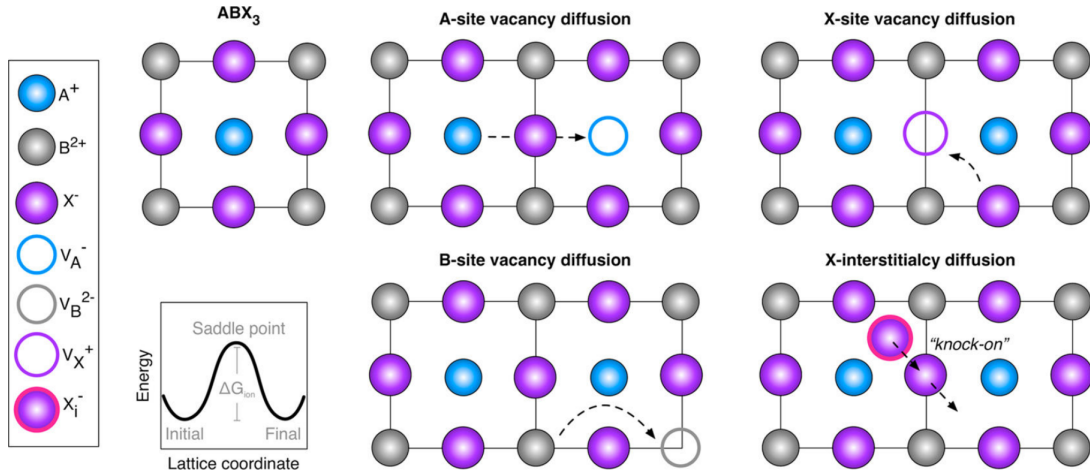
Figure 2.15: Illustration of possible mechanisms for ionic transport mediated by the activated diffusion of charged point defects in ABX_3 perovskite. The filled circles represent regular lattice sites containing charged ions, the empty circles represent charged vacancies, and the halide interstitial is highlighted. ΔG_{ion} denotes the activation energy for the respective defects. Reproduced with permission from [127]. Copyright 2018, American Chemical Society.

already takes place at very low illumination levels (~1 mW/cm^2 [34, 137, 138]. Barboni *et al.* recently proposed, from molecular dynamics (MD) simulations of iodine tracer diffusion, that this effect originates from a shift in the anti-Frenkel disorder equilibrium: the filling of interstitial trap sites with light generated holes leads to the formation of more defects (vacancies + interstitials) and thus increases the contribution of iodine vacancies to the measured ionic mobility [135].

- Senocrate *et al.* measured the MA$^+$ migration in the dark and under illumination by solid-state NMR and tracer diffusion experiments [33, 139]. They concluded that the diffusion coefficient for MA$^+$ species ($D_{MAI} \approx 10^{-14}\,\text{cm}^2\,\text{s}^{-1}$) is several orders of magnitude smaller as compared to iodide species and not affected by light illumination. Hence, MA species must have a considerable higher activation energy compared to iodine species, in line with DFT calculations [131].

The drift or diffusion of ions within the crystal lattice leads to several problems. The drift of ions in response to an electric field is considered to be responsible for the commonly observed current-voltage hysteresis in solar cell devices [35, 140–142]. There is a complex interplay between ionic and electronic response upon applying an electric field, and the exact causes for hysteresis are thus not easy to identify. These various complex and coupled phenomena have been summarized by Tress *et al.* (Figure 2.14). For example, ionic drift is responsible for a huge low-frequency dielectric response, which is enhanced upon light illumination due to the increased amount of iodide defect species, as described before [75, 119, 143]. A famous approach to study the hysteretic behaviour at interfaces is to measure transient capacitive currents in-

duced at the interfaces due to the ionic drift and interfacial recombination [144–146].

Recent results from both experimental and theoretical studies suggest that only the combination of ion migration coupled with the existence of interfacial trap states results in severe hysteresis [140, 147–150]. Weber *et al.* , employing time resolved Kelvin probe force microscopy at the cross section of cleaved devices, proposed that the formation (~3 ms) and slow release (~120 ms) of interfacial charges is the dominating factor for current–voltage hysteresis [150]. Simulations from Neukom *et al.* showed that if the charge carrier diffusion length of the perovskite absorber layer is long and the surface recombination velocity is low, highly-efficient devices without hysteresis are feasible despite the migration of ions [149]. These results could explain the recent success of various methods to reduce hysteresis. For example, Rong *et al.* proposed that hysteresis is caused by the polarization of the c-TiO$_2$/perovskite interface. The authors related it to the kinetics of accumulation of positive charges during J–V scans and subsequent surface recombination [151]. They were able to reduce the hysteresis by modifying the properties of the c-TiO$_2$ layer. Guerrero *et al.* suggested the presence of a charge injection barrier at the organic–perovskite interfaces as one major cause for hysteresis [146]. By fine-tuning the energy levels of the extraction layers the authors were able to substantially reduce device hysteresis. Other approaches include surface specific treatments [152], the use of thin interlayers between the perovskite and charge extraction layers [153] or optimizing the charge balance between the ETL and HTL [154]. All of these approaches resulted in highly-efficient devices with an increased V$_{OC}$ and low hysteresis. While ion migration in such optimized devices is not suppressed, it has no influence on the charge extraction dynamics and stabilized efficiency of the devices anymore.
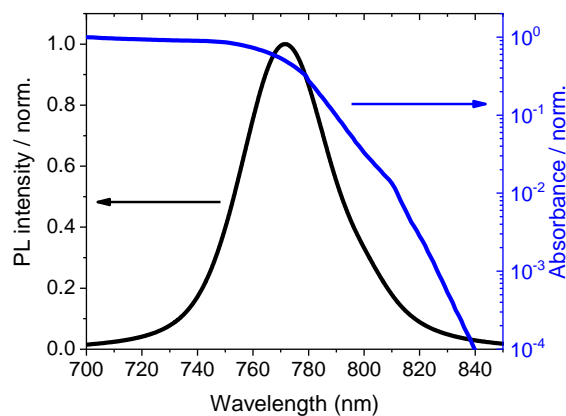
Figure 2.16: Photoluminescence spectrum (left axis) as measured by confocal PL (Sec. 3.2.7) and absorption spectrum (right axis) as measured by photothermal deflection spectroscopy (PDS, Sec. 3.2.9) of MAPbI$_3$ films on glass/PDS substrates.
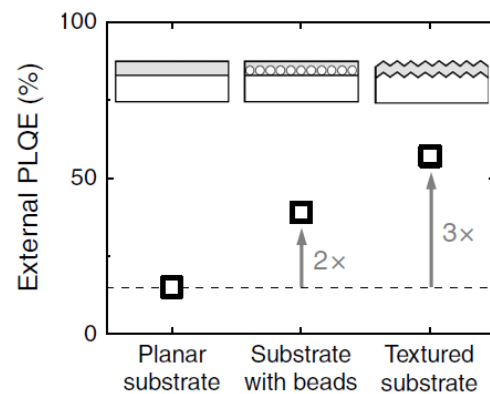
Figure 2.17: External PLQEs for MAPbI$_3$ films on different substrates. The planar film exhibited an PLQE of 20% (dashed line), while the film on a textured substrate exhibited PLQEs of 57%. Reproduced with permission from [155]. Copyright 2016, Nature Publishing Group.

However, the screening effects of mobile ionic defects makes the application of perovskite materials in transistors very challenging [28, 156, 157]. Moreover, the ionic movement can result in long-term instability due to various factors: electrode degradation [158], chemical reactions between the ions and other layers [145, 159] or decomposition of the perovskite by escape of volatile components [40]. One solution for these problems might be employing extrinsic alkali atoms (Rb, K, Na, Li) which were shown to strongly suppress ion migration and thus hysteresis [160–163].

2.2.6 Photoluminescence Properties

To reach the theoretical limits for solar cells (Sec. 2.1) and other optoelectronic applications, the luminescence of the absorber layer must be maximized [164]. Hence, to achieve a high internal quantum efficiency, non-radiative pathways need to be minimized, and every such loss will result in a reduction of the quasi-Fermi level splitting, which in turn reduces the obtainable device V_{OC} [165].
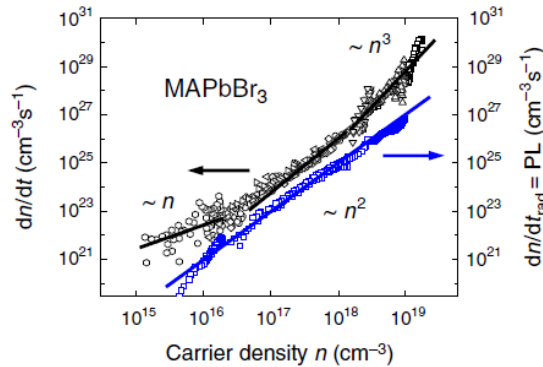
Figure 2.18: Total (black) and radiative (blue) recombination rate dependence on charge carrier density n derived from TA and PL measurements in the study by Richter *et al.* [155]. The radiative recombination rate scales quadratically with carrier density even in regimes where the total recombination rate is linear or cubic when plotted over excitation density. The authors concluded that PL is purely bimolecular. Reproduced with permission from [155]. Copyright 2016, Nature Publishing Group.
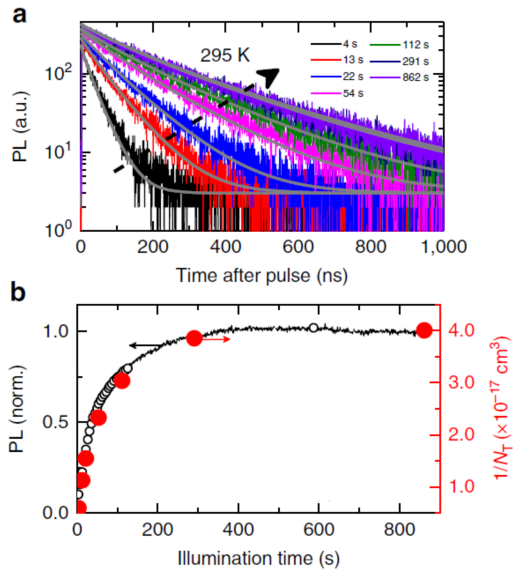
Figure 2.19: (a) Series of time-resolved PL decays from a MAPbI$_3$ film measured over time under illumination in N$_2$. (b) The PL over time determined from integrating acquired PL decays (black open symbols) or monitoring the PL count rate (black solid line). The red symbols are inverse trap densities $1/N_T$, where N_T are extracted from the fits to the data in (a) (grey lines). Reproduced with permission from [129]. Copyright 2016, Nature Publishing Group.

Metal halide perovskite materials exhibit high photoluminescence quantum yields with a rather low non-radiative recombination rate, especially considering their high

density of defects. This can be attributed to their high defect tolerance as described in the last sections [23]. Determining the internal photoluminescence quantum efficiency (PLQE, ν_{int}) in perovskite materials is complicated due to their high refractive index of $n \approx 2.5$ [166]. Due to Snell's law, only a small portion of the light generated within a film can be out-coupled, in the case that the film is smooth and without pinholes [46]. For perovskite films deposited on glass this results in an escape probability of around $\nu_{esc} \approx 13\%$ [155]. This might set an intrinsic limit on the measurable external PLQE, $\nu_{ext} = \nu_{esc} \cdot \nu_{int}$. A typical PL and the corresponding absorption spectrum of MAPbI$_3$, as measured in our laboratories, is shown in Figure 2.16. As can be seen the PL peak and absorption show a strong overlap (i.e. small Stokes-shift [46]). The fact that most of the light is trapped within the film results in the possibility for re-absorption of generated photons. The process in which re-absorbed photons are then re-emitted is called photon-recycling, and it has recently been experimentally observed in MAPbI$_3$ films [167]. In the scenario that a material exhibits a high ν_{int} of above 80%, photon recycling can be beneficial for a solar cell, while for much lower ν_{int} it is instead a parasitic loss channel, because the re-absorbed photons have a high chance to recombine non-radiatively [23, 46]. Richter *et al.* proposed that photon recycling might contribute significantly to the external PLQE of perovskite materials, and showed that enhancing the out-coupling efficiency of MAPbI$_3$ films does result in a strongly enhanced ν_{ext} ([155]; see Figure 2.17). Considering numerous recycling and out-coupling events, the correlation between internal and external PLQE can be written as [155, 168]:

$$\begin{aligned}
\nu_{ext} &= \nu_{esc} \cdot \nu_{int} + (1 - \nu_{esc})\nu_{int}^2 \cdot \nu_{esc} + \ldots \\
&= \nu_{esc}\nu_{int} \cdot \sum_{k}^{\infty} (1 - \nu_{esc})^k \cdot \nu_{int}^k \\
&= \frac{\nu_{int} \cdot \nu_{esc}}{1 - \nu_{int} + \nu_{esc} \cdot \nu_{int}}
\end{aligned} \tag{2.10}$$

Once a charge carrier is excited it can undergo mono-, bi-, or trimolecular recombination (Sec. 2.1.3). From intensity dependent transient absorption (TA) measurements, Richter *et al.* concluded that all three charge carrier recombination pathways are present for all MAPbX$_3$ perovskite materials [155]. The different regimes are exemplary shown in Figure 2.18 for the case of MAPbBr$_3$ (left axis), and the overall charge carrier recombination rate can be written as:

$$\frac{dn}{dt} = a \cdot n + b \cdot n^2 + c \cdot n^3 \tag{2.11}$$

Comparing TA to intensity dependent PL decay data, the authors concluded that radiative recombination in MAPbX$_3$ is purely bimolecular (see Figure 2.18, right axis). However, their data could only satisfactorily be described by assuming a non-radiative contribution to the bimolecular charge carrier recombination $b = b_{rad,int} + b_{non}$.

The authors proposed a general expression, taking non-radiative trap-assisted (SRH) recombination and Auger recombination into account (Sec. 2.1.3), connecting the charge carrier density in a perovskite film with the measurable external radiative PLQE by:

$$\nu_{\text{ext}}(n) = \frac{b_{\text{rad,int}} \cdot n^2}{a \cdot n + (b_{\text{rad,int}} + b_{\text{non}}) \cdot n^2 + c \cdot n^3} \tag{2.12}$$

The recombination constants for MAPbI$_3$ perovskite have been reported to be on the order of $a \approx (1 - 250) \cdot 10^6 \, \text{s}^{-1}$, $b = b_{\text{non}} + b_{\text{rad,ext}} \approx 8 \cdot 10^{-11} \, \text{cm}^3/\text{s}$, $b_{\text{rad,int}} \approx (0.8 - 20) \cdot 10^{-10} \, \text{cm}^3/\text{s}$ and $c \approx 10^{-28} \, \text{cm}^6/\text{s}$ [120, 155]. The values strongly depend on the fabrication process (growth conditions) and thus quality of the perovskite films, which especially explains the large spread in the reported values for a. At excitation fluences around 1 sun the charge carrier density in MAPbI$_3$ is ~$10^{15} \, \text{cm}^{-3}$ [155]. Hence, mono- and bimolecular recombination pathways are dominating at solar fluences and Auger processes only become dominant at high charge carrier densities above ~$10^{18} \, \text{cm}^{-3}$ (equation 2.11).

DeQuilettes *et al.* in detail studied the evolution of PL lifetimes of MAPbI$_3$ films upon constant laser illumination in N$_2$ atmosphere ([129]; see Figure 2.19). The authors observed enhanced PL yields and lifetimes, corresponding to a reduction of the trap density. Employing ToF-SIMS measurements, the authors revealed that the concentration of iodide atoms was reduced in the laser-exposed area. They proposed a photo-induced redistribution of iodide halide ions upon illumination, consistent with a reduced activation energy for iodide migration as discussed before (see Figure 2.20; Sec. 2.2.5). The reduced iodide interstitial concentration, and concurrent filling of iodide vacancy traps by I$^-$ and electrons was proposed to be the reason for the enhanced PL yields and lifetimes in the first few minutes of illumination.

DeQuilettes *et al.* also studied MAPbI$_3$ surfaces with confocal PL microscopy and revealed a strong heterogeneity in defect density [169]. Employing Lewis bases as surface-specific treatments to reduce non-radiative recombination caused by surface defects, the authors observed extended PL lifetimes, from ~1 µs for untreated, and up to ~8.8 µs for treated MAPbI$_3$ films. The same group employed both confocal and wide-field fluorescence imaging and revealed that charge carriers in MAPbI$_3$ show anisotropic diffusion due to differences in intergrain connectivity [170]. The authors observed trap-dominated variations in local photoluminescence intensity and attributed this effect to local variations in non-radiative recombination. The same conclusions were drawn by Draguta *et al.* from Spatially Resolved Emission vs. Excitation Measurements of MAPbI$_3$ films [171]. The authors observed strong intrafilm heterogeneities caused by a non-uniform trap state density distributions, with some regions exhibiting purely bimolecular recombination and others strong trap-mediated recombination at 1 sun excitation intensities.

Uratini *et al.* employed DFT calculations and studied the influence of defects at MAPbI$_3$ surfaces on charge carrier trapping. They proposed that the type of crystal surface termination strongly influences trapping rate and proposed that films grown
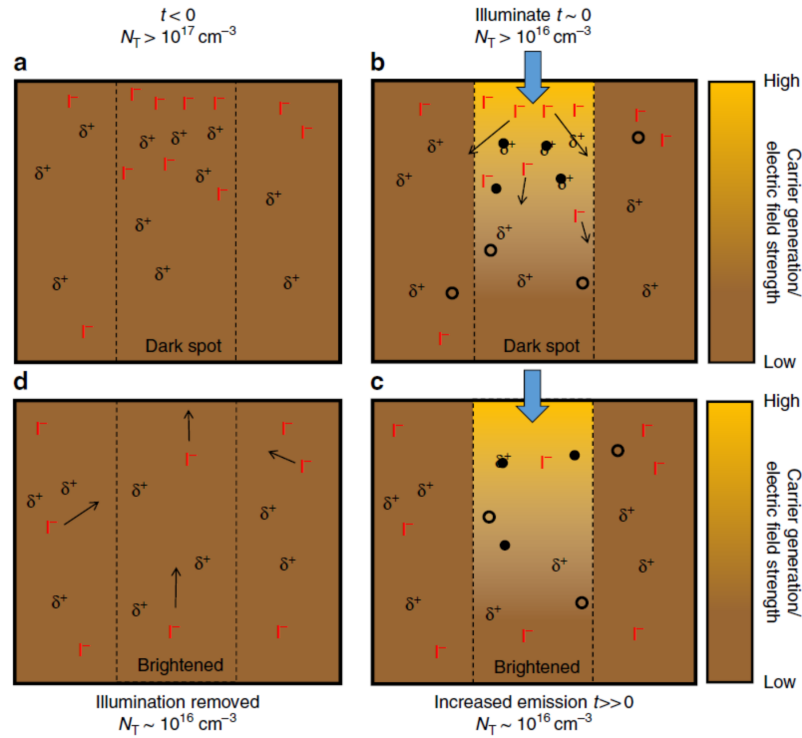
Figure 2.20: Proposed mechanism of photo-induced iodide redistribution on a cross-section of a MAPbI$_3$ film [129]: (a) The trap density in a 'dark spot' is initially high with a corresponding excess of iodide. (b) Upon illumination, electrons quickly fill traps, inducing an electric field (denoted by orange-brown colors) that causes iodide to migrate away and fill iodide vacancies. (c) The system exhibits a stabilized emission output with reduced concentration of iodide and traps in the illuminated region. (d) Concentration gradients possibly drive some iodide interstitals back until a new equilibrium is reached. δ^+ are iodide (I$^-$) vacancies, filled circles are electrons, open circles are holes. Reproduced with permission from [129]. Copyright 2016, Nature Publishing Group.

in *iodide rich* environments would show the highest trapping rates caused by iodide interstitials [172], in line with the results described above and discussed in Sec. 2.2.3.

Very recently, two studies reported internal PLQEs of over 90%. The first employed absolute-intensity PL measurements on Lewis-Base surface-passivated MAPbI$_3$ films [173]. The second incorporated Potassium (K) into a multiple-cation perovskite film, which strongly reduced ion migration and with it non-radiative recombination [161]. However, it is beyond the scope of this thesis to discuss these results in more detail. A good summary of the properties of light emission as well as causes for non-radiative losses in perovskite materials can be found in recent reviews by Stranks *et al.* [23, 174].

2.3   Application of Metal Halide Perovskites in Solar Cells

In 2012, Kim *et al.* reported the use of perovskite materials in the 'standard' n-i-p architecture. They used mesoporous TiO_2 as the electron transport layer (ETL) and small molecule solid state 2,2′,7,7′-Tetrakis[N,N-di(4-methoxyphenyl)amino]-9,9′-spiro-bifluorene (Spiro-OMeTAD) as the hole transport layer (HTL) and reached PCEs up to 9.7%. In the same year, Snaith and coworkers reported on a meso-superstructured n-i-p structure by replacing the mesoporous TiO_2 with Al_2O_3 as an inert scaffold and demonstrated an outstanding open-circuit voltage (V_{OC}) of 1.1 V and a PCE of 10.9% [13]. The insulating character of Al_2O_3 revealed the ambipolar charge-transport characteristics of $MAPbI_3$. Based on this knowledge, Lie *et al.* demonstrated a planar n-i-p structure using thin TiO_2 as the ETL and a vapor deposited $MAPbI_3$ film [175]. Finally, after the pioneering work of Jeng *et al.* [176], Docampo *et al.* fabricated decently efficient cells approaching 10% in the 'inverted' p-i-n structure using PEDOT:PSS and [6,6]-Phenyl-C61-butyric acid methyl ester ($PC_{60}BM$) as HTL and ETL respectively [177]. These three device architectures are commonly employed for perovskite solar cell fabrication and are shown schematically in Figure 2.21.

2.3.1   Device Architectures

In order to simplify the device architecture and reduce material costs, a lot of progress has also been made in the development of ETL-free or HTL-free solar cell architectures [178]. The efficiency and stability of such cells, however, still lag behind the commonly employed architectures and are not further discussed here.

2.3.1.1   Standard Architecture - n-i-p Structure

The 'regular' architecture (n-i-p) in the simplest form consists of a layer stack of FTO or ITO/ETL/perovskite/HTL/metal (middle of Figure 2.21). The most commonly used ETL materials are TiO_2 [179], SnO_2 [180–182] and ZnO [183], while for the HTL these are Spiro-OMeTAD [184] or the more stable Poly[bis(4-phenyl)(2,4,6-trimethyl-phenyl)amine (PTAA) [185]. In the mesosoporous configuration (Figure 2.21, left), a mesoscopic metal oxide, typically TiO_2, is applied on top of the ETL [44]. The HTL in this device architecture is typically doped using lithium bis(trifluoromethylsul-fonyl)imide (Li-TFSI) salt and 4-tert-Butylpyridine (tBP). In this study, the planar n-i-p structure is used for device results in Chapter 5.

2.3.1.2   Inverted Architecture - p-i-n Structure

The 'inverted' architecture for perovskite solar cells resembles the regular architecture known from organic solar cells which has been studied for over a decade, and consists of the architecture ITO/HTL/perovskite/ETL/HBL/metal [186, 187] (Figure 2.21, right). Typically used materials as HTL are NiO [188–190], PTAA [191–193], PEDOT:PSS and Poly-TPD, while for the ETL these are $PC_{60}BM$ and C_{60} [153, 192,
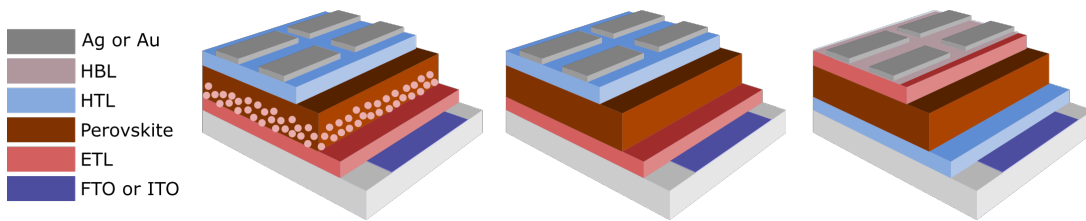
Figure 2.21: Schematic illustration of the three common perovskite architectures: Regular mesoporous n-i-p (left), regular planar n-i-p (middle) and inverted planar p-i-n (right).

193]. Similar to organic solar cells, an additional Hole blocking layer (HBL) material such as bathocuproine (BCP), TiO_2 or poly[(9,9-bis(3′-(N,N-dimethylamino)propyl)-2,7-fluorene)-alt-2,7-(9,9–dioctylfluorene)] (PFN) is employed to optimize charge extraction and minimize recombination at the ETL/metal (Ag,Cu,Au) interface. Recent literature developments with regard to PEDOT:PSS, poly[N,N′-bis(4-butylphenyl)-N,N′-bis(phenyl)benzidine] (poly-TPD) and $PC_{60}BM$ are summarized in the following.

PEDOT:PSS as HTL

PEDOT:PSS is a well-studied material and has been regularly employed in organic solar cells [194]. Due to the promising results from Jeng *et al.* [176] and Docampo *et al.* [177], it was employed as HTL in perovskite solar cells early on and decent device performances approaching 18% have already been reported by using a special 'hot-casting' deposition method for the perovskite film [195]. However, a high spread in reported PV parameters, especially the V_{OC}, had become apparent for devices employing PEDOT:PSS [196, 197]. It was proposed that severe surface recombination at the PEDOT:PSS interface limits the obtainable V_{OC} [189, 198]. Liu *et al.* proposed that this effect is caused by a chemical reaction between the methylammonium iodide, CH_3NH_3I (MAI) in the perovskite precursor solution and the PEDOT:PSS surface, which would result in a reduction of the work function of PEDOT:PSS [199]. Furthermore, devices employing PEDOT:PSS have been shown to degrade more rapidly under full illumination compared to devices employing e.g. NiO as the HTL [200]. This effect has been attributed to an increased rate of trap state formation at the PEDOT:PSS/perovskite interface [201]. Chuantian *et al.* proposed a method to obtain higher device V_{OC}'s by adding PSS-Na into the typically used Clevios PV P AI0843 PEDOT:PSS solution [202]. The modified PEDOT:PSS (m-PEDOT:PSS) film possessed higher transmittance and a higher work function, resulting in a better alignment with the perovskite valance band (VB). High V_{OC}'s of up to 1.11 V and 1.52 V were demonstrated for devices based on $MAPbI_3$ and $MAPbBr_3$ respectively.

Poly-TPD as HTL

Another typically polymer employed as HTL for perovskite solar cells is poly-TPD which has the advantage of possessing a higher work function as compared to PEDOT:PSS, resulting in a better alignment with the perovskite VB. However, Poly-

TPD is very hydrophobic and thus has low wettability for the perovskite solution, impeding full surface coverage. Thus, at first it has been reported only for vacuum deposited perovskite solar cells [203–205]. Later, Zhao *et al.* reported the fabrication of a perovskite layer on top of poly-TPD by solution processing [206]. The authors found that it was possible to form a PbI_2 precursor layer on poly-TPD with full coverage for subsequent conversion to $MAPbI_3$ by a two-step process (Sec. 2.3.2.3). Cheng *et al.* proposed that the atmosphere (N_2 or O_2) and substrate temperature during deposition of the PbI_2 layer is critical to yield optimized microstructure for subsequent conversion to $MAPbI_3$ [207]. Bi *et al.* studied the formation of perovskite by a two-step process on various polymers with different wetting properties and revealed that much larger grains with a lower defect density form on non-wetting surfaces [191]. To also enable the deposition of perovskite by a one-step process (Sec. 2.3.2.1), various groups reported that a short O_2 plasma [208–210] or UV-ozone treatment [207, 211, 212] improves the wettability of various hydrophobic polymers (e.g. PTAA, P3HT and Poly-TPD) and thus enables full perovskite film coverage. Another approach introduces an interfacial compatabilizer (amphiphilic PFN-Br) between hydrophobic polymer HTLs and the perovskite layer to improve the surface wettability without affecting the electronic properties of the devices [213]. When using FTO substrates, employing a piranha treatment (ITO will be etched away by this process) to improve the FTO surface wettability (Sec. 3.1.4) also allows for the deposition of perovskite layers [86, 214]. To summarize, inverted perovskite solar cells using poly-TPD show an enhanced V_{OC} compared to devices using PEDOT:PSS. This is due to a deeper lying work function [206], less surface recombination [198] and an enhanced grain size resulting from a reduced wettability [191, 212].

$PC_{60}BM$ as ETL

$PC_{60}BM$ has been employed as ETL in the first reports of inverted architecture perovskite solar cells [176, 177]. It is still the most commonly used ETL in the inverted architecture and also regularly employed as interlayer between the ETL and perovskite in the standard architecture [215]. The main motivation is the fact that the inverted architecture (using either $PC_{60}BM$ or C_{60}) yields devices without the commonly observed JV-hysteresis [108, 216, 217]. Various explanations for this effect have been put forward, such as a more balanced transport of electrons and holes [217], immobilization of ionic species [108, 218] and passivation of charge traps at the perovskite film surface [108, 216]. A combination of all these effects is the most realistic. Firstly, $PC_{60}BM$ is an efficient electron acceptor and promotes electron transport and extraction, which itself could help to reduce ion migration induced effects on the JV-characteristics as proposed by DeBastiani *et al.* [219]. Xu *et al.* proposed that $PC_{60}BM$ molecules are able to interact with Pb-I antisite defects, tying up iodide-rich surface sites or unincorporated iodide anions at the grain boundaries, and thus reduce ion migration [108]. Park *et al.* demonstrated a higher thermal stability of $MAPbI_3$ doped with small amounts of $PC_{60}BM$ and hypothesized that it binds mobile halides at grain

boundaries to their original sites in the perovskite crystal lattice, and thereby prevents them from migrating [220]. Furthermore, $PC_{60}BM$ was suggested to reduce the amount of surface traps, which in turn reduces charge carrier recombination at the perovskite/$PC_{60}BM$ interface and promotes efficient charge extraction [216, 217, 221].

2.3.2   Deposition Methods

Due to the efforts to optimize the perovskite microstructure, an immense amount of recipes for the deposition of perovskite layers have been developed and investigated [222]. Perovskite can easily be deposited from solution at low temperatures. Hence, it can not only be deposited by a typical spin-coating process, but offers the possibility to be printed by various methods (e.g. inkjet-printing [223], blade-coating [224] and slot-die coating [225]) and to be evaporated [226]. Such methods are important for a scale-up of perovskite to make it a viable solution for terawatt-scale energy production with low production costs in the future [18]. For research purposes the perovskite layer typically is spin-coated. In this section, the most common spin-coating methods to fabricate high quality perovskite layers are introduced and discussed. These methods are graphically illustrated in Figure 2.22.

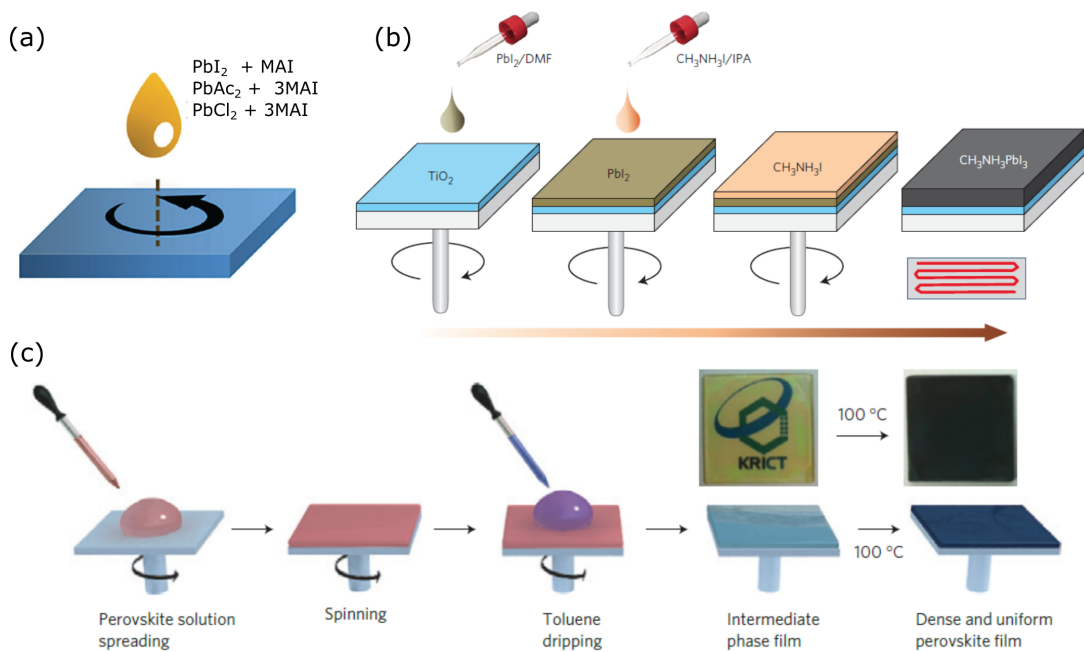**Figure 2.22:** Schematic illustration of common spin-coating methods for perovskite film fabrication: (a) One-step spin-coating. Reproduced with permission [227]. Copyright 2015, Wiley VCH. (b) Two-step spin-coating. Reproduced with permission [228]. Copyright 2014, Nature Publishing Group. (c) Solvent engineering technique. Reproduced with permission [229]. Copyright 2014, Nature Publishing Group.

2.3.2.1   One-step Recipes

For the so-called one-step recipes, the precursors of the perovskite are mixed together in a polar solvent - which can be GBL, DMF or DMSO. The solution is spin-coated in a single step and afterwards the substrates are annealed on a hotplate - typically at 100 °C for a certain time (see Figure 2.22 (a)). The solution chemistry of perovskite materials is a rather complex. It has been revealed that solutions of MAI:PbI$_2$ in DMF can be described as colloidal dispersion in a mother solution, rather than a pure solution [45]. For example, the amount of defects in the final film has been correlated to the amount of iodoplumbate coordination complexes in the precursor solution [230]. Furthermore, the colloid concentration of the precursor solution can have a direct impact on the crystal quality and morphology of the perovskite films as they are acting as nucleation centers [231]. Furthermore, different stages during the crystallization in a one-step process have been observed, which crucially depend on the lead anion employed as precursor [232–235]. The final microstructure of the perovskite films depends on, amongst others, the substrate, precursor combinations, colloidal concentration, annealing procedure and surrounding atmosphere during deposition (water, solvent vapors). Here, the most common one-step methods are shortly discussed.

Lead Iodide (PbI$_2$) Based Recipe

In a one-step process employing a 1:1 molar ratio of MAI and PbI$_2$ dissolved in GBL or DMF, the fast solvent evaporation during spin-coating results in the formation of needle like structures [45, 236] and such films do not yield complete surface coverage. The existence of shunting pathways between the ETL and HTL increases leakage currents and might result in recombination losses at the interfaces. Employing a strong molar excess of the organic component in the precursor solution (for example, an MAI excess with 3:1 (MAI:PbI$_2$)) results in films with improved surface coverage [45, 236–239]. However, a higher annealing temperature of ~150 °C is required to induce formation MAPbI$_3$. The resulting films possess an increased defect density and do not result in solar cells with high PCE [238]. Other studies reported that the use of additives (such as HI [217, 239–241], HCl [242] or PbSCN [243–247]) in a precursor solution with a 1:1 (MAI:PbI$_2$) ratio leads to smooth and reproducible films. This effect might be explained by a change of the pH-value of the precursor solution, which strongly affects the distribution of colloids as recently revealed by McMeekin *et al.* and Noel *et al.* [231, 248].

Lead Chloride (PbCl$_2$) based Recipe

To overcome the problem of incomplete surface coverage and high defect density, a recipe based on PbCl$_2$ as precursor was developed [13]. In this recipe, one equivalent of PbCl$_2$ is mixed with three equivalents of MAI in DMF. Two equivalents of MACl slowly evaporate out of the film, with various intermediate phases and crystal structures being formed during the long thermal annealing process (ca. 100 min at SI150°C) [237, 249], until the final MAPbI$_3$ forms. Recently is has been revealed, that

the as-spun film consists of a crystalline precursor MA_2PbI_2Cl phase, coexisting with disordered MACl. The gradual evaporation of MACl during the thermal annealing leads to the formation of high quality $MAPbI_3$ [250]. Fabrication procedures employing Cl as precursor often result in films with a a low defect density [251, 252]. This was explained by the fact that a small amount of chloride ($< 1\%$) actually stays in the film and results in better optoelectronic properties, possibly due to a reduction of intrinsic defects [249, 253, 254]). When fine tuning the spin-coating and annealing procedure, the $PbCl_2$ route results in films with a reduced amount of pinholes compared to the PbI_2 based recipes. However, a certain amount of pinholes often remains and the films show a rather rough surface [238, 255].

Lead Acetate ($PbAc_2$) Based Recipe

Similar to the use of $PbCl_2$ as lead anion, Buin *et al.* introduced lead acetate (Pb-$(CH_3COO)_2\cdot 3H_2O$; $PbAc_2$) in the precursor solution [105]. They revealed that films grown in iodide poor conditions (using Ac or Cl as lead anion) possess much lower trap densities compared to films fabricated with PbI_2. Zhang *et al.* introduced a recipe for devices using $PbAc_2$ and showed that the resulting layers were ultrasmooth and without any pinholes [238]. The annealing process took less than $5\,min$ due to the volatile nature of the byproduct methylammonium acetate (MA(OAc)) [234]. Furthermore, the acetate anion is unlikely to be incorporated into the perovskite crystal lattice due to its small ionic radius [238]. This recipe was further improved by adding hypophosporous acid solution (HPA) into the precursor solution [256]. The addition of HPA resulted in an enhanced grain size with the grains growing with their z-axis perpendicular to the substrate. The films showed better optoelectronic properties due to a reduced energetic disorder and defect density. The authors attributed these effects to the reducing character of HPA, which could reduce trace amounts of I_2 in the precursor solution during thermal annealing, thus providing a better precursor stoichiometry [256]. As mentioned above, the pH-value of the precursor solution in a one-step recipe also plays an important role for the final film quality, as it affects the colloid concentration [248]. Because it has been shown that HPA changes the pH value of a perovskite solution, this could be another factor in the synergistic effect when using it as an additive. Finally, Levchuk *et al.* showed that during synthesis of MAI - using hydroiodic acid (HI) with HPA as a stabilizer - a small amount of impurities remains in the MAI powder if not sufficiently purified [257]. Such impurities (stemming from the stabilizer HPA) were shown to form $PbHPO_3$ nanoparticles in the precursor solution which, in the right concentration, resulted in better solar cell performances by acting as nucleation centers for perovskite crystal growth. Hence, the intentional addition of HPA into a $PbAc_2$ based precursor solution might profit from this effect, too.

The $PbAc_2$ recipe can be used both in the standard and inverted architectures [258]. It is, however, especially suited for the inverted architecture, as it yields full film coverage and a very low surface roughness. This allows it to be coated by a very

thin layer of $PC_{60}BM$ without producing pinholes in the ETL, reducing the series resistance ([259]; Sec. 2.1). For most parts of this study, a recipe based on $PbAc_2$ as precursor with the addition of HPA was chosen as it yielded reproducible results, full film coverage and large perovskite grains suitable for various characterization methods.

2.3.2.2 Solvent-engineering Recipe

The so-called solvent-engineering recipe was introduced in 2014 by Jeon *et al.* and to some extent revolutionized the way of producing pinhole free perovskite films (being the 7th highest cited perovskite publication) [229]. Similar to the one-step methods, all the precursors are mixed in one vial, but a combination of two solvents is employed, either GBL+DMSO or DMF+DMSO. During the spin-coating process, an antisolvent (e.g. Toluene, Chlorobenzene, Anisole etc.) is dripped onto the rotating substrate which results in the formation of an intermediate A-PbX_2-DMSO complex [260, 261]. During the subsequent thermal annealing process, pinhole free $APbX_3$ perovskite films are formed (see Figure 2.22 (c)). This method makes it possible to freely mix the different perovskite precursors and thus tune the bandgap and energetics. However, the solution chemistry and conversion process critically depend on the precursor composition [261, 262], the employed antisolvent [260, 261] and the timing of the treatment [263].

Mutli-cation Recipes

Employing multiple cations in a perovskite film was pioneered by Pellet *et al.* ([264]). They introduced formamidinium ($CH(NH_2)_2$, FA) in the conversion solution using a two-step recipe Sec. 2.3.2.3. Adapting this approach, Jeon *et al.* optimized the composition of the precursor solution in a solvent-engineering process by studying the compositional engineering of:

$$(FAPbI_3)_{1-x}(MAPbBr_3)_x. \tag{2.13}$$

A maximum PCE of up to 18% was achieved with the composition $(FAPbI_3)_{0.85}$(MAPbBr_3)$_{0.15}$. Bi *et al.* [265] used a lead excess in such a double cation ('MAFA') containing precursor solution, with a nominal composition of:

$$(FA_{0.85-x}MA_{0.15+x})Pb(I_{0.85-x}Br_{0.15+x})_3 + x\,PbI_2 \tag{2.14}$$
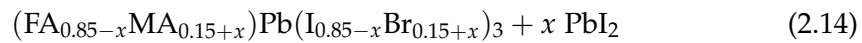
Excess PbI_2 of up to $x \approx 0.16$ resulted in improved performance and record V_{OC}'s up to 1.18 V. A breakthrough in perovskite research was reported by Saliba *et al.* . The authors employed a triple-cation precursor solution containing small amounts of Cesium (Cs), with the optimized nominal composition reported as 'CsMAFA' [266]:

$$Cs_{0.05}(FA_{0.83}MA_{0.13})_{0.95}Pb(I_{0.83}Br_{0.13}) + 0.02\,PbI_2 \tag{2.15}$$
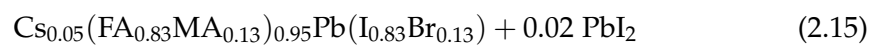
The Cs is able to be incorporated into the perovskite lattice and suppresses non-perovskite yellow phase impurities (δ-phase) in the perovskite films by tuning the tolerance factor ([267]; Sec. 2.2.1), This composition leads to an enhanced reproducibility, more phase pure films with a reduced defect density and strongly increased device stability. The addition of Rubidium (Rb) into CsMAFA or MAFA precursor solutions further enhances the performance with record V_{OC}'s of up to 1.24 V [185, 268]. The CsMAFA recipe and composition was the most commonly used in 2017 and 2018.

Quite recently, first groups employed potassium (K) as a dopant in the perovskite solution, which was shown to suppress the commonly observed hysteresis in devices [160, 163, 269]. However, later it was revealed that K and Rb are not able to be incorporated in the perovskite lattice. Rather it was suggested that they are present at the grain boundaries and surfaces or even phase segregate [161, 270, 271]. Recently it as been shown that Rb and Cs lead to a better halide homogenization in the films which results in more homogeneous electronic properties and improved solar cell performance [272]. K might have a similar effect and in addition has been proposed to inhibit ion migration by 'decorating' the grain boundaries and surfaces where it passivates trap states [161]. Another reason for the observed improvements using Cs or Rb could be a recent discovery by Gratia *et al.* . They reported the formation of hexagonal polytypes during the crystallization process when employing a solvent-engineering recipe, which were shown to be suppressed by the introduction of a small amount of Cs in the precursor solution [262].

2.3.2.3 Two-step Recipe

The so-called two-step recipe was introduced by Burschka *et al.* in 2013 [273]. In this recipe, first an inorganic layer of PbI_2 (the precursor layer) is coated on top of a substrate. Subsequently, the inorganic film can be converted to perovskite by various methods:

- Immersing the substrate into a conversion solution containing organic halides (e.g. MAI, FAI, MABr, MACl) dissolved in 2-Propanol (the original method by Burschka *et al.* used a pure MAI solution for conversion to $MAPbI_3$)
- Spin-coating of a conversion solution on top of the PbI_2 film ([274]; see Figure 2.22 (b))
- Exposing the PbI_2 film to an atmosphere containing organic halide vapour (VASP) [275]

While these methods typically result in pinhole free films, both for mesoporous as well as planar device configurations, the microstructure and final composition of the films is difficult to control. A lot of parameters can influence the conversion process [276], for example:

- The morphology of the precursor PbI_2 film must be fine-tuned by the choice of solvent (DMF, DMSO or, for best results, a mixture of DMF+DMSO [15, 277]), the temperature of the substrate and solution during spin-coating and the annealing temperature

- The concentration of the conversion solution during dipping or spin-coating
- The duration and temperature of the dipping process (VASP) or the wait time before starting the spin-coating process after applying the conversion solution
- The annealing temperature and duration, as well as the atmosphere during the conversion process

All these factors define the final microstructure and if any residual PbI$_2$ or excess organic halides are present in the film. While recently very high performance devices with efficiencies above 20% have been reported using the two-step method - employing either a mixture of MAI, FAI and MACl or FAI and MABr as the conversion solution [15, 277] - this method is only suited for small sized substrates and is difficult to scale up.

2.4 Current State of Research

2.4.1 Humidity Induced Degradation

Perovskite materials are prone to humidity induced degradation, which is often ascribed to the volatile and hygroscopic nature of the methylammonium cation [278, 279]. However, the exact processes governing the degradation rate, such as the humidity level, the combined effect of humidity and illumination, the role of crystal surface terminations, and more, are still openly debated in the perovskite research community. In addition to inducing degradation, humidity can actually be used to improve the crystal growth of perovskite materials under certain conditions, which makes the effect of water even more complicated to analyze [280]. In a recent review from Huang *et al.* , the effects - positive and negative - of H$_2$O on perovskite materials are summarized [41]. Here, we will consider important studies and developments in the understanding of humidity induced degradation, to provide a general conceptual understanding of this degradation pathway.

One of the first reports studying the stability of perovskite materials in humid atmospheres was published by Habisreutinger *et al.* [281]. They revealed that the stability under thermal stress at 80 °C in ambient air can be greatly enhanced by employing a carbon nanotube/polymer composite as HTL instead of the more commonly employed Spiro-OMeTAD or PTAA, which are typically doped with hygroscopic Li-TFSI [282, 283]. The authors attributed this effect to an increased barrier to moisture ingress and to a reduced thermally-induced escape probability for the volatile organic components in MAPbI$_3$. In a follow up study, the authors synthesized a new HTL material ('EH44') which does not requires to be doped by the hydrophilic Li-TFSI. Devices employing EH44 showed greatly improved stability against thermal stress and moisture [284]. Christians *et al.* recently employed EH44 as HTL in a study focused on stability and, by also tailoring the other interfaces in the device stack, achieved over 1000 h of operational stability for highly-efficient, state of the art under full light illumination [285].
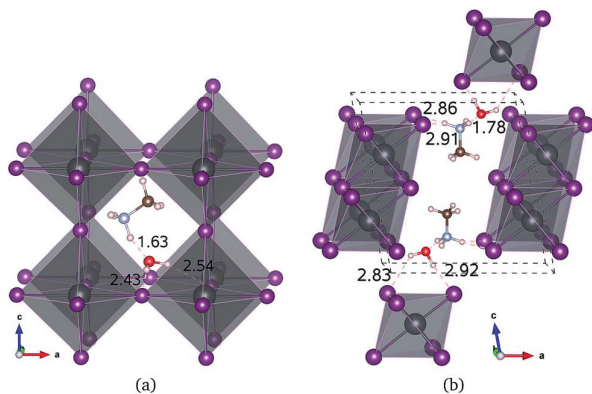
Figure 2.23: Proposed water intercalated phase $MAPbI_3$ _H_2O (a) and monohydrate phase $MAPbI_3$ ·H_2O (b) from DFT calculations by Jong *et al.* Hydrogen bonds are marked with dotted lines and the bond lengths are presented in units of angstrom. (dark grey: Pb; purple: I; brown: C; light blue: N; red: O; light pink: H). Reproduced with permission [286]. Copyright 2018, The Royal Society of Chemistry.

In 2015, Christians *et al.* and Yang *et al.* revealed the semi-reversible formation of a dihydrate perovskite phase, $(CH_3NH_3)_4PbI_6·2H_2O$ [287, 288]. This degradation occurred more rapidly under illumination [287] and the choice of the HTL material strongly influenced the degradation rate [288]. Later, Leguy *et al.* revealed an intermediate hydration step during the exposure of $MAPbI_3$ to humidity, which was completely reversible upon re-exposure to a dry atmosphere [289]. The authors showed that the intermediate phase is a monohydrate perovskite phase, $CH_3NH_3PbI_3·H_2O$, which forms upon exposure humidity levels of around 70%. Only after exposure to very high humidity levels ($\geq$ 80%) did they observed the formation of the dihydrate phase. Once the dihydrate phase has formed, it can irreversibly degrade via the following reaction:

$$(CH_3NH_3)_4PbI_6 \cdot 2H_2O \Rightarrow 4CH_3NH_3I + PbI_2 + 2H_2O \qquad (2.16)$$

To examine this process more closely, Li *et al.* performed in-situ atomic force microscopy (AFM) and X-ray diffraction (XRD) measurements on $MAPbI_3$ films after exposure to 80% humidity [290]. They observed that the initial formation of the monohydrate phase coincides with the appearance of additional grain boundaries and step like features in the films, which persisted upon drying the samples overnight. Most importantly, they found no morphological changes for films exposed to humidity levels of $\leq$ 50% for more than 140 h. Song *et al.* employed laser beam induced current (LBIC) mapping on $MAPbI_3$ films and proposed that the degradation process consists of three stages - the reversible formation of a monohydrate phase, the semi-reversible formation of a dihydrate phase, and lastly the irreversible decomposition into MAI and PbI_2 [291].

Mosconi *et al.* presented a computational study, based on first principle calculations, and predicted an easy infiltration of water molecules into the perovskite structure which would not result in a change of the structural properties [292]. The infiltration of H_2O into $MAPbI_3$ was observed experimentally by Müller *et al.* using infrared spectroscopy [278]. The authors proposed that water infiltrates the $MAPbI_3$ crystal lattice for humidity levels as low as 10%, which was not accompanied by the forma-

tion of any monohydrate phases. The authors suggested that H_2O has a strong effect on the hydrogen bonds between between the MA and the surrounding Pb-I cage. In addition, they reported an enhanced conductivity of films exposed to humidity which they attributed to enhanced ionic (proton) conduction. Interestingly, recent in situ grazing incidence neutron scattering (GISANS) measurements by Schlipf *et al.* suggest that water is only fully incorporated into the $MAPbI_3$ crystal lattice at humidities above $\approx$73%, a point at which the monohydrate phase starts to form and a change in morphology begins to appear. Only above 93% humidity was the dihydrate phase observed. For lower humidities, the authors suggested that $MAPbI_3$ absorbs a considerable amount of water ($\approx$10 vol%) which is, while not entering the bulk, absorbed on the crystal surfaces and possibly grain boundaries [293]. These results are consistent with the fact that no monohydrate phase was observed at lower humidities in the measurements by Müller *et al.* [278]. A similar conclusion was drawn by Zhu *et al.*, who studied the uptake of water with in situ infrared spectroscopy, mass monitoring, and X-ray diffraction [294]. They concluded that while water can enter the perovskite lattice at ambient conditions, it does not strongly interact with the perovskite, and no hydrogen bonds are formed until the monohydrate phase appears at high humidity levels.
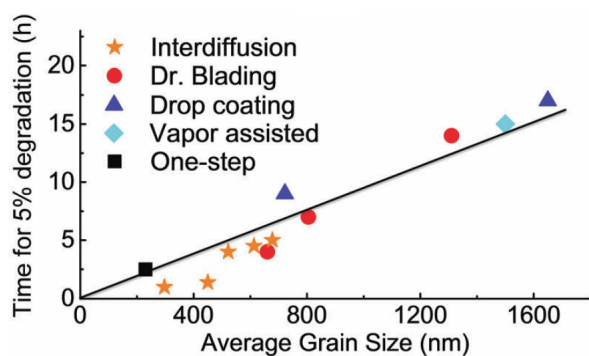

Figure 2.24: Time needed for degradation of black perovskite films with various grain sizes (fabricated by different methods as denoted) by 5% (of their total area) into a white perovskite phase at 85% humidity. The white degradation product was assigned to be either a mono- or dihydrate phase in that study. Reproduced with permission [295]. Copyright 2017, The Royal Society of Chemistry.

Recently, Jong *et al.* proposed from DFT calculations that water exothermically intercalates into the $MAPbI_3$ crystal lattice ($H_2O\_MAPbI_3$), and interacts with both the PbI_6 framework and the methylammonium ions *via* hydrogen bondings ([286]; see Figure 2.23). The authors proposed that these hydrogen bond interactions reduce the activation energy for vacancy mediated ionic transport and thus enhance ionic conductivity, in line with the experimental results discussed above. Finally, it was suggested that the reduced activation energies for ionic transport might be a reason for the long term instability of $MAPbI_3$ films in humid atmospheres, even at lower humidity levels. A scaling behavior of moisture induced grain degradation in $MAPbI_3$ films was proposed by Wang *et al.* [295]. They found a linear relationship between the grain size of their films and the conversion into mono- and/or dihydrate white perovskite phases (see Figure 2.24). Employing high resolution transmission electron microscopy (HRTEM) and scanning transmission electron microscopy (STEM), they

proposed that the grain boundaries of MAPbI$_3$ films consist of an amorphous, defect rich phase, which absorbs and reacts with water molecules faster than the surface and bulk of the films.

Zhao *et al.* studied the degradation of complete photovoltaic devices in dry and humid atmospheres in the dark and under illumination. They proposed that at lower humidity levels the redox chemistry dominates the degradation and decomposition of full devices (reaction of Pb^{2+} with the electrodes), and that moisture would enhance the diffusion of ions and accelerate this process, rather than to act as a reagent in the decomposition of the perovskite itself [296]. In slight contrast, Ma *et al.* degraded full devices in which the perovskite films were prepared with differing surface stoichiometry and proposed that the amount of polar MA$^+$ molecules at the layer surface has a strong affect on the humidity induced degradation rate of perovskite films and devices [297].

2.4.2 Oxygen Induced Degradation

The first report on oxygen induced photodegradation of MAPbI$_3$ was published in 2015 by Aristidou *et al.* [42]. Employing fluorescent molecular probe studies, the authors revealed that exposure of perovskite films to oxygen and light leads to an electron transfer from photoexcited MAPbI$_3$ to molecular oxygen, which results in the generation of superoxide (O$_2 \Rightarrow$ O$_2^-$). The superoxide molecule in turn can react with a methylammonium cation (CH$_3$NH$_3^+$) in the perovskite lattice by deprotonating it, thus resulting in the decomposition of MAPbI$_3$ into PbI$_2$ and other byproducts. They proposed the following degradation reaction:

$$CH_3NH_3PbI_3^* + O_2^- \Rightarrow CH_3NH_2 + PbI_2 + 1/2\,I_2 + H_2O \qquad (2.17)$$
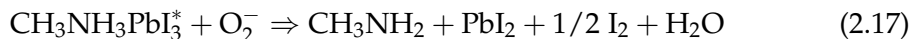
Bryant *et al.* degraded unencapsulated devices in the standard architecture, in dry atmosphere and under illumination, and found a rapid degradation of the PV parameters on a timescale of minutes to hours [298]. The rate of degradation was found to be much faster when compared to the degradation in humid air (85%) and illumination. The authors proposed that charge extraction layers, which rapidly extract electrons from the perovskite layer before they can react with oxygen to form superoxide, could help to reduce the rate of oxygen induced photodegradation [42, 298, 299]. Subsequently, Lin *et al.* employed PC$_{60}$BM as ETL in the inverted architecture and observed a strongly reduced degradation rate for devices in dry air atmosphere and under illumination when compared to devices in the standard architecture [221]. The authors attributed this effect to the passivation effects of PC$_{60}$BM as well as to its function as an oxygen barrier, rather than PC$_{60}$BM's capability as electron extracting contact (Sec. 2.3.1.2). Furthermore, they showed that the position of the LUMO level of the fullerene (employed as ETL) has an effect on how strongly oxygen induced degradation is suppressed. This direct dependence of the rate of superoxide generation on the LUMO position of fullerenes has previously been proposed for polymer

solar cells [300]. In a collaboration with Boris Rivkin, we also did not observe any difference between degradation of inverted devices using $PC_{60}BM$ in either N_2 or dry air atmosphere, further supporting that the use of $PC_{60}BM$ strongly suppresses oxygen induced degradation pathways [301].
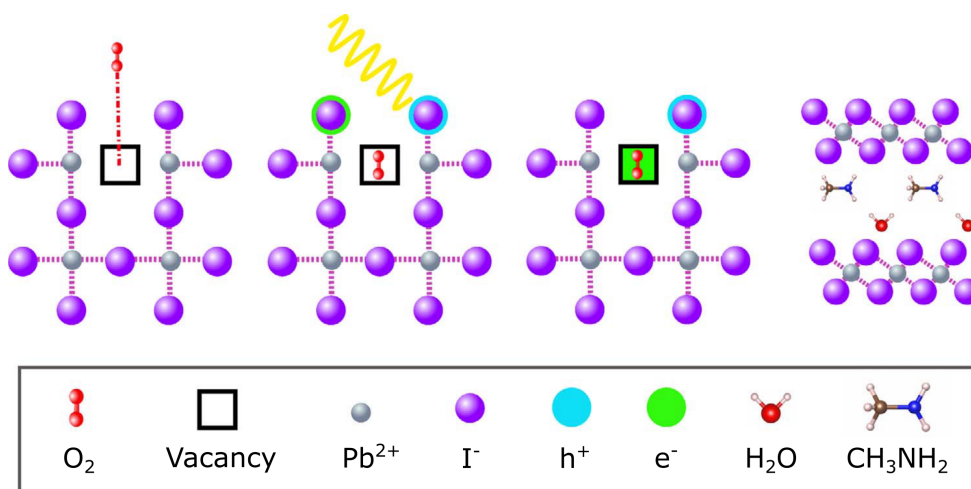

Figure 2.25: Schematic illustration of oxygen induced photodegradation of MAPbI$_3$: (a) Oxygen diffuses and incorporates into the lattice at vacancy sites, (b) MAPbI$_3$ becomes photoexcited (creation of electrons and holes), (c) superoxide formation by electron transfer to O$_2$, and (d) reaction with CH$_3$NH$_2$ and degradation into PbI$_2$, H$_2$O, I$_2$ and CH$_3$NH$_2$. Reproduced with permission from [302]. Copyright 2017, Nature Publishing Group.

Recently, fast diffusion of oxygen through the perovskite crystal lattice was observed by isothermal gravimetric analysis (IGA) [302]. Aristidou *et al.* hereby revealed that the rate of superoxide generation depends on the perovskite crystal grain size, with larger grains degrading significantly slower compared to smaller grains. A treatment by coating the perovskite film with either a salt solution containing iodide, or by I$_2$ vapor exposure, both were shown to slow down the rate of degradation. The authors suggested, supported by ab initio simulations, that oxygen molecules can reside in iodide vacancy sites within the perovskite crystal lattice, and that direct electron transfer from the perovskite to oxygen is energetically favorable. The superoxide molecules would subsequently react with MA$^+$, resulting in degradation as described by equation 2.17. The overall oxygen induced degradation mechanism proposed by Aristidou *et al.* is schematically depicted in Figure 2.25 [302].

In slight contrast to this report, experiments by Senocrate *et al.* indicate that oxygen incorporation in MAPbI$_3$ happens in the form of oxide ions (O^{2-}) rather than superoxide species [303]. Employing ToF-SIMS depth profiles, the authors proposed that incorporation of O$_2$ into the lattice is strongly enhanced upon light illumination. Employing tracer diffusion, they found fast oxygen diffusion and proposed that there is strong thermodynamic driving force towards degradation of MAPbI$_3$ and formation of H$_2$O under illumination.

There are also a number of theoretical studies (employing ab initio calculations),

which suggest various possible interactions, and reactions, between oxygen and the surface of MAPbI$_3$, or with defects within the crystal lattice. For example, calculations from Aristidou *et al.* propose that the combination of water and oxygen results in a strongly enhanced degradation rate, due to the fact that water catalyzes the reaction by stabilizing the reactive superoxide species [304]. All of these studies support the idea that superoxide is generated when photogenerated carriers are present in the film, resulting in a deprotonation of the MA molecule [302, 304–306]. To summarize, most studies suggest that the number of defects in the perovskite film, especially those of iodide vacancies, have a direct impact on the rate of oxygen induced photodegradation. As defects are often connected to the perovskite microstructure and grain boundaries in the films, there might be a direct correlation as we will reveal in Chapter 4.

2.4.3   Effects of Variations in Precursor Stoichiometry

In this section, literature reports studying the influence of precursor solution stoichiometry and/or film composition on the properties of MAPbI$_3$ films and devices will be discussed. The possibility of tuning the perovskite composition by adding multiple components in the precursor solution, such as FA, MA, I, Br, Cs, Rb and K, has been mentioned in Section 2.3.2.2. At this point, literature reports focusing on the composition MAPbI$_3$ will be discussed. The definitions regularly used in this thesis are:

- A 'stoichiometric precursor solution' contains the compounds in the right molar ratio to yield phase pure MAPbI$_3$. For example, a 1:1 molar ratio of MAI:PbI$_2$, a 3:1 molar ratio of MAI:PbCl$_2$ or a 3:1 molar ratio of MAI:PbAc$_2$. A 'stoichiometric film' denotes a film which has been fabricated with a stoichiometric precursor solution

- An 'overstoichiometric precursor solution' contains an excess of organic halides, for example, MAI or MABr. An 'overstoichiometric film' is fabricated by an overstoichiometric precursor solution

- An 'understoichiometric precursor solution' contains an excess of lead, for example, PbI$_2$, PbCl$_2$ or PbAc$_2$. An 'understoichiometric film' is fabricated by an understoichiometric precursor solution

In the early research of perovskite materials, a stoichiometric precursor solution was typically employed, both for one-step recipes as well as the solvent-engineering recipe (Sec. 2.3.2.1, 2.3.2.2). The first reports studying the influence of stoichiometry on perovskite film properties were published in 2014. In the following sections, reports employing two-step and one-step (including solvent-engineering) recipes will be discussed separately.

Results for Two-Step Recipes

During a two-step process, the amount of residual PbI_2 in the film and especially the final microstructure and surface composition is difficult to control. This stems from the fact that no over- or understoichiometric precursor solution can be employed in this recipe. Rather, the annealing and conversion processes must be fine-tuned to determine the final film composition and properties (see Sec. 2.3.2.3).

Chen *et al*. studied $MAPbI_3$ films fabricated by a two-step process in the standard architecture using TiO_2 as ETL. By controlling the annealing time, the authors were able to vary the amount of excess PbI_2 in the films, and found small amounts of residual PbI_2 had a positive effect on the PV parameters. This was attributed to a passivation effect at the grain boundaries, resulting in reduced non-radiative recombination [307]. Cao *et al*. performed a similar study, and found that a $\approx 2\%$ remnant of PbI_2 in films yielded optimum device performance [308]. Results from femtosecond spectroscopy measurements showed a slower charge carrier trapping rate in films with excess PbI_2, which was attributed to a passivation effect at the $TiO_2/MAPbI_3$ interface [309]. Wang *et al*. measured longer luminescence lifetimes of $FTO/TiO_2/m$-$TiO_2/MAPbI_3$ films with residual PbI_2, which also resulted in improved device performance. Again, the effect was attributed to an increased passivation effect at the m-$TiO_2/MAPbI_3$ interface [310].

In contrast to these results, by introducing an optimized two-step fabrication procedure, Thakur *et al*. proposed the advantages of phase pure $MAPbI_3$ layers without residual PbI_2, for which they found a higher photon absorption and longer charge carrier lifetimes [311]. The authors hypothesized that morphological differences in the films might be the reason for why earlier studies reported improved device performance for films with excess PbI_2. In line with these results, Liu *et al*. varied the amount of residual PbI_2 by altering the microstructure of the inorganic PbI_2 film before the conversion into $MAPbI_3$. Despite higher initial efficiencies, the cells with a small amount of excess PbI_2 showed reduced stability upon illumination in inert atmosphere as well as ambient conditions when compared to devices without excess PbI_2 [312].

Results for One-step and Solvent-engineering Recipes

Roldán-Carmona *et al*. were the first group to study the influence of stoichiometry in $MAPbI_3$ solar cells in the standard architecture, with mesoporous TiO_2 as ETL, fabricated by solvent-engineering. An excess of 5-10% PbI_2 resulted in improved device performance, possessing an increase in all PV parameters [313]. The authors attributed this effect to increased crystallinity and improved electron extraction efficiency from the mesoporous TiO_2 due to better energetic alignment and stronger interfacial coupling at that interface. Similarly, Kim *et al*. studied $MAPbI_3$ (as well as CsMAFA devices) in the standard architecture, and found an enhanced PCE and reduced hysteresis for devices fabricated from a precursor solution containing a $\approx$ 5.7% molar excess of PbI_2 in the precursor solution. Employing contact potential dif-

ference (CPD) measurements, they attributed the reduced hysteresis to a suppressed effect of ion migration on charge separation [314]. Chang *et al.* studied the effect of stoichiometry in the inverted architecture (ITO/PEDOT:PSS/MAPbI$_3$/PC$_{60}$BM/ LiF/Al) and found the maximum PCE for a $\approx$4% excess PbI$_2$ in the precursor solution using a solvent-engineering process [315]. Jahandar *et al.* performed a very similar study using the exact same device architecture and recipe. In contrast to the results from Kim *et al.*, they found the best device performance for MAPbI3 films prepared with a slightly overstoichiometric precursor solution ($\approx$5% excess MAI/- FAI/Cs), with an enhancement in V$_{OC}$, J$_{SC}$ and FF [316]. The authors attributed their results to larger crystalline grains and an enhanced crystallinity for films fabricated from overstoichiometric solutions.

Yu *et al.* studied the hysteretic behavior of devices with MAI:PbI$_2$ molar ratios of 0.95:1, 1:1, and 1:0.95 on compact TiO$_2$ substrates at various temperatures [241]. They pointed out the important role of the TiO$_2$/MAPbI$_3$ interface, and were the first to report reduced hysteresis and better performance for overstoichiometric devices. They attributed it to a tuning of the native defects within the perovskite layer, and suggested that an increase in the concentration of MA-vacancies could be the reason for the observed enhances hysteresis for devices with excess PbI$_2$. In line with these results, Son *et al.* proposed that defects in the grain boundaries could be healed by using excess MAI in the precursor solution [317]. The authors reported reduced hysteresis and increased V$_{OC}$ and FF for devices with $\approx$6% excess MAI, and attributed the effect to suppressed carrier recombination at and near grain boundaries, as well as maximized charge extraction. They proposed that the excess MAI is self-formed and crystallizes at the surfaces and grain boundaries [317].

Hsu *et al.* performed scanning electrochemical microscopy (SECM) measurements in a photoelectrode array system, and varied the amount of excess PbI$_2$ in the precursor solution between 0% and 15% using a solvent-engineering process. A stronger photoresponse, longer diffusion lengths, and longer charge carrier lifetimes were found for films containing a small excess of $\approx$ 2.5% PbI$_2$ [318]. The location of excess PbI$_2$ in MAPbI$_3$ films which were thermally annealed after fabrication for different times was studied by high-resolution transmission electron microscopy (HRTEM) [319]. It was proposed that, during the additional annealing step, PbI$_2$ mainly forms in grain boundary regions, and that by fine tuning the process a certain amount of PbI$_2$ is beneficial to device performance. Berwerger *et al.* employed scanning microwave microscopy (SMM) to spatially resolve the electronic properties and related morphology of pristine and degraded MAPbI$_3$ films fabricated under varying humidity levels. The authors proposed that PbI$_2$ can have both beneficial and detrimental effects on device performance, depending on the composition of the film and the exact location of excess PbI$_2$ in the film [320]. Recently, Zheng *et al.* employed GIWAXS measurements to show that both the tuning of the MAI:PbI$_2$ ratio in MAPbI$_3$ films, as well as the addition of Cs, Rb and K in multi-cation perovskite films, can directly influence the facet orientation of the films and the efficiency of devices [321, 322].

Petrus *et al.* studied the moisture stability of perovskite films and devices, on compact TiO$_2$ in the standard architecture, with precursor stoichiometries of 1.05:1, 1:1 and 1:1.05 (MAI:PbI$_2$) using a solvent-engineering process. Very small grains were found for overstoichiometric films, which exhibited a recrystallization and grain re-orientation process upon short exposure to a humidity of 90% and subsequent drying. This resulted in a strong increase of the initially very low PCE. In contrast, the initially (before humidity exposure) better performing understoichiometric and stoichiometric devices began to slightly degrade immediately upon exposure to high humidity and subsequent drying. For longer exposure times to humidity however, the understoichiometric devices showed the highest stability, which the authors ascribed to small amounts of PbI$_2$ being located at the grain boundaries (passivation effect) and/or the termination of the film surface with Pb and I atoms [323]. Such terminations might serve as barrier to moisture ingress. In a similar study, Ma *et al.* studied the degradation of devices in the inverted architecture (PEDOT:PSS and C$_{60}$ as HTL and ETL respectively), at high humidities (80%) with stoichiometries of 1.1:1, 1:1 and 0.9:1 (MAI:PbI$_2$) using a solvent-engineering process. The degradation rate was fastest for the overstoichiometric devices, and similar for the stoichiometric and understoichiometric devices. The authors proposed that the amount of polar MA$^+$ molecules at the layer surface is the main cause of the bulk degradation in high humidity conditions, and will determine determine the overall degradation behavior [297]. These two studies will be discussed in further detail in Section 5.2.4.

Lastly, by employing UPS measurements, Wang et al. revealed that MAPbI3 surfaces can be either n-doped (excess PbI$_2$) or p-doped (excess MAI), depending on the stoichiometry of the precursor solution in a one-step deposition process [106]. Emara *et al.* studied this effect in more detail, by probing a high number of perovskite films fabricated by various methods with XPS and UPS [324]. The authors found a direct correlation between the surface composition (N/Pb atomic ratio) and the ionization potential of the films. The latter study, and its implications, will be examined more closely in Section 5.2.2.

3. Materials and Experimental Methods

3.1 Film and Device Fabrication

The technique used to deposit thin films to substrates is spin-coating. A vacuum-chuck is employed which can be rotated at various speeds up to 10000 rpm enabling layer thickness control. Films are either spin-coated in ambient air, in a self-built drybox flushed with dry air (< 1000 ppm H_2O) or in a nitrogen filled glovebox (< 2 ppm O_2 and H_2O). A thermal evaporator placed inside the nitrogen filled glovebox is used to evaporate metal contacts. The thermal evaporator provides three sources and allows evaporation of the materials Au, Ag, Ca, Cr and MoO_3.

In the following sections detailed information about the materials used, precursor solution preparation and film and device fabrication procedures are presented. A procedure for applying fractional variations in precursor stoichiometry is explained in greater detail (Sec. 3.1.3) which will be used for the results presented in Chapter 5.

3.1.1 Materials and Substrates

In Table 3.1 details and properties of all materials and solvents used in this study for thin film fabrication are summarized. In addition, some of the materials and substrates are discussed in more detail in the following.

Solar Cell Substrates

Indium tin oxide (ITO) substrates were bought from PsiOTec Ltd. Centrally positioned 7x12 mm^2 ITO stripes were pre-patterned to 12x12 mm^2 sodalime glass substrates. The ITO has a sheet resistance of $15 \, \Omega \, \text{sq}^{-1}$. On every such substrate, eight solar cell pixels with an area of 4.5 mm^2 were fabricated.

PDS Substrates

The substrates for photothermal deflection spectroscopy (PDS) measurements are so-called Spectrosils from UQG Optics. They are circular with a diameter of ~12 mm and made from high purity, fused silica glass with a high transmission over the UV-Vis spectrum, especially in the UV regime.

Glass substrates

Glass substrates (Microscope slides, Thermo Scientific) were used for PL measurements. They were cut into slides of 12x12 mm^2 before use.

Perovskite Precursors

The choice of the perovskite precursors is paramount for fabricating high quality perovskite films. Levchuk *et al*. found that during synthesis of MAI - using hydroiodic acid (HI) with HPA as a stabilizer - a small amount of impurities remains in the MAI

powder if not sufficiently purified [257]. Such impurities (stemming from the stabilizer HPA) form $PbHPO_3$ nanoparticles in the precursor solution which, in the right concentration, can even result in better solar cell performances by acting as nucleation centers for perovskite crystal growth. This effect is exploited using the $PbAc_2$ recipe (Sec. 3.1.2), for which HPA is intentionally added into the precursor solution. Currently, nearly all groups use the highly purified organic precursors from Greatcell Solar, because they yield the most reproducible results.

3.1.2 Precursor Solution Preparation

Lead Acetate Trihydrate ($PbAc_2$) Recipe

For the $PbAc_2$ recipe, MAI and $PbAc_2$ are dissolved with a 3:1 molar ratio in DMF (Sec. 2.3.2.1). The weight percentage (also called mass mass fraction) w_{PVK} (also written as wt%) of the perovskite precursors in solution is defined by:

$$w_{PVK} = \frac{m_{MAI} + m_{PbAc_2}}{m_{MAI} + m_{PbAc_2} + m_{DMF}} \tag{3.1}$$

with m_X denoting the respective masses of MAI, $PbAc_2$ and DMF. Using $m_{DMF} = \rho_{DMF} x V_{DMF}$, the required volume of DMF to obtain a defined w_{PVK} is given:

$$V_{DMF} = \left[\frac{m_{MAI} + m_{PbAc_2}}{w_{PVK}} - m_{MAI} - m_{PbAc_2} \right] \cdot \frac{1}{\rho_{DMF}} \tag{3.2}$$

Directly before spin-coating, 6.43 µl HPA solution per 1 ml DMF are added into the precursor solution. In Chapter 5, $w_{PVK} = 0.40 := 40$ wt% is used. For the results in Chapter 6, a higher weight percentage of 42 wt% is used.

Solvent-engineering (sol-eng) Recipe

For the sol-eng recipe employed in Chapter 5, 1.25 M PbI_2 and 1.25 M MAI are dissolved in 1 ml GBL:DMSO (7:3, v/v), corresponding to 41.02 wt%. For the sol-eng recipe employed in Chapter 6, 1.2 M PbI_2 and 1.15 M MAI, corresponding to a precursor stoichiometry of $z = PbI_2:MAI = 1:0.95$, are dissolved in 1 ml DMF:DMSO (4:1, v/v). The procedure for varying z is explained in Section 3.1.3. All solutions were stirred at 70 °C for minimum 2 hours. After cooling down to room temperature, they were filtered through a 0.45 µm PTFE filter.

3.1.3 Performing Controlled Stoichiometric Variations

In the following, the method for performing fractional stoichiometric variations, needed for the results in Chapter 5, is presented. It is explained in great detail for the $PbAc_2$ recipe and afterwards shortly described for the sol-eng recipe. In order to perform controlled stoichiometric variations of a precursor solution, high precision pipettes and balances are needed and several parameters must be determined:

Table 3.1: List of materials and solvents used in this thesis.

Materials	Company	CAS number	M_w $\left[\mathrm{g\,mol^{-1}}\right]$
PbI$_2$, 99.99%	TCI chemicals	10101-63-0	461.01
PbBr$_2$, 99.99%	TCI chemicals	10031-22-8	367.01
PbAc$_2$·3H$_2$O, 99.999%	Millipore Sigma	6080-56-4	379.33
CH$_3$NH$_3$I (MAI)	Greatcell Solar	14965-49-2	158.97
CH$_3$NH$_3$Br (MABr)	Greatcell Solar	6876-37-5	111.97
Bathocuproine (BCP), 99.99%	Millipore Sigma	4733-39-5	
PC$_{60}$BM, >99.5%	Solenne BV	160848-22-6	
Poly-TPD	1-Material	472960-35-3	
Spiro-OMeTAD	Borun Chemicals	207739-72-8	
F4-TCNQ, 97%	Millipore Sigma	29261-33-4	276.15
Hypophosporous acid (HPA) 50 wt% in H$_2$O	Millipore Sigma	6303-21-5	66
Solvents/Solutions	Company	CAS number	ρ $\left[\mathrm{mg\,ml^{-1}}\right]$
N,N-Dimethylformamide (DMF) anhydrous, 99.8%	Millipore Sigma	68-12-2	944
Dimethyl sulfoxide (DMSO) anhydrous, >99.9%	Millipore Sigma	67-68-5	1110
γ-Butyrolactone (GBL) >99%	Millipore Sigma	96-48-0	1120
Chlorobenzene anhydrous, 99.8%	Millipore Sigma	108-90-7	1106
CLEVIOS™P VP AI 4083 PEDOT:PSS (1:6), ~1.5 wt% in H$_2$O	Heraeus		
Hypophosporous acid solution HPA, 50 wt% in H$_2$O	Millipore Sigma	6303-21-5	1206

- the density ρ_{PVK} of the perovskite solution, containing MAI and PbAc$_2$ in a certain molar ratio
- the exact volume and density of the perovskite solution after each variation step
- the density ρ_{MAI} of the MAI/DMF stock solution, which is added to the perovskite solution in small amounts

With these values, the solid concentrations c_{PbAc_2} in the perovskite solution and c_{MAI} in the stock solution (in [mg/ml]) can be exactly determined.

Variations for the PbAc$_2$ Recipe

First, MAI and PbAc$_2$ are mixed together in a certain intended molar ratio (defined as stoichiometry y = MAI:PbAc$_2$ throughout this manuscript) and dissolved in anhydrous DMF with a weight percentage of $w_{PVK} = 42$ wt%. Thereafter, 6.43 μl HPA per 1 ml DMF is added into the solution, which changes the weight percentage of the perovskite precursors in the solution to $w_{PVK} = 41.8$ wt%. The density of this solution is determined by weighing exact volumes (for example, 200 μl). For a stoichiometry of $y = 2.96$, a density of $\rho_{PVK} = 1263$ mg/ml was determined, which yields a perovskite solid concentration of

$$c_{PVK} = \rho_{PVK} \cdot w_{PVK} = 527.9 \text{ mg/ml}. \tag{3.3}$$

Using the known stoichiometry $y = 2.96$ and the molar weights of PbAc$_2$ ($m_{W-PbAc_2} = 379.33$ mg ml^{-1}) and MAI ($m_{W-MAI} = 158.97$ mg ml^{-1}) to calculate the weight percentage of PbAc$_2$ (w_{PbAc_2}) in the perovskite solution by

$$w_{PbAc_2} = \frac{m_{W-PbAc_2}}{m_{W-PbAc_2} + y \cdot m_{W-MAI}}, \tag{3.4}$$

Table 3.2: Example calculation for performing controlled stoichiometric variations for the PbAc$_2$ recipe. Starting from $y = 2.96$, the stoichiometry is varied in steps of $\Delta y = 0.02$ until $y = 3.06$. For each stoichiometry, two samples with 40 μl solution each, are fabricated. The MAI/DMF stock solution has a solid concentration of c_{MAI}=332.1 mg ml^{-1}

Stoichio-metry y	Amount of PbAc$_2$ [mg]	Density [mg/ml]	w_{PVK} [wt%]	PbAc$_2$ per 1 ml [mg]	PbAc$_2$ per sample [mg]	MAI to add [mg]	MAI/DMF solution to add [μl]
Start: Mix 200 mg PbAc$_2$ with 248.1 mg MAI and add 655.5 μl DMF and 4.22 μl HPA							
2.96 (x2)	200	1263	41.80	235.7	9.43		4.57
2.98 (x2)	181.14	1261.5	41.73	234.1	9.36	1.52	4.10
3.00 (x2)	162.42	1260	41.66	232.6	9.30	1.36	3.63
3.02 (x2)	143.82	1258.5	41.60	231.1	9.24	1.21	3.16
3.04 (x2)	125.34	1257	41.53	229.6	9.18	1.05	2.70
3.06 (x2)	106.98	1255.5	41.46	228.1	9.12	0.9	

one can determine the $PbAc_2$ solid concentration by

$$c_{PbAc_2} = c_{PVK} \cdot w_{PbAc_2} = 235.7 \, \text{mg ml}^{-1}. \tag{3.5}$$

Accordingly, a MAI/DMF stock solution (with $w_{MAI} = 29 \, \text{wt\%}$) is prepared and after measuring the density, the solid concentration is determined to be $c_{MAI} = 332.1 \, \text{mg ml}^{-1}$. In the same manner, the density of the perovskite solution and the solid concentration c_{PbAc_2} are determined for each stoichiometry. These values are used to determine the remaining weight of $PbAc_2$ in the precursor solution after each spin-coating step. Subsequently, the required amount of MAI/DMF stock solution to change the stoichiometry by Δy can be calculated. An example calculation for stoichiometries of $2.96 < y < 3.06$ and variation steps $\Delta y = 0.02$ is presented in Table 3.2. This method allows the use of one perovskite solution for a complete batch, which minimizes possible sources of errors if preparing multiple perovskite solutions with different stoichiometries.

For understoichiometric films with a deficiency of MAI or excess of PbI_2 (Δy_{PbI_2}) in the solution, one expects the final composition of the perovskite film to be:

$$(3 - \Delta y_{PbI_2}) \, \text{M MAI} + 1 \, \text{M PbAc}_2 \Rightarrow 1 \, \text{M MAPbI}_3 + \Delta y_{PbI_2} \, \text{M PbI}_2 + 2 \, \text{M MAAc} \curvearrowright \tag{3.6}$$

For overstoichiometric films with an excess of MAI (Δy_{MAI}) one expects:

$$(3 + \Delta y_{MAI}) \, \text{M MAI} + 1 \, \text{M PbAc}_2 \Rightarrow 1 \, \text{M MAPbI}_3 + \Delta y_{MAI} \, \text{M MAI} + 2 \, \text{M MAAc} \curvearrowright \tag{3.7}$$

In both cases it is assumed that due to the volatile nature of MAAc and its inability to be incorporated in the perovskite structure (Sec. 2.3.2.1), two equivalents MAAc evaporate out of the film during the thermal annealing process. Hence, the final film is composed of $MAPbI_3$ with a certain molar excess Δy of either PbI_2 or MAI.

Variations for the sol-eng Recipe

The perovskite solution with a molar ratio of $z = PbI_2:MAI = 1:0.95$ and $w_{PVK} = 42.96 \, \text{wt\%}$ has a density of $\rho_{PVK} = 1463.2 \, \text{mg ml}^{-1}$ and a PbI_2 solid concentration $c_{PbI_2} = 473.47 \, \text{mg ml}^{-1}$ was determined. A stock solution of MAI in DMF/DMSO (4:1, v:v) (40 wt%) with a solid concentration of $c_{MAI} = 504 \, \text{mg ml}^{-1}$ was also prepared. It was added to the perovskite solution in the desired amounts to change the stoichiometry by Δz, analogue to the method described above for the $PbAc_2$ recipe. The final films are composed of $MAPbI_3$ with a certain molar excess Δz of either PbI_2 or MAI.

3.1.4 Device and Film Fabrication Procedures

In this section details about cleaning, spin-coating and evaporation procedures are given. For spin-coating, the nomenclature in the following is: spin-speed [rpm]/ acceleration [rpm s^{-1}]/spin-time [s] for a non-dynamic spin-coating process, and

spin-speed[rpm]/spin time [s] for a dynamic spin-coating process. Dynamic spin-coating describes the application of the solution while the substrate is already spinning. It can sometimes be beneficial for film formation.

Cleaning of the Substrates

ITO, FTO and glass substrates are cleaned in six steps:

- Scrubbing the substrates with a toothbrush using soap and distilled water
- Rinsing the substrates with deionized H_2O and then Acetone
- Sonicating in Acetone for 10 min in an ultrasonic bath
- Sonicating in 2-Propanol for 10 min in an ultrasonic bath
- Blow drying the substrates with a N_2 gun
- Either oxygen-plasma cleaning for 10 min or UV-ozone treatment for 10 min

For devices employing poly-TPD as the HTL (Chapter 5), FTO substrates are cleaned with piranha solution to improve the wettability of the perovskite solution. Piranha solution is prepared by mixing sulfuric acid (H_2SO_4) and hydrogen peroxide (H_2O_2, 30%) in a 3:1 (v:v) ratio [86]. The latter hereby must be added to the sulfuric acid very slowly. Piranha solution is highly corrosive and an extremely powerful oxidizer. The cleaning procedure for these substrates is as follows:

- Scrubbing the substrates with a toothbrush using soap and distilled water
- Rinsing the substrates with deionized H_2O and then 2-Propanol
- Blow drying the substrates with a N_2 gun
- Placing the pre-cleaned substrates in a petri dish containing piranha solution for 30-60 min
- Rinsing the substrates with deionized H_2O
- Blow drying the substrates with a N_2 gun

Inverted Architecture Recipes

The HTL films were deposited on the substrates in ambient air directly after a oxygen-plasma (ITO) or piranha cleaning (FTO):

- PEDOT:PSS was shortly ultra sonicated and filtered through a 0.45 µm PVDF filter before use. The ITO substrates were covered with PEDOT:PSS solution and then spin-coated at 4000 rpm/2000 rpm s^{-1}/45 s in ambient air.
- For PSS-Na doped PEDOT:PSS (m-PEDOT:PSS), PSS-Na was dissolved in H_2O (15 mg ml^{-1}). The PSS-Na solution mixed with normal PEDOT:PSS in a 4:1 (v:v) ratio, shortly ultra sonicated and filtered through a 0.45 µm PVDF filter before use. The ITO substrates were covered with m-PEDOT:PSS solution and then spin-coated at 4000 rpm/2000 rpm s^{-1}/45 s in ambient air.
- poly-TPD was dissolved in Toluene (1 mg ml^{-1}) and doped with F4-TCNQ (0.1 mg ml^{-1}). The solution was heated at 90 °C until fully dissolved. After cooling down to room temperature, the solution was spin-coated at 2000 rpm/ 1000 rpm s^{-1}/40 s onto FTO substrates in ambient air.

Directly after HTL deposition, the substrates were transferred into a drybox:

- The $PbAc_2$ solution was spin-coated at $2000\,\text{rpm}/1000\,\text{rpm s}^{-1}/60\,\text{s}$. A dry air gun was used to dry the samples for ~30 s directly after spin-coating. The substrates were allowed to dry for further 5 min at room temperature. Afterwards, they were annealed at $100\,°C$ for 5 min.
- The sol-eng solution was spin-coated at $1000\,\text{rpm}/200\,\text{rpm s}^{-1}/15\,\text{s}$, and then at $4000\,\text{rpm}/2000\,\text{rpm s}^{-1}/25\,\text{s}$. Five seconds before the end of the second spin-coating step, 600 ml Toluene was dripped on top of the spinning substrate. Afterwards, the films were directly annealed at $100\,°C$ for 15 min.

$PC_{60}BM$ and BCP were deposited after transferring the substrates into a N_2 filled glovebox:

- $PC_{60}BM$ was dissolved in Chlorobenzene ($20\,\text{mg ml}^{-1}$) and stirred at $70\,°C$ for minimum 2 hours. After cooling down to room temperature, the solution was filtered through a $0.25\,\mu m$ PTFE filter and then dynamically spin-coated on top of the perovskite films at $2000\,\text{rpm}/40\,\text{s}$. Afterwards, the films were annealed at $100\,°C$ for 10 min.
- BCP was fully dissolved in 2-Propanol ($0.5\,\text{mg ml}^{-1}$) under heavy stirring at $120\,°C$ overnight. The solution was stored in the N_2 glovebox and was used for months. BCP was dynamically spin-coated at $6000\,\text{rpm}/30\,\text{s}$.
- The substrates were transfered to a thermal evaporator and 80 nm Ag were evaporated. The first few nm were evaporated with a slow rate of ~$0.2\,\text{nm s}^{-1}$, after which the rate was increased to $1\,\text{nm s}^{-1}$.

Standard Architecture Recipes

The ETLs were deposited on ITO/FTO substrates in ambient air directly after a 10 min oxygen-plasma treatment:

- SnO_2-NP solution was prepared by diluting SnO_2 colloid precursor (15% in H_2O) with distilled H_2O to 2.67% before use. The solution was spin-coated on top of ITO substrates at $3000\,\text{rpm}/30\,\text{s}$ and annealed at $150\,°C$ for 30 min in ambient air. Before the deposition of perovskite, the SnO_2-NP films were subjected to UV-Ozone treatment for 15 min.
- For $SnO_2/PC_{60}BM$ films, $SnCl_4 \cdot 5H_2O$ was dissolved in anhydrous 2-propanol ($0.05\,\text{M}$) and stirred for 30 min. The solution was spin-coated at $3000\,\text{rpm}/1000\,\text{rpm s}^{-1}/30\,\text{s}$ in ambient air. Thereafter, the substrates were dried at $100\,°C$ for 10 min and annealed at $180\,°C$ for 60 min. $PC_{60}BM$ was dissolved in anhydrous chlorobenzene ($4\,\text{mg ml}^{-1}$) and dynamically spin-coated on top of SnO_2 in a N_2 filled glovebox at $4000\,\text{rpm}/40\,\text{s}$ and afterwards annealed at $70\,°C$ for 5 min.

Directly after ETL deposition, the substrates were transferred into a drybox (for SnO_2-NP) or a N_2 glovebox (for $SnO_2/PC_{60}BM$):

- The $PbAc_2$ solution was spin-coated at $2000\,rpm/1000\,rpm\,s^{-1}/60\,s$ on top of ITO/SNO_2-NP. A dry air gun was used to dry the samples directly after spin-coating for ~$30\,s$. The substrates were allowed to dry for further $5\,min$ at room temperature. Afterwards, they were annealed at $100\,°C$ for $5\,min$.

- The perovskite solution for the sol-eng recipe was spin-coated at $5000\,rpm/500\,rpm\,s^{-1}/23\,s$ on top of $FTO/SnO_2/PC_{60}BM$ in a N_2 glovebox. $18\,s$ after the spin-coating program began, $300\,ml$ anisole was dynamically dispensed onto the spinning substrate. The film was transferred to a hotplate immediately after spin-coating and annealed for $15\,min$ at $100\,°C$.

- Spiro-OMeTAD solution was prepared by dissolving $85.7\,mg$ Spiro-OMeTAD in $1\,ml$ anhydrous chlorobenzene with additives of $28.8\,µl$ tBP and $20\,µl$ Li-TFSI salt in acetonitrile ($520\,mg\,ml^{-1}$). The solution was spin-coated on top of $MAPbI_3$ at $2500\,rpm/1000\,rpm/40\,s$ in a drybox. Afterwards, the devices were kept in a closed container with a relative humidity of ~10–20% overnight to induce oxidation.

- The substrates were transfered into a thermal evaporator and $80\,nm$ Ag were evaporated. The first few nm were evaporated with a slow rate of ~$0.2\,nm\,s^{-1}$, after which the rate was increased to $1\,nm\,s^{-1}$.

3.2 Analytical Techniques

3.2.1 Atomic Force Microscopy (AFM)

To determine the surface topography of the perovskite thin films, atomic force microscopy (AFM) is employed (Figure 3.1). A cantilever with a very small radius tip is used to raster over the film surface. In the so-called *tapping mode*, the cantilever is driven into a forced vibration close to its eigenfrequency. When the tip gets close to the surface, it is first attracted by Van-der-Waals interactions and then strongly repelled due to the Pauli-principle. The resulting potential is called Lennard-Jones-potential. The attracting and repulsive forces result in a shift of the tip's eigenfrequency which modulates the amplitude and phase of the driven oscillation. These modulations can be detected by measuring the deflection of a laser which is pointed onto the cantilever head. The deflection is measured using a four-point-probe diode.

3.2.2 Scanning Electron Microscopy (SEM) and Energy Dispersive X-ray Diffraction Spectroscopy (EDX)

Scanning electron microscopy (SEM) is based on the interaction between high-energy electrons and a specimen over which they are scanned to resolve the surface on a nanoscale (see left of Figure 3.2). Electrons are either accelerated using thermoionic emitters (tungsten or lanthanum hexaboride) or for better resolution with a field emission gun (FEG), which can be either cold type or Schottky type. The
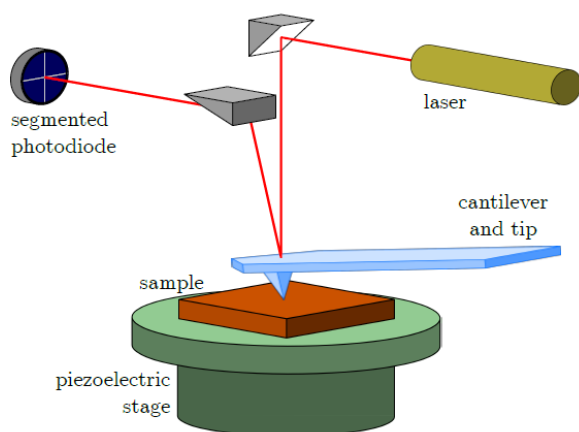
Figure 3.1: Schematics of a typical AFM which determines a sample's topography by measuring the deflection of a laser pointed on top of a cantilever (Reproduced from [325]).

instruments used for this project had Schottky type FEGs which have an increased electrical conductivity at high temperatures (also termed warm field emission). This method yields electrons with a high intensity and very specific velocity, making it possible to gain good images even at very low acceleration voltages. The SEM was also equipped with an X-ray detector allowing energy dispersive X-ray diffraction spectroscopy (EDX).

The accelerated electrons are focused on a certain point on the sample with a very small beam diameter by electromagnets, allowing high resolutions down to ~1 nm. Through interaction with the specimen, various characteristic signals are produced: secondary electrons (SE), reflected and elastically back-scattered electrons (BSE), characteristic X-rays (EDX) and light (cathodoluminescence) ([326]; see right of Figure 3.2). The low energy secondary electrons (few meV) emitted from the surface region of a specimen (top few nm) are detected either in a low angle cone (inlens mode) or at higher angles (SE mode). The inlens mode yields information about material contrast, while the SE mode provides information about the topography of a specimen. Back-scattered electrons emerge from locations a bit deeper in the film and are strongly dependent on the atomic number Z of the atoms. Hence, they can yield information about the distribution of different elements. Characteristic X-rays are produced when an atom is hit by an electron with sufficient energy to eject an inner shell electron. Outer shell electrons fill the free spot and emit photons with a characteristic energy, thus allowing the identification of different elements. These photons have a higher energy and thus can be detected from deeper within the film. In addition to the characteristic X-rays, a background of continuum X-rays is produced by inelastic scattering processes of the electrons (Bremsstrahlung).

The interaction volume of the electron beam and the sample depends on the density of the film, the atomic number Z of the atoms in the film and the accelerating voltage of the electron beam. To estimate the interaction volume, we used the free software CASINO ("monte CArlo SImulation of electroN trajectory in sOlids") [327]. The software is able to simulate electron trajectories in thin films based on their chemical

composition and density for different acceleration voltages. In addition, a phi-rho-Z curve is generated, which yields information about the characteristic X-Ray generation depth for each element in a film [326]. The quantitative analysis with EDX becomes difficult for light elements with $Z < 11$. The characteristic X-rays from these elements have a low fluorescence yield and because of their low energy are also easily reabsorbed by the sample. While detection of light elements (3<Z<11) is possible, the derived values should serve qualitative purposes only.
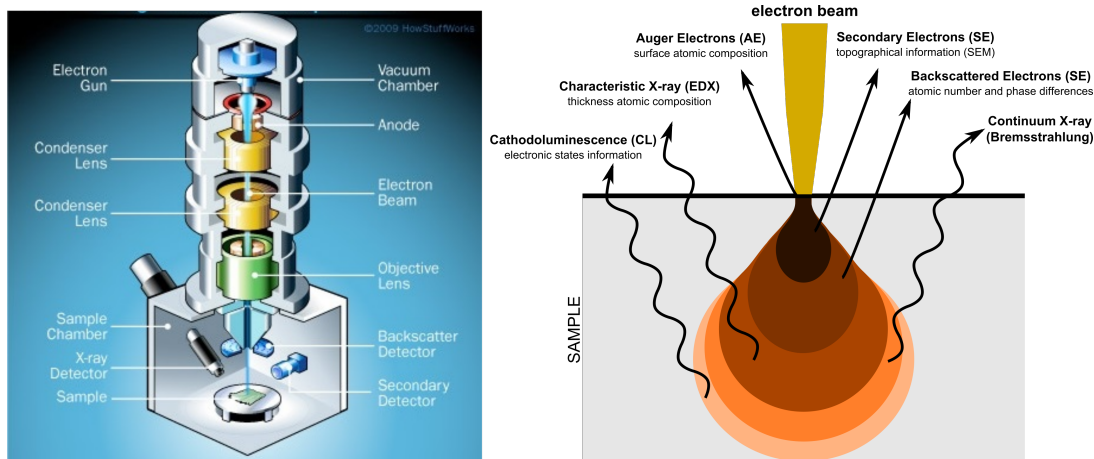
Figure 3.2: Schematics of a scanning electron microscopy [328]. Illustration of the interaction volume of the electron beam and the sample, showcasing which sample depth yields which information [329].

3.2.3   X-ray Diffraction (XRD) Spectroscopy

X-ray diffraction (XRD) measurements were performed in a collaboration with Zhiping Wang at Oxford University. The XRD spectra of the prepared films were measured using a Rigaku SmartLab X-ray diffractometer with CuKa1 (1.54060 Å) and a HyPix-3000 2D hybrid pixel array detector.

3.2.4   Photoluminescence Quantum Efficiency (PLQE)

The photoluminescence quantum efficiency (PLQE) was measured using an integrating sphere (Ulbricht-sphere) setup (see Figure 3.3). An integrating sphere consists of a hollow spherical cavity. Its inside is covered with a highly reflective coating and has one small entrance and exit hole. Light inside a sphere is scattered diffusively (Lambertian reflection) and therefore after numerous scattering processes the intensity is evenly distributed over all angles. The intensity of the light hitting the exit port is therefore directly proportional to the incoming intensity. It can be measured by a spectrometer, which is calibrated beforehand to calculate the absolute optical power. A laser with a spot size of ~2 mm is directed into the sphere, and the light generated
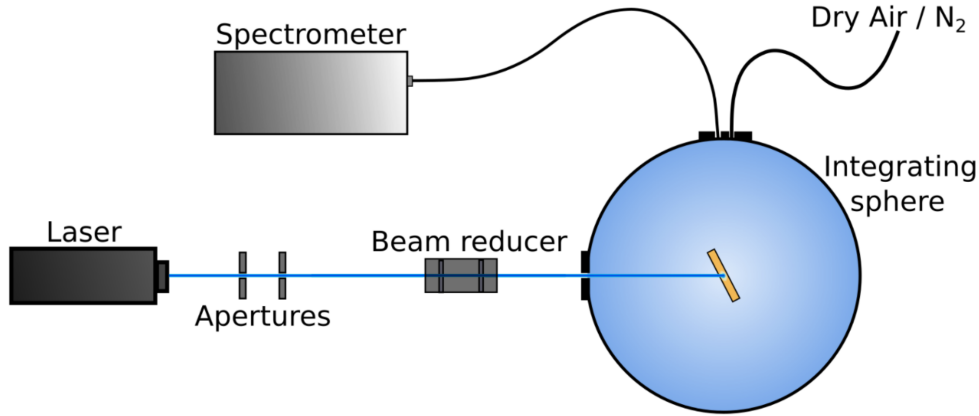
Figure 3.3: Schematic of the PL setup used for determination of the PLQE in this work. Adapted from [57].

in the sphere collected by a fiber which is connected to a spectrometer. It was possible to change the atmosphere inside the sphere, for measurements to be performed in ambient air, dry air or N_2.

An accurate method for calculating the PLQE was introduced by deMello *et al.* [330]. Four different measurements are needed to account for absorption, reflectance and scattering processes (see Figure 3.4):

- A dark measurement accounts for possible stray light guided into the sphere and the noise of the spectrometer. This measurement is subtracted from the three following measurements.
- A 'no-sample' measurement measures the laser peak without a sample inside the sphere to determine the laser's total optical power.
- An 'off-axis' measurement, during which the sample is rotated out of the laser beam and is only hit indirectly from the scattered light.
- An 'on-axis' measurement, during which the sample is hit directly by the laser after entering the sphere. This measurement contains information about absorption, reflectance and scattering of the sample.

These measurements are used to calculate the PLQE of the sample [330]:

$$\text{PLQE} = \frac{I_{\text{on}} - (1 - A) \cdot I_{\text{off}}}{L_{\text{off}} \cdot A} \tag{3.8}$$

Here, I_{on} and I_{off} are the areas under the PL emission peak from the on-axis and off-axis measurements respectively. L_{off} is the area under the laser peak for the off-axis measurement and A is the absorption calculated by

$$A = (1 - \frac{L_{\text{on}}}{L_{\text{off}}}), \tag{3.9}$$

with L_{on} the area under the laser peak for the on-axis measurement.

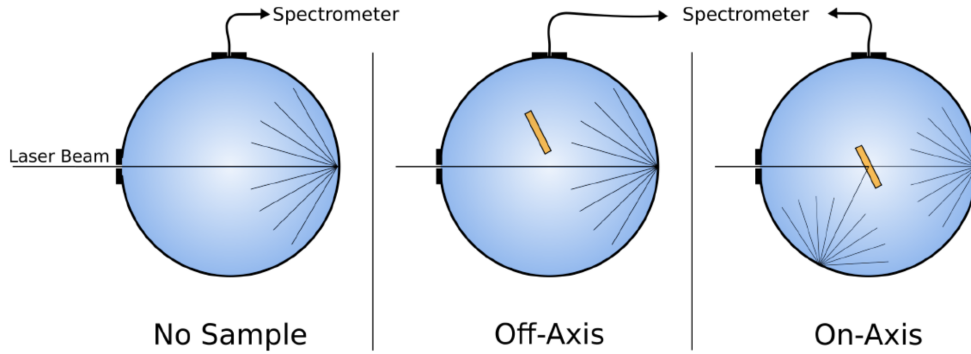The PLQE measurements in Chapter 6 were performed by Alexandra Bausch and Lukas Falk.

Figure 3.4: Schematic illustration of the three measurements - no-sample, off-axis, and on-axis - needed to determine the PLQE based on the method by deMello *et al.* [330]. Adapted from [57].

3.2.5 Electroluminescence Quantum Efficiency (ELQE)

For determination of the electroluminescent quantum efficiency (ELQE) of full devices, the same integrating sphere setup as in PLQE measurements is used. The devices are connected to a source measure unit (SMU) to allow measurement of the emission power at various voltages. The internal quantum efficiency is defined as the ratio of the total number of photons generated inside the emitter N_{int} to the number of injected electrons N_{e}. Due to internal light trapping only a fraction χ_{out} of the light is outcoupled. Hence, the external quantum efficiency is defined as:

$$\text{ELQE}_{\text{ext}} = \frac{N_{\text{ext}}}{N_{\text{e}}} = \chi_{\text{out}} \cdot \text{ELQE}_{\text{int}} = \chi_{\text{out}} \frac{N_{\text{int}}}{N_{\text{e}}} \tag{3.10}$$

The number of outcoupled photons can be calculated by integrating the wavelength weighted measured power $\Phi_e(\lambda)$ over wavelength by:

$$N_{\text{ext}} = \frac{1}{hc} \cdot \int_{\lambda_1}^{\lambda_2} \Phi_e(\lambda)\,\lambda \mathrm{d}\lambda \tag{3.11}$$

ELQE_{ext} can then be calculated by measuring the current I_{D} flowing through the device:

$$\text{ELQE}_{\text{ext}} = \frac{e}{I_{\text{D}}hc} \cdot \int_{\lambda_1}^{\lambda_2} \Phi_e(\lambda) \cdot \lambda \mathrm{d}\lambda. \tag{3.12}$$

3.2.6 Photoelectron Spectroscopy (XPS/UPS)

The PES measurements were performed in a Thermo Scientific ESCALAB 250Xi. X-ray photoelectron spectroscopy (XPS) measurements were performed using an XR6 monochromated Al Kα source ($h\nu = 1486.6$ eV) and a pass energy of 20 eV. Ultraviolet photoelectron spectroscopy (UPS) measurements were carried out using a double-differentially pumped He discharge lamp ($h\nu = 21.22$ eV) with a pass energy of 2 eV and a bias of $\Delta U = -10$ V. An illustration of the measurement principles of XPS and UPS is shown in Figure 3.5.
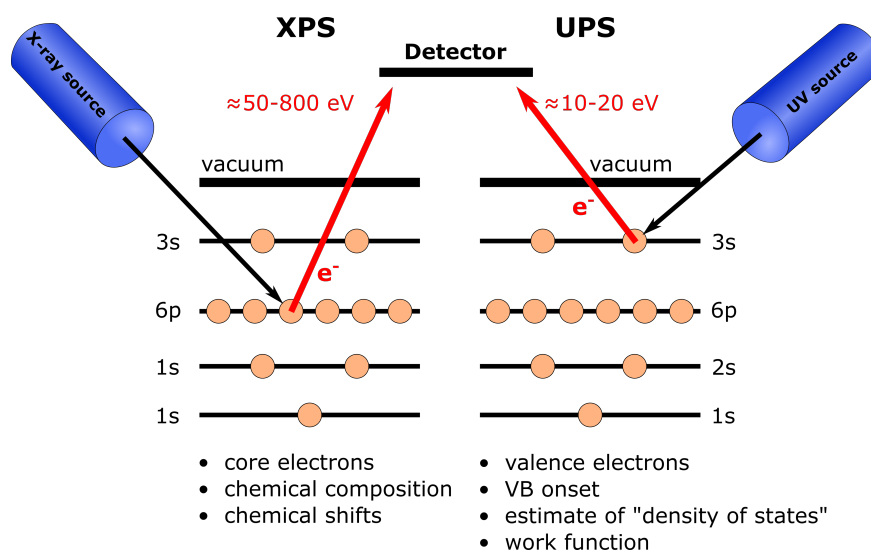
Figure 3.5: Illustration of the principles of XPS and UPS measurements.

XPS probes the core level electrons by collecting photoelectrons produced upon X-ray illumination. The binding energy is specific for each element and also depends on its chemical environment. It yields information about chemical composition by comparing the peak intensities corrected by the corresponding atomic sensitivity factors. XPS probes the top ~10 nm of a film, which is determined by the inelastic free mean path of the emitted electrons.

UPS allows measuring the kinetic energy of valence band electrons emitted upon absorption of ultraviolet light. It is based on the photoelectric effect: If the energy of the absorbed photon is high enough, the valence band electrons can overcome the vacuum level of the material and leave it. Typically, samples are negatively biased with a voltage ΔU to shift the vacuum level of the sample above that of the detector. It is important to correct for the work function (WF) of the detector, for referencing: We measured the Fermi level for our detector to be at $E_F^{\mathrm{Det}} = 31.1$ eV for $\Delta U = -10$ V. The kinetic energy E_K of electrons emitted from a film can now be measured correctly. A UPS spectrum consists of two parts: the valence band onset ($E_{K_{\mathrm{max}}}$) and a background caused by inelastically scattered electrons resulting in a secondary electron cut-off (SECO). The electrons contributing to the SECO are just able to leave the material

($E_{K_{\min}}$). The SECO determines the WF of the material, while the valence band onset defines the difference between the Fermi level and the valence band maximum. The sum of the latter and the WF defines the ionization potential (IP):

$$
\begin{aligned}
\mathrm{WF} &= \mathrm{h}\nu + E_{K_{\min}} - E_F^{\mathrm{Det}} \\
\mathrm{IP} &= 21.22\,\mathrm{eV} - \left(E_{K_{\max}} - E_{K_{\min}} \right)
\end{aligned}
\tag{3.13}
$$

The XPS measurements in Chapter 4 were performed by Qing Sun. The XPS and UPS measurements in Chapter 5 were performed by Vincent Lami.

3.2.7 Confocal Photoluminescence Measurements

Confocal PL measurements were performed in the group of Prof. Dr. Jana Zaumseil in collaboration with Dr. Yuriy Zakharko (see Figure 3.6). To excite the perovskite films, the spectrally separated output of a WhiteLase SC400 supercontinuum laser source (Fianium) operated in pulsed mode (405 nm, ~10 ps pulse width, 0.5 MHz repetition rate) was used. The samples were mounted on a XYZ Nano-LP200 piezo-stage (Mad City Labs Inc.) and illuminated with a focused beam through a ×50, 0.65 N.A. objective (Olympus). The emitted photons were collected with the same objective. After passing through a long-pass filter to filter out the excitation wavelength, they were detected by a silicon single-photon avalanche diode (Micro Photon Devices). Photon counts were recorded with a PicoHarp 300 time-correlated single photon counting system (TCSPC, PicoQuant). The 2D PL intensity maps were acquired using a confocal raster-scanning with a piezo-stage at a step size of 0.2 μm and a dwell time of 10 ms.
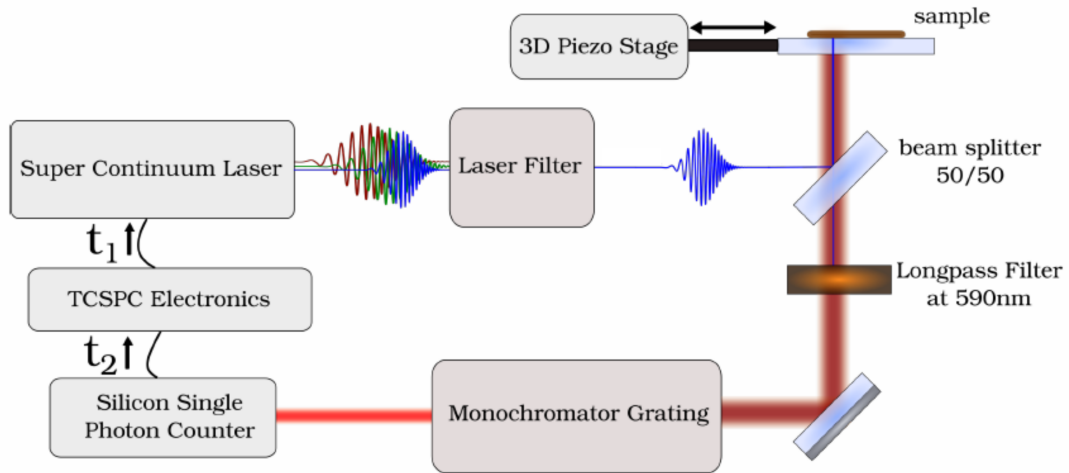

Figure 3.6: Schematic illustration of the confocal PL setup: The pulsed laser light from a supercontinuum laser becomes monochromated and is focussed on the sample with a beam splitter. The sample PL goes through a long pass filter to filter out the excitation wavelength and stray light. A Silicon Single Photon counter detects the photons. The TCSPC electronics determines the time difference between the laser pulse t_1 and detection of PL t_2.

3.2.8   UV-Vis Spectroscopy

In UV-Vis spectroscopy the light from a light source emitting in the UV, visible and infrared region (~200-1200 nm) is sent through a monochromator and guided through the sample film. The sample interacts with the monochromated light which excites electronic transistions in the material. The transmitted light is recorded to determine the absorbance of the sample at every wavelength. In principle, knowing the layer thickness d of the film and using the lambert-beer law, the absorption coefficient $\alpha(\lambda)$ can be determined:

$$A = \log(\frac{I_0}{I}) = \alpha(\lambda)d \tag{3.14}$$

However, this calculation is only valid if an integrating sphere is used to determine the reflectance and scattering of light when the light hits the sample. The UV-Vis machine used in this work was not equipped with an integrating sphere. Hence, the measured value was called absorbance A and used to determine the bandgap and compare different samples qualitatively. The resolution of UV-Vis for very low absorption values is limited.

3.2.9   Photothermal Deflection Spectroscopy (PDS)

Photothermal deflection spectroscopy (PDS) is a method to determine the absorption (in the range of ~350-1100 nm) of thin films with very high sensitivity (see Figure 3.7). In addition, possible light absorbing electronic states within the bandgap of a semiconductor - so called sub-bandgap states - can be measured. The probe light generated by a 150 W xenon short arc lamp is turned into pulsed light by a chopper wheel and then send through a monochromator. The monochromated pulsed light (pump beam) is absorbed by the sample which generates a (pulsed) heat wave. The heat wave changes the refractive index of the surrounding liquid (Fluorinert) which in turn results in a deflection of a 633 nm probe laser that is aligned just above the sample surface. The magnitude of the deflection is determined by a lock-in amplifier. The deflection angle ϕ depends on the absorption coefficient $\alpha(\lambda)$ and the incident light intensity I_0, hence, $\alpha(\lambda) \propto \phi/I_0(\lambda)$. More detailed information about the setup and calculation of $\alpha(\lambda)$ can be found in the Master's thesis of David Becker-Koch and Alexandra Bausch, who developed this experiment [331, 332].
Plotting the measured absorption onset over energy E, the Urbach energy E_U can be determined by fitting the absorption tail close to the bandgap, at which the absorption drops exponentially:

$$A(E) = k \cdot \exp(\frac{E}{E_U}) \tag{3.15}$$

he Urbach energy is a measure of the energetic disorder in a semiconductor film, as it originates from local states extending into the bandgap.
The PDS measurements in Chapter 4 were performed by David Becker-Koch. The PDS measurements in Chapter 6 were performed by Alexandra Bausch.
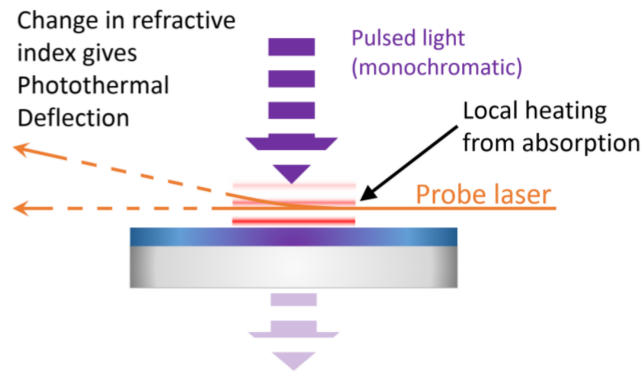
Figure 3.7: Schematic illustration of the working principle of a PDS measurement: The pulsed monochromatic beam (purple) gets absorbed by the film, which generates a heat wave (red). The heat wave changes the refractive index of the surrounding (Fluorinert), which leads to a deflection of the probe beam (orange). Courtesy of P. Hopkinson.

3.2.10 Profilometer

The layer thickness of the films were measured with a Veeco Dektak 150 profilometer. A profilometer scans the surface with a stylus (made of diamond) with a diameter of $12.5\,\mu$m. It records changes of the vertical position of the stylus. The software gives height differences in absolute values. It can measure thicknesses down to ~10 nm with high precision. To measure relative height differences on a substrate, normally the films are scratched with a sharp metallic tweezer and the stylus driven over the scratch. The layer thicknesses were measured for tooling the quartz crystals of the evaporator as well as for analyzing the layer thicknesses of various thin films.

3.2.11 Solar Simulator and IV Measurement Setup

Solar cell device characterization was carried out according to ASTM G-173 standard testing conditions. An ABET AAA Sun 3000 solar simulator was used as light source to simulate a $100\,\mathrm{mW/cm^{-2}}$ AM1.5G spectrum, calibrated using a reference silicon photo diode. The air mass AM1.5 resembles solar irradiance at mid latitudes where the sun is on average about $48.2°$ above the horizon. The light intensity was corrected by a spectral mismatch factor. The electrical characterization of the devices were performed with an arduino based self-built setup to control the connected pixels on each device which were then measured using a Keithley 2450 Source Measure Unit (SMU). The data was read out with a Labview coded software. Light J-V curves were measured from 1.2 V to 0 V and back in steps of 0.025 V and an equilibration time of 25 ms. Dark J-V curves were measured from 1.2 V to -0.5 V and back in steps of 0.025 V and an equilibration time of 25 ms.
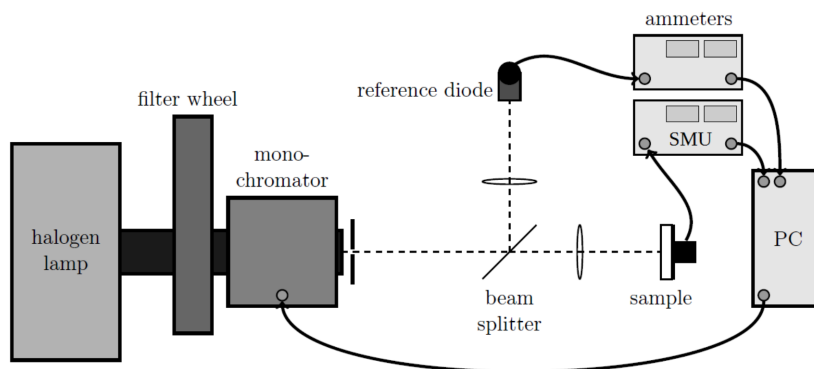
Figure 3.8: Schematic illustration of the EQE setup: The light from a halogen lamp becomes monochromated and is directed onto a pixel of a solar cell. A beam splitter is used to determine the optical power with a reference diode and a labview program analyzes the measured currents of the pixel and reference diode.

3.2.12 External Quantum Efficiency (EQE)

The external quantum efficiency (EQE) is defined as the ratio of photogenerated electrons (in a solar cell at short circuit conditions) to the number of incident photons at a certain wavelength. Sometimes it is termed incident photon-to-current conversion efficiency (IPCE). Knowing the wavelength dependent photon flux of the solar spectrum (AM1.5 G), the integration of the measured EQE spectrum can be used to predict the short-circuit current density (J_{SC}) of a solar cell:

$$J_{SC,pred} = \int_{\lambda_1}^{\lambda_2} e \cdot EQE(\lambda) \, I_{AM1.5}(\lambda) \, d\lambda \qquad (3.16)$$

This value can be compared to the one measured under the solar simulator at 1 sun illumination. The EQE was determined by a home-built setup (see Figure 3.8). Light from a halogen bulb is directed through a monochromator and focussed on a single pixel of a solar cell device with a spectral range between 350 nm and 900 nm. A beam splitter is used to determine the intensity of the light focussed on the sample with a reference diode which was calibrated with a NIST-traceable photodiode prior to each measurement. The current from the illuminated pixel was measured with a SMU. To analyze the data, a labview program was used.

3.2.13 Sample Holder and Environmental Rig

The sample holder (designed by P. Hopkinson) and home-built environmental rig (designed in [333]) for controlling the atmosphere inside the sample holder during degradation studies are shown in Figure 3.9. Ultrapure N_2 (99.999%) is used as the
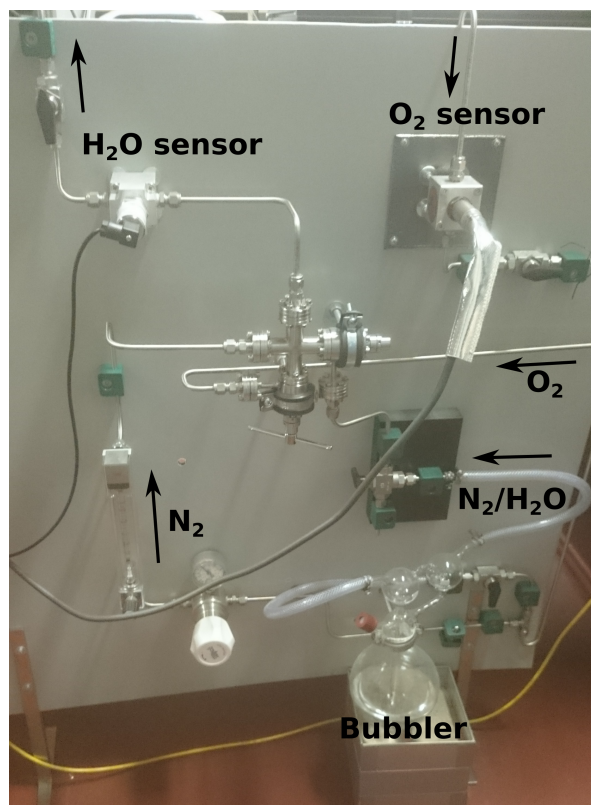
Figure 3.9: Photograph of the home-built environmental rig used to flush the sample holder with exactly controlled levels of $N_2/O_2/H_2O$.

carrier gas and can be mixed with O_2 (99.99%) in precisely controlled ratios. In addition, the N_2 can be sent through a water containing bubbler to control the amount of water in the gas. The humidity and oxygen levels of the gas mix are measured with sensors (EasyDew humidity sensor from Michell instruments and Cambridge Sensotec 2100) before and after passing through the sample holder respectively. The sample holder can store up to four solar cells or films and allows for simultaneous degradation and electrical measurements.

Part I

Oxygen Induced Photodegradation

4. The Influence of Microstructure

4.1 Introduction

This chapter is based on our recently published article in the journal Advances Energy Materials with the title "Role of Microstructure in Oxygen Induced Photodegradation of Methylammonium Lead Triiodide Perovskite Films" [334]. Most Figures are reproduced or adapted with permission from Wiley"=VCH. This project was performed in collaboration with Qing Sun, who performed the XPS measurements and fabricated and measured the films based on the solvent-engineering recipe.

When we began to study oxygen induced photodegradation of MAPbI$_3$ perovskite films in the beginning of 2016, only one publication in the literature had so far reported on this degradation pathway [42]. The authors revealed that the exposure of MAPbI$_3$ to oxygen and light leads to an electron transfer from MAPbI$_3$ to molecular oxygen, creating superoxide (O$_2^-$). The superoxide reacts with the methylammonium cations by deprotonating them, resulting in the decomposition of MAPbI$_3$ into PbI$_2$ and other byproducts. However, no one had yet studied the influence of the perovskite microstructure on the degradation rate. Following that idea, we chose to compare the oxygen induced degradation rate of two perovskite films with strongly different microstructure. First, the microstructure, device efficiency and photoluminescence properties of the two films are analyzed in detail (Sec. 4.2). Then, MAPbI$_3$ films and devices are degraded under exactly controlled environmental conditions and characterized by various methods (Sec. 4.3). Finally, the results are carefully discussed and put into the context of recent literature reports, which we already summarized in Section 2.4.2.

4.2 Varying the Microstructure

The microstructure of MAPbI$_3$ films is determined by various factors, such as the precursor composition, fabrication procedure and substrate layer (Sec. 2.3.2). In order to compare two different microstructures while still using pinhole free films, we fabricated perovskite films (ITO/PEDOT:PSS/MAPbI$_3$) and devices (ITO/PEDOT:PSS/MAPbI$_3$/PC$_{60}$BM/BCP/Ag) using a one-step procedure with lead acetate trihydrate as the precursor as well as a solvent-engineering procedure. In the following, we regularly use the abbreviations PbAc$_2$ films/devices and sol-eng films/devices, to denote films or devices fabricated with the respective recipe. The details of the film and device preparation are described in Section 3.1.4.
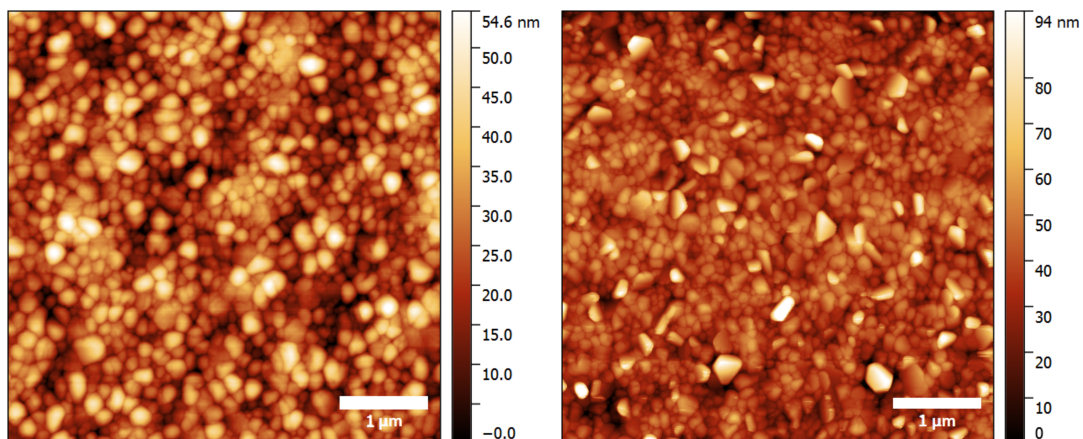
Figure 4.1: AFM images of ITO/PEDOT:PSS/MAPbI$_3$ films prepared by the PbAc$_2$ (left) and sol-eng (right) recipe. The corresponding rms-roughnesses are 9.34 nm and 12.84 nm, respectively. The measurements were performed by Qing Sun. Reproduced with permission from [334]. Copyright 2017, Wiley-VCH.

4.2.1 AFM and SEM

Comparing the two films - in the structure of ITO/PEDOT:PSS/MAPbI$_3$- with AFM, we can see that the PbAc$_2$ recipe results in bigger and more regular shaped grains than the sol-eng recipe (Figure 4.1). The surface roughness is low for both recipes (9.34 nm for PbAc$_2$ and 12.84 nm for sol-eng), which is especially important for the planar architecture in the inverted structure to enable complete surface coverage of the thin ETL layer PC$_{60}$BM. In scanning electron microscopy (SEM) top view images the bigger grain size and more ordered structure for films based on the PbAc$_2$ recipe can be again clearly seen (Figure 4.2 (a)+(b)). Both techniques yielded pinhole-free perovskite films (see Figure A.1 in the Appendix for SEM images with a lower magnification). SEM cross-section images reveal that the PbAc$_2$ films are composed of single grains extending through the whole layer thickness (Figure 4.2 (c)+(d)). This allows charge carriers generated in a perovskite grain to be transported within a single grain towards the adjacent transport layers. In contrast, the sol-eng films exhibit very small and irregular grains with multiple grain boundaries present throughout the film cross-section.

4.2.2 Device and Photoluminescence Efficiency

Champion IV-curves of devices in the architecture ITO/PEDOT:PSS/MAPbI$_3$/PC$_{60}$BM/ BCP/Ag as well as representative EQE spectra (together with the corresponding integrated J$_{SC}$) for both recipes are shown in Figure 4.3. Both recipes result in hysteresis-free devices with champion PCEs of 15.5% and 10.5% for the PbAc$_2$ and sol-eng recipes, respectively. The averaged photovoltaic parameters over various batches are presented in Table 4.1. The PCE and J$_{SC}$ of representative devices, measured over time at a fixed voltage, reveal that both recipes yield devices with a stable power out-
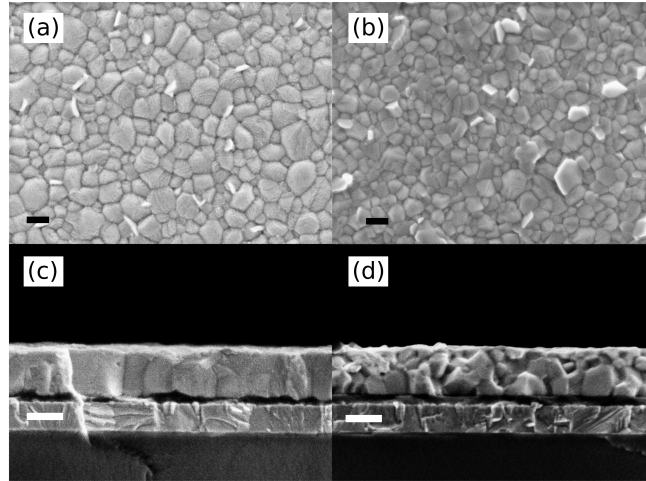
Figure 4.2: SEM top view and cross-section images of a,c) pristine $PbAc_2$ and b,d) sol-eng films on ITO/PEDOT:PSS. The scale bars represent 200 nm.

put (Figure 4.4). This hysteresis-free behavior is typical for devices using $PC_{60}BM$ in the inverted architecture (Sec. 2.3.1.2). The lower PCE for the sol-eng recipe is mainly due to a strongly reduced J_{SC}, as well as a slightly reduced FF.

Table 4.1: Statistics of PV parameters (in the reverse and forward scan) for $PbAc_2$ (158 devices) and sol-eng (130 devices) solar cells with the structure ITO/PEDOT:PSS/$MAPbI_3$/ $PC_{60}BM$/BCP/Ag.

	$PbAc_2$ reverse	$PbAc_2$ forward	sol-eng reverse	sol-eng forward
V_{OC} [V]	0.91 ± 0.04	0.90 ± 0.04	0.93 ± 0.06	0.92 ± 0.06
J_{SC} [mA/cm^2]	19.3 ± 0.9	19.3 ± 0.9	14.0 ± 1.1	14.0 ± 1.1
FF [%]	78.1 ± 2.5	77 ± 2.6	64 ± 10.9	63.3 ± 11.7
PCE [%]	13.68 ± 0.7	13.41 ± 0.77	8.24 ± 0.87	8.05 ± 0.96

Another important quantity for the optoelectronic quality of perovskite films is their defect density. It was recently proposed that most of the defects - especially dangling bonds (from undercoordinated lead ions or iodide terminations) - are present at the film surface [152, 169, 170, 173, 302, 335] (Sec. 2.2.6). PL spectra for $PbAc_2$ and sol-eng films on glass substrates, normalized to the maximum of the PL intensity of $PbAc_2$, reveal much higher PL for $PbAc_2$ films (Figure 4.5). The corresponding PLQEs of the films are 10% and 0.1%, respectively. These results suggest that sol-eng films possess a strongly enhanced surface trap density.

We want to briefly discuss possible reasons why devices prepared with the sol-eng recipe show a lower J_{SC} and FF when compared to the $PbAc_2$ recipe. The use of $PC_{60}BM$ in the inverted device architecture in principle should help minimize the impact of surface defects on device efficiency (Sec. 2.3.1.2). Furthermore, grain bound-
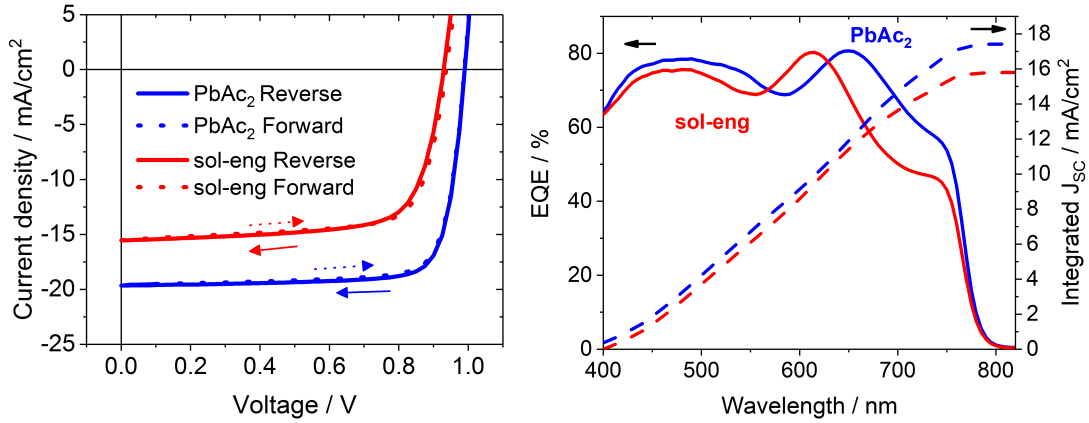
Figure 4.3: Current–voltage curves of champion devices with the structure ITO/PEDOT:PSS/MAPbI$_3$/PC$_{60}$BM/BCP/Ag with perovskite active layers prepared by PbAc$_2$ (blue) and sol-eng (red) (left) as well as corresponding EQE spectra and integrated J$_{SC}$ of typical pixels (right). Reproduced with permission from [334]. Copyright 2017, Wiley-VCH.

aries (GB) have been suggested to be electrically benign due to the fact that defects at GBs, for example, resulting from dangling bonds at the surface or boundary regions, only form shallow trap states. Most of these defects are filled at illumination intensities of 1 sun and should not strongly impede device efficiency ([103, 336, 337]; Sec. 2.2.3). However, GBs can possibly act as barrier for charge transport. A facet dependent charge carrier mobility in highly orientated MAPbI$_3$ films has, for example, been reported by Cho *et al.* [338]. Leblebici *et al.* found significant intra-grain heterogeneity in the J$_{SC}$ and V$_{OC}$ for MAPbI$_3$ films prepared by a one-step PbCl$_2$ route (Sec. 2.3.2.1), which the authors attributed to a facet dependent defect concentrations. It was suggested that controlling the facet orientation, especially at the interfaces with the hole- and electron transporting materials, is important to reach highest efficiencies [339]. PL studies by DeQuilettes *et al.* revealed the existence of differences in intergrain connectivity [170]. Hence, we assume that an increased density of charge traps at the multiple grain boundaries with varying facets, as well as a reduced intergrain connectivity, might be the main reasons for the reduced J$_{SC}$ and FF in devices fabricated by the sol-eng recipe. Although the sol-eng films have a similar layer thickness and therefore absorb the same amount of light as the PbAc$_2$ films (Sec. 4.3.2), some charges are lost due to poor charge transport and an increased recombination rate throughout the film.

4.3   Degradation of Bare Films in Various Levels of Oxygen

To directly study the effect of different microstructures on the rate of oxygen induced photodegradation, we degraded bare MAPbI$_3$ films deposited either on ITO/PEDOT:PSS (for device, SEM and XPS studies) or on glass/PDS substrates (for UV-Vis and PDS measurements). We chose these sample structures, because degrading
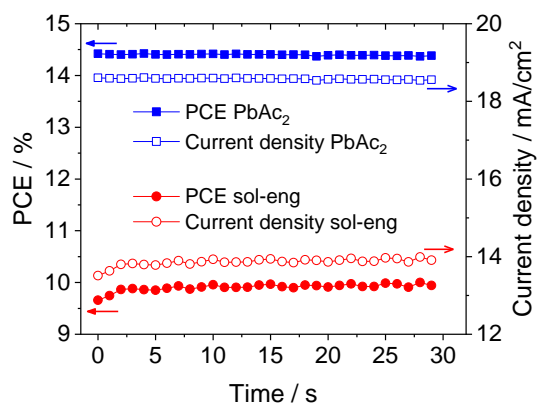
Figure 4.4: Power conversion efficiency and current density solar cells fabricated by PbAc$_2$ and sol-eng recipes over 30 s continuous illumination at maximum power point (0.78 V and 0.7 V for PbAc$_2$ and sol-eng, respectively). Reproduced with permission from [334]. Copyright 2017, Wiley-VCH.
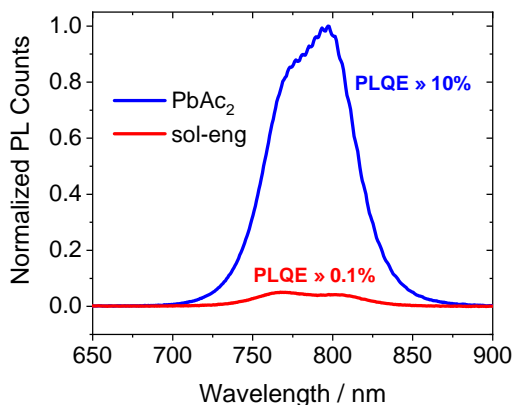
Figure 4.5: Photoluminescence spectra of PbAc$_2$ and sol-eng films prepared on spectrosil. Reproduced with permission from [334]. Copyright 2017, Wiley-VCH.

complete devices would complicate the interpretation of results: The ETL (in our case PC$_{60}$BM) has been proposed to serve as an oxygen diffusion blocking layer and might extract electrons from the MAPbI$_3$ film before they can react with oxygen ([221, 298]; Sec. 2.4.2). In that case, oxygen induced degradation would be greatly suppressed and not allow us to ascertain the influence of microstructure. Complete devices also add additional degradation pathways, such as degradation of the metallic contact due to iodide diffusion, which could further complicate the interpretation of the results ([40, 158]; Sec. 2.2.5). Recently, we have studied the degradation of complete devices in the inverted architecture under full illumination and under various atmospheres. We observed that an oxygen containing atmosphere has little to no influence on the degradation rate as compared to a N$_2$ atmosphere, further supporting that PC$_{60}$BM suppresses oxygen induced degradation on a short timescale (Rivkin *et al.* [301]).

The MAPbI$_3$ films were spin-coated in a drybox and directly afterwards transferred into a N$_2$ glovebox. The substrates were loaded into a sample holder which was then connected to our environmental rig (Sec. 3.2.13). The sample holder was flushed with either pure N$_2$, or N$_2$ + O$_2$ with varying levels of oxygen. The temperature and oxygen level of the gas flowing through the sample holder were tracked throughout the experiment (see Figure A.2 in the Appendix for the example of a degradation in 10% O$_2$). The perovskite films were then degraded under 1 sun simulated sunlight (100 mW/cm^2) for 10 h (Sec. 3.2.11). For device studies the samples were transferred back to a nitrogen filled glovebox, completed by adding PC$_{60}$BM/BCP/Ag (Sec. 3.1.4), and subsequently measured under the solar simulator. For the other characterization methods (UV-Vis, PDS, XPS and SEM), the degraded bare
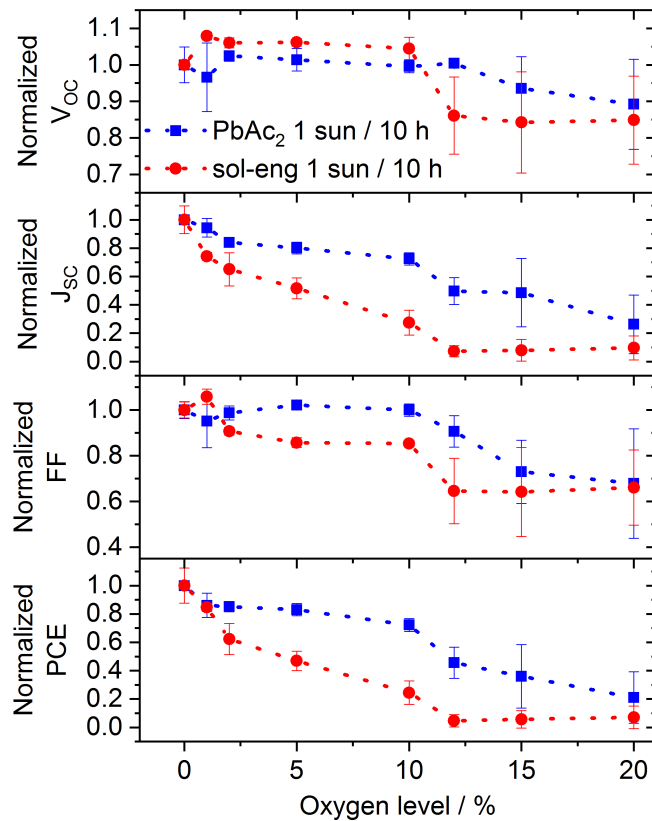
Figure 4.6: Solar cell characteristics of ITO/PEDOT:PSS/MAPbI$_3$/PC$_{60}$BM/BCP/Ag solar cells, with the bare MAPbI$_3$ layer degraded for 10 h under various oxygen levels at 1 sun illumination before completion of the device, normalized to the values of the device where the bare MAPbI$_3$ layer was degraded in N$_2$ atmosphere. Reproduced with permission from [334]. Copyright 2017, Wiley-VCH.

MAPbI$_3$ films were examined.

4.3.1 Photovoltaic Devices

In order to ensure that any observed degradation was only induced by the combination of O$_2$ and light illumination, we checked if illumination in pure N$_2$, or alternatively storage in O$_2$ in the dark, induces any degradation of the perovskite films. For that purpose, devices from the same batch were compared: some of them were stored in the N$_2$ filled glovebox, some were degraded under 1 sun simulated sunlight in N$_2$ atmosphere for 10 h and some were stored in 20% O$_2$ in the dark for 30 h in the sample holder. Afterwards, all of these devices were completed by adding PC$_{60}$BM/BCP/Ag and measured under the solar simulator. All JV-curves are very similar for the tested conditions (see Figure A.3 in the Appendix). Therefore, it can be concluded that neither dark storage in O$_2$ nor light illumination in N$_2$ atmosphere induces any degradation (in comparison to devices stored for the same amount of
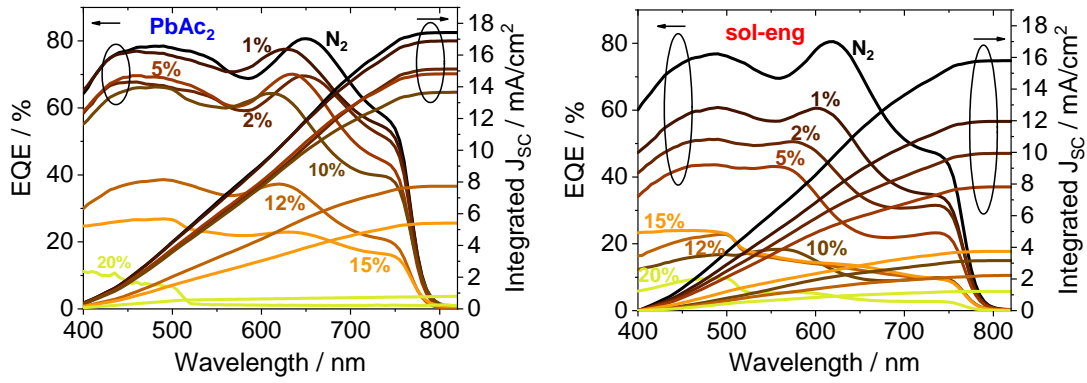
Figure 4.7: EQE spectra of the degraded PbAc$_2$ (left) and sol-eng (right) devices, respectively. Reproduced with permission from [334]. Copyright 2017, Wiley-VCH.

time in N$_2$ in the dark) on the timescale of 10 h. This confirms previous studies [298, 340, 341]. Thus, the PV parameters of MAPbI$_3$ films degraded in N$_2$ atmosphere for 10 h were taken as a reference and the PV parameters for the various oxygen levels were normalized with respect to these devices.

Up to an oxygen level of 10%, the V$_{OC}$ and FF are roughly unchanged, while the J$_{SC}$ already shows a decrease for oxygen values as low as 1% (Figure 4.6). The strength of the drop in J$_{SC}$, however, is quite different for the two recipes, with the sol-eng devices showing a much stronger decrease. Above an oxygen value of 10%, an additional decrease in all PV parameters can be observed. After degradation in 20% O$_2$ the PCE is below 25% of its initial value for the PbAc$_2$ recipe, while for the sol-eng recipe, an O$_2$ level of only 12% results in PCEs close to zero.

EQE measurements for the various oxygen levels confirm the observed trend in J$_{SC}$ (Figure 4.7). While the EQE of PbAc$_2$ devices is only slightly reduced for oxygen levels up to 10%, the sol-eng devices show a strong reduction in EQE even for very low oxygen levels. The fact that the reduction in EQE, being connected to a reduced number of extracted charges, happens over the whole visible spectrum hints to a reduced light absorption of the perovskite layer. To test this hypothesis, we show UV-Vis measurements in the next section.

For a better understanding of the dynamics of the degradation process at various oxygen levels, time dependent degradation studies for the PbAc$_2$ recipe were performed. Bare PbAc$_2$ films on ITO/PEDOT:PSS were degraded at 15% O$_2$ for 3.6, 8 and 10 hours as well as at 5% O$_2$ for 6, 10, 19 and 30 hours, completed to devices, and measured. Hence, the devices at 5% O$_2$ were degraded at a third of the oxygen level for triple the time duration in comparison to the ones at 15% O$_2$. The results of this study are shown in Figure 4.8. It is evident that already at early times a degradation is present for both oxygen levels. The rate of degradation is, however, strongly enhanced for 15% O$_2$. For 5% O$_2$ mainly the J$_{SC}$ is degrading, with only a minor reduction of V$_{OC}$ and FF. Even after 30 h of degradation, the devices still possess above 60% of their initial PCE. In contrast, at 15% O$_2$ for 10 h, the devices are already below
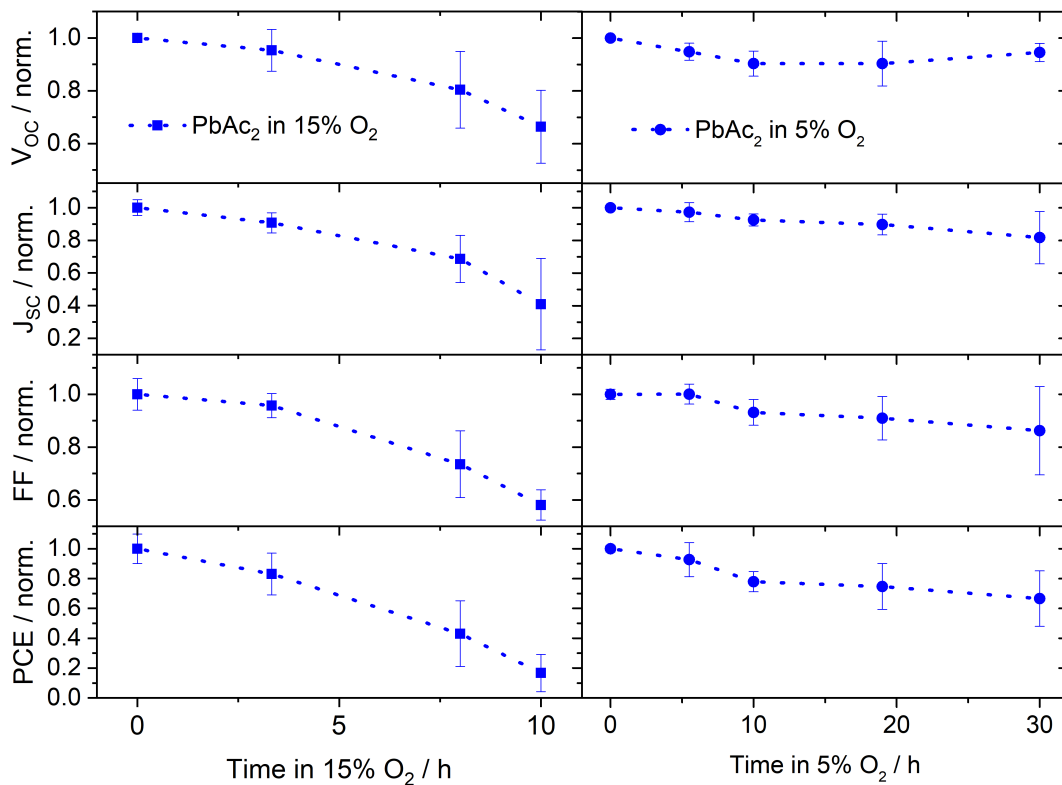
Figure 4.8: Time dependant study of the photovoltaic parameters and hysteresis index ($PCE_{Reversescan}$/ $PCE_{Forwardscan}$) for the case of $PbAc_2$ films degraded at 15% O_2 (left) and 5% O_2 (right) at 1 sun illumination for various times. Reproduced with permission from [334]. Copyright 2017, Wiley-VCH.

20% of their initial PCE. This stems from the fact that not only is the J_{SC} degrading, but also the FF and V_{OC} exhibit a strong decrease. These results show that the degradation does not behave linearly when comparing the relation of time to oxygen level.

4.3.2 UV-Vis and PDS

UV-Vis measurements of pristine and degraded films on glass substrates (1 sun for 10 h at various oxygen levels) were conducted to track the degradation of bulk absorbance (Figure 4.9). For $PbAc_2$ films, the absorbance only slightly drops for oxygen levels of up to ~5% O_2. For 10% O_2 and above, the absorbance drops more strongly and exhibits an absorption onset at ~520 nm, which can be attributed to the formation of PbI_2 in the film [298, 302]. In contrast, for sol-eng films the absorbance decreases strongly over all wavelengths already at 1% O_2, and the absorption onset of PbI_2 can be observed for oxygen levels as low as 5%. This behavior becomes apparent when comparing the absorbance value at 700 nm for both recipes at different oxygen levels (Figure 4.10). The drop in absorbance is strongly suppressed for the $PbAc_2$ films
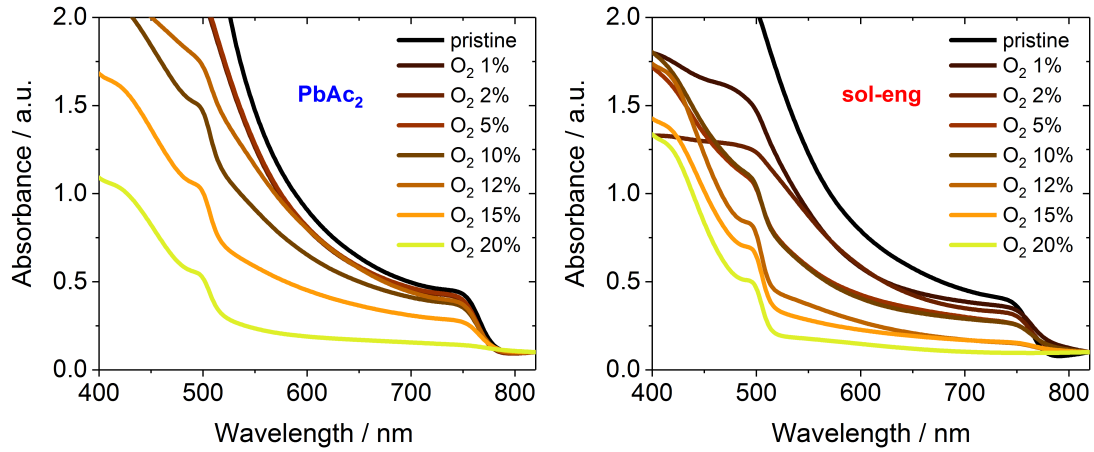
Figure 4.9: UV–Vis measurements of degraded films for PbAc$_2$ (left) and sol-eng (right) on ITO/PEDOT:PSS at various oxygen levels for at 1 sun for 10h. The measurements were performed by Qing Sun. Reproduced with permission from [334]. Copyright 2017, Wiley-VCH.

when compared to the sol-eng films. These observations fit with the EQE and J-V results and suggest that there is a loss in the amount of MAPbI$_3$ and a conversion towards PbI$_2$ occurring in the films, in line with literature reports [302, 303]. In sol-eng films, the rate of this process is strongly enhanced. We conclude that the reduction in absorbance over the visible spectrum is the main cause for the decreased device J$_{SC}$.

To study changes of the absorption onset of the MAPbI$_3$ films upon degradation, PDS measurements were employed. The Urbach energy can be determined from these measurements and serves as a measure for the electronic quality of the perovskite films ([84, 86], see Sec. 3.2.9). For pristine films, as well as for films degraded at oxygen levels up to 5%, the Urbach energy is fairly unchanged at around 18.5 meV (Figure 4.11). Above 5% O$_2$, the sol-eng films show a steady increase, reaching around 22 meV for 8% O$_2$ and around 24 meV for 10% O$_2$. At 12% O$_2$ no value could be determined, because the bulk of the film was completely converted to PbI$_2$ (see photographs in Figure 4.11). For PbAc$_2$, the Urbach Energy is unchanged up to 10% O$_2$, above which it shows an increase to above 22.5 meV for 12% O$_2$. Only at 15%, when most of the film is completely converted to PbI$_2$, no value could be determined.

The fact that the Urbach energy at lower oxygen levels is unchanged for both recipes seems surprising at first, considering that the sol-eng films are already degraded to a great extent. As an explanation we assume that, while parts of the film are already converted to PbI$_2$, other parts still consist of MAPbI$_3$. The Urbach energy can only provide information about the absorption onset of MAPbI$_3$ itself, and is thus not sensitive towards the degraded parts which consist of PbI$_2$ and byproducts. Therefore, we assume that since the non-degraded parts of the film exhibit the same steep absorption onset, they are still composed of high-quality MAPbI$_3$ perovskite. The charge carrier generation and separation processes in these regions might thus still be very efficient. Only when nearly the entire bulk of the film is degraded -

occurring at 8% and 12% O_2 for sol-eng and PbAc$_2$ films respectively - the Urbach energy exhibits a steep rise and the electronic properties become hampered. This would also explain why slightly degraded devices, despite a strong drop in J_{SC}, still exhibit a decent V_{OC} and FF.
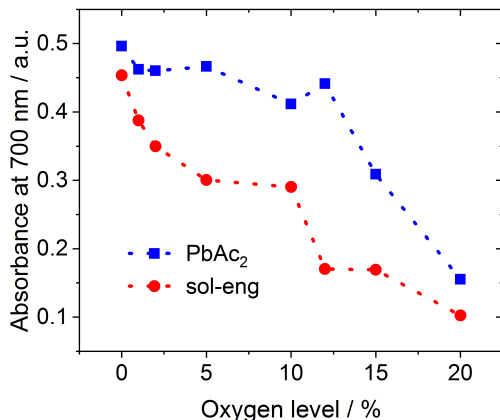

Figure 4.10: Absorbance at 700 nm for Glass/MAPbI$_3$ films using PbAc$_2$ (red) and sol-eng (blue) recipes, degraded at various O_2 levels at 1 sun for 10 h. Taken from the UV-Vis data in Fig. 4.9. Reproduced with permission from [334]. Copyright 2017, Wiley-VCH.
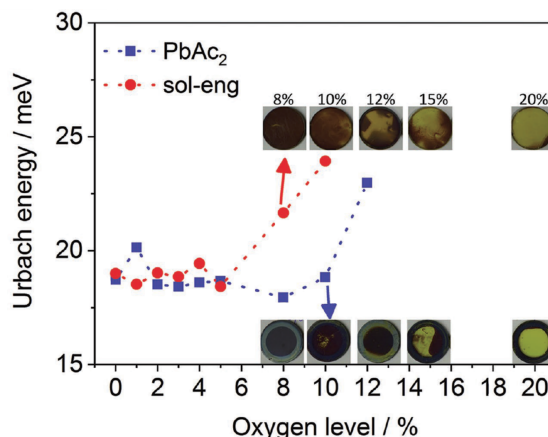
Figure 4.11: Urbach energies of degraded films prepared on spectrosil determined by PDS measurements. The measurements were performed by Alexandra Bausch. Reproduced with permission from [334]. Copyright 2017, Wiley-VCH.

4.3.3 XPS

To study changes in surface composition of the degraded films in more detail, we performed XPS measurements. These measurements were performed by Qing Sun. For completeness, the main results of these measurements are briefly discussed here. A detailed analysis will be presented in Qing Sun's Ph.D. thesis.

In Figure 4.12 (a) the N1s peak from the C-N bond of the CH$_3$NH$_3$ cation in MAPbI$_3$ perovskite as determined by XPS is plotted for pristine and degraded films. Consistent with the already mentioned conversion from MAPbI$_3$ to PbI$_2$, a loss of nitrogen (N1s at 402.6 eV) at the film surface for both recipes can be observed. While a small N1s signal can still be observed for PbAc$_2$ at 12% O_2, for sol-eng the N1s signal completely disappears for oxygen levels as low as 2%. From the complete XPS spectra, the I/Pb atomic ratio can also be determined (Figure 4.12 (b)). For both pristine films, the I/Pb ratio is at around 3.8 and in Section 5.2.2 we discuss possible reasons why it is above the expected I/Pb ratio of 3 for MAPbI$_3$ in more detail. After dedgradation, the I/Pb ratio is reduced more strongly for the sol-eng recipe and is already below the expected ratio of 3 for 2% O_2, while for PbAc$_2$ it only drops below 3 for oxygen values above 10%. We conclude that the top surface of PbAc$_2$ is much more stable when compared to sol-eng, in line with the previous results.
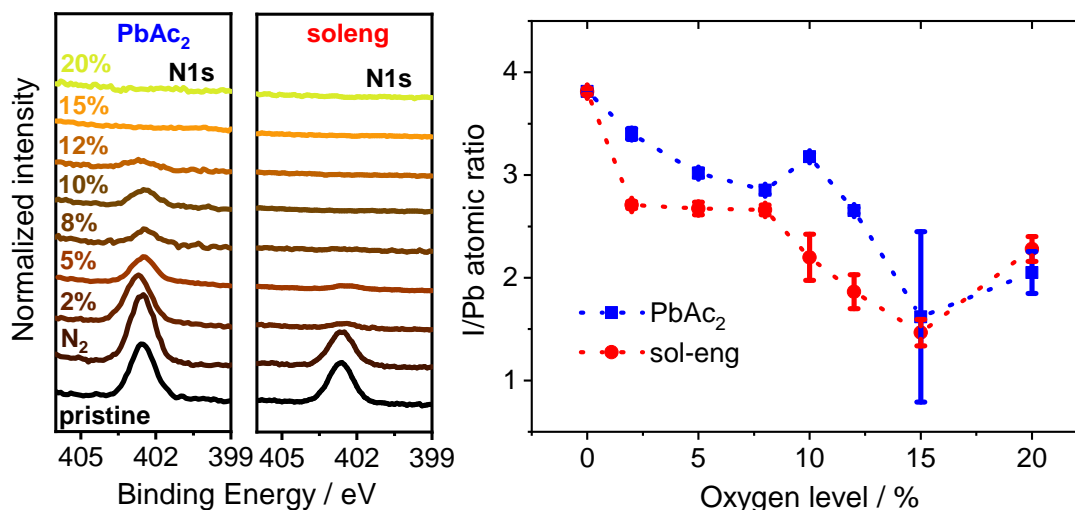
Figure 4.12: N1s spectra (left) and calculated I/Pb atomic ratios from XPS measurements on pristine and degraded (10 h under various oxygen levels at 1 sun illumination) MAPbI$_3$ layers on ITO/PEDOT:PSS fabricated using PbAc$_2$ and sol-eng recipes. The measurements were performed by Qing Sun. Adapted with permission from [334]. Copyright 2017, Wiley-VCH.

4.3.4 Degradation of the Microstructure - SEM

The dynamic degradation of the MAPbI$_3$ microstructure was studied in more detail by taking a series of SEM images for ITO/PEDOT:PSS/MAPbI$_3$ films degraded at various oxygen levels (Figure 4.13). It must be mentioned that as the size of the shown sections is on the order of 2x2 µm^2, this analysis can only give a rough visualization of the degradation process. The presented SEM images were chosen to be as representative for the degradation process as possible. As expected, the films degraded in N$_2$ atmosphere for 10 h do not show any sign of degradation. For PbAc$_2$ films degraded at 2% and 5% O$_2$, the grain structure is still identifiable (in particular in the cross-section images), however, small structures start to appear at the film surface, implying the onset of grain damage. In the cross-section images, these structures are also visible in form of small cracks close to the film's surface. For 10% and 12% O$_2$ the grain structure is hard to identify (in top-view) anymore, with more and more small holes appearing on the film's surface. From the cross-section it becomes clear that these holes progress deep into the film and also the lower parts of the film start to become damaged. However, at this stage of degradation the total layer thickness is not reduced yet. For 15% O$_2$, the whole film is degraded and the surface does not show any grain structure anymore. The cross-section reveals that the whole film becomes irregular and much thinner.

Sol-eng films exhibit completely different behavior. In the top-view images the grain structure is already not identifiable anymore at 2% and 5% O$_2$ and has transformed. More importantly, the cross-section images reveal that even for these low levels of oxygen the films become much thinner, while at the bottom parts of the films the
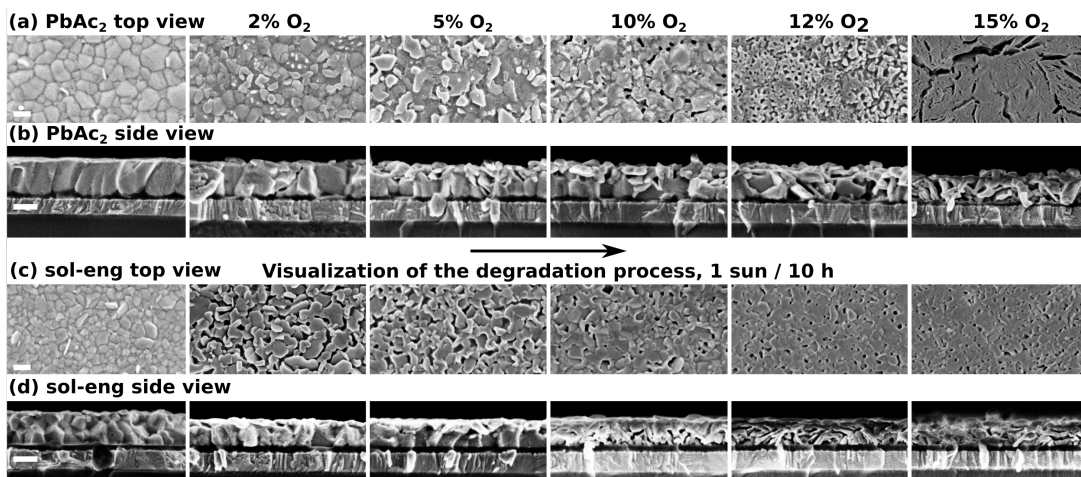
Figure 4.13: SEM top view and cross-section pictures of a,b) PbAc$_2$ and c,d) sol-eng showing changes in morphology for different degradation states from left, degraded in N$_2$ to right, degraded in 15% O$_2$, all for 10 h at 1 sun illumination. Scale bars represent 200 nm. Reproduced with permission from [334]. Copyright 2017, Wiley-VCH.

MAPbI$_3$ grains are still visible. At higher oxygen levels of 10% and above, the entire film is degraded and the microstructure does not change much anymore. Overall, these results are consistent with the UV-Vis, EQE and XPS results from the previous sections: the fact that the top surface of sol-eng films degrades very rapidly already at low levels of oxygen, explains the observed strong drop of J$_{SC}$ and absorbance. Deeper in the bulk, the grains still consist of high-quality MAPbI$_3$, which yields decent device performance (V$_{OC}$ and FF) and a low Urbach energy.

In order to better resolve the details of the microstructural degradation, we also degraded PbAc$_2$ films deposited directly on ITO substrates. Thereby, the MAPbI$_3$ grain size is increased (around 1-2 µm), which can be attributed to the worse wettability of the perovskite solution on ITO compared to PEDOT:PSS ([191]; Sec. 2.3.1.2). The films were degraded at a low oxygen level of 5% and measured by SEM (see Figure 4.14 for images with high magnification and Figure A.4 in the Appendix for an image with lower magnification). There are two primary observations: first, degradation commences at the grain boundaries and progresses inward. Second, while the bulk of some grains is already completely degraded, some grains are still intact, and others are in a partly degraded state. We attribute this heterogeneity in the degradation rate between various grains to a varying and heterogeneous defect density across the MAPbI$_3$ film.

4.4 Summary

In this chapter, the oxygen induced photodegradation of MAPbI$_3$ films with two different microstructures was studied. The analysis of the microstructure by AFM and SEM revealed that the PbAc$_2$ recipe results in films with large grains which extend
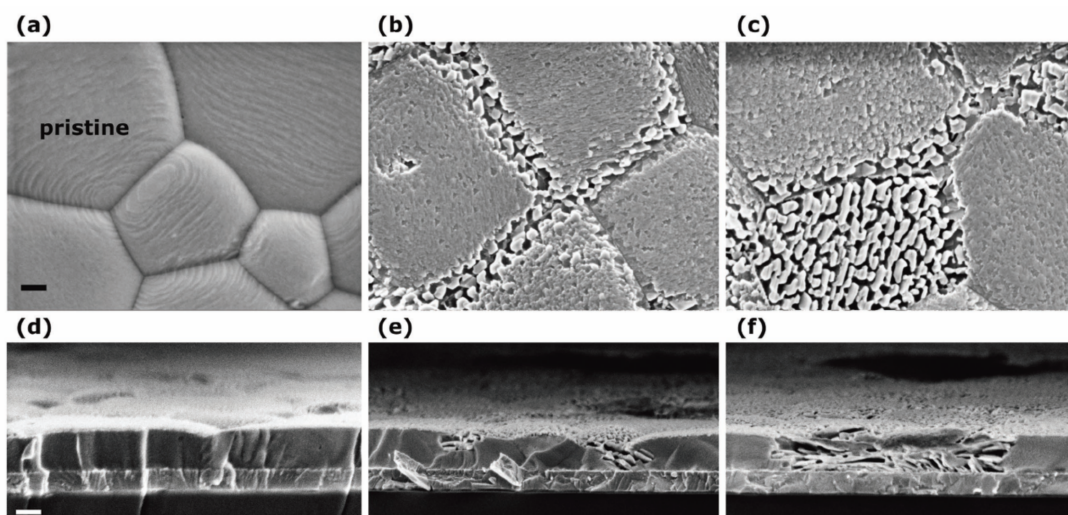
Figure 4.14: SEM top-view and cross-section images of PbAc$_2$ films deposited on ITO substrates, degraded at 5% O$_2$: a,d) pristine layers, b,e) initial stages of degradation, and c,f) later stages of degradation. Scale bars represent 200 nm. Reproduced with permission from [334]. Copyright 2017, Wiley-VCH.

throughout the whole layer thickness (~300 nm), and the corresponding devices in the architecture ITO/PEDOT:PSS/MAPbI$_3$/PC$_{60}$BM/BCP/Ag yielded a PCE of up to 15.5%. Films prepared with the sol-eng recipe, in contrast, consist of smaller and more irregular grains with multiple grain boundaries throughout the layer. We propose this microstructural heterogeneity to be the reason for the observed lower device J$_{SC}$ and FF, resulting in PCEs of only 10.5%. The PL intensity of the films is very different, with PLQEs of 10% and 0.1% for PbAc$_2$ and sol-eng, respectively. As PLQE is a surface sensitive technique, we assume that there is an increased density of defects at the film surface and at the multiple grain boundaries of the sol-eng films.

To further examine this effect, we degraded bare ITO/PEDOT:PSS/MAPbI$_3$ films in dry N$_2$ with various levels of oxygen (1%, 2%, 5%, 10%, 12%, 15%, 20%) under 1 sun simulated sunlight for 10 h and afterwards analyzed the degraded films and completed photovoltaic devices (ITO/PEDOT:PSS/MAPbI$_3$/PC$_{60}$BM/BCP/Ag). The PV parameters and EQE of degraded devices revealed that the observed drop in PCE, mainly caused by a reduction in J$_{SC}$, is strongly enhanced for the sol-eng recipe. UV-Vis and XPS measurements suggest that the degradation is happening at the film surface due to a loss of MAI species and thus conversion of MAPbI$_3$ into PbI$_2$. The rate of this process is strongly enhanced for the sol-eng films. The Urbach energy of degraded films for both recipes shows no increase for oxygen levels below 8%. We assume that despite degradation, the electronic quality of the remaining MAPbI$_3$ in the films is still high, which also yields an explanation for the still decent device V$_{OC}$ and FF for slightly degraded films.

In line with these results, the microstructural analysis with SEM shows that especially the top surface of the sol-eng films is degrading much more quickly. While the
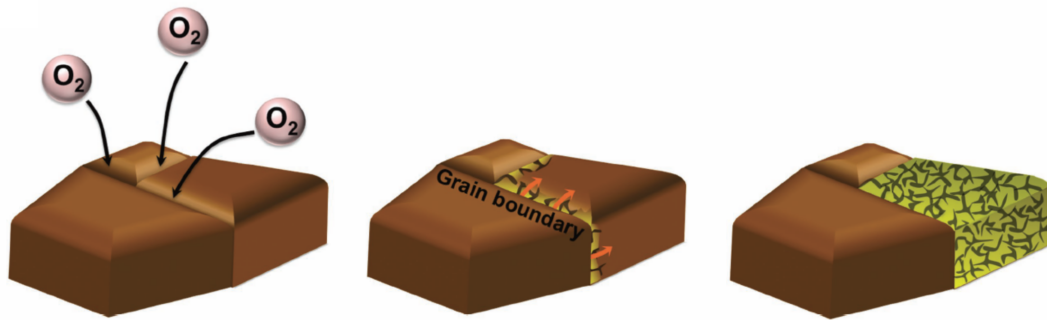
Figure 4.15: Schematic illustration of the degradation process for a perovskite films with large grains protruding throughout the whole film. The degradation commences at the defect density rich grain boundaries and progresses into the grain interior. Reproduced with permission from [334]. Copyright 2017, Wiley-VCH.
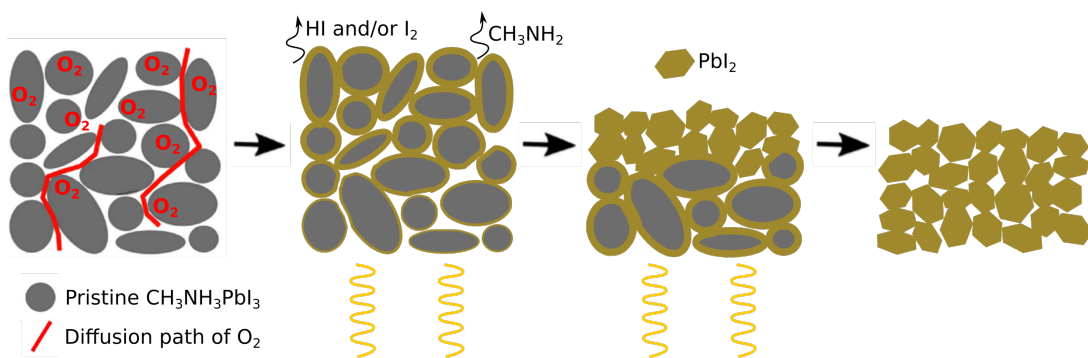

Figure 4.16: Schematic illustration of the degradation process for a perovskite film with multiple, irregular grains throughout the layer thickness. The top surface starts to degrade first and converts to PbI_2 by releasing HI, I_2 and CH_3NH_2, while the lower parts of the film still partly consist of $MAPbI_3$. Adapted and modified from [302].

large grains for the $PbAc_2$ films only show slight damage for degradation in the low oxygen levels, the sol-eng films already exhibit a 30-40 nm reduced layer thickness. This reduction explains the strongly enhanced decrease in absorbance and J_{SC} for the sol-eng films and devices respectively. For $PbAc_2$ films deposited on ITO substrates, we revealed that the degradation is initiated at surfaces and grain boundaries. There are two explanations for why the degradation rate is higher in grain boundary regions: a higher defect density when compared to the bulk region, and easier infiltration of oxygen molecules resulting in a higher rate of superoxide generation. In line with the latter argument, time dependent degradations at two different oxygen levels for the $PbAc_2$ recipe revealed that degradation does not progress linearly when comparing the relation of time to oxygen level. We assume this effect stems from faster infiltration of oxygen molecules into the perovskite bulk lattice at higher oxygen levels. This assumption is supported by a recent study by Senocrate *et al.* , who studied the change of electrical and ionic conductivity of $MAPbI_3$ films upon exposure to illumination and various partial pressures of oxygen. Slow dynamics on a timescale of

hours were observed at low partial pressures of oxygen [303], suggesting that the diffusion of oxygen molecules is slowed down for low oxygen levels. Additionally, we observed a strong variance in the rate of degradation between different grains. We attribute this effect to a strong heterogeneity in trap state density for MAPbI$_3$ films, as recently proposed by a number of PL studies [169–171, 342], with iodide vacancies being the suggested preferred site for superoxide formation [302]. To conclude the results of this chapter, we schematically depict the degradation for PbAc$_2$ films - with large and regular grains - and sol-eng films - with small and irregular grains - in Figures 4.15 and 4.16, respectively.

Part II

Fractional Variations in Precursor Stoichiometry

"To err is human, to forgive divine"
Alexander Pope

This quote relates to metal halide perovskites because, at first, they might seem to be divine, because of their intriguing optoelectronic materials despite a high defect density. However, we will reveal in this chapter that the MAPbI$_3$ perovskite composition is not very forgiving to human error when preparing the precursor solution. We study the effect of fractional variations in precursor solution on various properties of the resulting perovskite films in great detail, including surface composition and energetics, device efficiency and stability and photoluminescence properties. We conclude that MAPbI$_3$ perovskite is not, in fact, divine.

5. Effect on Photovoltaic Devices

5.1 Introduction

This chapter is based on our recent publication in the journal Energy and Environmental Science [343] with the title: "Fractional Deviations in Precursor Stoichiometry Dictate the Properties, Performance and Stability of Perovskite Photovoltaic Devices". Most of the graphs in this chapter are reproduced or adapted with permission of The Royal Society of Chemistry. This chapter would not have been possible without the contributions of Vincent Lami, who performed the XPS/UPS measurements and Alexandra Bausch, who performed PDS measurements. The XRD measurements were performed in collaboration with Dr. Zhiping Wang in the group of Prof. Dr. Henry Snaith at Oxford University.

Early on in research of perovskite materials, their reported properties showed quite a large variation when examined by different researchers [25, 31, 344]. The reasons for this behavior are many, but to a great extent stem from the complicated solution chemistry ([45]; Sec.2.3.2) and defect physics (Sec. 2.2.3) of perovskite materials. Minor details in the fabrication process, such as the recipe itself (including composition), the surrounding atmosphere (solvents, O_2, humidity), the annealing protocol or the method of applying an antisolvent can all influence the microstructure, crystallinity, or defect density, and with it the final electronic properties of a perovskite film [18, 345, 346]. In our experience, the $PbAc_2$ based recipe (Sec.2.3.2.1) on ITO/PEDOT:PSS substrates provided results that could be reproduced satisfactorily. The enhanced reproducibility in comparison to other recipes can be explained by three factors: the addition of HPA to the precursor solution, simple one-step solution coating with a short annealing step and the lack of an additional antisolvent treatment [258]. Especially the antisolvent treatment can induce great variations from sample to sample, because it is applied by hand and the right pressure must be applied [346, 347].

However, when analyzing the PV parameters obtained during the oxygen degradation study (Table 4.1 in Chapter 4), we noticed that despite following the same experimental procedure, a certain batch to batch variation was still present. While the variation in J_{SC} and FF was negligible, the average V_{OC} varied slightly. This rather unexpected behavior can be visualized by plotting histograms of the V_{OC} values for one single batch, as well as seven different batches, using the $PbAc_2$ recipe in the inverted structure with ITO/PEDOT:PSS/$MAPbI_3$/$PC_{60}BM$/BCP/Ag (Figure 5.1). The Gaussian distribution clearly shows that the spread in V_{OC} is more severe for seven batches. A possible cause of such a behavior could be small variations in the stoichiometry of the precursor solution, as previously shown for other recipes ([315–317]; Sec. 2.4.3).

As described in Section 2.3.2.1, the PbAc$_2$ precursor solution consists of a mixture of MAI and PbAc$_2$ with a 3:1 molar ratio, dissolved in DMF. We developed a method to fractionally vary the composition of the precursor solution in small steps. The procedure is explained in great detail in Section 3.1.3. While a number of recent studies analyzed the effect of precursor stoichiometry and film composition on the properties of perovskite films and devices (Sec. 2.4.3), studies varying the precursor stoichiometry in very small steps are rare. Such a study specifically for the PbAc$_2$ recipe has not been yet reported. Therefore, in this chapter the influence of the exact precursor stoichiometry on the properties of perovskite films is studied in detail employing various characterization methods (Sec. 5.2). In addition, we also studied the effect of such fractional variations on photovoltaic devices employing other recipes and device architectures (Sec. 5.3). Our results indicate that even small stoichiometric variations can significantly impact the properties of MAPbI$_3$ films and devices, and provide a partial explanation for the wide variation in properties and performance observed in early perovskite devices, even up to today.
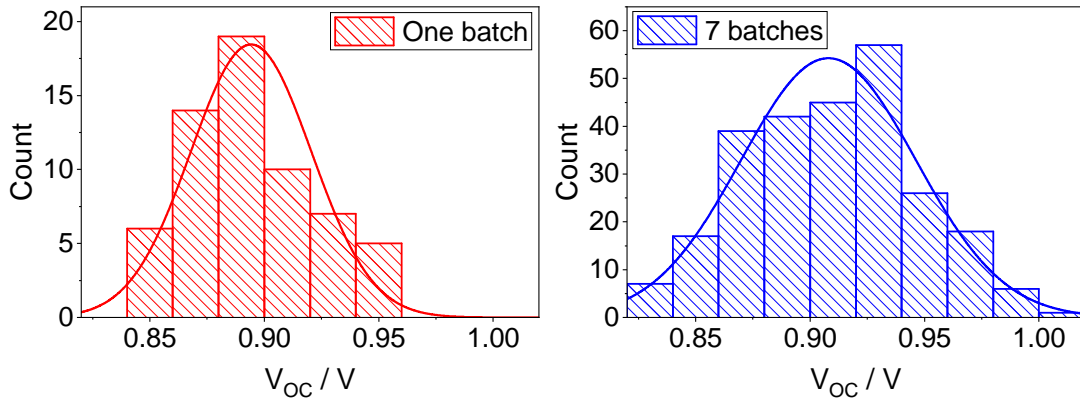

Figure 5.1: Statistics of V$_{OC}$ of solar cells with the architecture ITO/PEDOT:PSS/MAPbI$_3$/ PC$_{60}$BM/BCP/Ag from one single batch (left) and 7 different batches (right) from devices made for the study in chapter 4.

5.2   Results for p-i-n Devices Employing the PbAc$_2$ Recipe

The molar ratio MAI:PbAc$_2$ used in the PbAc$_2$ recipe is defined as the stoichiometry y =MAI:PbAc$_2$. This recipe and variable are used throughout this chapter, with y being varied in small steps between $2.96 < y < 3.07$. The experimental procedure is explained in detail in Section 3.1.3. The color scale to represent different stoichiometries y throughout this chapter is shown in Figure 5.2. Films and devices with $y > 3.00$ and $y < 3.00$ are denoted as 'overstoichiometric''understoichiometric' respectively.

Figure 5.2: Color scale to represent various precursor stoichiometries of y = MAI:PbAc$_2$ throughout this chapter.

5.2.1 Photovoltaic Parameters

Solar cells with the architecture ITO/PEDOT:PSS/MAPbI$_3$/PC$_{60}$BM/BCP/Ag made from precursor solutions with various stoichiometries ($2.94 < y < 3.075$) were fabricated in this study. Apart of the MAPbI$_3$ film, all other layers were always prepared identically (Sec. 3.1.4). The PV parameters of a representative batch with $2.985 < y < 3.075$ and variational steps $\Delta y = 0.1$ are plotted in Figure 5.3. The PCE (d) varies over a wide range of ~2.5%. While the J$_{SC}$ (b) and FF (c) are largely unchanged for $y < 3.065$ (with a maximum J$_{SC}$ at $y \approx 3.00$), there is a strong increase of V$_{OC}$ (a) with values below 0.8 V for understoichiometric devices and above 1 V for the highest stoichiometry. Due to a strong decrease of J$_{SC}$ and FF for $y > 3.055$, the maximum PCE is obtained for $y = 3.055$. The observed trend for J$_{SC}$ was confirmed by measuring EQE spectra of the devices (Figure 5.4 (a)). While the general shape of the EQE spectra is unchanged, the absolute EQE values decrease for $y \gtrsim 3.025$.

The trends of the PV parameters were repeatedly observed in several batches over the course of this project (Figure 5.5). Especially the quasi-linear increase of V$_{OC}$ and the drop of J$_{SC}$ for higher stoichiometries can be observed for all batches. Batch 3 in Figure 5.5 (blue) corresponds to the data shown in Figure 5.3 and was chosen because it is most representative for the observed trends. Representative JV curves from devices in Figure 5.3 reveal that all devices are hysteresis free which can be attributed to the passivation effect from PC$_{60}$BM (Figure 5.6 (a); Sec. 2.3.1.2). Furthermore, a closer look on the JV curves reveals that the steepness of the curves at V$_{OC}$- apart for $y = 3.075$ - is the same for all stoichiometries. This is direct evidence that the series resistance of the devices is not strongly affected by a change in stoichiometry (Sec. 2.1.2).

We also tested if we observe the same trend in V$_{OC}$ if employing an excess of another organic halide in the precursor solution, namely, methylammonium bromide (MABr). Starting from a slightly understoichiometric precursor solution with of $y = 2.96$ (MAI:PbAc$_2$), we added a MABr/DMF stock solution to obtain stoichiometries of $y =$(MAI+MABr):PbAc$_2$ = $2.96 + \Delta y_{MABr}$ = 2.98/3.00/3.04. The PV parameters of this batch reveal that the V$_{OC}$ follows a similar trend as when using excess MAI, increasing from 0.77 V for understoichiometric devices to above 0.9 V for $y = 3.04$, together with a minor increase of J$_{SC}$ and FF (Figure A.5 in the Appendix). This fits with the results of other groups. For example, Zhao *et al.* also employed MABr as an additive in the same device stack employing the PbAc$_2$ recipe (however without the addition of HPA). The authors found a strongly enhanced J$_{SC}$ and FF,
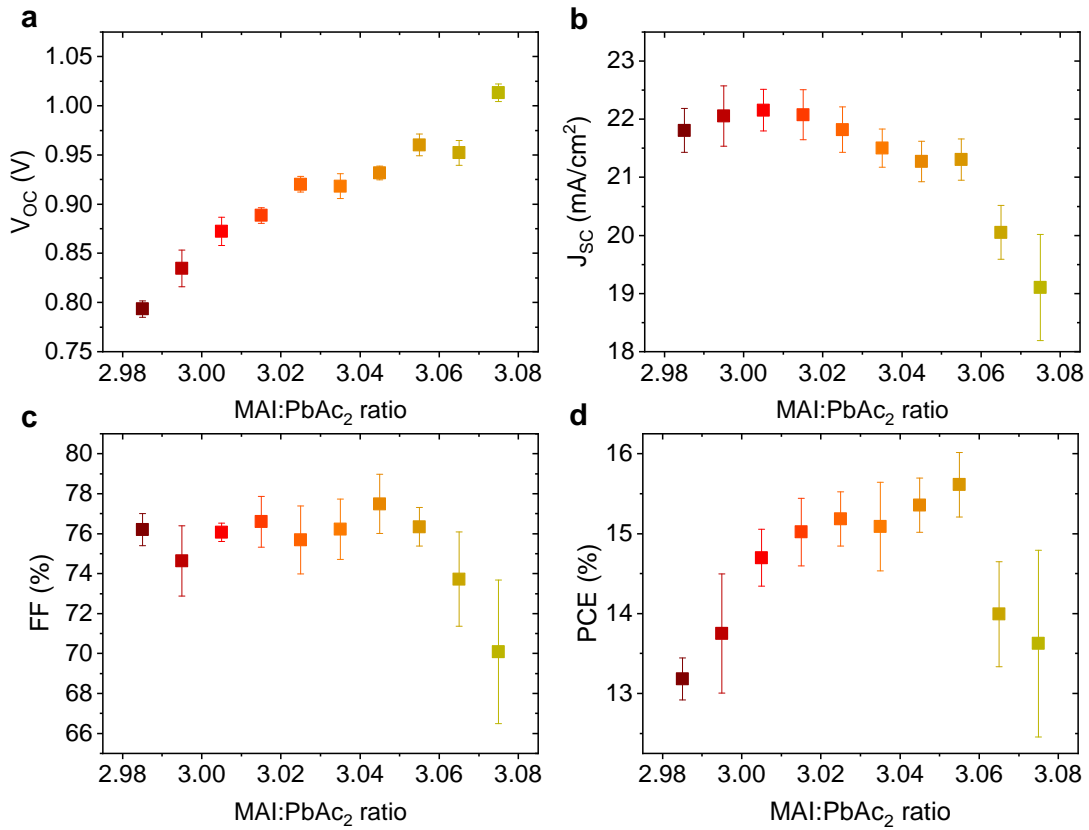
Figure 5.3: Photovoltaic parameters of solar cells with the architecture ITO/Poly-TPD/MAPbI$_3$/PC$_{60}$BM/BCP/Ag with varying stoichiometry y = MAI:PbAc$_2$, (a) V$_{OC}$, (b) J$_{SC}$, (c) FF and (d) PCE. The data is the average from 8-12 pixels within one batch. Reproduced with permission from [343]. Copyright 2018, The Royal Society of Chemistry.

but only a slightly enhanced V$_{OC}$, for an excess of $\Delta y = 0.015$ in the precursor solution compared to their reference devices [348]. However, it should be pointed out that their reference device without the addition of MABr showed rather poor performance ,with a low FF and some hysteresis. Similar to their results, we also observe a minor increase in J$_{SC}$ and in FF, however that for V$_{OC}$ is much more clear.

Such a strong increase of V$_{OC}$ is rather unexpected, however, small variations in precursor stoichiometry might explain the typically reported variations in V$_{OC}$ within the device architecture ITO/PEDOT:PSS/MAPbI$_3$/PC$_{60}$BM/BCP/Ag, ranging from around 0.6 V to 1.1 V [196]. Having a closer look on representative dark-JV curves of devices with various stoichiometries (Figure 5.6 (b)) reveals a shift in the 'knee'-position of the curves which is comparable in size to the observed increase in device V$_{OC}$. This shift is direct evidence of an increase in the built-in field (V$_{bi}$) of the devices 2.1. A shift in V$_{bi}$ could, for example, be present due to a change in the bandgap of the perovskite films. To test this hypothesis, UV-vis spectra of ITO/PEDOT:PSS/MAPbI$_3$ films for various stoichiometries were measured (Figure 5.4 (b)). The bandgap was determined using a Tauc plot (Figure A.6 in the Appendix) and the derived values
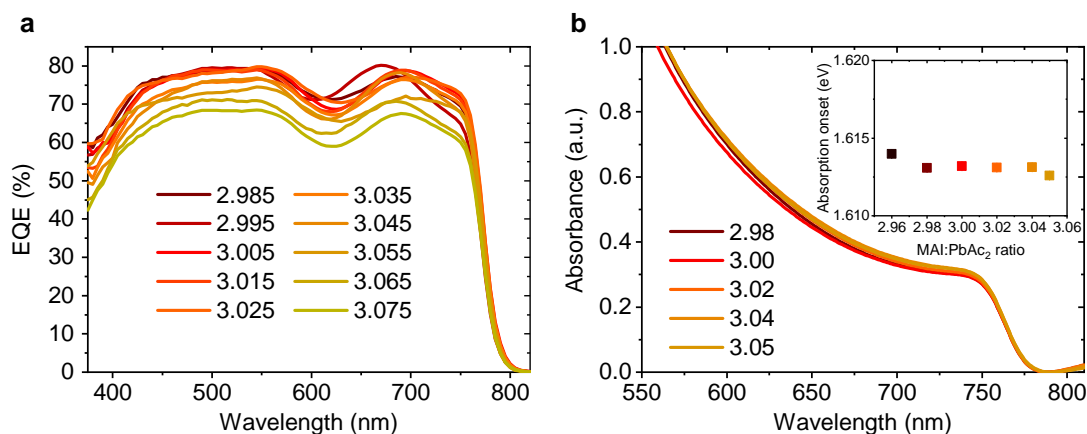
Figure 5.4: (a) External quantum efficiency (EQE) of representative pixels from the batch shown in Figure 5.3. (b) Representative UV-Vis spectra of MAPbI$_3$ films on ITO/PEDOT:PSS with various stoichiometries. The inset shows the bandgap, derived by fitting a Tauc-plot. Adapted with permission from [343]. Copyright 2018, The Royal Society of Chemistry.

are plotted in the inset of Figure 5.4. The bandgap is around 1.61 eV, as expected for MAPbI$_3$ perovskite [89, 349], and does not change with stoichiometry. Hence, a change in bandgap cannot be the reason for the observed shifts of V$_{OC}$ and V$_{bi}$.

5.2.2 XPS, EDX and UPS Results

Another possible reason for an increased V$_{bi}$ could be changes in the surface energetics of the MAPbI$_3$ films. These might be, for example, caused by changes in surface composition (Sec. 2.4.3). Therefore, we decided to perform XPS, EDX and UPS measurements on ITO/PEDOT:PSS/MAPbI$_3$ films with various stoichiometries. We have recently revealed that the surface energetics and composition of MAPbI$_3$ films can be very sensitive to the processing parameters and might show a large variation even on the same sample (Sun *et al.* [347]). However, in that study we also showed that the PbAc$_2$ recipe results in more homogeneous MAPbI$_3$ surfaces when compared to the sol-eng recipe, which is more sensitive towards the processing routine. To ensure good statistics and to minimize the effect of such possible inhomogeneity, the XPS, EDX and UPS measurements were performed on various spots for each sample and various samples for each stoichiometry were measured.

XPS Results

In Figure 5.7 (a)-(c) representative XPS peaks for ITO/PEDOT:PSS/MAPbI$_3$ films with various stoichiometries are presented. In the C1s spectrum, the C-C bond at ~284.8 eV can be attributed to adventitious surface carbon and can be used for energy referencing [34, 180]. As this peak does not show a shift with varying stoichiometry, the relative position of the other peaks is trustworthy. All other peaks can be attributed to MAPbI$_3$ perovskite [350]. The Pb4f, I3d, N1s and C1s peaks all shift towards lower binding energies with increasing stoichiometry, as indicated by the grey
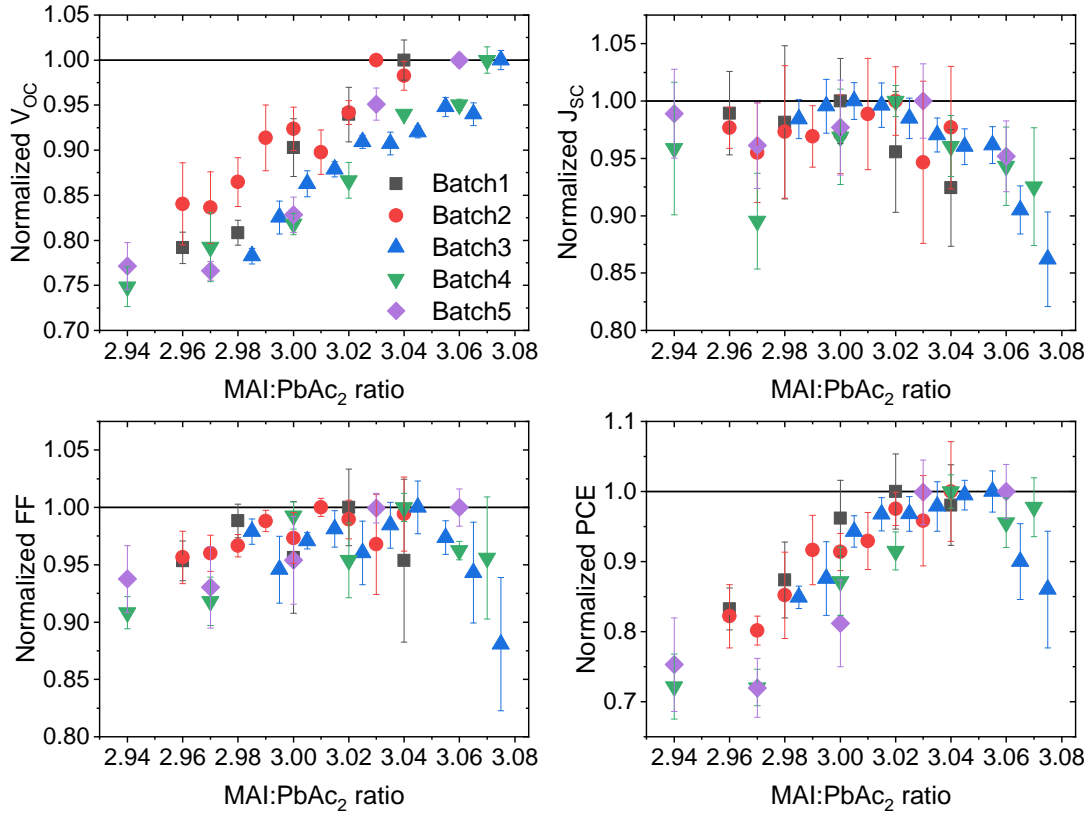
Figure 5.5: Normalized PV parameters of 5 different batches of solar cells with the architecture ITO/PEDOT:PSS/MAPbI$_3$/PC$_{60}$BM/BCP/Ag with varying stoichiometry $2.94 < y < 3.075$. The data is the average from 8-12 pixels within one batch.

arrows. All measured data points for the Pb4f$_{7/2}$, N1s and I3d$_{5/2}$ peaks are plotted in Figure 5.8. We observe that the I3d and N1s peak intensities are strongly increasing with respect to stoichiometry. The corresponding I/Pb and N/Pb atomic ratios (versus stoichiometry) are plotted in Figure 5.7 (d) and exhibit a strong linear increase. The N/Pb ratio changes from slightly below 1 (which is the expected value for precisely stoichiometric MAPbI$_3$) for understoichiometric films to above 1.6 for $y = 3.07$. Similarly, the I/Pb ratio increases from $\approx$3.5 to above 4.2. The fact that the slope is nearly the same for both N/Pb and I/Pb (the scale of the figure's y-axes is chosen to be the same) directly reveals that N and I are present in the same excess at the surface of the films.

We would like to briefly discuss possible reasons for why we consistently measure an I/Pb atomic ratio of above 3, even for precisely stoichiometric films where one would expect a ratio of exactly 3. A similar I/Pb atomic ratio of around 3.5-3.8 was regularly measured with XPS for both PbAc$_2$ and sol-eng films in the last chapter (Sec. 4.3.3) as well as in our recent publication [347]. Two studies have been published recently in which Hard X-ray PES (HAXPES) measurements on triple cation perovskite films at different photon energies (employing a synchrotron source) were
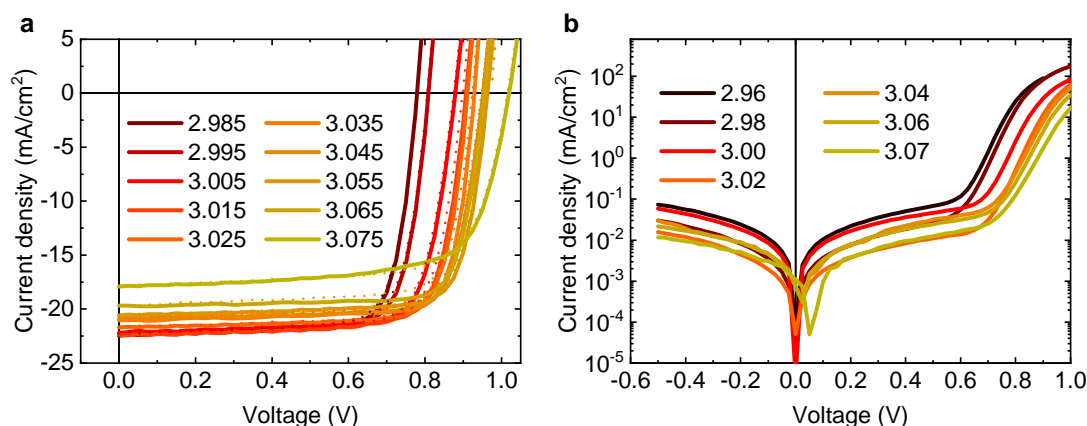
Figure 5.6: Representative JV (a) and dark JV (b) curves of solar cells with various stoichiometries y. The data in (a) are devices from the batch presented in Figure 5.3. Reproduced with permission from [343]. Copyright 2018, The Royal Society of Chemistry.

performed. Employing different photon energies allows probing the average elemental composition at various depth of the films. The inelastic free mean path (IFMP) of electrons increases when the core electrons are emitted with a higher kinetic energy (Sec. 3.2.6). The authors of this study found higher than expected I/Pb ratios at the surface (~5 nm), which they ascribed to small amounts of unreacted FAI. Probing deeper within the film (~20 nm), they measured slightly lower than expected I/Pb ratios [351, 352]. Hence, it seems that even for films based on an exact stoichiometric precursor solution, an excess of iodide is always present at the surface of perovskite films. Interestingly, this is only the case for iodide, as nitrogen exhibits the expected atomic ratio of close to N/Pb = 1 in our measurements.

The expected relative excess of N and I in the final MAPbI$_3$ film for a stoichiometry of $y = 3.075$ are $0.075/1 = 7.5\%$ for N and $0.075/3 = 2.5\%$ for I (see Sec. 3.1.3 and equation 3.6). The fact that the amount of N on the film surface increases by more than 60% for N and 20% for I (Figure 5.7 (d)) suggests that the employed excess of I and N is distributed unevenly in the film and we suspected that it is mainly present in the surface region of the films. To test this hypothesis, we performed EDX measurements at different accelerating voltages to allow us to quantify the elemental composition at different film depths ([353], Sec. 3.2.2).

EDX Results

MAPbI$_3$ is very sensitive to electron beam induced degradation, which could impede a clear interpretation of the results [354]. To counteract this effect, the exposure time during the EDX measurements was kept as short as possible, while ensuring high enough integral count statistics. Furthermore, the scanned area was chosen to be sufficiently large, as to not concentrate the electron beam energy on a small spot for too long. The sensitivity for detection of particular elements is dependent on their atomic number Z, as well as the chosen accelerating voltage. Especially for light ele-
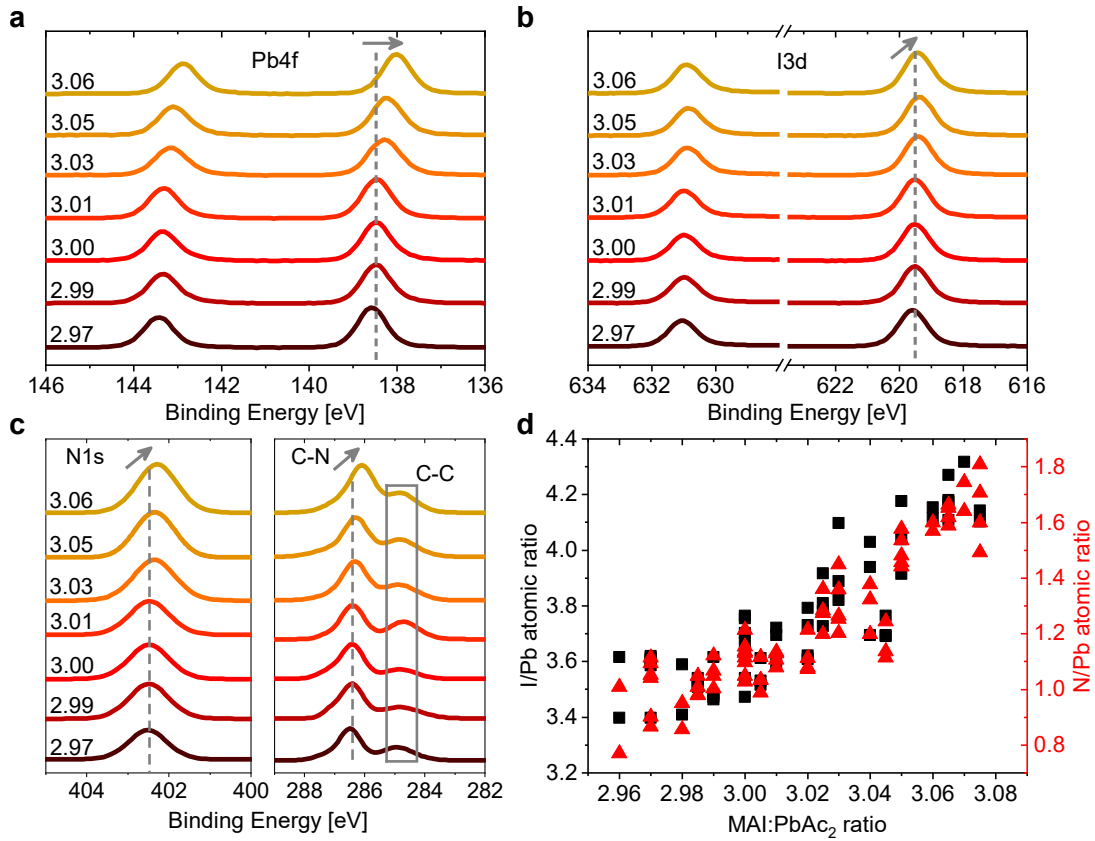
Figure 5.7: Variation of XPS peak positions and intensities of the Pb4f (a), I3d (b) and N1s (c) peaks with changing stoichiometry. (d) I/Pb (left y-axis) and N/Pb (right y-axis) atomic ratios over stoichiometry determined by XPS. The meausurements were performed by Vincent Lami. Reproduced with permission from [343]. Copyright 2018, The Royal Society of Chemistry.

ments ($Z < 11$), the quantitative analysis with EDX becomes less accurate (Sec. 3.2.2). Hence, only the quantitative values of the heavy I ($Z_I = 53$) and Pb ($Z_{Pb} = 82$) elements will be analyzed in more detail. The characteristic X-ray lines used for analysis are the I L$_\alpha$ line at ≈ 3.93 keV and the Pb M$_\alpha$ line at ≈ 2.35 keV [355]. The discrete and specific energies necessary to excite an X-ray line is called the critical excitation potential. The acceleration voltage of the incident electron beam is suggested to be, at minimum, a factor of 1.5 higher than that of the corresponding line to be analyzed [326]. Therefore, the minimum accelerating voltage to analyze the I L$_\alpha$ line was chosen to be 6 kV. To estimate the interaction volume of the electron beam with the sample, we performed simulations with the free software CASINO ([327]; see Sec. 3.2.2 for details). We assumed a density of 4.16 g/cm^3 for MAPbI$_3$ in the simulation [356]. The simulated trajectories for accelerating voltages of 6 kV and 10 kV are plotted in Figure 5.10. Here, the blue lines denote electrons becoming scattered and absorbed by the film and the red lines denote elastically backscattered electrons. The simulation for 6 kV shows that most of the electrons are absorbed in regions close to
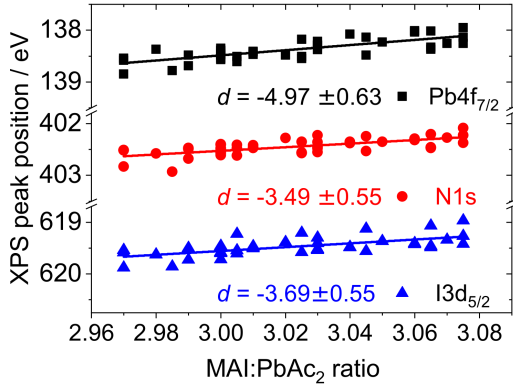
Figure 5.8: Shift in XPS peak positions of Pb4f$_{7/2}$, N1s and I3d$_5$/2 with changing stoichiometry and corresponding fits with slope d.
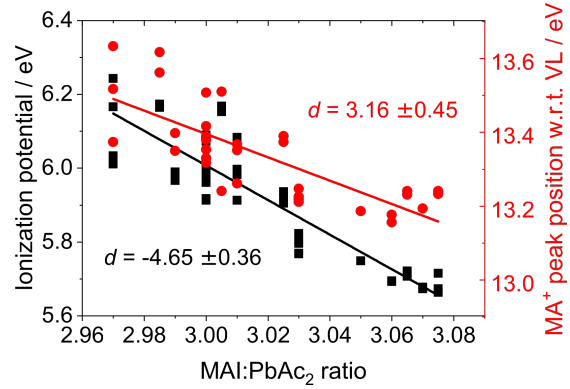
Figure 5.9: Ionization potential (left) and position of the MA$^+$ peak w.r.t. vacuum level (right) over stoichiometry and corresponding fits with slope d.

the film surface, while only few of them reach the PEDOT:PSS interface. For 10 kV the electrons are absorbed throughout the entire MAPbI$_3$ film with a fraction of them entering the ITO ((In$_2$O$_3$)$_{0.9}$(SnO$_2$)$_{0.1}$) and PEDOT:PSS layers and some reaching the glass (SiO$_2$) substrate. The corresponding phi-rho-Z curves for the element iodide are plotted in the bottom of 5.10. phi-rho-Z curves provide information about the depth

Table 5.1: Atomic percentages for various elements of Glass/ITO/PEDOT:PSS/MAPbI$_3$ films with various stoichiometries determined by EDX at acceleration voltagess of 6 kV (top) and 10 kV (bottom).

| Element/y **6 kV**	C K [%]	N K [%]	O K [%]	S L [%]	Si K [%]	In L [%]	Sn L [%]	I L [%]	Pb M [%]
2.97	10.63	6.83	18.72	7.81	0	0	0	43.99	12.03
2.99	10.55	6.99	18.28	7.76	0	0	0	44.28	12.15
3.00	10.20	6.99	17.90	7.50	0	0	0	45.22	12.19
3.01	10.36	7.07	18.11	7.76	0	0	0	44.82	11.88
3.03	9.94	7.14	17.76	8.20	0	0	0	45.14	11.83
3.05	10.17	6.75	17.66	7.68	0	0	0	45.82	11.94
10 kV	[%]	[%]	[%]	[%]	[%]	[%]	[%]	[%]	[%]
2.97	7.10	4.05	29.59	2.55	3.63	11.73	1.98	30.76	8.61
2.99	6.83	4.22	29.70	2.53	3.16	11.78	2.02	31.12	8.65
3.00	6.87	4.03	29.87	2.70	3.20	12.18	2.10	30.45	8.61
3.01	6.72	3.45	29.82	2.97	3.53	11.94	1.89	31.00	8.67
3.03	6.93	3.89	29.86	2.62	4.34	11.18	1.81	30.67	8.68
3.05	6.69	3.79	30.16	2.72	3.23	11.92	1.94	30.86	8.69
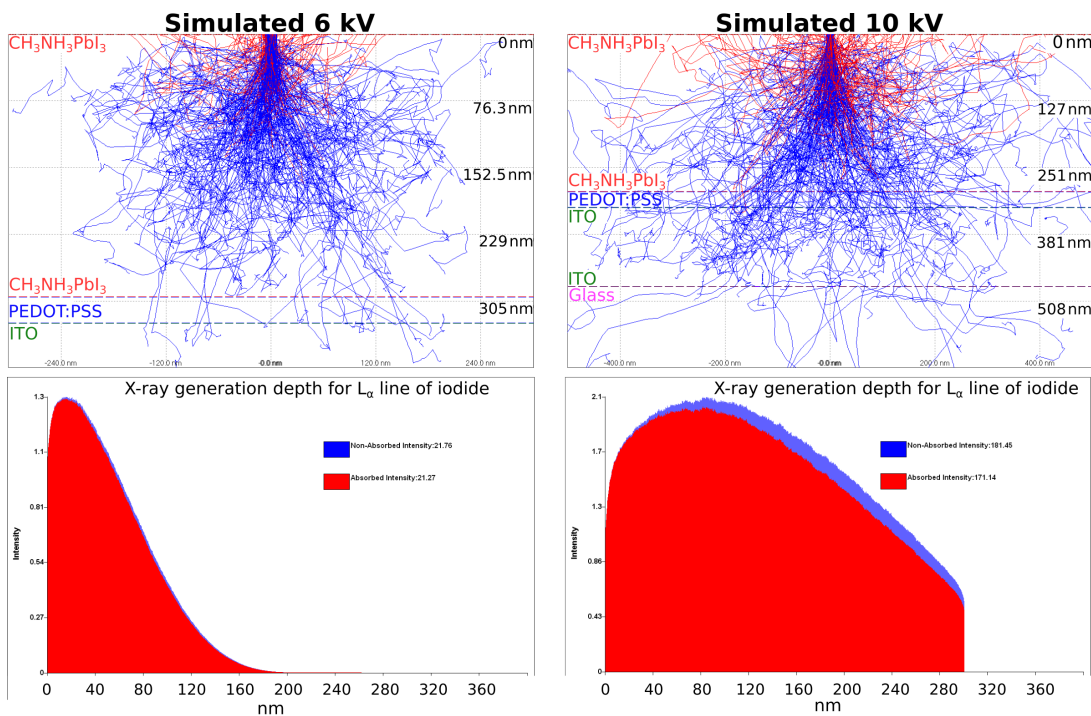
Figure 5.10: Simulation of electron trajectories in MAPbI$_3$ films at 6 kV and 10 kV acceleration voltage (top) and corresponding generation depth for X-rays of the L$_\alpha$ line of iodide (bottom). The simulation was performed using the free software CASINO.

from which the produced characteristic X-rays of a certain element are measured by the X-ray detector [326]. The simulation shows that in case of 6 kV the main signal of the I L$_\alpha$ line is measured in the top ~70 nm of the film. In contrast, for 10 kV a signal is detected from regions throughout the whole bulk. Hence, using the two accelerating voltages should allow to quantify the atomic ratio of iodide at different average depths in the MAPbI$_3$ films. Typical EDX spectra for 6 kV and 10 kV (for the case of $y = 3.00$) are shown in Figure A.7 in the Appendix. The averaged atomic percentages of the elements measured with EDX are presented in Table 5.1. A minimum of 10 different spots was measured for each stoichiometry. The analyzed emission lines (K,L or M) are also denoted. In the case of 6 kV all elements of MAPbI$_3$ (C, N, I, Pb) are detected together with a small signal from PEDOT:PSS (S) and oxygen (which we attribute to surface contamination). In contrast, for 10 kV signals from the glass substrate (Si, O) and ITO layer (Sn, In) are also detected. We can now compare the I/Pb atomic ratios determined from the EDX measurements with the linear fit to the I/Pb atomic ratios obtained from the XPS measurements (shown in Figure 5.7 (d)), as plotted in Figure 5.11. For measurements at 10 kV, the I/Pb ratio is unchanged for the various stoichiometries, while for measurements at 6 kV it increases in a similar fashion as in the XPS measurements, although slightly lower in strength. Because the simulations are completely in line with our results, these results provide evidence
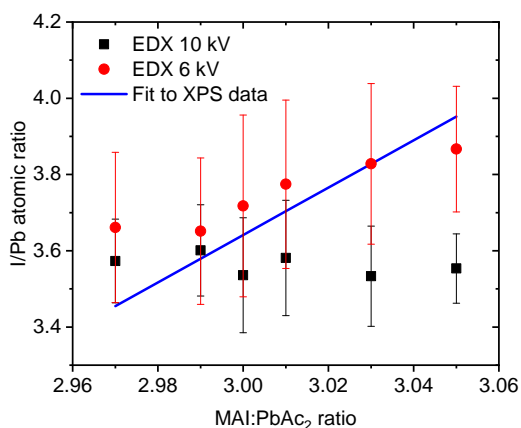
Figure 5.11: Energy dispersive X-ray (EDX) measurements on MAPbI$_3$ films with various stoichiometries on ITO/PEDOT:PSS at 10 kV (black) and 6 kV (red) acceleration voltage as well as a fit to the data obtained by XPS in Figure 5.7 (d). Reproduced with permission from [343]. Copyright 2018, The Royal Society of Chemistry.

that the excess MAI from the precursor solution is indeed situated closer towards the film surface. The fact that the increase in I/Pb from the XPS measurements is a bit stronger when compared to the EDX measurements, we suggests that the highest concentration of excess MAI is located at the immediate film surface (top 10 nm). This excess gradually decreases deeper into the film, eventually disappearing (after approximately 50 nm). Determining the exact film depth at which the N/Pb and I/Pb ratios start to increase is, however, not possible with our analysis.

UPS Results

Representative UPS measurements of ITO/PEDOT:PSS/MAPbI$_3$ films with various stoichiometries are plotted in Figure 5.12 (a). The left part of the figure shows the secondary electron onset from which the work function of the films can be determined (Sec. 3.2.6). Within the experimental error of the UPS measurement (≈ 0.1 eV) the work function is roughly at 4.95 ± 0.10 eV for all stoichiometries. In general, there was a rather strong scatter for the derived work function values, especially for stoichiometries around $y = 3.00$ which impeded the observation of clear trends. A more detailed analysis is shown in Figure 5.13, in which the work function data is plotted over the corresponding N/Pb atomic ratio. As can be seen, while the spread of values around N/Pb = 1 is very high, a slight trend towards lower work functions for overstoichiometric films can be observed. This trend becomes clearer when only looking at data from films prepared within one batch as also plotted in the same figure. The work function of the films determines the position of E$_F$ in the perovskite bandgap and thus the observed trend, albeit being small, will influence the final energetics.

The right axis of Figure 5.12 (a) shows the VB onset w.r.t. E$_F$ which shows a clear shift towards smaller values. The ionization potential can be derived from that data and is plotted together with a fit to the data with slope d in Figure 5.9 (b). The IP decreases from ≈ 6.1 eV for understoichiometric films to ≈ 5.7 eV for $y = 3.07$ with a slope of $d = -4.65 \pm 0.36$. In addition, we analyzed the position of the peak corresponding to MA$^+$ in the UPS spectrum and plot its position with respect to the ionization potential [324] (see Figure A.8 in the Appendix for exemplary peaks in
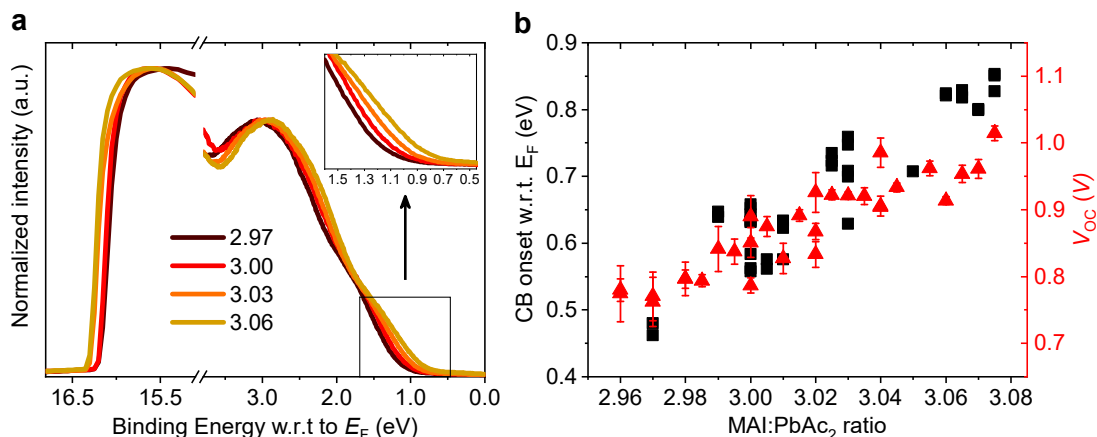
Figure 5.12: (a) Variation of the UPS spectrum for representative stoichiometries w.r.t. the fermi level (E_F). The secondary electron onset and the density of states at the VB are shown on the left and right, respectively, while the inset is a zoomed in region of the onset of the VB, referencing to the HOMO level. (b) Observed change of the conduction band (CB) position w.r.t. E_F, calculated from the HOMO level and the bandgap (UV-vis) and that of the V_{OC} in devices fabricated with various stoichiometries. The meausurements were performed by Vincent Lami. Reproduced with permission from [343]. Copyright 2018, The Royal Society of Chemistry.

the UPS spectra). This peak also shows a shift towards lower values with increasing stoichiometry, however with a smaller slope of $d = -3.16 \pm 0.45$. We now can compare the shifts of these two peaks with the shifts of the earlier mentioned XPS peak positions (Figure 5.8). Comparing the fitted slope of the Pbf4$_{7/2}$ peak position ($d = -4.97 \pm 0.63$) with that of the IP suggests a direct correlation. This effect can possibly be attributed to the fact that the top of the valence band is associated with the antibonding interaction between Pb6s and I5p atomic orbitals [72]. We can also compare the slopes of fits to the shift in the N1s ($d = -3.49 \pm 0.55$) and I3d ($d = -3.69 \pm 0.55$) peak positions with that of the peak attributed to MA$^+$ in the UPS spectrum. Again, a strong correlation between them can be observed.

Wang *et al.* already demonstrated that changing the elemental composition of MAPbI$_3$ (MAI rich/poor, or alternatively PbI$_2$ poor/rich) can determine the energetics of perovskite films by inducing p- or n-type doping respectively [106]. The authors employed precursor solutions with strong changes in stoichiometry, ranging from MAI/PbI$_2$ = 3.3 to MAI/PbI$_2$ = 0.6, and proposed that I interstitials would induce p-doping and Pb vacancies would induce n-doping. Emara *et al.* studied the effect in more detail and revealed that the surface composition and IPs of MAPbI$_3$ films fabricated by different methods show a large spread. They were able to relate the measured changes in the N/Pb atomic ratio (from 0.5 to 1.5) to a shift in IP (from 5.7 eV to 6.4 eV). In line of these results, we want to provide a comparison of our results with those of Emara *et al.* . Therefore, we plot our IPs over the N/Pb atomic ratio measured at the same spot of the samples with XPS in Figure 5.14, and use the same scales for the x- and y-axes for an easier comparison. In the range be-
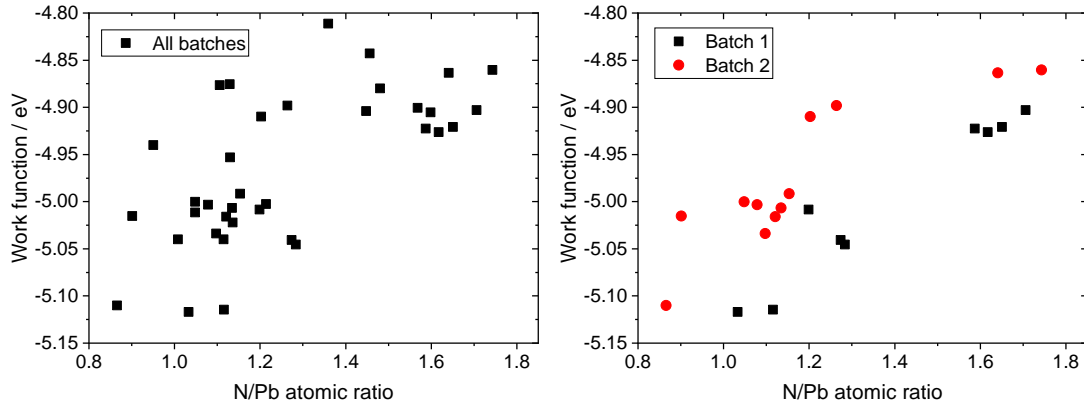
Figure 5.13: Work function values derived from the secondary electron onset in UPS measurements over the corresponding N/Pb atomic ratio. All data (left) and data from two different batches (right).
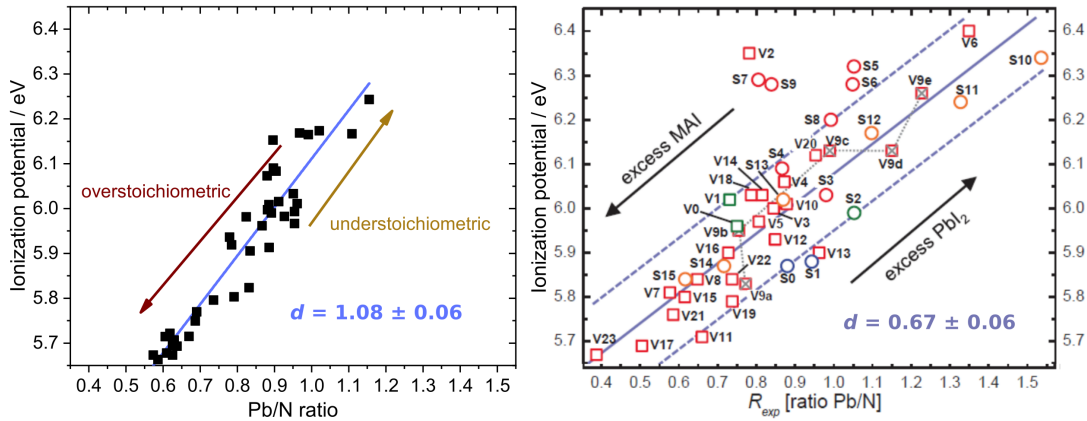

Figure 5.14: Ionization potential plotted over the Pb/N atomic ratio of ITO/PEDOT:PSS/MAPbI$_3$ films with varous stoichiometries (left). Comparison with the data obtained by Emara *et al.* (right), reproduced with permission [324]. Copyright 2016, Wiley VCH.

tween N/Pb= 0.6 and N/Pb= 1 both results are qualitatively very similar. A linear fit to their data gives a slope of $d = 0.67 \pm 0.06$ while our fits give a higher slope of $d = 1.08 \pm 0.06$. Additionally, the results of Emara *et al.* show a much larger spread. This, however, can be explained by the fact that they measured films fabricated by many different methods. Still, both results qualitatively agree very well.

In a recently published study, we have shown that long term exposure of MAPbI$_3$ samples to UHV conditions results in a loss of MAI species at the surface resulting in a "homogenization" of the surface composition (Sun *et al.* [347]). To study the impact of vacuum storage on films with various stoichiometries, we stored some of them for 48 h in the UHV chamber and afterwards remeasured them to track changes in composition and IP. We plot the measured IP over the corresponding N/Pb and Pb/N atomic ratios in Figure A.9 in the Appendix and include the measurements of fresh samples for a direct comparison. The N/Pb (Pb/N) atomic ratio is strongly decreas-
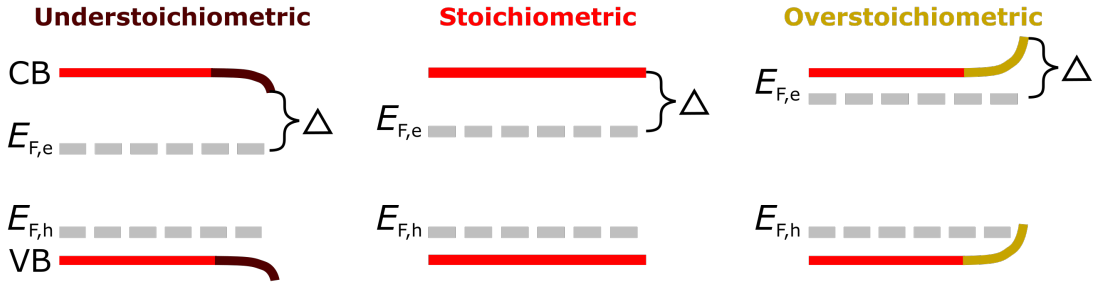
Figure 5.15: Schematic illustration of the possible quasi-Fermi level splitting and the maximum obtainable V_{OC} for understoichiometric, stoichiometric and overstoichiometric perovskite layers. The position of the quasi-Fermi level for holes, $E_{F,h}$, remains unchanged as the PEDOT:PSS/perovskite interface is not affected. The position of the quasi-Fermi level for electrons, $E_{F,e}$, rises in energy as it is limited by the Fermi level of the metal electrode, which in our case is always at least an energetic distance Δ below the conduction band at the surface.

ing (increasing) to values below (above) 0.8 (1.3) for all samples, irrespective of their initial composition. Furthermore, the IP is shifted to high values of around 6.2-6.5 eV. As can be seen, the data fits more nicely into the observed trend for the fresh films when using N/Pb as x-axes. We therefore propose that plotting the ionization potential over the measured N/Pb atomic ratio is the best way to compare values for different films qualitatively.

Using the values derived from the discussed analysis, we can now compare the shift in the position of E_F within the MAPbI$_3$ bandgap with the observed shift in device V_{OC}. For that purpose, we plot the CB onset w.r.t. E_F versus stoichiometry as well as the derived device V_{OC}'s in Figure 5.7 (f). The CB w.r.t. E_F can be easily calculated using the measured value of the MAPbI$_3$ bandgap and subtracting it from the measured value of VB w.r.t. E_F. Both values show a comparable absolute increase, although that of V_{OC} being a bit lower. We assume that the observed changes in the MAPbI$_3$ surface energetics directly correlate with the position of the quasi-Fermi level for electrons. The proposed energetics at the surface of the perovskite films are schematically plotted in Figure 5.15. Our argument is that $E_{F,e}$ must be at least an energetic distance Δ below the conduction band at the film surface [357, 358], while the position of the quasi-Fermi level for holes ($E_{F,h}$) remains unchanged. The latter we assume because our results suggest that the composition of the perovskite bulk are unchanged, leaving the PEDOT:PSS/MAPbI$_3$ interface unaffected of the changes in precursor stoichiometry. Hence, the difference between $E_{F,e}$ and $E_{F,h}$ in the MAPbI$_3$ film increases, which results in a higher maximum obtainable device V_{OC}. Furthermore, this theory would also explain the observed increase in V_{bi}.

One open question is, how the measured organic excess at the film surface is incorporated into the perovskite film. The most straightforward interpretation is that it is present in the form of MA$^+$ and I$^-$ interstitials within the perovskite crystal lattice, and are bound together to preserve charge neutrality at the surface instead of forming an extra layer of MAI on top of the perovskite lattice ([102, 134], Sec. 2.2.3).
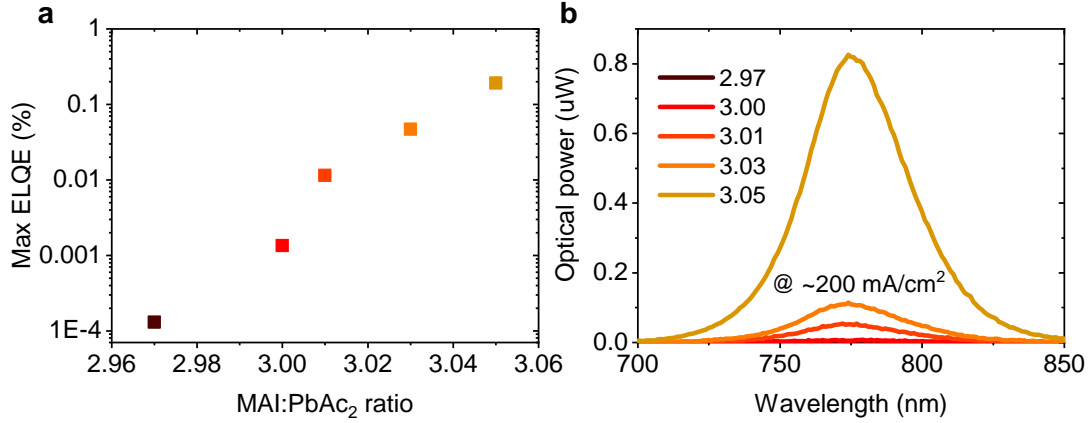
Figure 5.16: Maximum attainable ELQE (in %) from ITO/PEDOT:PSS/MAPbI$_3$/PC$_{60}$BM/ BCP/Ag devices with various stoichiometries y. (b) EL spectra at a fixed current density of 200 mA/cm^2.

For example, Hawash *et al*. have demonstrated that even after evaporating 120 nm MAI on top of pristine MAPbI$_3$, the Pb4f signal of MAPbI$_3$ is still detected with XPS, which shows that no conformal MAI layer forms on top of MAPbI$_3$ [359]. Rather they suggested that the interaction chemistry between MAI and MAPbI$_3$ must be considered and will determine the final surface composition. Emara *et al*. drew the same conclusion, because they did not observe any additional secondary features in XRD measurements even for highly overstoichiometric films [324].

5.2.3 ELQE Measurements

The notion that a perfect solar cell should also behave as a perfect light emitting diode was first put forward by Miller *et al*. [165]. When a solar cell is at V$_{OC}$ under illumination, all generated charge carriers reside inside the film until they recombine radiatively or non-radiatively via traps. In the case that all non-radiative recombination pathways are suppressed, the cell should emit light which exactly counterbalances the incoming light, which means it exhibits unity electroluminescent quantum efficiency (ELQE). However, due to the existence of non-radiative recombination channels (deep trap states, interface recombination etc.), only a certain fraction of the injected charge carriers will result in radiative recombination which can be measured by ELQE. A reduction in V$_{OC}$ is thus always related to a reduction in ELQE and the two values are connected by [165, 360, 361]:

$$V_{OC} \approx V_{OC,rad} - \frac{k_B T}{e} \ln \text{ELQE}_{ext} \qquad (5.1)$$

Here, V$_{OC,rad}$ is the maximum attainable V$_{OC}$ in the radiative limit, which is around 1.34 V for MAPbI$_3$ with a bandgap of around 1.6 eV ([362]; Sec. 2.1.3).
In the case that the observed increase in device V$_{OC}$ for higher y is due to reduced

non-radiative recombination in the MAPbI$_3$ absorber layer, it should correlate with an increase of ELQE$_{ext}$. Such reduced recombination could, for example, be due to changes in the recombination rate at the MAPbI$_3$/PC$_{60}$BM interface caused by the described changes in surface energetics of MAPbI$_3$. In Figure 5.16 we plot the maximum attainable ELQE$_{ext}$ (in %) (a) as well as the EL spectra at a fixed current density of 200 mA/cm^2 (b) for devices with various stoichiometries. Indeed, ELQE$_{ext}$ increases over nearly four orders of magnitude from ELQE$_{ext}$ $\approx$ 1 $\cdot$ 10^{-6} to ELQE$_{ext}$ $\approx$ 2 $\cdot$ 10^{-2}. Using equation 5.1 this increase should result in a change of V$_{OC}$ of roughly

$$\Delta V_{OC} \approx \frac{k_B T}{e}(\ln 10^{-6} - \ln 2 \cdot 10^{-2}) \approx 0.19\, V, \tag{5.2}$$

from $y = 2.97$ to $y = 3.06$. This value closely correlates with the observed increase in device V$_{OC}$ (Figures 5.3 and 5.5). We want to mention that this analysis is performed with the maximum attainable ELQE$_{ext}$. The best comparison is performed when measuring ELQE$_{ext}$ at voltages and injection currents close to the operating parameters of a solar cell (V$_{OC}$ and J$_{SC}$). [361, 363]. However, due to the resolution of our system we were unable to measure any ELQE$_{ext}$ at very low injection currents. However, we believe that the observed trend at the higher injection currents represents the relevant behavior, and that equation 5.1 is still qualitatively valid. We can conclude that a reduced non-radiative recombination rate at the MAPbI$_3$/PC$_{60}$BM interface is responsible for the strongly enhanced V$_{OC}$, in line with the measured energetic changes at that interface and the suggested higher quasi-Fermi level splitting (Sec. 5.2.2).

5.2.4   Stability of Full Devices

In Figure 5.17 (a)-(d) the evolution of the photovoltaic parameters of the devices shown in Figure 5.3, stored at $\approx$25 °C and 30-60% relative humidity in the dark for 3700 h, are presented. The data points present the averaged values of the reverse and forward scan directions. The evolution of all parameters is strongly influenced by the exact precursor stoichiometry. While for slightly understoichiometric devices the initial PCE drops to ~80% of its initial value after 3700 h, only a minute excess of MAI ($y > 3.00$) is required to result in reduced stability. This effect becomes stronger for higher stoichiometries, so that for $y = 3.025$ the PCE drops to ~50% and for $y > 3.035$ to ~30% of its initial value.

   As one can see, the V$_{OC}$ shows an initial increase for all stoichiometries apart of $y = 3.075$. The exact trend of this increase and the time of the subsequent drop again depend on the exact stoichiometry. For example, while for $y = 2.985$ (with a low initial V$_{OC}$ of ~0.8 V) the V$_{OC}$ increases for storage times up to around 2000 h (with a subsequent small drop), for $y = 3.045$ (initial V$_{OC}$ of $\approx$0.92 V) it only increases in the first $\approx$1000 h.

The J$_{SC}$ is the parameter which is affected the strongest by the exact precursor stoi-
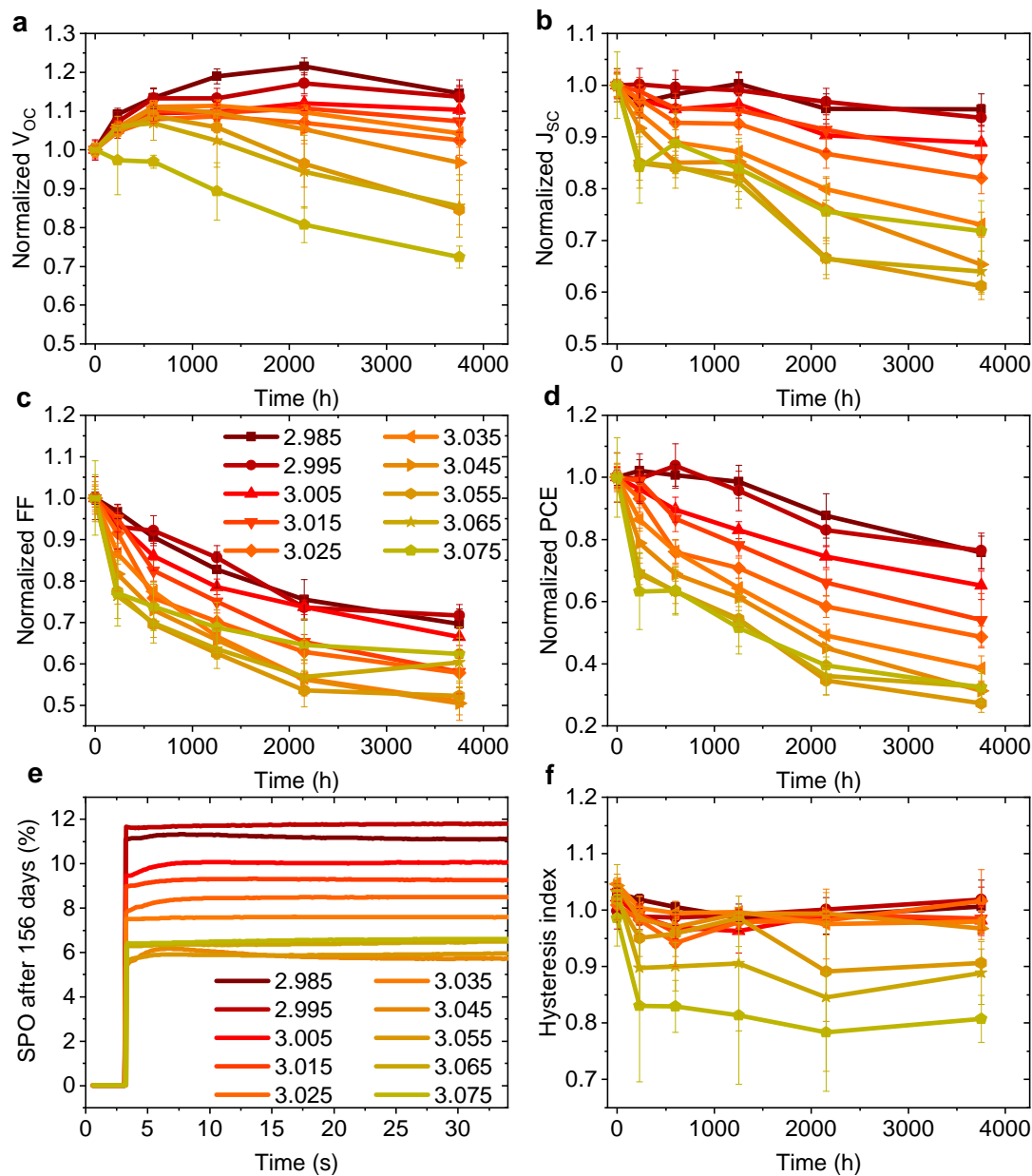
Figure 5.17: (a-d) Evolution of photovoltaic parameters in reverse scan of non-encapsulated devices (average of ~8-12 pixels) from the batch shown in Figure 5.3 stored at ~25 °C and ~30-60% RH in the dark between the measurements. (e) Stabilized power output (SPO) of the best pixel for each stoichiometry after 156 days of storage. (f) Hysteresis index over time defined by PCE$_{\text{Reverse}}$/PCE$_{\text{Forward}}$ of the same devices. Reproduced with permission from [343]. Copyright 2018, The Royal Society of Chemistry.

chiometry. For understoichiometric devices it only drops to $\approx 95\%$ of its initial value even after 3700 h of storage. In stark contrast, for overstoichiometric devices a reduction in J_{SC} is already visible in the first couple hundreds of hours. The initial drop is again stronger the more the precursor solution is overstoichiometric. For example, for $y > 3.035$ the J_{SC} is already at 85% of its initial value after ≈ 500 h of storage. For longer storage times, the described trend becomes even more obvious. The only device that does not perfectly fit the observed trend of J_{SC} is $y = 3.075$. However, this might be explained by the fact, that the initial J_{SC} for this stoichiometry is already much lower compared to the other devices which in turn might lead to the observed lower relative decrease.

The FF drops to $\approx 70\%$ of its initial value for $y < 3.01$ and to 50-60% of its initial value for the higher stoichiometries after 3700 h. Again, a stronger initial drop (< 700 h) for higher stoichiometries can be observed. However, a stoichiometry depending trend for the FF is not as evident as it was for the J_{SC}.

A measurement of the stabilized power output (SPO) after 156 days of the best pixels for each stoichiometry reveals that all devices still deliver a stable power output and confirms the trend of PCE in panel (d) (Figure 5.17 (e)). In panel (f) the hysteresis index, defined as the ratio of the PCE in reverse and forward scan direction, is plotted. An increased hysteresis becomes apparent only for $y > 3.04$. All other stoichiometries show a negligible hysteresis even after 3700 h of storage. We also tracked the storage stability for Batch1 and Batch2 in Figure 5.5 (Figures A.10 and A.11 in the Appendix). The evolution of these batches' PV parameters shows very similar trend as described above, with slightly understoichiometric devices being the most stable ones. These results also reveal that decreasing the stoichiometric even further ($y < 2.98$) does not result in further improved stability, but rather in an increased hysteresis. In addition, for Batch 2 also a reduced J_{SC} can be observed for $y = 2.96$. Hence, a slightly understoichiometric precursor solution yields the most stable devices when stored in ambient air and in the dark.

We now want to discuss on possible reasons for the strongly different degradation behavior. The degradation of the FF is the parameter the least affected by the exact precursor stoichiometry. This might be explained by the fact that the decrease of FF is mainly connected to the degradation of the other layers in the solar cell stack (PEDOT:PSS, $PC_{60}BM$, Ag). For example, the acidic nature of PEDOT:PSS has been proposed to hamper the long term stability of inverted (organic and perovskite) devices by etching the ITO substrate or reacting with the active layer [364–366]. Another study proposed that In and Sn atoms from the ITO substrate are able to migrate into the perovskite film at ambient conditions and result in degradation [367]. In addition, it has been proposed that metal impurities are able to migrate through the contact layers into the perovskite layer (possibly even at room temperature) and react with the perovskite film [368, 369]. However, all devices studied here had the same device structure and all layers apart of the $MAPbI_3$ film were fabricated identically. Hence, the effect of the described degradation pathways on the observed degradation rate
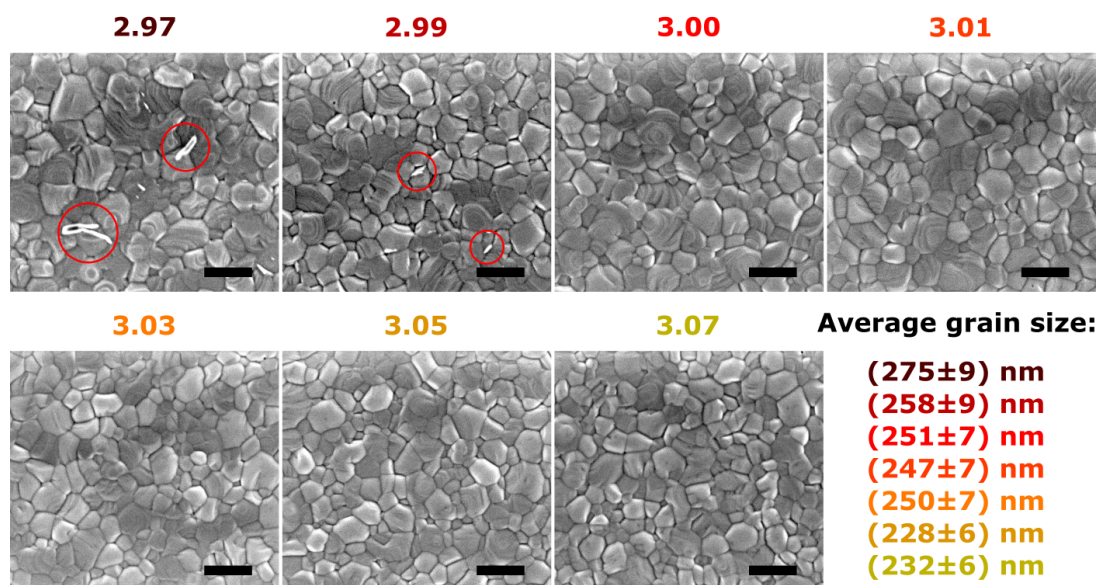
Figure 5.18: Representative SEM images of MAPbI₃ films on ITO/PEDOT:PSS with various stoichiometries. The average grain size is calculated from more than 500 indivudal grains using the software ImageJ. Adapted with permission from [343]. Copyright 2018, The Royal Society of Chemistry.

should be similar for all stoichiometries. We therefore conclude that the different trends in degradation must be exclusively caused by the changes in precursor stoichiometry.

In Section 2.4.1 we discussed literature reports on humidity induced degradation pathways and we want to discuss some of them here again. Our samples were stored at 30-60% humidity and we did not observe the formation of a white monohydrate phase in our devices, as for example observed by Wang *et al.* for high humidity levels of 85% [295]. However, we still believe that humidity is the main cause for the observed trends of degradation. To verify this, we stored some overstoichiometric samples with $y = 3.04$ for 150 days in the nitrogen filled glovebox and compared their PV parameters to samples from the same batch which had been measured directly at day 1. The fresh device yielded average values of: PCE = 13.4%; FF = 76.6%; J_{SC} = 20mA/cm^2; V_{OC} = 0.88 V. The devices stored for 150 days yielded very similar average values: PCE = 13.9%, FF = 77.2%, J_{SC} = 20.4mA/cm^2 and V_{OC} = 0.88 V. Hence, the humidity during storage of the samples must account for the observed degradation. In a relevant study, Ma *et al.* degraded films with different surface stoichiometry and proposed that the amount of polar MA$^+$ molecules at the layer surface effects the degradation dynamics of perovskite films [297]. In line with our results, especially the J_{SC} of devices with an excess MA at the film surface degraded the fastest. Similarly, Petrus *et al.* measured devices of different stoichiometric before and after exposure to 75% humidity for various times [323]. For the overstoichiometric samples they observed an initial increase in crystallinity and reorientation of the
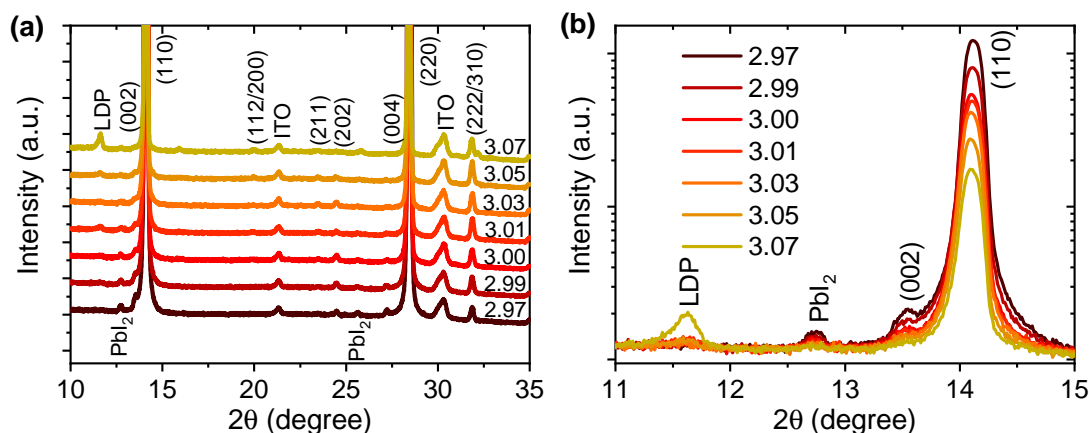
Figure 5.19: (a) Linear presentation of XRD spectra for various stoichiometries on ITO/PE-DOT:PSS, shifted and magnified for a better visibility of the side peaks. (b) Logarithmic presentation of the low angle area of the spectrum presented in (a). The measurements were performed in Oxford in collaboration with Dr. Zhiping Wang. Reproduced with permission from [343]. Copyright 2018, The Royal Society of Chemistry.

perovskite crystals which resulted in an enhancement of the (very low) initial J_{SC} after dehydration. However, for longer exposure times the overstoichiometric devices degraded much quicker when compared to the stoichiometric and understoichiometric devices. The authors proposed that the addition of a small excess of PbI_2 in the precursor solution slightly enhances the moisture stability of $MAPbI_3$ films.

The best explanation can possibly be drawn from the high amount of volatile and reactive MA species at the layer surface. MA molecules are known to be of hygroscopic nature, as are most alkylammonium salts [370]. In line of that, several ab initio calculations have proposed that MAI terminated surfaces are prone to reactions with water molecules, especially in comparison to PbI_2 terminated surfaces [371–374]. We believe that the increased amount of such species at the surface of our overstoichiometric films results in an enhanced reactivity even at low ambient levels of humidity and thus strongly reduced storage stability at ambient conditions even in the dark.

5.2.5   Microstructure - SEM and XRD Measurements

In Chapter 4 we revealed that the microstructure of perovskite films can not only determine the efficiency of devices, but also their stability. To explore if a change in microstructure for films with different stoichiometries could be an additional factor determining the differences in efficiency and storage stability, we performed SEM and XRD measurements on ITO/PEDOT:PSS/MAPbI$_3$ films with various stoichiometries.

As previously revealed in Section 4.2, the PbAc$_2$ recipe yields pinhole free films with grains extending throughout the whole film thickness. To compare the surface structure of films with different stoichiometry, we took SEM top-view images, which are shown in Figure 5.18. For $y < 3.00$ a few white flakes can be observed on the film surface which are situated close to the grain boundaries. We suspect that these flakes
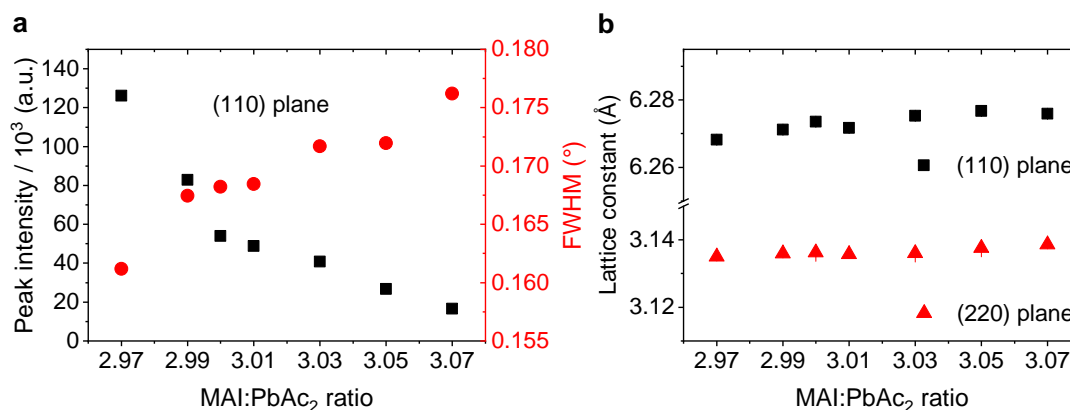
Figure 5.20: (a) Peak intensity and full width half maximum (FWHM) of the (110) peak (Figure 5.19) for various stoichiometries. (b) Lattice constant over stoichiometry for the (110) and (220) MAPbI$_3$ crystal planes. Reproduced with permission from [343]. Copyright 2018, The Royal Society of Chemistry.

consist of excess PbI$_2$, due to the fact that heavier elements with higher Z should provide brighter contrast in SEM as explained in Section 3.2.2. The same interpretation of white particles has recently also been put forward by Jiang *et al.* in films with excess PbI$_2$ [277]. Wang *et al.* have shown that the degradation rate of perovskite films in high humidity conditions of $> 80\%$ - when the monohydrate perovskite phase starts to form - correlates linearly to the perovskite grain size ([295]; see Sec. 2.4.1). However, in our case at low to medium humidity levels (30-60%, depending on the weather and season), we did not find evidence for the formation of the monohydrate white perovskite phase. Because the average grain size might still have an effect on storage stability in these conditions, we estimated the average grain size of films by analyzing a minimum of 400 grains for each stoichiometry. The area of the non-spherical shaped grains was determined with the software Image-J (see Figure A.12 in the Appendix) and the diameter was calculated assuming the grains are round: $d = \sqrt{4A/\pi}$. The average grain size only slightly decreases with increasing stoichiometry, with $r = 275 \pm 9\,$nm for $y = 2.97$ and $r = 232 \pm 6\,$nm for $y = 3.07$. Especially for $2.99 \leq y \leq 3.03$ the grain size is nearly unchanged around $d \approx 250\,$nm, a region in which the device stability shows strong variations (Figure 5.17).

Regarding the effect of grain size on device efficiency, there is no real consensus about how important large grains are for device efficiency, with state of the art devices still mostly comprised of grains with $< 500\,$nm in size. However, the majority of studies propose advantages of larger grain sizes, often with the argument that it would lower the defect density [222]. We, however, observe the trend that understoichiometric devices with the largest grain size actually yield the lowest efficiency. We can therfore conclude that the minor variations in grain size do not have a major impact on the strong differences in efficiency and storage stability.

To study the crystal structure of the films, we performed XRD measurements in
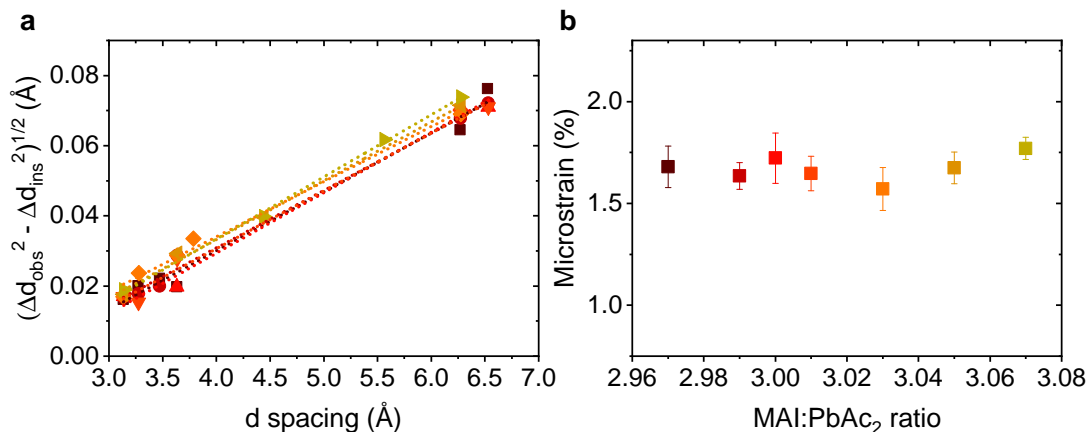
Figure 5.21: (a) A modified Williamson-Hall plot of $\left(\Delta d_{\mathrm{obs}}^2 - \Delta d_{\mathrm{ins}}^2\right)^{\frac{1}{2}}$ versus d spacing extracted from the corresponding diffraction profiles shown in Figure 5.19 (a) (see B in the Appendix for details). The slopes of the solid lines from linear fits indicate the extent of microstrain for the different stoichiometries. (b) Calculated microstrain of samples with different stoichiometry. Reproduced with permission from [343]. Copyright 2018, The Royal Society of Chemistry.

$2\theta/\omega$ scan mode (Figure 5.19). The corresponding crystal planes are labeled at the position of the peaks. All stoichiometries show primary reflections at 14.1° and 28.44° which can be assigned to the (110) and (220) planes from the perovskite tetragonal crystal structure ([375], Sec. 2.2.1). All other peaks, apart from the (222/310) peak at ~31.87°, are strongly suppressed. Especially, we observe no secondary phases for $y \leq 3.05$ and all peaks can be attributed to tetragonal MAPbI$_3$. For $y = 3.07$ a small peak at $\approx 11.6°$ appears. This peak has been observed previously and was attributed to a low-dimensional phase (LDP) of MAPbI$_3$ in highly overstoichiometric perovskite films [311, 376, 377]. While we employ only a slight excess of MAI in the precursor solution, we have revealed before that most of it is situated close to the film surface. Hence, we believe that for $y \geq 3.07$ the MAI excess at the surface becomes so high that 2D-sheets of MAI start to form, because not all of the excess MAI can be intercalated in the 3D crystal lattice anymore [376, 377].

Figure 5.19 (b) shows the enlarged low angle region of the XRD spectrum, in logarithmic scale. For $y < 3.01$ a small peak at ~12.6° originating from PbI$_2$ can be observed, which is in line with the previous assignment of the white flakes in the SEM images to PbI$_2$. It seems possible to fine tune the amount of excess PbI$_2$ in the film very precisely using the PbAc$_2$ recipe, as we had hypothesized in Section 3.1.3. The signal intensity of the (110) peak decreases by nearly one order of magnitude from $y = 2.97$ to $y = 3.07$. For a deeper analysis, we plot the signal intensity FWHM of the (110) peak over stoichiometry, as well as the lattice constants derived from analyzing the (110) and (220) peaks in Figure 5.20. The signal intensity drops strongly from $y = 2.97$ to $y = 3.00$ and a bit less so until $y = 3.07$. This decrease is accompanied by a slight increase in the FWHM. The lattice parameters plotted in panel (b) remain
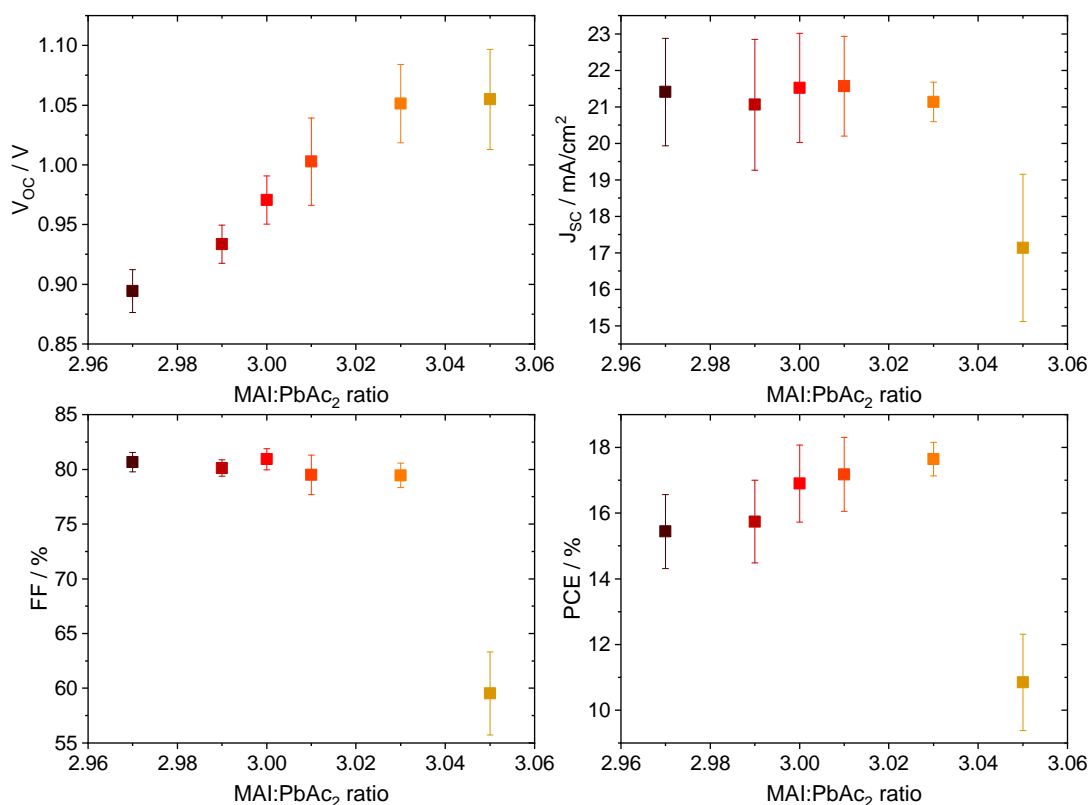
Figure 5.22: PV parameters of solar cells with the architecture ITO/m-PEDOT:PSS/MAPbI$_3$/PC$_{60}$BM/BCP/Ag with varying stoichiometry y = MAI:PbAc$_2$, (a) V$_{OC}$, (b) J$_{SC}$, (c) FF and (d) PCE. The data is the average from 6-8 pixels within one batch.

largely unchanged for all stoichiometries. Generally, a broadening or a shift of the XRD peaks could be caused by a reduced grain size (Scherrer broadening) or an increased microstrain in the perovskite films [86, 231]. Enhanced strain in perovskite films has been shown to result in an increased degradation rate [378]. To find out if an increase of microstrain is induced by variations in stoichiometry, we employed a modified Williamson–Hall method for analysis [379]. The method is described in detail in the Appendix B, as introduced in [86]. The fits of the analysis as well as the calculated microstrain (in %) is plotted in Figure 5.21. We observe nearly constant microstrain values for the different stoichiometries. We there conclude that changes in crystal defects are unlikely to be the origin of the wide variation in performance and stability we describe above and that the small increase in FWHM might be induced by a slightly decreased average grain size which we observed in SEM.

5.3 Effect for Other Recipes and Architectures

The previously discussed results were all based on MAPbI$_3$ layers fabricated by the PbAc$_2$ recipe. However, it remains an open question how universal the results are
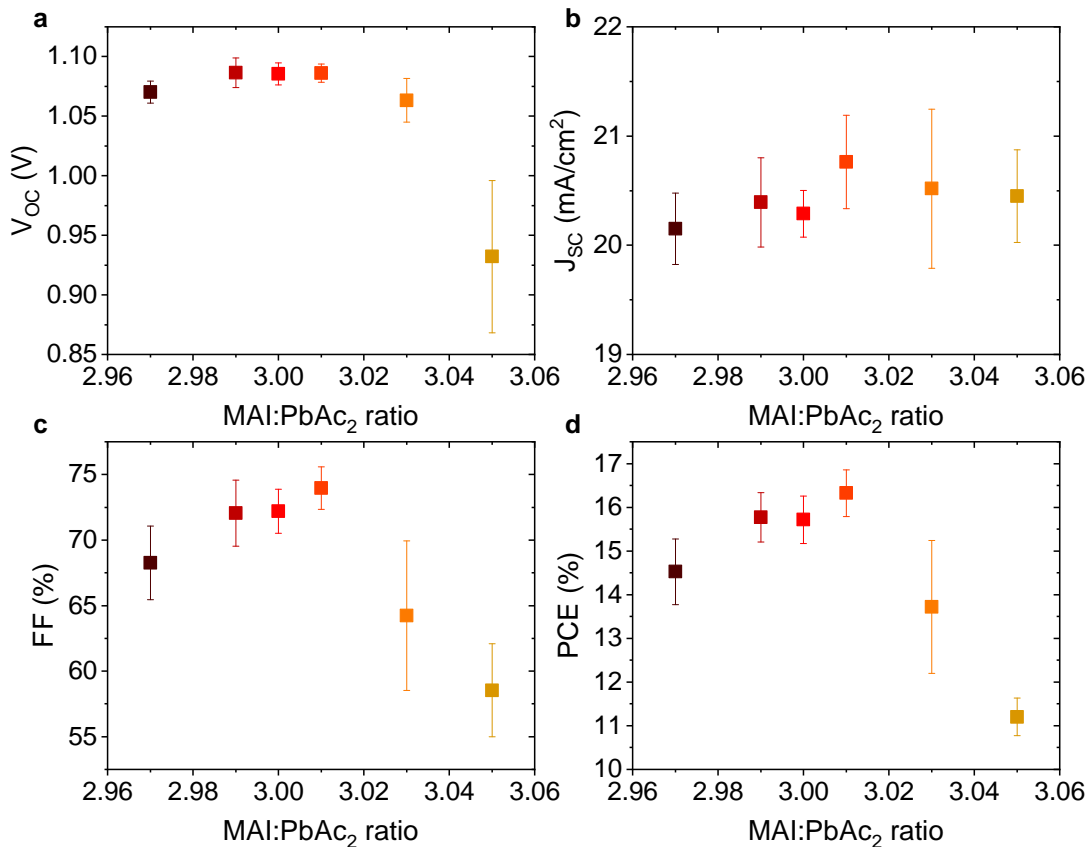
Figure 5.23: PV parameters of solar cells with the architecture ITO/Poly-TPD/MAPbI$_3$/PC$_{60}$BM/BCP/Ag with varying stoichiometry y = MAI:PbAc$_2$, (a) V$_{OC}$, (b) J$_{SC}$, (c) FF and (d) PCE. The data is the average from 8-12 pixels within one batch. Reproduced with permission from [343]. Copyright 2018, The Royal Society of Chemistry.

and how other recipes and device architectures are affected by variations in precursor stoichiometry. Therefore, we studied the effect on devices using various ETL's and HTL's employing the PbAc$_2$ recipe as well as the sol-eng recipe in the inverted as well as the standard architecture. In Table 5.2 all studied layer stacks and the employed recipes are summarized. The PV parameters for these devices are presented in Figure 5.22-5.26.

ITO/m-PEDOT:PSS/Pbac$_2$/PC$_{60}$BM/BCP/Ag (Figure 5.22)

We employed PSS-Na doped PEDOT:PSS (m-PEDOT:PSS) in the inverted architecture using the PbAc$_2$ recipe (Sec. 3.1.4). The enhanced PSS content was proposed to increase the work function of PEDOT:PSS and hence the achievable V$_{OC}$ ([202]; Sec. 2.3.1.2). The V$_{OC}$ shows a similar linear increase as for undoped PEDOT:PSS, however, higher absolute values with champion V$_{OC}$'s of up to 1.1 V are obtained. The trend in J$_{SC}$ and FF is also similar as for the undoped case, with only small changes for $y \leq 3.03$ and a strong drop of both parameters for $y = 3.05$. The FF's are very high, reaching values above 80%, another improvement which can be attributed to

the use m-PEDOT:PSS film. Hence, the PCE shows a maximum of 18% for $y = 3.03$.

FTO/Poly-TPD/Pbac$_2$/PC$_{60}$BM/BCP/Ag (Figure 5.23)

We employed the PbAc$_2$ recipe in the inverted architecture using poly-TPD as HTL (Sec. 3.1.4). Piranha treated FTO substrates were used to improve the wettability of the perovskite solution on poly-TPD. As described in Section 2.3.1.2, poly-TPD has been proposed to yield higher device V_{OC}'s due to its deeper lying work function and a reduced interface recombination [198]. The J_{SC} is similar for all stoichiometries. The V_{OC} shows high values of above 1.06 V even for understoichiometric layers and does not changes much for $y \leq 3.03$, while for $y = 3.05$ a strong drop is observed. The FF shows an increase from around 68% to 74% ($y = 2.97$ to $y = 3.01$) and a subsequent strong drop to below 65% for $y \geq 3.03$. Hence, the maximum PCE of around 16.5% is reached for a slightly overstoichiometric precursor solution ($y = 3.01$).

FTO/Poly-TPD/sol-eng/PC$_{60}$BM/BCP/Ag (Figure 5.24)

We also employed the sol-eng recipe with poly-TPD as HTL in the inverted architecture (Sec. 3.1.4) and varied the $z =$MAI/PbI$_2$ molar ratio in the precursor solution in the range $0.95 < z < 1.05$ as described in Section 3.1.3. The V_{OC} is around 1.02 V for $z = 0.95$ and then drops linearly to around 0.8 V for $z = 1.05$. The J_{SC} is unchanged around 21 mA/cm^2 for $0.95 < z \leq 1.00$, shows a maximum of 22 mA/cm^2 for $z = 1.01$ and then drops to below 19 mA/cm^2 for $z = 1.05$. The FF shows a maximum of around 66% for $z = 0.95$ and decreases quasi-linearly to around 55% for $z \geq 1.03$. These trends result in a maximum PCE of 15% for $z = 0.95$ which quasi-linearly drops to below 9% for $z = 1.05$.

ITO/SnO$_2$-NP/PbAc$_2$/Spiro-OMeTAD/Ag (Figure 5.25)

We studied stoichiometric variations using the PbAc$_2$ recipe in the standard architecture with SnO$_2$-NP as ETL and Spiro-OMeTAD as HTL (Sec. 3.1.4). The V_{OC} is roughly unchanged for all stoichiometries at around 1.02 V (with a small maximum of 1.04 V for $y = 3.03$). The J_{SC} is at around 22 mA/cm^2 for $y \leq 3.01$, shows a maximum of 23 mA/cm^2 for $y = 3.03$ and then strongly decreases to below 18 mA/cm^2 for $y = 3.05$. The FF shows a minimum of around 73% for $y = 2.97$ and then slightly increases up to 79% for $y = 3.05$. Hence, the PCE is unchanged at around 16% for $y \leq 3.01$, shows a maximum of 18% at $y = 3.03$ and strongly decreases to around 13% for $y = 3.05$.

FTO/SnO$_2$/PC$_{60}$BM/sol-eng/Spiro-OMeTAD/Ag (Figure 5.26)

Stoichiometric variations were also studied using the sol-eng recipe (Sec. 3.1.3) in the standard architecture with SnO$_2$/PC$_{60}$BM as ETL and Spiro-OMeTAD as HTL (Sec. 3.1.4). The V_{OC} is slightly below 1 V for $z \leq 1.00$, shows a maximum of around 1.03 V for $z = 1.01$ and then drops to below 0.95 V for $z \geq 3.03$. The J_{SC} is very low at around 14 mA/cm^2 for $z \leq 0.97$, increases to around 18 mA/cm^2 for $z = 0.99$ and $z = 1.00$ and shows a maximum of around 20 mA/cm^2 for $z \geq 1.01$. The FF
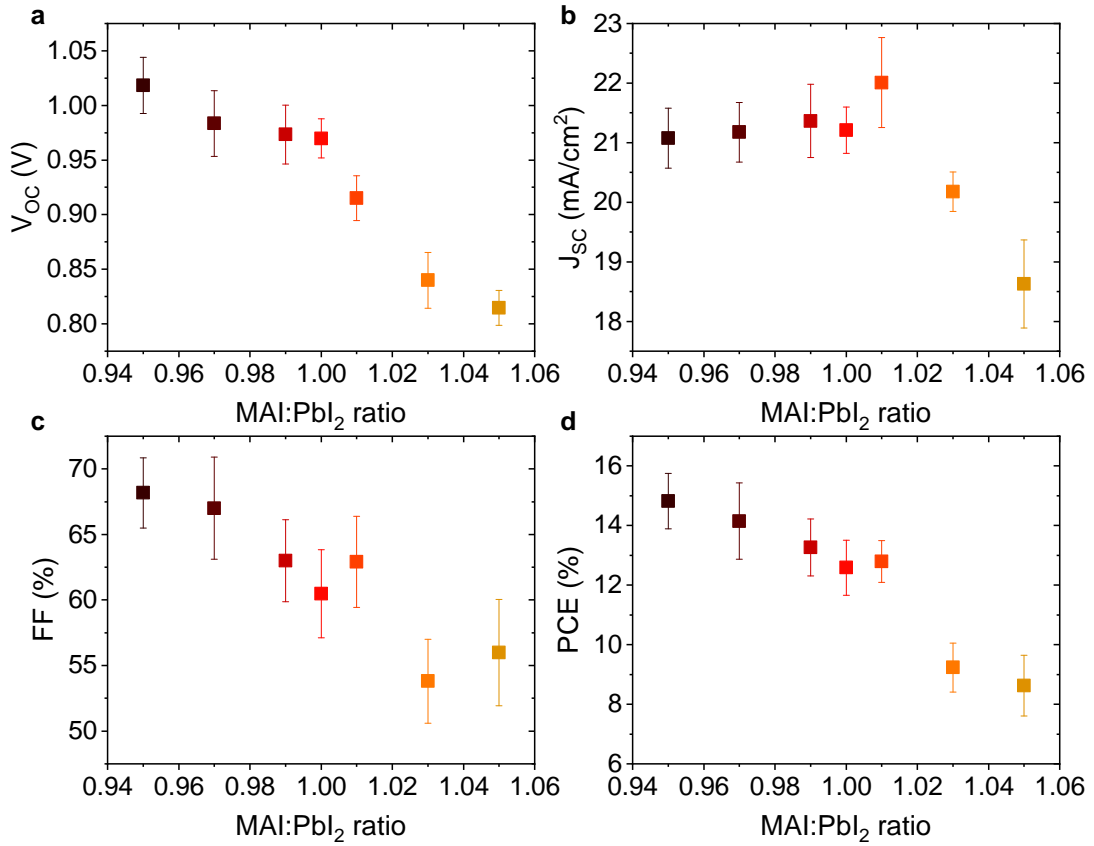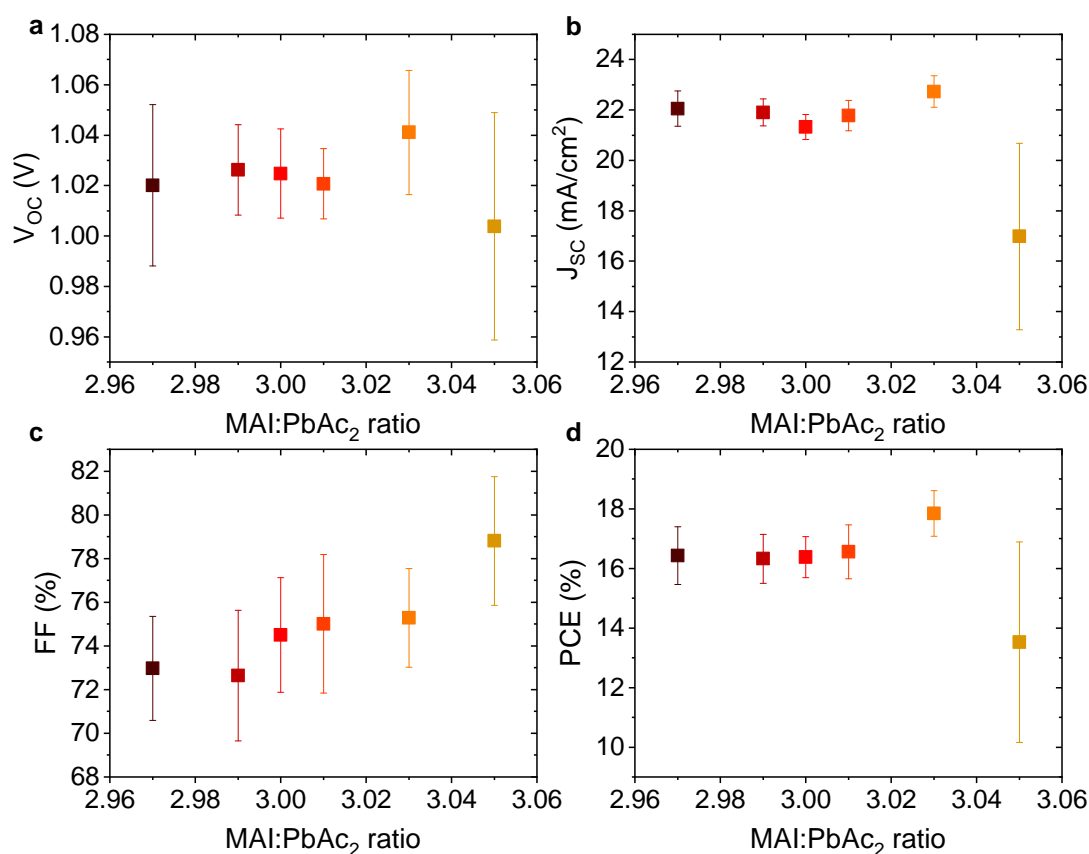
Figure 5.24: PV parameters of solar cells with the architecture ITO/Poly-TPD/MAPbI$_3$/PC$_{60}$BM/BCP/Ag with varying stoichiometry z = MAI:PbI$_2$, (a) V$_{OC}$, (b) J$_{SC}$, (c) FF and (d) PCE. The data is the average from 10-14 pixels within one batch. The devices were fabricated and measured in Oxford in collaboration with Dr. Matthew T. Klug.

is roughly unchanged around 67.5% for all stoichiometries, while it exhibits a large spread. Hence, the PCE is below 12% for $z \leq 1.00$, shows a maximum of 14% for $z = 1.01$ and then drops to around 12% for $z \geq 1.03$.

To summarize, the results reveal that for other recipes and device architectures, too, small variations in precursor stoichiometry lead to obvious changes in the photovoltaic parameters. Without a more detailed characterization of the film surface we can only speculate what is the exact reason for the different trends observed. However, the results clearly show how sensitive the MAPbI$_3$ composition is to small variations in precursor stoichiometry.

Table 5.2: Device architectures and corresponding recipes for which various stoichiometries were tested.

Figure	Perovskite recipe	Layer stack
Figure 5.22	$PbAc_2$	$ITO/m\text{-}PEDOT:PSS/Pbac_2/PC_{60}BM/BCP/Ag$
Figure 5.23	$PbAc_2$	$FTO/Poly\text{-}TPD/Pbac_2/PC_{60}BM/BCP/Ag$
Figure 5.24	PbI_2 sol-eng	$FTO/Poly\text{-}TPD/sol\text{-}eng/PC_{60}BM/BCP/Ag$
Figure 5.25	$PbAc_2$	$ITO/SnO_2\text{-}NP/PbAc_2/Spiro\text{-}OMeTAD/Ag$
Figure 5.26	PbI_2 sol-eng	$FTO/SnO_2/PC_{60}BM/sol\text{-}eng/Spiro\text{-}OMeTAD/Ag$

Figure 5.25: PV parameters of solar cells with the architecture $ITO/SnO_2\text{-}NP/MAPbI_3/$ Spiro-OMeTAD/Ag with varying stoichiometry $y = MAI:PbAc_2$, (a) V_{OC}, (b) J_{SC}, (c) FF and (d) PCE. The data is the average from 8-12 pixels within one batch. Reproduced with permission from [343]. Copyright 2018, The Royal Society of Chemistry.
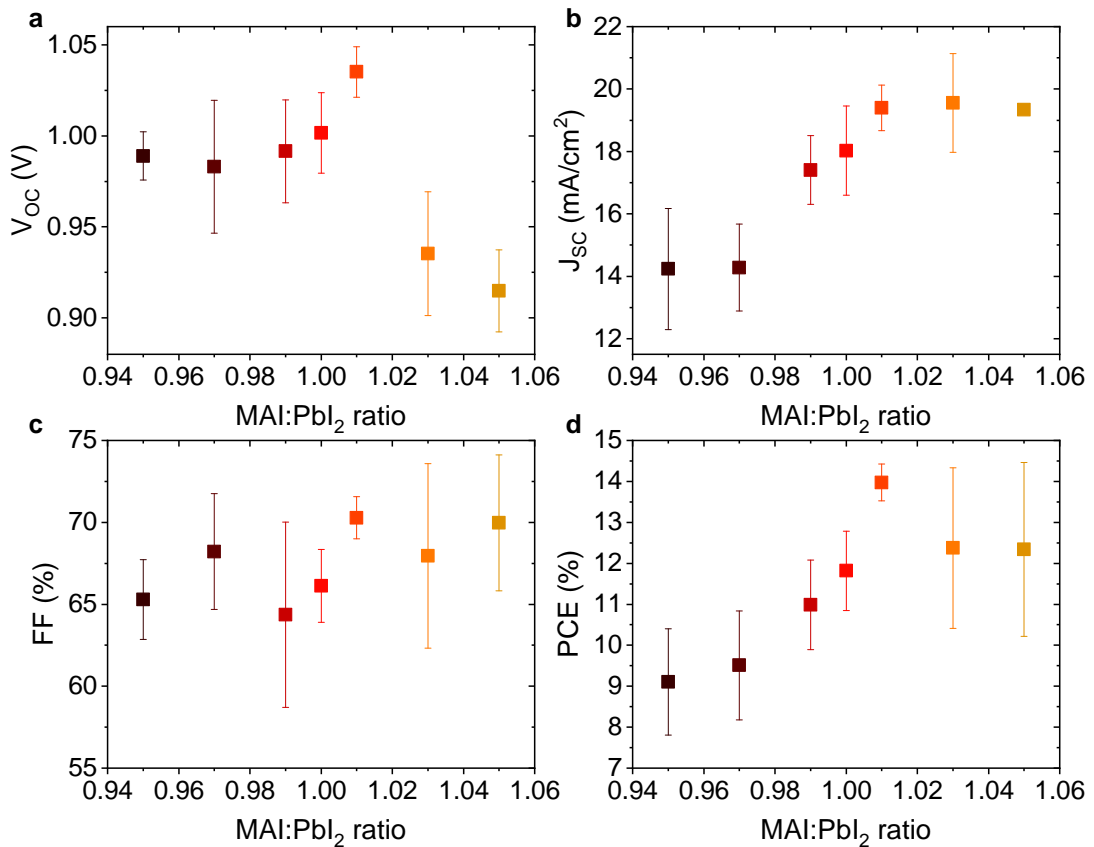
Figure 5.26: PV parameters of solar cells with the architecture FTO/SnO$_2$/PC$_{60}$BM/ MAPbI$_3$/Spiro-OMeTAD/Ag with varying stoichiometry z = MAI:PbI$_2$, (a) V$_{OC}$, (b) J$_{SC}$, (c) FF and (d) PCE. The data is the average from 6-8 pixels within one batch. The devices were fabricated and measured in Oxford in collaboration with Dr. Zhiping Wang. Reproduced with permission from [343]. Copyright 2018, The Royal Society of Chemistry.

5.4 Summary

This chapter focused on understanding reproducibility issues during the fabrication of $MAPbI_3$ perovskite films. We developed a method to fractionally vary the stoichiometry of a $PbAc_2$ based precursor solution around its supposed stoichiometry ($y = MAI:PbAc_2 = 3$), yielding overstoichiometric films for an excess of MAI ($3 < y \leq 3.075$), and understoichiometric films for an excess of PbI_2 ($2.96 \leq y < 3.00$).

The PV parameters of devices in the architecture $ITO/PEDOT:PSS/MAPbI_3/PC_{60}BM/BCP/Ag$ showed large variations: the V_{OC} exhibits a quasi-linear increase with a relative change of more than 15% when changing the stoichiometry from $y = 2.98$ to $y = 3.06$. XPS measurements revealed that the N/Pb and I/Pb atomic ratios at the film's surface also increase linearly: for films with $y = 3.075$ the values are increased by ~60% (N/Pb) and ~20% (I/Pb), while the corresponding increase of the N/Pb and I/Pb ratios in the precursor solution are only 7.5% and 2.5% respectively. Analyzing and comparing XPS and EDX results, we conclude that excess MAI is incorporated in the $MAPbI_3$ crystal lattice as MA^+ and I^- interstitials in the top ~10-50 nm of the films. UPS measurements revealed strong effects on the surface energetics of the films: the ionization potential shifts by more than 0.4 eV towards lower values when changing the stoichiometry from $y = 2.97$ to $y = 3.06$, with a concurrent shift of the Fermi level position by around 0.3 eV towards the valence band. Hence, the film surface becomes more p-type for higher stoichiometries. We explain the correlation between the energetic shifts and the observed increased device V_{OC} with an increased built-in potential and larger quasi-Fermi level splitting in the devices, and concurrent reduced recombination at the $MAPbI_3/PC_{60}BM$ interface.

The dark storage stability in ambient conditions is also strongly influenced by the exact stoichiometry: films with $2.97 < y \leq 3.00$ show a very high stability, with the most stable devices retaining more than 80% of their initial PCE after more than 7000 h. In contrast, the stability is reduced for films with $y > 3.00$, with a clear trend towards lower stability for higher y. Based on literature reports, we assume that the increased amount of hygroscopic MAI species in the surface region of the films facilitates ingress of water and enhances reactivity with water molecules.

Employing SEM and XRD, we found only minor changes in the microstructure of the films. The grain size is very similar for all y with only a slight decrease for the highest stoichiometries. The absolute intensity of the main (110) tetragonal reflection in the XRD spectra exhibits a decrease by nearly one order of magnitude. However, microstrain analysis revealed that the microstrain in the films is similar for all stoichiometries and we thus conclude that changes in microstructure or crystal defects are not the main cause for the strongly reduced storage stability for higher stoichiometries.

Finally, we also studied the effect of fractional variations in precursor stoichiometries for other device architectures employing the $PbAc_2$ as well as the sol-eng recipe. The effect of stoichiometry on the PV parameters is very different for the various ar-

chitectures and without a more detailed analysis of the perovskite films, we could only speculate upon the exact reasons for the observed trends. However, the large spread in PCE clearly reveals the strong sensitivity of the photovoltaic parameters towards the exact stoichiometry also for other $MAPbI_3$ recipes and device architectures.

6. Photoluminescence Properties and the Effect of Atmosphere

6.1 Introduction

Maximizing luminescence in photovoltaic devices is necessary to approach the theoretical limits of the V_{OC} and ultimately to reach the Shockley-Queisser limit (Sec. 2.1.3). In Section 2.2.6 recent literature reports on the light-emission and light-soaking properties of MAPbI$_3$ are discussed. This chapter aims to explore the effect of fractional variations in precursor stoichiometry (again employing the PbAc$_2$ recipe; Sec. 3.1.3) on the photoluminescence properties of MAPbI$_3$ films. In section 6.3 we will discuss measurements of the steady-state PL quantum efficiency (PLQE) (Sec. 3.2.4), additionally exploring the role of atmosphere. In section 6.4 we employ confocal PL microscopy (Sec. 3.2.7) to study the role of stoichiometry y and atmosphere at a microscopic level, with the aim of understanding how defect-related processes govern the PL in perovskite materials.

Part of the measurements were performed by Alexandra Bausch and Lukas Falk, as stated in the figures. The confocal PL measurements were performed in collaboration with Dr. Yuriy Zakharko in the group of Prof. Dr. Jana Zaumseil. Some of the results in this chapter will be submitted to the Journal of Materials Chemistry C soon.

6.2 Microstructure and Urbach energy - SEM/PDS

We start by comparing the microstructure of MAPbI$_3$ films with various stoichiometries deposited on glass substrates. Top-view SEM images (Fig. 6.1) reveal that the films are composed of much larger grains when compared to ITO/PEDOT:PSS/MAPbI$_3$ (Sec. 5.2.5). The enhancement of the grain size is similar to that observed on ITO substrates in Section 4.3.4, and we again attribute it to a reduced wettability of the perovskite solution on glass when compared to PEDOT:PSS. When examining the understoichiometric films ($y = 2.97$), a few white flakes can be observed on top of the film surface, similar to the results in Section 5.2.5. We attribute these, as before, to small amounts of excess PbI$_2$ and the flakes completely vanish for $y \geq 3.00$. The grain size is largely unchanged for $y \leq 3.01$, with an average diameter of ~1-2 μm, while for $y = 3.03$ the grains become slightly smaller (~1 μm). For $y = 3.03$, we also observe a few grains which exhibit a darker contrast. We cannot entirely explain this effect, however, we believe it might be caused by bad contacting for this particular sample, because the insulating glass substrate can result in charging issues. Still, qualitatively, the microstructure for $y = 3.03$ is similar to that observed for $y \leq 3.01$. For $y = 3.05$, the microstructure exhibits stronger changes, with the grains becoming
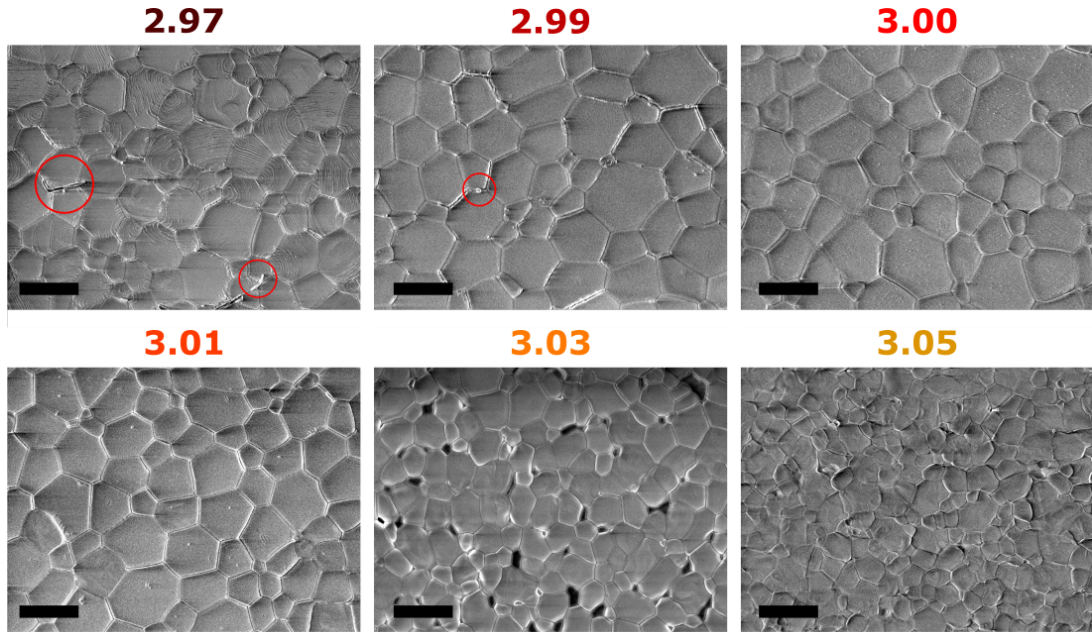
Figure 6.1: Top-view SEM images of Glass/MAPbI$_3$ films with various stoichiometry y. The red circles denote possible excessive PbI$_2$ on the surface (compare Figure 5.18). The scale bars denote 2 μm.

smaller (~0.5-1 μm) and showing less uniform shapes. Before presenting PL measurements, we want to perform measurements with PDS as another optical method for single layer samples. From these measurements, we extracted the Urbach energy (E_U) of films with various stoichiometries (Figure 6.2) and an exemplary PDS data set is shown in Figure A.13 in the Appendix. For $y \leq 3.00$ E_U is unchanged at around 18-18.5 meV. These values are comparable to those measured in Section 4.3.2. For $y > 3.00$ E_U exhibits a quasi-linear increase with values close to 21 meV for $y = 3.05$. Typically, the Urbach energy serves as a measure for the degree of energetic disorder within the films [84, 256]. For example, it is correlated to the shallowness of the bands tails and Gaussian disorder [380, 381]. It is very interesting that small changes in precursor stoichiometry influence the energetic disorder of the films, however, we want to stress that the increase of E_U even for $y = 3.06$ is rather low. We believe that the effects of a slightly increased E_U on the PL properties of the films are small, and rather the density and distribution of non-radiative trap states will determine these properties (Sec. 2.2.3). At this point, we can however speculate on the reasons for the observed increase based on literature reports: we assume, based on the XPS/EDX results in the last chapter (Sec. 5.2.2), that the increased disorder is caused by the enhanced amount of MA$^+$ and I$^-$ species (interstitials) in the perovskite lattice, especially close to the surface [62, 382]. For example, the increased amount of polar MA$^+$ cations could result in stronger local variations in the electrostatic potential (polarization fluctuations). Such an effect was proposed by Wright *et al.* in the case of FAPbI$_3$ [381] and by Senanayak *et al.* in the case of MAPbI$_3$ [156]. With the result that the

effect of variations in stoichiometry on the absorption onset is rather lower, we now report steady-state and spatially resolved PL measurements.
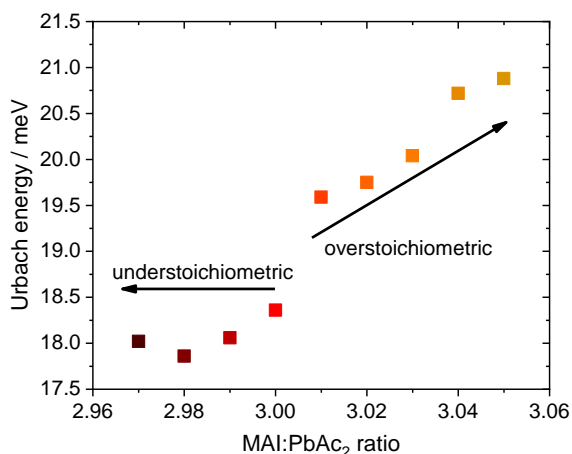

Figure 6.2: Urbach Energy of films with various stoichiometries, as determined by PDS measurements (see Figure A.13 in the Appendix for exemplary measurements). The measurements were performed by Alexandra Bausch. Reproduced with permission from [343]. Copyright 2018, The Royal Society of Chemistry.

6.3 PLQE Measurements

We studied the evolution of the PLQE by measuring films with $2.985 \leq y \leq 3.025$ and small variational steps $\Delta y = 0.005$ under constant laser illumination (532 nm) corresponding to ~2-3 sun intensity (Figure 6.11 (a)). To study the impact of the surrounding atmosphere on the evolution of the PLQE, we flushed the integrating sphere either with N_2 (99.999%) or dry air (~80% N_2, ~20% O_2, H_2O < 0.2%) over the course of the measurement, as shown in the figure. Initially, all films exhibit a very low PLQE, below 0.5%, after which it increases during constant illumination in N_2. We attribute this increase to trap-filling and redistribution of iodide in the films ([129]; see Sec. 2.2.6 and Figure 2.20). However, the dynamics of this process are strongly affected by the exact stoichiometry. While slightly understoichiometric films show rather slow rise time dynamics and do not exhibit a stabilized PLQE during the initial 20 min in N_2, overstoichiometric films show significantly faster rise times and reach stabilized PLQEs, although lower in magnitude. The evolution of the PLQE upon switching the atmosphere to dry air shows even stronger differences: understoichiometric and slightly overstoichiometric films ($2.985 \leq y \leq 3.005$) exhibit an increase of the PLQE, while for $y > 3.005$ a quenching can be observed. We repeated this experiment for bigger variation steps ($\Delta y = 0.03$, Figure 6.3 (b)), and qualitatively observe the same trend. Such a PL boost upon exposure to oxygen might be caused by oxygen-induced trap healing. A reversible PL boost upon switching the atmosphere between N_2 and oxygen under illumination has, for example, been reported by Tian *et al.* as well as Galisteo-Lopez *et al.* [383, 384]. It was proposed that trap states responsible for non-radiative charge recombination can be deactivated by a photochemical reaction involving oxygen. More recent studies propose that generated superoxide species passivate trap centers [385, 386], or that oxidation of interstitial iodine inactivates
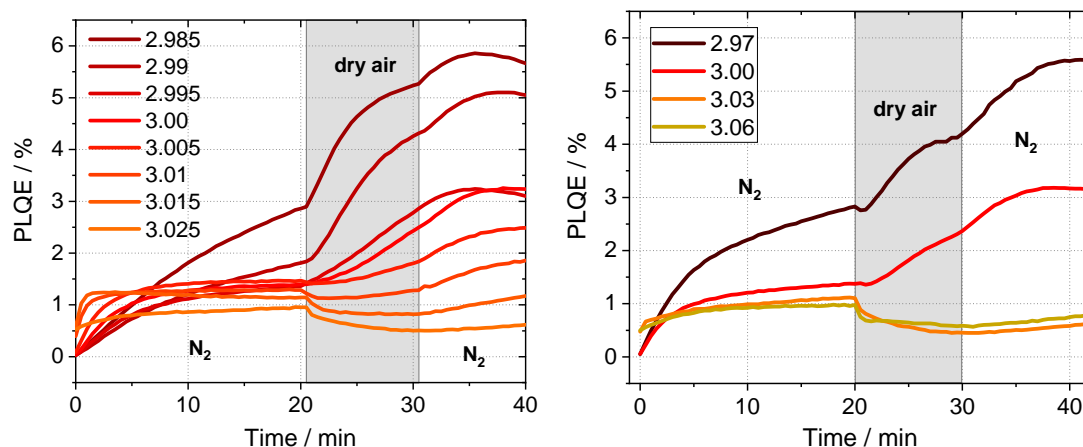
Figure 6.3: PLQE spectra of Glass/MAPbI$_3$ films with various stoichiometries y, with small variation steps (left) and large variation steps (right). The samples were fabricated in a basement room without natural light. The measurements were performed by Alexandra Bausch. Reproduced with permission from [343]. Copyright 2018, The Royal Society of Chemistry.

a source of deep traps ([306]; Sec. 2.2.3). Both processes are proposed to be (semi)-reversible and reduce non-radiative recombination pathways, thus enhancing the PL.

During the course of this study, we moved our fabrication and measurement laboratories to a new building. We repeated the same experiment as described above for various stoichiometries, as shown in Figure 6.4. The results are in stark contrast to what we observed before: first, the initial PLQEs are much higher. Films with $y = 2.97$ show a PLQE of around 7%, $y = 2.99/3.00$ exhibit a bit lower PLQEs of around 4%, and films with $y > 3.00$ have the lowest PLQE of 1.5%. Second, upon changing the atmosphere to dry air, the evolution of the PLQE is completely different from that observed before: for all films, there is a strong drop of the PLQE, and after switching back to N$_2$, it recovers again. In Figure 6.4 (b) we plot the same data, normalized to the value of the PLQE before changing the atmosphere to dry air. The relative evolution in the first 20 min is very similar for all films, while in dry air the understoichiometric films even exhibit the strongest reduction of the PLQE. The recovery phase in N$_2$ is qualitatively very similar for all films. We also performed an experiment in which we started to measure the PLQE in dry air, and switched the atmosphere to N$_2$ after 10 min (Figure 6.5). While all films show a minor initial increase, the PLQE stabilizes much quicker as in N$_2$ atmosphere and already slightly starts to decrease again. We attribute this behavior to a competition between light-induced enhancement of the PLQE (trap filling + iodide redistribution, as described before [129]) and a decrease of the PLQE caused by the onset of degradation due to the exposure to oxygen and and generation of superoxide species ([302]; Chapter 4). The result is a quasi-stable PLQE state. Upon changing the atmosphere to N$_2$, a strong increase of the PLQE is observed, verifying that dry air rather serves as a PLQE quencher in these experiments.

It is complicated to ascertain the reasons for this behavior, which we constantly
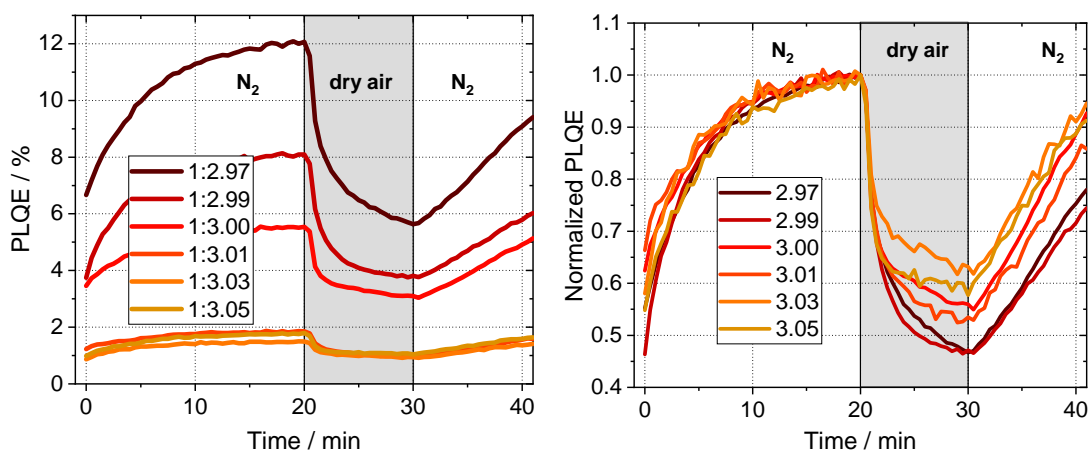
Figure 6.4: PLQE spectra of Glass/MAPbI$_3$ films with various stoichiometries y, with small variation steps (left) and large variation steps (right). The samples were fabricated by Lukas Falk in a laboratory with natural light.

observed in the new laboratories. However, we can provide our best speculation: the main difference between the two laboratories is that natural light can enter the new fabrication lab (in conjunction with a slightly higher intensity of interior light), while the old fabrication lab was situated in the basement with only low intensity interior light. One could imagine that the additional light during fabrication of our films in a drybox already results in a kind of "pre-boost" for these films, reducing non-radiative recombination pathways. Based upon the results of Figure 6.3, such "pre-healed" films would show higher initial PLQEs, especially those with $y < 3.00$. This is exactly the trend which we observe in Figure 6.4. In addition, such samples might not show a further boost in oxygen, but start to degrade right away due to oxygen induced photodegradation ([302]; Chapter 4). As a comparison, a long term PL measurement performed in our old laboratories for films fabricated using the PbAc$_2$ and a PbCl$_2$ recipe (Sec. 2.3.2) is shown in Figure A.14 in the Appendix [332]. The atmosphere is being changed between N$_2$ and dry air in certain time intervals. The evolution of the PLQE reveals a complicated dependence on the atmosphere and history of the films: in the beginning, the PLQE exhibits a boost in dry air, while at later times the PLQE is quenched upon switching from N$_2$ to dry air.

Recently, Brenes *et al*. proposed that MAPbI$_3$ films (which were prepared by our PbAc$_2$ recipe; Sec. 3.1.4) can be passivated by a combined treatment of exposure to light, oxygen and water [386]. The authors found a strong increase in PL yield upon laser soaking the films, with exceptionally long PL lifetimes exceeding 30 μs. It was revealed that the treatment is surface-specific and neither changes the bulk charge carrier mobility nor influences the density of deep traps in the bulk. The increased carrier lifetimes, and the charge carrier mobility being unchanged, resulted in carrier diffusion lengths of up to 77 μm. The effect was attributed to suppressed ionic migration and a reduction of shallow surface trap states that promote non-radiative recom-
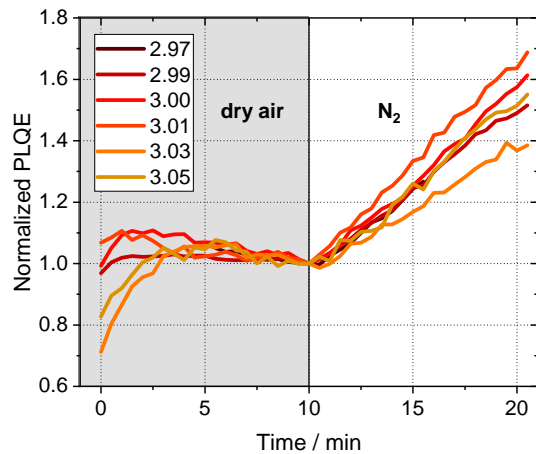
Figure 6.5: Evolution of the PLQE, starting with dry air atmosphere (greyed area) and then switching to N_2. The measurements were performed by Lukas Falk.
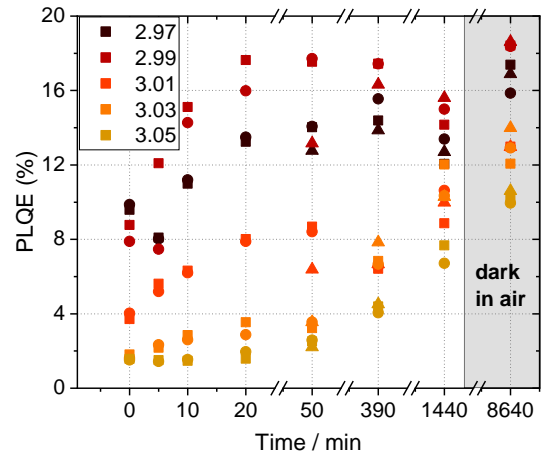
Figure 6.6: PLQE after different storage times in ambient conditions (~30% humidity). The PLQE measurement is performed in N_2. The data points are PLQE values derived after around ~1 min laser illumination, that means without a strong light induced PLQE boost.

bination. The formation of a nanometer-thin amorphous shell (formed because of the presence of water molecules) of inert degradation products was proposed, which helps to make the enhancements of the PL irreversible. In comparison, a treatment in dry air alone was shown to be semi-reversible upon storage in dark conditions [386].

Taking these results into account, we performed a similar study for $MAPbI_3$ films with various stoichiometries. Here, we measured the PLQE in N_2 after only 1 min of laser illumination, to not induce a strong PL boost. Afterwards, we took the samples out of the integrating sphere and left them to rest in ambient conditions (~30% humidity), under low levels of white light illumination (~1 mW/cm^{-2}). Subsequently, the PLQE was measured again in N_2 after various storage times. In this experiment, the samples are exposed to a much lower light intensity when compared to the study by Brenes *et al.*, who only studied the evolution of the PL upon direct laser illumination. The evolution of the PLQE is plotted in Figure 6.6. Initially, we observe the same trend as described above: the understoichiometric films show the highest PLQE of ~8-10%, while more overstoichiometric films exhibit a rather low PLQE of only ~2%. After an only 5 min treatment in air, an increase of the PLQE is observed for all films, with the effect being strongest for lower y. Films with $y = 3.03$ and $y = 3.05$ barely show any increase. After 50 min, films with $y = 2.99$ reach a PLQE of around 19%, while films with $y > 3.00$ are still below 8%. We remeasured the samples after 24 h (1440 min) and observe that the PLQE for the overstoichiometric films has increased, while for the understoichiometric films it did show a further enhancement. Subsequently, we stored these samples 5 more days in air (in dark conditions, to not induce too strong degradation due to the combination of oxygen+light) and afterwards re-
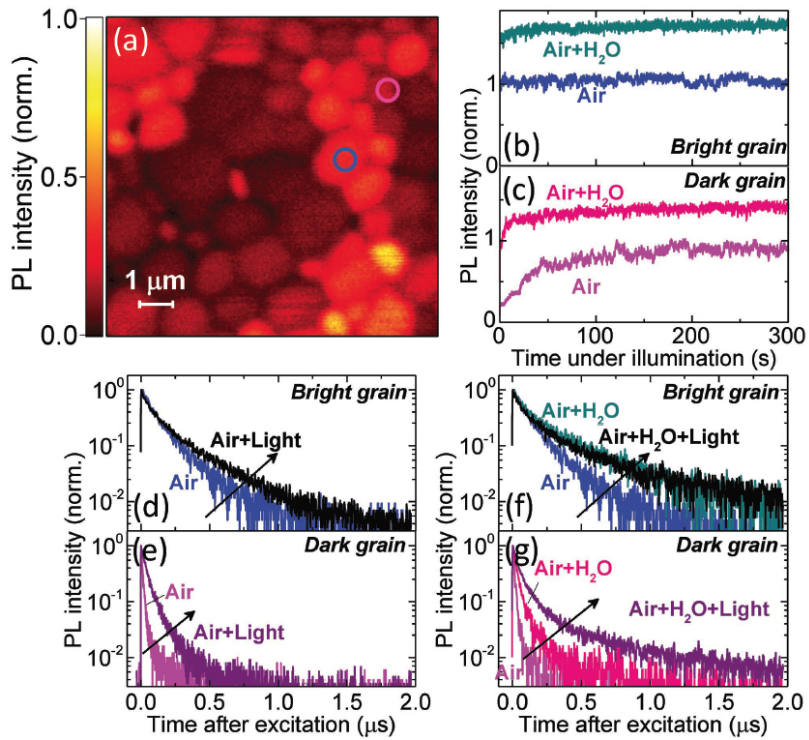
Figure 6.7: Confocal PL study by Brenes *et al.* [387], in which they spatially studied the evolution in PL intensity and lifetime of bright and dark grains (MAPbI$_3$ fabricated by the PbAc$_2$ route) upon exposure to dry air or humidified dry air. The strongest enhancements in PL intensity and lifetime are observed for dark grains, and in the case that both O$_2$ and H$_2$O are present, while the magnitude of the enhancements is much lower for bright grains.
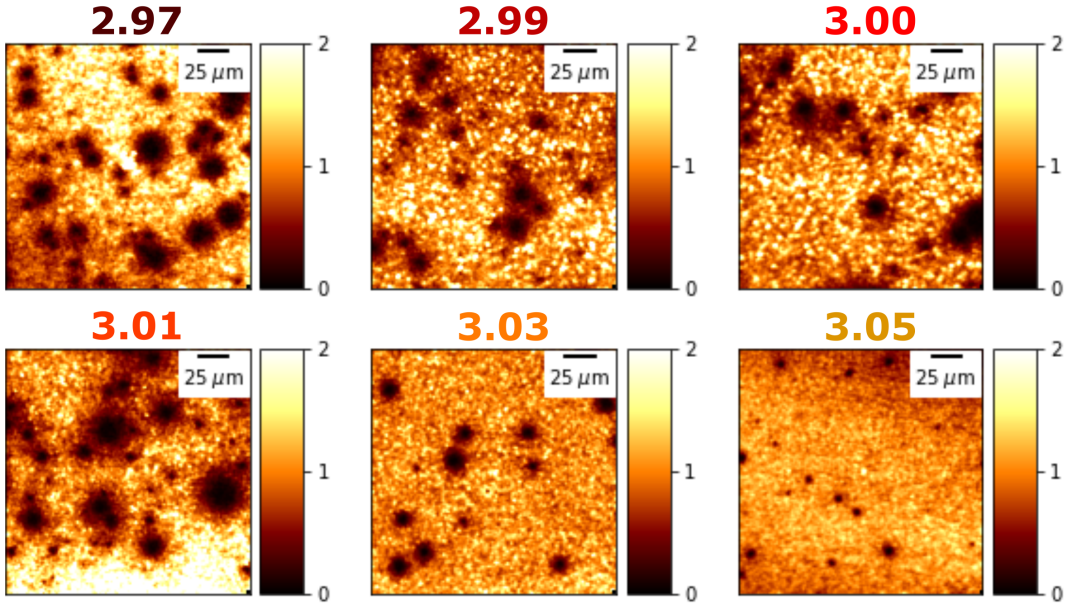
Figure 6.8: Confocal PL intensity maps for a 200x200 μm^2 region on MAPbI$_3$ films with various stoichiometries. The data is normalized to the average value for each map.

measured the PLQE. We observe another enhancement of the PLQE, which is very similar in size for all stoichiometries. Finally, to verify that no strong degradation occurred during the initial 24 hours treatment, we tracked the PL peak positions, as shown exemplary for $y = 2.97$ and $y = 3.03$ in Figure A.15 in the Appendix. We observe no changes of the peak shapes during the first 50 min of treatment and only very marginal changes after 400 min and 24 hours. In order to study the dynamics of the PL increase upon exposure to illumination and ambient atmosphere on a microscopic level, we performed confocal PL microscopy.

6.4   Confocal Photoluminescence Microscopy

The experimental details of the confocal PL microscope setup are summarized in Section 3.2.7. The films are photo-excited using a 405 nm pulsed laser (10 ps, 0.5 MHz repetition rate). The laser is focused on a ~0.5 μm big spot on the sample. We use a formula by Richter *et al.* to estimate the initial charge carrier density upon pulsed laser excitation [155]

$$n_0 = \frac{a \cdot P}{E_{\text{ph}} \cdot f} \cdot \frac{1}{\pi(\frac{d}{2})^2 \cdot t}, \tag{6.1}$$

with $a \approx 0.8$ being the absorption of our MAPbI$_3$ films at 405 nm (determined with our PLQE setup), P the measured laser power, $E_{\text{ph}} = hc/\lambda$ the photon energy, $f = 0.5$ MHz the laser repetition rate, $d \approx 0.7$ μm the focal spot size of the laser and $t \approx 300$ nm the film thickness. We excited our films with a medium laser intensity of $P \approx 1$ nW, generating an initial carrier density of $n_0 \approx 10^{16}$ cm^{-3}. This

was done to avoid filling of all shallow trap states responsible for non-radiative trap-assisted (SRH) recombination, as we are interested in the evolution of the PL upon healing such traps [388]. A similar laser intensity (and repetition rate) has also been employed in another recent study by Brenes *et al.* , in which the evolution of PL intensity and lifetime of MAPbI$_3$ films under various atmospheres (nitrogen, dry air and humidified N$_2$) were studied with confocal PL microscopy. Because these results are directly relevant to ours, we plot them in Figure 6.7 [387] for an easier comparison: the authors studied the difference in evolution between bright and dark grains upon laser illumination in dry or humidified air. Dark grains showed strong enhancements of PL intensity and lifetime in the presence of oxygen, while the effect for bright grains was much smaller. The enhancements were further intensified when H$_2$O was present during the treatment when compared to dry air alone. Similar to their previous study (described above [386]), the authors proposed that generated superoxide passivates shallow trap states (iodide vacancies) and that moisture forms a thin passivating shell on the grain surfaces, thereby converting the surfaces into amorphous regions and eliminating the vacancies [387].
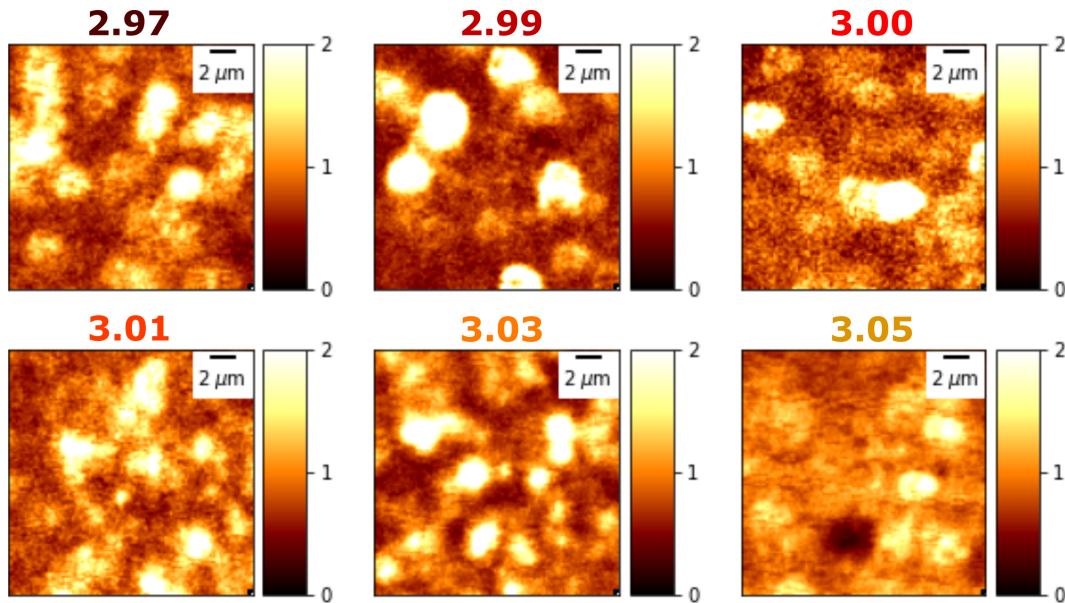

Figure 6.9: Confocal PL intensity maps for a 20x20 µm^2 region on MAPbI$_3$ films with various stoichiometries. The data is normalized to the average value for each map.

In Figure 6.8 we plot 200x200 µm^2 PL maps for various stoichiometries, normalized to the overall average PL intensity. We observe strong heterogeneity in PL: For $y \leq 3.03$ big areas of around 2-25 µm^2 in size can be observed, which emit close to zero PL. These areas are not related to holes or microstructural defects in the films. Recently, two studies reported on strain being present in perovskite thin films and proposed that it influences the material's stability and optoelectronic properties [378, 389]. Employing scanning X-ray diffraction spectroscopy at two different

synchrotrons, combined with high-resolution transmission electron microscopy, such strained regions were shown to be on the ten-micrometer scale (super-grains) or even ten-nanometer scale [389]. Strongly strained regions exhibited the highest luminescence losses, which was related to an enhanced defect concentration. Hence, we believe our measurements show some of these defect-rich super-grains. Interestingly, especially for $y = 3.05$ the density and size of these regions seems to be suppressed. In addition, the heterogeneities in PL intensity seem to become less for higher y.

As a next step, we chose representative 20x20 μm^2 big areas to study the spatial PL in more detail. These PL maps, again normalized to their average intensity, are shown in Figure 6.9. It is evident, that the PL intensity exhibits strong heterogeneity, which we attribute to a varying defect density in different regions of the films, similar to the results obtained in other studies and discussed before ([170, 171, 386, 387]; Sec. 2.2.6). Some areas of the film exhibit very bright PL, and judging from the size, these regions can be attributed to strongly luminescent single grains. Other areas exhibit a medium, and others a very low PL signal. Such areas can be attributed to defect-rich grains or grain boundary regions with a higher monomolecular recombination constant ([129, 170]; Sec. 2.2.6). PL maps were collected at three times; after 5, 10, and 20 minutes of exposure to light (~0.5 mW/cm^2, using the microscope lamp) and ambient atmosphere. The time to record one map was less than 1 min and the time the samples spent in ambient atmosphere before recording the first 20x20 μm^2 PL map was maximum 10 min. To spatially study the evolution of the PL intensity and lifetime, we chose different regions of the film exhibiting bright, medium and dark PL intensities. The chosen areas are presented in Figure 6.10. We normalized the spatial PL intensity of the overall map as well of the three regions to their initial ($t = 0$ min) PL intensity. This was done to track the enhancement of the PL intensity (PL enhancement factor) due to the trap healing previously discussed and the results are plotted in Figure 6.11. There are two trends that are worth noting. Firstly, there is a strong relationship between film stoichiometry and overall PL enhancement. For the highest stoichiometries of $y = 3.03/3.05$, there is little enhancement, and furthermore the Pl does not further increase after a 5 min treatment. For lower values of y, a larger PL enhancement is observed as y decreases. Additionally, for these films as time progresses the enhancement factor is significantly increased. Secondly, by examining the initially dark, medium, and bright grains independently, we observe another trend. While all regions see an inverse relationship between ratio y and enhancement factor, this trend is strongest for the dark and medium regions, and weakest for initially bright regions.

To further investigate the disparities between films with different stoichiometries, we analyzed the evolution of their PL decay. Generally, there is no clear consensus on how to fit PL decay data for perovskite materials. However, to account for the presence of a local distribution of mono-exponential decay rates, which arises due to a distribution of shallow trap states, phenomenologically, a stretched exponential
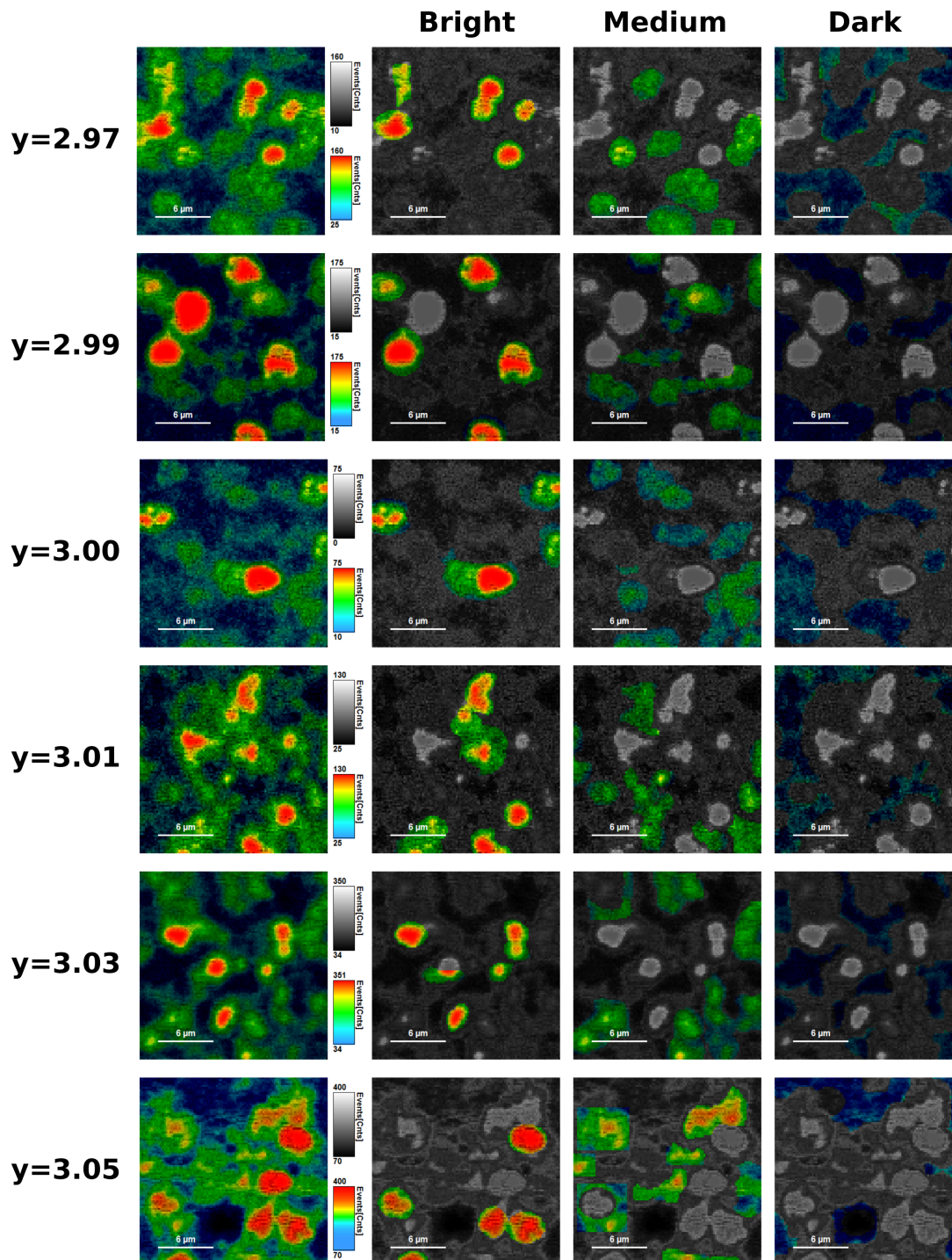
Figure 6.10: Panels on the most left side show the PL maps presented in Figure 6.9. To their right, regions of interest are categorized. For each map, regions with bright, medium and dark PL intensity are chosen, as denoted by the colored areas. These regions are used for further analysis of the evolution of the PL intensities and lifetimes.
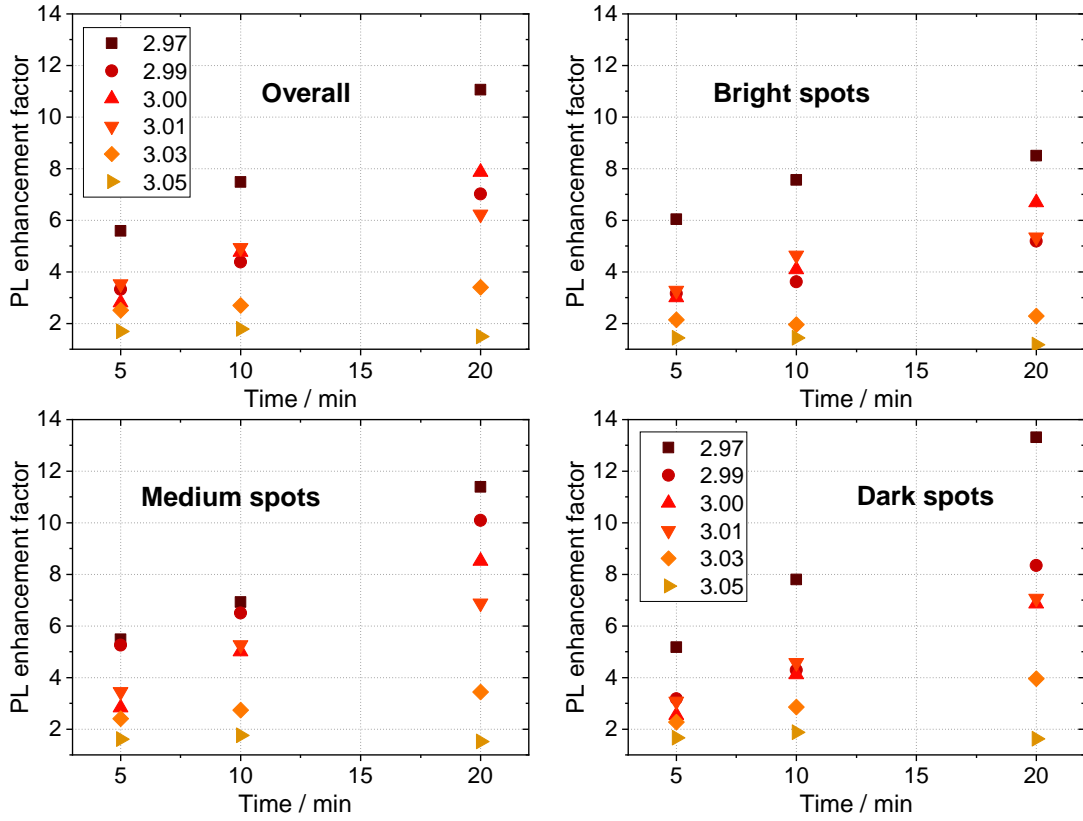
Figure 6.11: PL enhancement factor, determined for the overall 20x20 μm² PL maps as well as bright, medium and dark regions (Figure 6.10). In between the measurements, the samples were stored in ambient air under illumination ((~0.5mW/cm²) for the stated time.

function is typically employed

$$\mathrm{PL}(t) = A \cdot \exp\left(-(\frac{t}{\tau})^b\right), \tag{6.2}$$

with the distribution coefficient b [120, 390, 391]. For our data, however, PL decays with a fast early-time decay ($< 100\,\mathrm{ns}$) were not satisfactorily described if using a stretched exponential only. We found that a combination of a single exponential (to model the fast initial decay) and a stretched exponential described the data best (see Figure A.16 in the Appendix for exemplary fits):

$$\mathrm{PL}(t) = \mathrm{PL}_0 + A_1 \cdot \exp\left(-\frac{t}{\tau_1}\right) + A_2 \cdot \exp\left(-(\frac{t}{\tau_2})^{b2}\right) \tag{6.3}$$

$$\tau_{\mathrm{str}} = \frac{\tau_2}{b_2} \cdot \Gamma(\frac{1}{b_2}) \tag{6.4}$$

In equation 6.4, the Γ-function, $\Gamma(z) = \int_0^\infty x^{z-1} \cdot e^{-x} dx$ is employed to determine the average lifetime (τ_{str}) of the stretched exponential function [390]. Subsequently, we
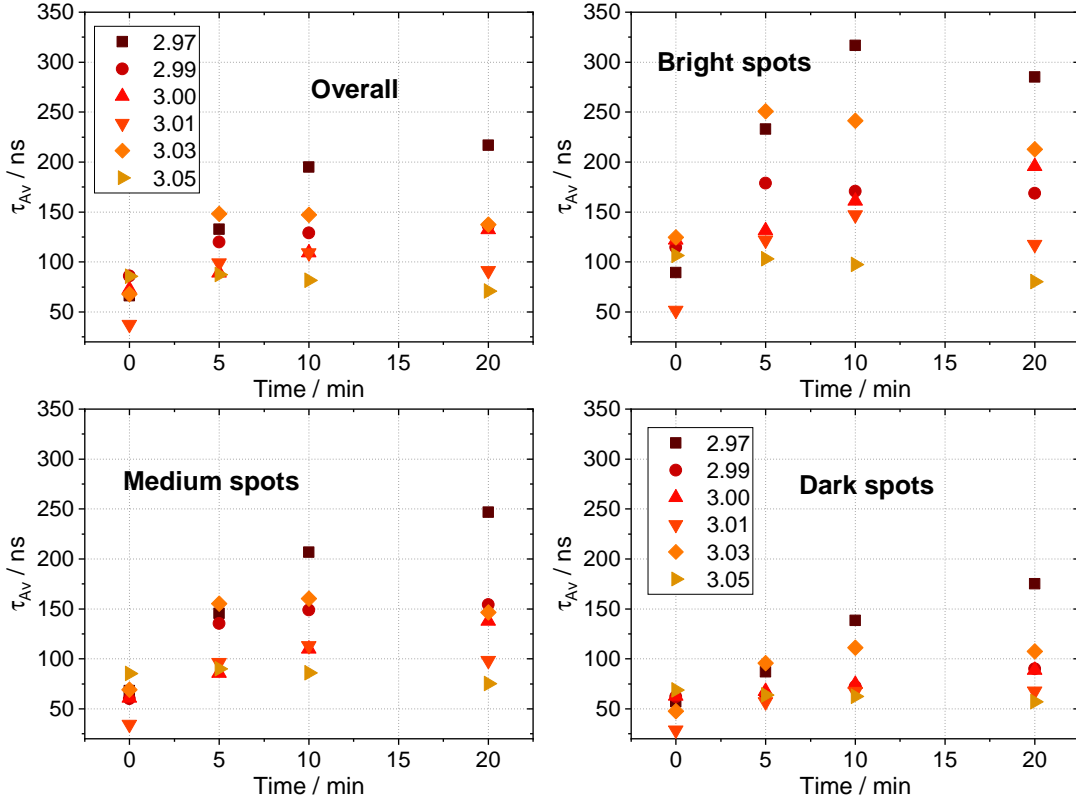
Figure 6.12: Average lifetime (τ_{Av}) derived from fits to the PL decay data (using equation 6.3) for the overall PL map, as well as bright, medium and dark regions (see Figure 6.10). In between the measurements, the samples were stored in ambient air under illumination (($\sim$0.5mW/cm^2) for the stated time.

determined the amplitude averaged lifetime τ_{Av} for a qualitative comparison by:

$$\tau_{Av} = \frac{A_1 \cdot \tau_1 + A_2 \cdot \tau_{str}}{A_1 + A_2} \tag{6.5}$$

We show the fit results for all y and different regions in Tables A.1, A.2 and A.3 in the Appendix, and want to stress again that the values for τ_1, τ_{str} and b_2 have no direct physical meaning, but rather describe a distribution of trap states responsible for non-radiative recombination. In general, values of b_2 closer to 0 imply a more heterogeneous distribution of decay rates, and values closer to 1 a more homogeneous one [381]. We plot the evolution of b_2 for the different regions and stoichiometries in Figure A.17 in the Appendix and observe the following trends: for dark and medium regions, the initial values of b_2 are lowest for $y \leq 3.01$ and higher for $y = 3.03/3.05$. For the bright regions, b_2 is generally a bit higher for all stoichiometries and the just described trend for different y is less clear. After 20 min treatment, the values of b_2 have increased for all stoichiometries, however strongest for $y \leq 3.01$. Hence, b_2 is very similar for all stoichiometries after the treatment, and even lowest for $y = 3.03$

for all regions apart of the bright ones. These results are a hint for that the trap density is initially most heterogeneous for the dark regions and lower y, but becomes more homogeneous for all regions and stoichiometries after the treatment.

For a quasi-quantitative comparison of the lifetime fit results, we plot τ_{Av} over time for the overall PL map was well as the different regions in Figure 6.12. The dependence of τ_{Av} on the exact stoichiometry and its evolution with time is more complex when compared to the results of the PL enhancement factor. Initially ($t = 0\,min$), τ_{Av} does not show a clear correlation with stoichiometry and we attribute the differences to sample to sample variation. However, as expected, brighter regions exhibit a higher initial lifetime (~100 ns), while dark regions show a very low initial lifetime ($<$ 100 ns). The evolution of τ_{Av}, in short, can be described in the following: with time, understoichiometric films show an ongoing increase of τ_{Av}, while more overstoichiometric films show an initial increase, but a subsequent decrease. In addition, the effects are stronger for decreasing y (with the exception of $y = 3.03$). For $y = 3.05$, the τ_{Av} is nearly constant with only a small decrease, in line with the observed small PL enhancement factors for this stoichiometry.

For a more qualitative comparison, we plot the PL decays for both bright and dark grains for under- ($y = 2.97$), exact- ($y = 3.00$), and over- ($y = 3.03$) stoichiometric films as shown in Figure 6.13. Comparing bright vs. dark grains at each stoichiometry, we can see that at early times ($t < 100\,ns$), the decay rate is dramatically faster for the dark grains, indicating a higher rate of trap-assisted SRH recombination ([155, 170, 392, 393]; Sec. 2.2.6). After 20 min, many of these traps are healed and the fast decay is significantly suppressed. If we instead compare the films with different stoichiometries, we observe a more complex behavior. As a function of time, we again see a greater and ongoing effect for $y = 2.97$ films when compared to $y = 3.03$, which shows an initial effect after 5 min, but no more after 20 min. The exact stoichiometric films show the smallest overall, but also ongoing effects after 20 min. We want to mention that the changes in the shape of the decay, especially at later times, are accounted for in the fits by a change of b_2 as described above.

6.5   Summary

In this chapter, we studied the steady-state PLQE and spatially mapped PL intensities and lifetimes for MAPbI$_3$ films with various stoichiometries.

SEM measurements revealed that for $2.97 \leq y \leq 3.00$ the MAPbI$_3$ grain size on glass substrates is barely unchanged, while for higher stoichiometries the grains become slightly smaller. PDS measurements were employed to study the energetic disorder of the films and, while the Urbach energy is unchanged at low values of around 18 meV for $2.97 \leq y \leq 3.00$, it exhibits a linear increase for $y > 3.00$ up to around 21 meV for $y = 3.06$. We propose that the increased amount of MAI species in the surface region leads to the observed increase in energetic disorder, however, we do not believe that these results have a strong effect on the photoluminescence
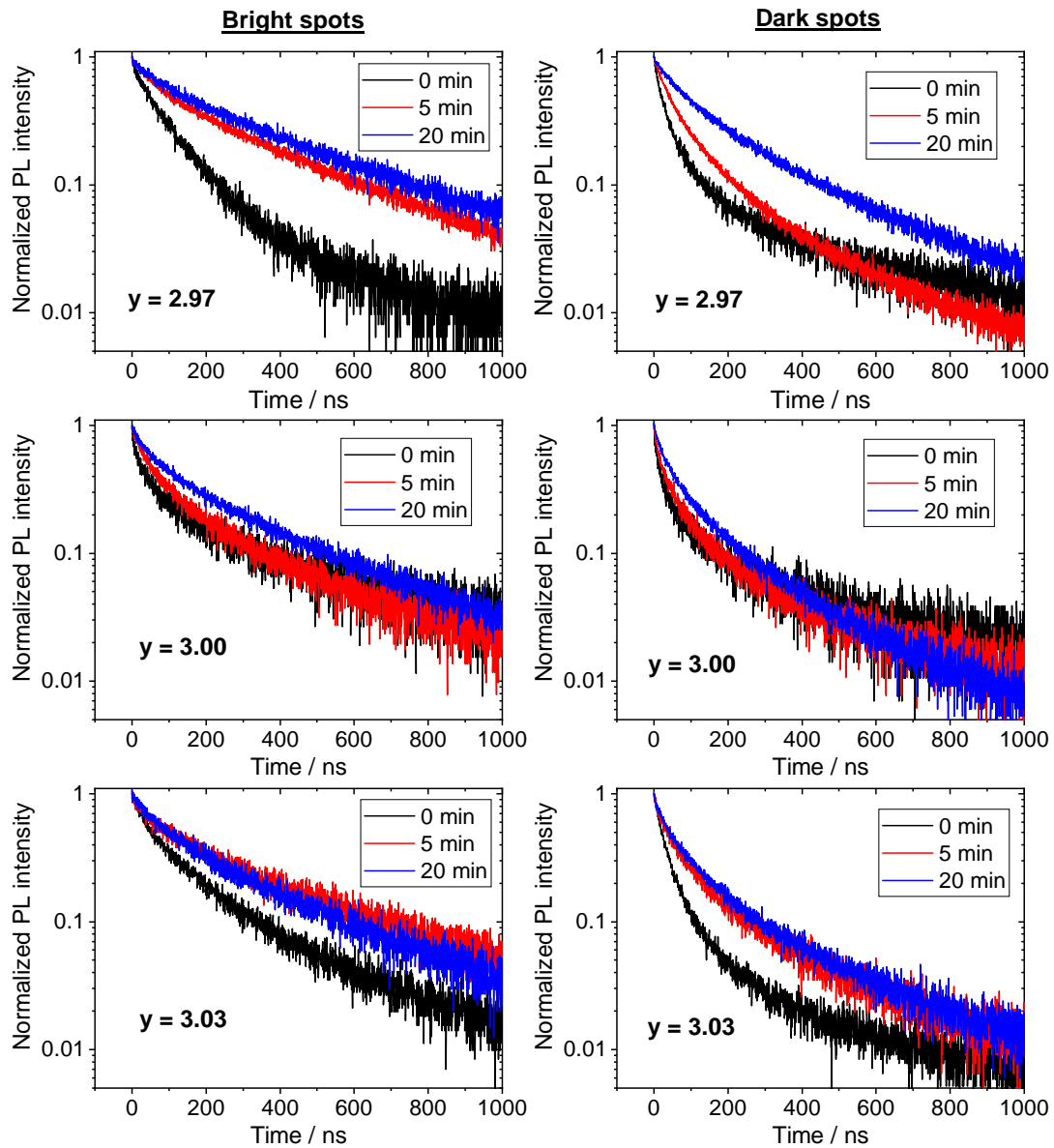
Figure 6.13: Analysis of the PL lifetime decay for representative films: PL decay for bright (left) and dark (right) spots for $y = 2.97$, $y = 3.00$ and $y = 3.03$ after 0, 5 and 20 minutes.

properties of the films.

The PLQE data revealed that upon switching the surrounding atmosphere from N_2 to dry air, depending on the stoichiometry and history of the sample, either PL enhancement or quenching can be observed. As an example, for films with low initial PLQE, exposure to dry air results in a boost for films with $y \leq 3.005$, while more over-stoichiometric films exhibit a quenching of the PLQE. In contrast, for samples which were fabricated under slightly different laboratory conditions (specifically exposure to natural as opposed to fluorescent light), understoichiometric films exhibit much higher initial PLQEs when compared to overstoichiometric ones. Upon exposure to dry air, these films exhibit a decrease in PLQE for all stoichiometries. We attribute this effect to a "pre-healing" of the trap states, due to increased exposure to light during the fabrication of the samples. We also studied the evolution of the PLQE upon storing films in ambient atmosphere under low levels of illumination. Understoichiometric samples exhibited a strong enhancement of the PLQE within 5-20 min, while there was nearly no effect for overstoichiometric films on this time scale. Upon longer storage times in air, the overstoichiometric films also displayed an enhancement of the PLQE; however, in total it was not as large as for the understoichiometric ones, which reached very high external PLQEs close to 20%.

Confocal PL microscopy was employed to spatially study the evolution of the PL intensities and lifetimes for $MAPbI_3$ films with various stoichiometries, upon a treatment of low levels of illumination in ambient conditions. We observed strong heterogeneities in the PL intensities across the films, with some regions exhibiting very low, and others very high, PL intensities. These heterogeneities are slightly suppressed for films with $y \geq 3.03$. In line with literature reports, and as already discussed in the oxygen degradation study (Sec. 4.4), we attribute this effect to a spatially varying density of defects [169–171, 342]. Dark regions are connected to an increased rate of monomolecular non-radiative recombination. In addition, we observed large regions with diameters of ~5-20 μm which exhibited nearly zero PL intensity, and attribute these areas to strained regions in the perovskite films, as recently reported by Jones *et al*. [389].

We then studied representative 20x20 μm^2 areas of the films in more detail, and tracked the evolution of PL intensity and lifetimes for regions with initially bright, medium and dark PL signal. The enhancement in PL intensity was strongest for understoichiometric films, as well as initially dark regions. For more overstoichiometric films and initially bright regions, the effect was significantly smaller. The evolution of the lifetimes, however, showed more complex behavior. Dark regions initially exhibit shorter lifetimes, which corresponds to a higher defect density. As time under illumination progressed, the lifetimes of all regions showed an increase, which we attribute to a suppressed contribution of short lifetime components from shallow trap states in the films. This increase in the PL lifetime was ongoing with respect to time for the understoichiometric films In contrast, for more overstoichiometric films, despite an initial increase, the lifetime plateaued or even began to decrease after ~10-20 min.

To summarize the results in this chapter, we propose a mechanism for why the PL is more strongly enhanced for understoichiometric films in Figure 6.14. We believe that understoichiometric films show a higher number of shallow trap states below the conduction band, which can possibly be attributed to an increased number of iodide vacancies. These traps, in line with recent literature reports, are healed when exposed to the oxygen in air and illumination. As the number of such traps is higher for understoichiometric films, the relative enhancement is much higher when compared to overstoichiometric films with an initially smaller number of these kinds of traps.
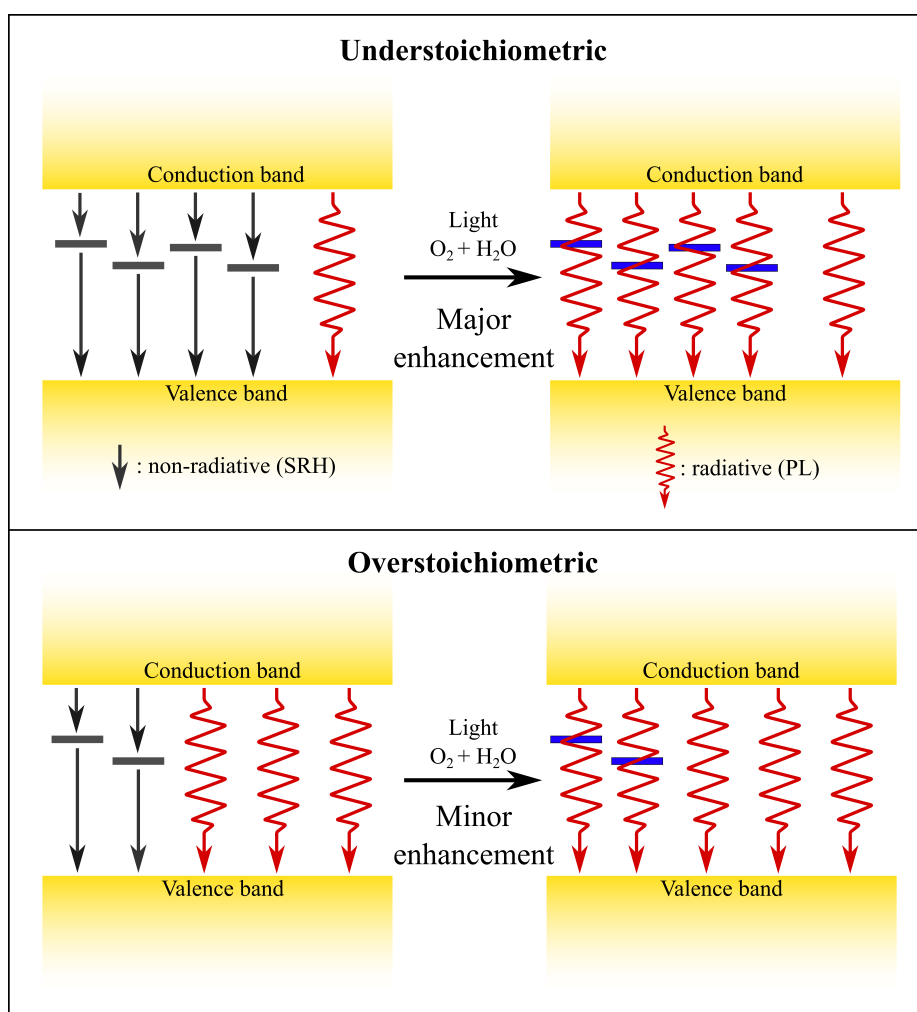
Figure 6.14: Mechanism for explaining the PL boost upon light soaking in ambient air: Understoichiometric films exhibit a high density of vacancy related shallow trap states (dark grey) resulting in monomolecular non-radiative recombination (grey arrows, top left). Upon healing these traps (blue) with O_2, H_2O and light, the initial PL intensity (red) is strongly enhanced (top right). Overstoichiometric films initially possess a lower density of such traps, because of the excess MAI at the film surface (bottom left). Upon treatment, the number of healed traps is smaller, which results in a lower relative PL enhancement (bottom right).

7. Conclusion and Outlook

The scope of this thesis is to derive a better fundamental understanding of two urgent topics of research on metal halide perovskite materials: stability and reproducibility. Since this field of research is rapidly growing and changing, in Chapter 2 the diverse optoelectronic properties of metal halide perovskite semiconductors are examined in great detail by studying and discussing recent literature reports, with a focus on the most typically employed composition, methylammonium lead triiodide ($MAPbI_3$). Special focus is given to the current understanding of the material's stability upon exposure to oxygen and humidity, as well as to a detailed discussion about reports examining variations of the precursor stoichiometry and film composition.
In Chapter 3 we introduce a method to change the perovskite precursor's stoichiometry in small steps in a controlled manner. Furthermore, the experimental details and analytical methods for characterization of the films are described.

Role of Microstructure in Oxygen Induced Photodegradation of $MAPbI_3$

In Chapter 4, we study the role of microstructure in oxygen induced photodegradation of $MAPbI_3$ thin films. For that purpose, we prepared $MAPbI_3$ perovskite films employing two different recipes: one based on lead acetate trihydrate ($PbAc_2$) as precursor and one based on a solvent-engineering (sol-eng) method. By studying the microstructure of the films (deposited on ITO/PEDOT:PSS substrates) with AFM and SEM, we reveal striking differences: films based on the $PbAc_2$ recipe consist of large and ordered perovskite grains extending throughout the whole film thickness. In contrast, films based on the sol-eng recipe consist of small and irregular grains with multiple grain boundaries throughout the film. The difference in microstructure is reflected in device efficiency (ITO/PEDOT:PSS/$MAPbI_3$/$PC_{60}BM$/BCP/Ag), with higher efficiencies of up to 15.5% for the $PbAc_2$ recipe and only 10.5% for the sol-eng recipe. PLQE measurements of the films yield PLQEs of 10% and 0.1% for $PbAc_2$ and sol-eng films respectively, suggesting a higher defect density in the sol-eng films. Bare ITO/PEDOT:PSS/$MAPbI_3$ films were degraded under simulated sunlight (1 sun, 10 h) and various levels of oxygen (1%, 2%, 5%, 10%, 12%, 15% 20%). The degraded films were completed to full solar cell devices (ITO/PEDOT:PSS/$MAPbI_3$/ $PC_{60}BM$/BCP/Ag) and measured (PV parameters, EQE), as well as characterized by UV-Vis, XPS, PDS and SEM. The degradation rate is strongly enhanced for the sol-eng films: a decrease of J_{SC} and absorbance is already observed for the lowest levels of oxygen. Comparing UV-Vis, XPS and SEM measurements, we conclude that especially the surface of sol-eng films degrades much more quickly when compared to $PbAc_2$ films, manifested by a loss of MA species at the layer's surface and conversion into PbI_2 and byproducts. The layer thickness of the sol-eng films is already reduced by around 30 nm for the lowest oxygen levels. The overall degradation process is

greatly slowed down for films based on the PbAc$_2$ recipe, whose large ordered grains only show minor damage for low oxygen levels.

We also degraded PbAc$_2$ films deposited on ITO, which consist of much larger grains, and find a strong heterogeneity in the degradation rate across the same film. Observing the degraded films in SEM, some grains were found to be completely degraded, while others were still intact. In addition, the degradation commences at grain boundaries and surfaces and then progresses inwards. Our results are in line with recent literature reports concerning oxygen induced photodegradation and trap state heterogeneity in MAPbI$_3$ films, which suggest that iodide vacancies are the preferred site for superoxide formation and subsequent degradation of MAPbI$_3$ into PbI$_2$ and byproducts. We assume that the amount of such vacancies is on average higher in grain boundary regions, thus explaining both the enhanced degradation rate for the sol-films (smaller grains and higher defect density), as well as the fact that degradation commences at grain boundaries. We also performed a time dependent degradation study at low (5%) and high (15%) oxygen levels for PbAc$_2$ films, and find that the degradation rate does not progress linearly when comparing the relation of time to oxygen level. Taking all results into account and comparing it with recent literature reports, we suggest that oxygen diffusion into the bulk of the films is strongly slowed down for $\lesssim 10\%$ O$_2$.

Our results demonstrate that exposure to oxygen and light dramatically affects the long-term stability of perovskite films and devices. However, these results do not consider the fabrication environment, which can vary widely – not only between groups, but also for different times of day or year. These include the atmosphere during fabrication (N$_2$, dry air, humidity), but also the illumination the devices are exposed to during fabrication: this can be solar, incandescent, or fluorescent, can be bright or dim, for long exposure times or short. Devices which are fabricated in dry air may already incorporate oxygen, which could then serve to degrade the film, while those fabricated in N$_2$ atmosphere would not. The sensitivity of perovskite materials to these conditions means that understanding all of these factors is crucial to synthesizing stable and viable devices in the future.

Furthermore, future studies should explore the resistance towards oxygen induced photodegradation of other perovskite composition: Studying MA- or I-free compositions (FAPbI$_3$, MAPbBr$_3$) would allow to understand the role of the employed cation in the degradation process. The stability of the nowadays most commonly employed triple-cation composition (Cs$_{0.05}$(FA$_{0.83}$MA$_{0.13}$)$_{0.95}$Pb(I$_{0.83}$Br$_{0.13}$), Cs-MAFA) should also be studied. Finally, multi-cation compositions including Rb or K have recently been reported to yield highly-efficient and hysteresis-free devices, and should also be explored for their resistance towards oxygen induced photodegradation.

Effect of Fractional Deviations in Precursor Stoichiometry

To make perovskite materials a technologically viable alternative, reproducibility is a vital factor. The reported properties of perovskite materials, however, often show a large variation when examined by different researchers. By studying the effect of the exact precursor stoichiometry on the properties of $MAPbI_3$, Chapter 5 and 6 are aimed at a better understanding of such reproducibility issues. To achieve this, we developed a method to fractionally vary the stoichiometry of a $PbAc_2$ based precursor solution around its supposed stoichiometry ($y =$MAI:$PbAc_2 = 3$), and the resulting films are termed overstoichiometric for an excess of MAI, and understoichiometric for an excess of PbI_2.

In Chapter 5, several characterization methods were employed to study the impact of such fractional variations on the properties of $MAPbI_3$ films and devices in the structure ITO/PEDOT:PSS/$MAPbI_3$/PC_{60}BM/BCP/Ag. XPS and UPS measurements demonstrate that the surface composition and energetics of the films prepared by the $PbAc_2$ recipe are strongly influenced by the exact precursor stoichiometry. The strong increase in the N/Pb and I/Pb atomic ratio at the layer's surface with increasing stoichiometry are accompanied by a shift of the ionization potential, which directly correlates to the measured increase in V_{OC} and $ELQE_{ext}$ of photovoltaic devices. By comparing XPS and EDX measurements, we propose that excess MAI in the precursor solution is mainly present in the surface region ($\approx$10-50 nm) of the films. One possible explanation for this effect is that during the thermal annealing process, with the substrates being heated from the substrate side, the excess material diffuses to the layer surface during the crystallization process.

By studying the storage stability of ITO/PEDOT:PSS/$MAPbI_3$/PC_{60}BM/BCP/Ag photovoltaic devices in ambient atmosphere in the dark, we revealed that the degradation rate is also strongly influenced by the exact precursor stoichiometry. We suggest that while the excess MAI at the layer surface results in better energetic alignment and a higher built-in field, such MAI species are highly reactive and therefore more prone to humidity induced degradation. We propose that excess MAI is incorporated into the crystal lattice as MA^+ and I^- interstitials, enhancing the volatility and reactivity of the film surface upon exposure to humidity. For slightly understoichiometric devices, we observe incredible long-term storage stability, with the most stable device retaining 80% of its initial PCE after 7200 h of storage in ambient conditions.

Employing SEM and XRD, we provide evidence that the microstructure of the $MAPbI_3$ films is not strongly affected by the exact precursor stoichiometry. However, we observe a significant decrease in the intensity of the main tetragonal $MAPbI_3$ reflection in the XRD spectra for higher stoichiometries. This might be connected with a reduced crystallinity, and could potentially have an effect on the reduced storage stability. However, performing microstrain analysis, we found that the microstrain of the films is not affected by the exact stoichiometry, and conclude that changes in microstructure are not the main cause for the strongly decreased storage stability. Fi-

nally, we studied the effect of fractional variations in precursor stoichiometries for other device architectures employing the $PbAc_2$ as well as the sol-eng recipe. Our results clearly show that again, the exact stoichiometry has a strong effect on the photovoltaic parameters, with the PCE exhibiting a large spread for most of the studied architectures.

Chapter 6 aimed at understanding the photoluminescence properties and the effect of atmosphere upon variations in precursor stoichiometry. PLQE measurements revealed the high sensitivity of the films towards small variations in the fabrication process. For films with initially low PLQE, understoichiometric films exhibit an enhancement of the PLQE upon switching the atmosphere from N_2 to dry air, while it is quenched for overstoichiometric films. In contrast, films with high initial PLQEs do not exhibit a PL boost in dry air, but a reduction, which is similar in strength for all stoichiometry. We speculate that this effect stems from a "pre-healing" of the understoichiometric films, due to a higher level of illumination during device fabrication.

We spatially tracked the evolution of PL intensities and lifetimes upon exposure to ambient air and light by confocal PL microscopy measurements for films with various stoichiometry. Strong heterogeneities in the PL intensities are observed across the films. In line with literature reports, we attribute this effect to a spatially varying defect density, with dark regions being attributed to regions with an increased rate of monomolecular non-radiative recombination. We analyzed the evolution of PL for regions with initially bright, medium and dark PL signal. The enhancement in PL intensity is strongest for understoichiometric films, as well as initially dark regions. For more overstoichiometric films and initially bright regions, the effect is significantly smaller. The evolution of the lifetimes exhibit a more complex behavior: It initially shows an increase for all regions and stoichiometries, which we attribute to a suppressed contribution of fast decay components from shallow trap states in the films. However, with progressing time under illumination, understoichiometric films show an ongoing increase of the lifetime, while for more overstoichiometric films it saturates or begins to decrease.

Comparing our results with recent literature results, we assume that understoichiometric films possess a higher number of shallow trap states, which can possibly be attributed to an increased number of iodide vacancies. Such traps are healed when exposed to ambient conditions and illumination. Because the number of iodine vacancy related traps is higher for understoichiometric films, the relative enhancement of PL intensity is much more significant when compared to overstoichiometric films, which initially possess a smaller number of traps.

In conclusion our results show how sensitive the efficiency, surface composition and energetics, storage stability and photoluminescence properties of $MAPbI_3$ films are on the exact precursor stoichiometry and the history of the sample. We believe that the changes in the amount of MAI we employed to fractionally vary the precursor stoichiometry are so small, that unintentional errors when preparing the precursor solution could be the reason for often reported discrepancies and irreproducibility

in the perovskite research community using recipes based on $MAPbI_3$. Hence, the results obtained in this study are of great importance and reveal the extreme sensitivity to small changes in the fabrication process.

Future studies could focus on examining the effects of such fractional variations for other perovskite compositions, such as $FAPbI_3$, the most commonly employed triple cation composition ($Cs_{0.05}(FA_{0.83}MA_{0.13})_{0.95}Pb(I_{0.83}Br_{0.13}$, CsMAFA) or recently discover multi-cation compositions including Rb or K. Particularly, the effect on the stability of perovskite films and devices under full illumination should be studied in more detail. Here, two different directions should be examined to further the understanding of the material properties: Firstly, the combined effect of various atmospheres and light illumination on the degradation rate of bare perovskite films with various stoichiometries. Secondly, the stability of fully encapsulated devices under illumination. To enable long-term stability in future applications, perovskite devices will probably need to be encapsulated, and here other intrinsic degradation mechanisms, possibly depending on the exact precursor composition, will become important.
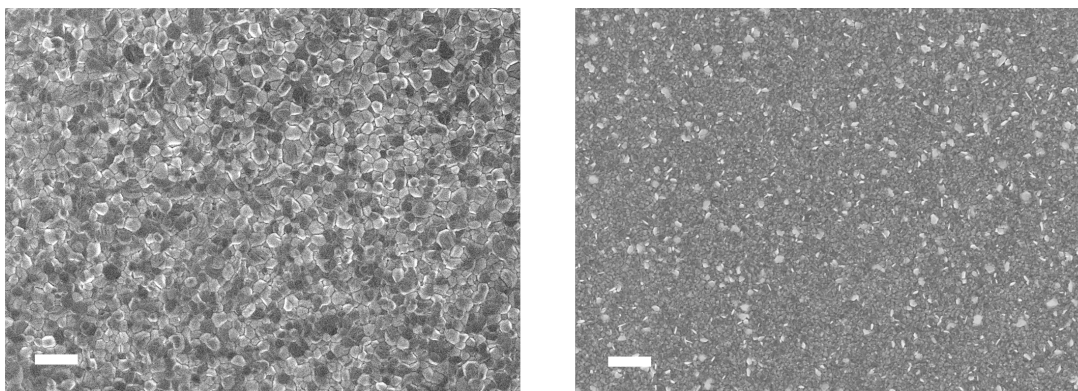
A. Appendix

Figure A.1: SEM images for ITO/PEDOT:PSS/MAPbI$_3$ films using PbAc$_2$ (left) and sol-eng (right) recipes with a lower magnification, revealing that the films are free of pin-holes. The scale bar is 1 μm.
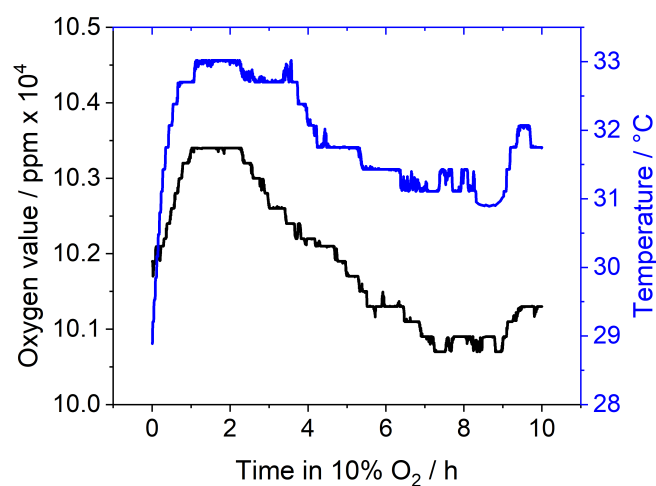

Figure A.2: Tracking of the oxygen level (left axis) and temperature (right axis) of the gas flowing through the sample holder throughout a typical degradation at 10% O$_2$.
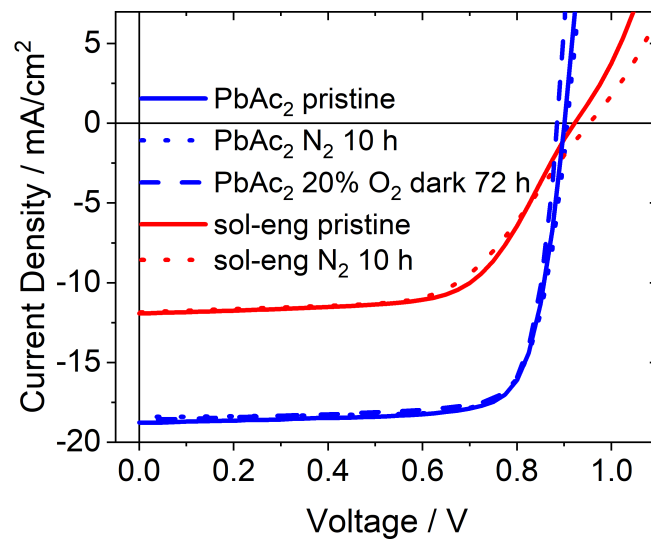
Figure A.3: JV-curves for ITO/PEDOT:PSS/MAPbI$_3$/PC$_{60}$BM/BCP/Ag solar cells, with the bare MAPbI$_3$ films stored either in the glovebox (pristine), degraded for 10 h in N$_2$ or stored for 72 h in 20% O$_2$ before completion, both for PbAc$_2$ (blue) and sol-eng (red).

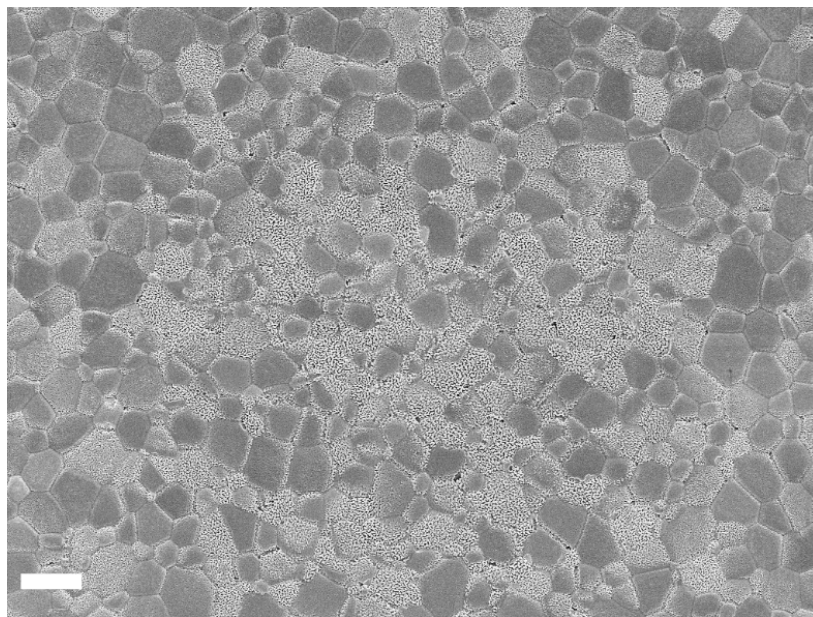**Figure A.4:** SEM top view of ITO/MAPbI$_3$ films prepared by the PbAc$_2$ recipe with a smaller magnification than in Figure 4.14 in the main text. The scale bar is 2 µm.
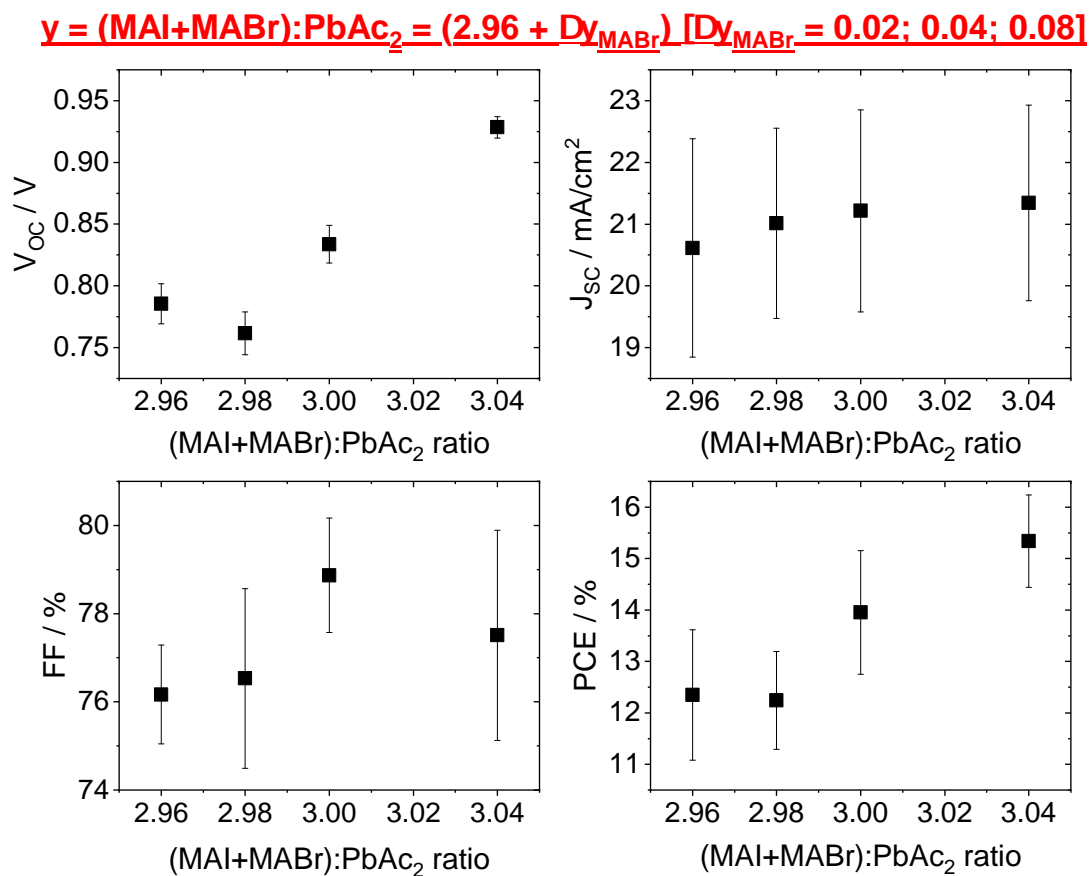
Figure A.5: PV parameters of a batch with ITO/PEDOT:PSS/MAPbI$_3$/PC$_{60}$BM/BCP/Ag in which, starting from y = 2.96, MABr instead of MAI was added into the PbAc$_2$ precursor solution (with $\Delta y = 0.02; 0.04; 0.08$).
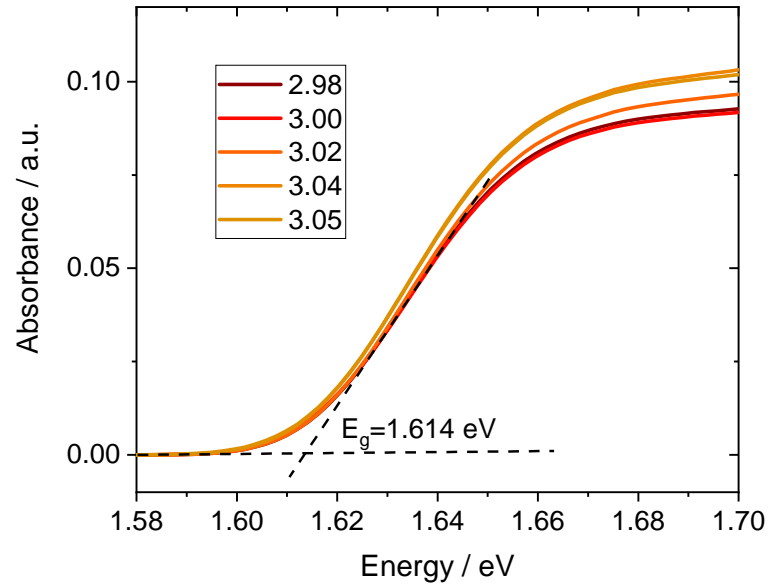
Figure A.6: Tauc plots for ITO/PEDOT:PSS/MAPbI$_3$ films with various stoichiometries. The bandgap is derived from the crossing of the two dashed lines.
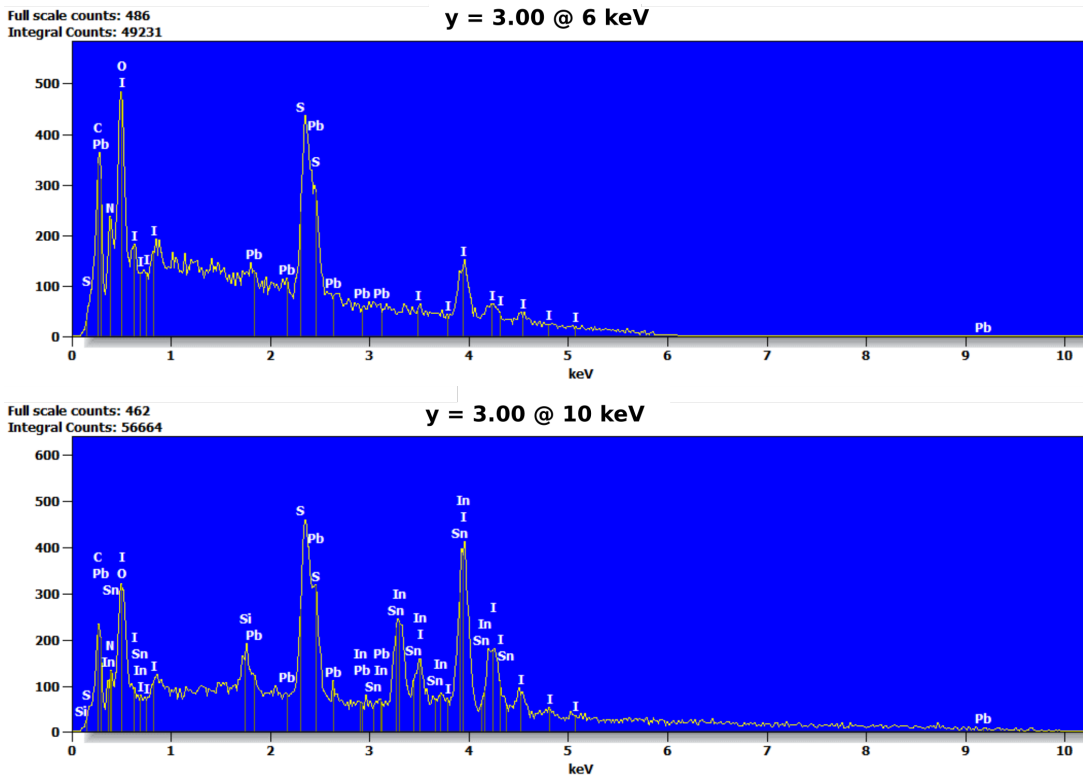
Figure A.7: Typical EDX spectra for the case of ITO/PEDOT:PSS/MAPbI$_3$ films with $y = 3.00$ at 6 keV and 10 keV acclearation voltage.
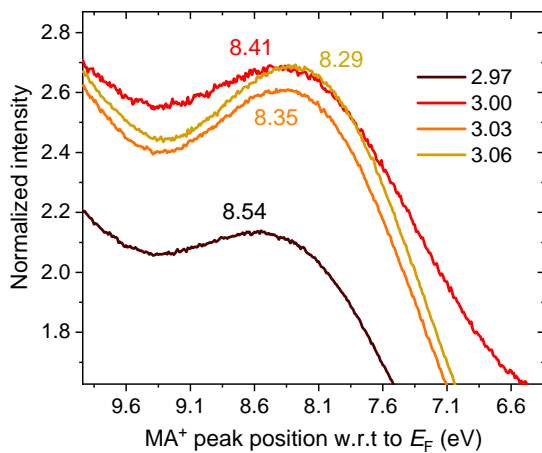
Figure A.8: Examples of the MA^+ peak position for various stoichiometries with repect to E_F from the UPS measurements. The complete data is shown in Figure 5.9.
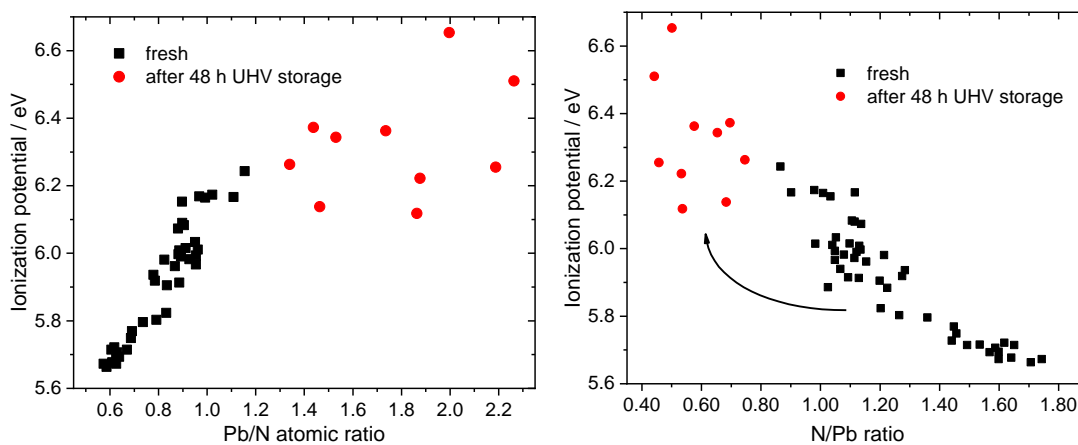
Figure A.9: Ionization potential of ITO/PEDOT:PSS/MAPbI$_3$ films with various stoichiometries, plotted over their N/Pb (left) or Pb/N (rightt) atomic ratio obtained from XPS measurements. The films were measured fresh (black) and some of them again after storage for 48 h in the UHV chamber of the XPS system (red).
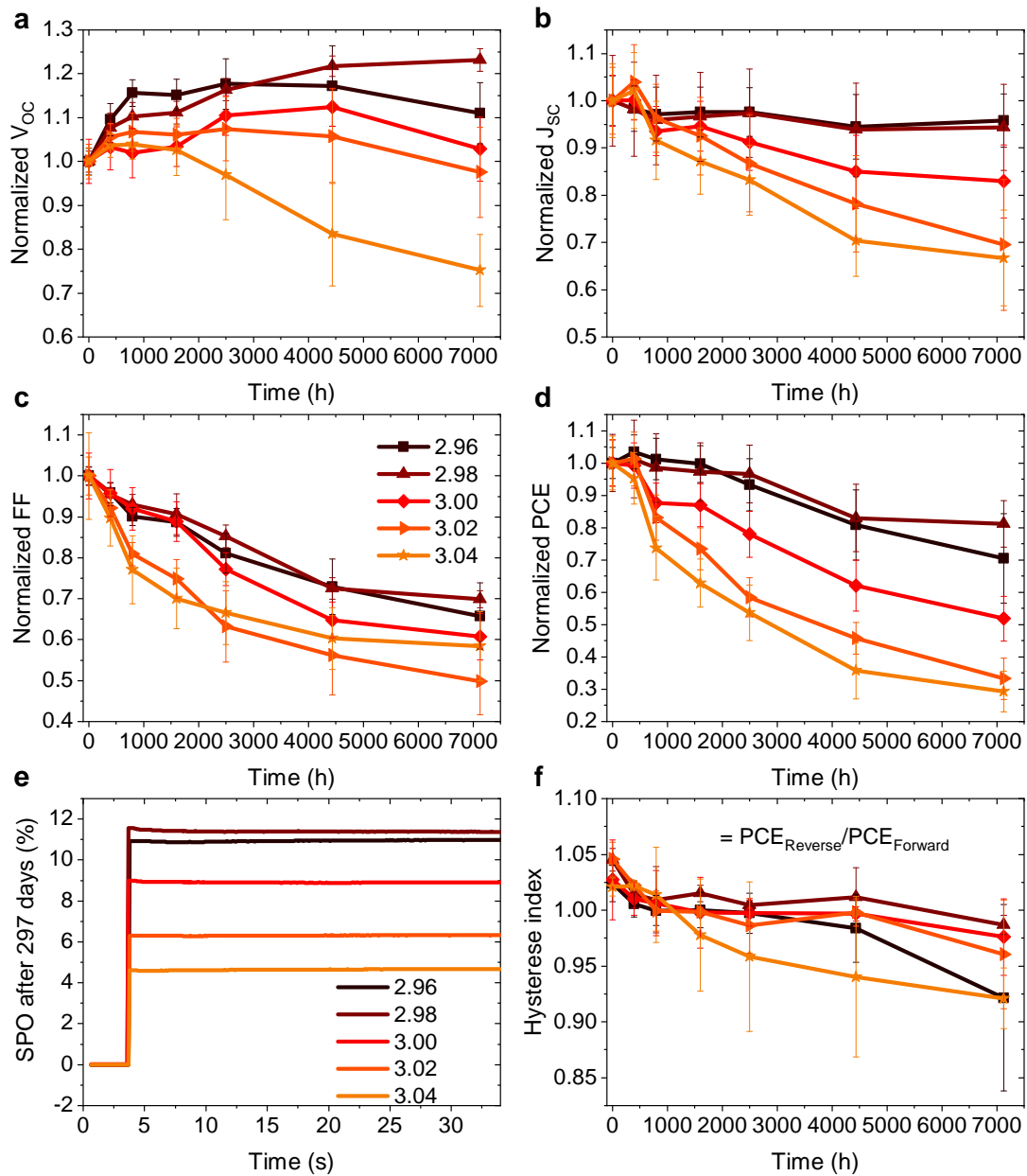
Figure A.10: Tracking of the normalized photovoltaic parameters in reverse scan with dark storage in ambient atmosphere of Batch 1 in Figure 5.5, (a) V_{OC}, (b) J_{SC}, (c) FF, (d) PCE, (d) SPO after 245 days and (e) hysteresis index.
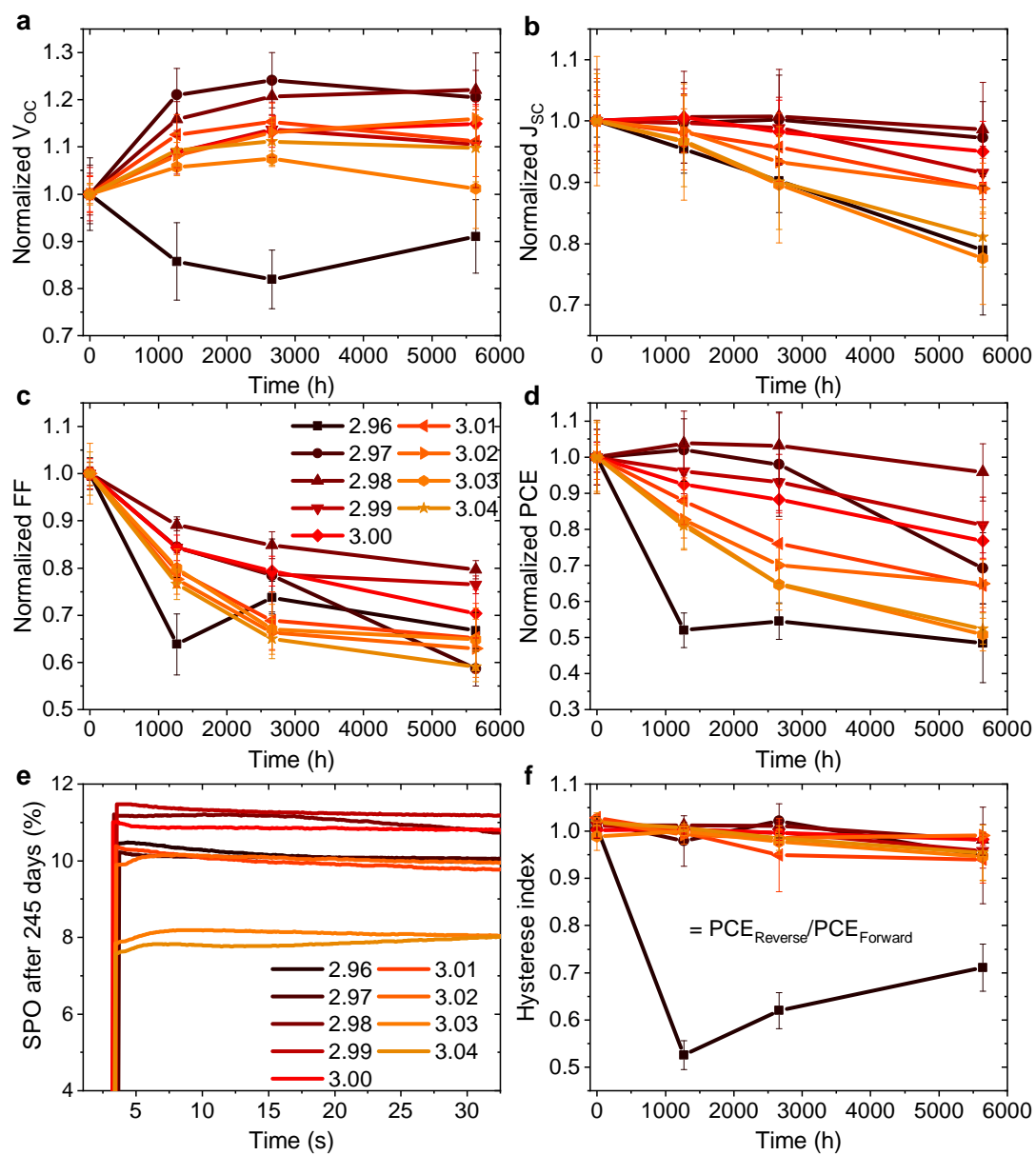
Figure A.11: Tracking of the normalized photovoltaic parameters in reverse scan with dark storage in ambient atmosphere of Batch 2 in Figure 5.5, (a) V_{OC}, (b) J_{SC}, (c) FF, (d) PCE, (d) SPO after 297 days and (e) hysteresis index.
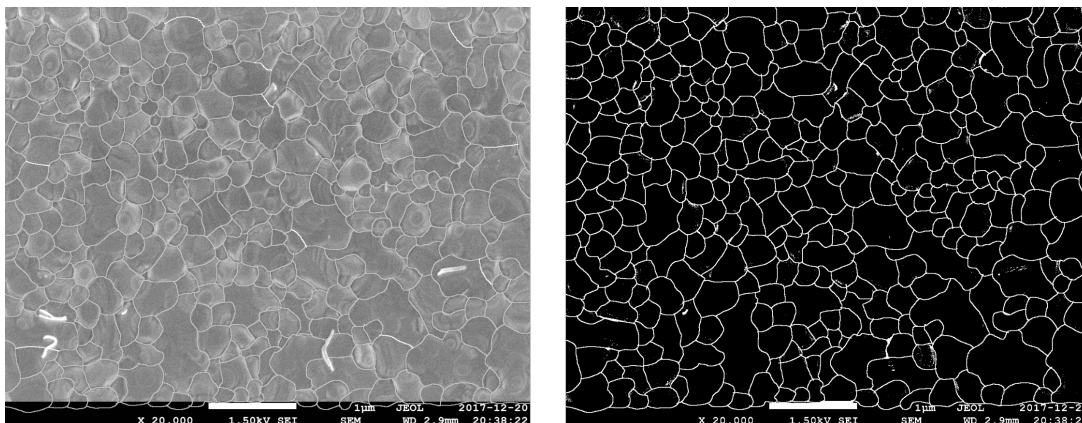
Figure A.12: Determination of the average grain area with Image J: The area of the grains was determined with the 'Analyze Particles' tool in ImageJ (using the imgage on the right) and subsequently this area was used to calculate the grain diamaters assuming the grains are round: $d = \sqrt{\frac{4A}{\pi}}$.
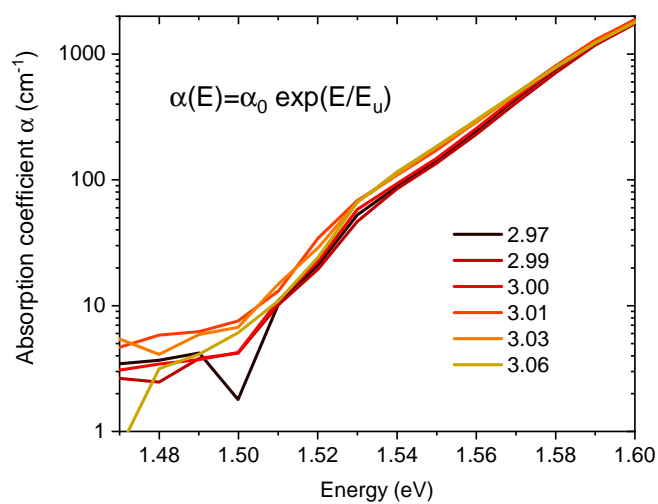
Figure A.13: Exemplary PDS measurements for films fabricated with the $PbAc_2$ recipe and various stoichiometries. Reproduced with permission from [343]. Copyright 2018, The Royal Society of Chemistry.
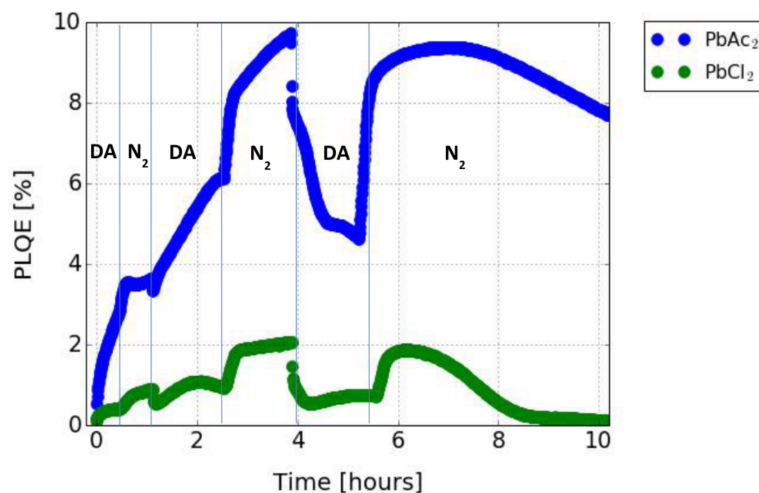
Figure A.14: Long term PLQE measurements of MAPbI$_3$ films fabricated by the PbAc$_2$ and PbCl$_2$ routes. The atmosphere is switched between N$_2$ and dry air every couple of hours. The evolution of PLQE shows that it strongly depends on the history of the film, if in dry air the PLQE exhibits a boost or a quenching. The measurements were performed by Alexandra Bausch. Reproduced from [332].
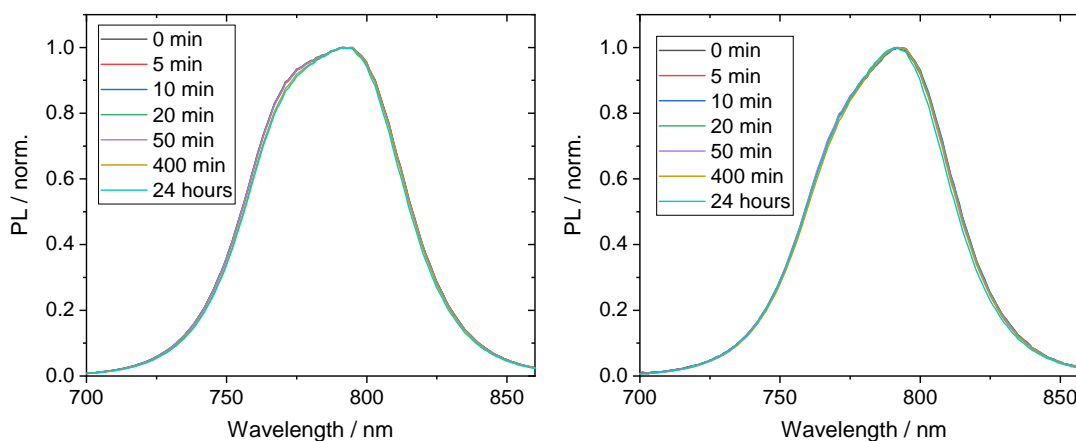
Figure A.15: Tracking of the PL peak positions for $y = 2.97$ (left) and $y = 3.03$ during the long term study presented in Figure 6.6. There is only a minor change of the peak positions after 400 min and 24 hours and we conclude that there are no strong microstructural changes in the MAPbI$_3$ films on these timescales.
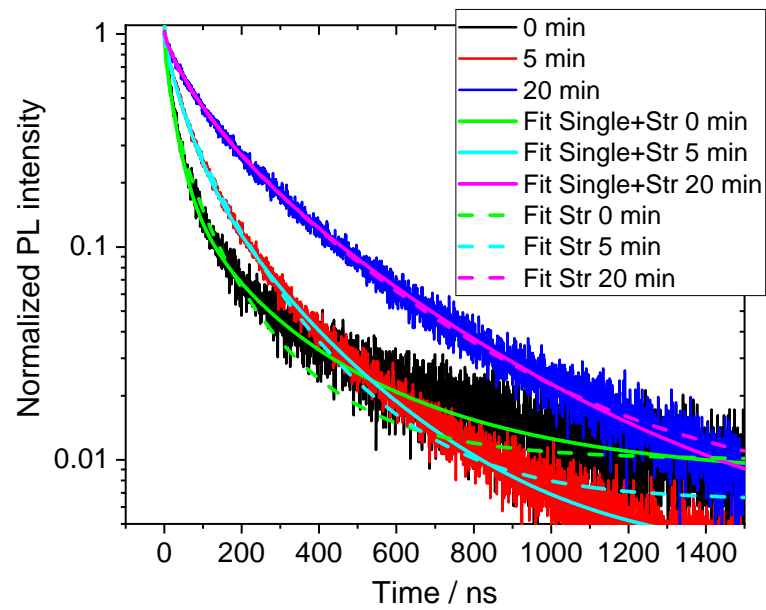
Figure A.16: Exemplary PL decay fits using a stretched exponential (equation 6.2) or a combination of a single and stretched exponential (equation 6.3) for $y = 2.97$ after 0, 5 and 20 minutes of treatment. The combination of a single and a stretched exponential describes various different decays best, while a stretched exponential alone shows some deviations for faster decaying PL. The fit results for all stoichiometries and regions of interest (bright, medium, dark) are presented in Tables A.1, A.2 and A.3.
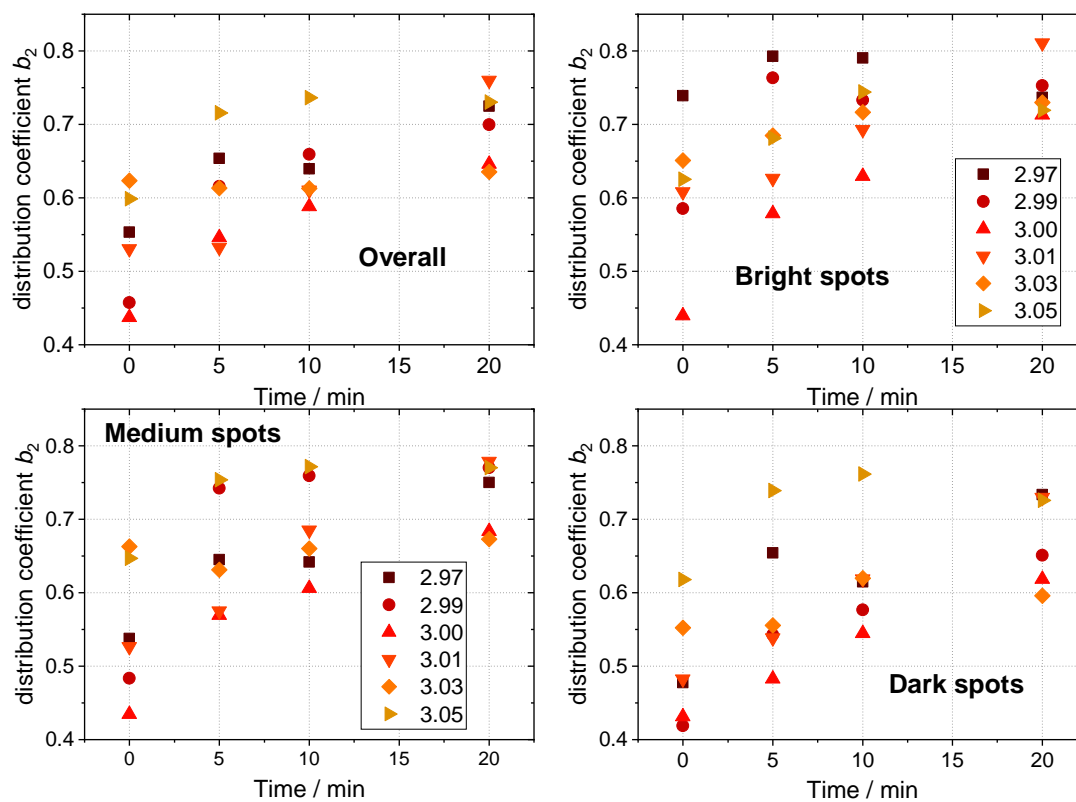
Figure A.17: Evolution of the distribution coefficient b_2 of the stretched exponential function in equation 6.3 for the overall PL map, as well as bright, medium and dark regions. The fit results for all stoichiometries and regions of interest (bright, medium, dark) are presented in Tables A.1, A.2 and A.3.

Table A.1: Fit results using equation 6.3 for **bright** PL regions (see Figure 6.10). Example fits are shown in Figure A.16. The values for τ_{Av} (equation 6.5) are bolded and plotted in Figure 6.12. Errors are omitted for better readability.

Fit parameters/y	2.97	2.99	3.00	3.01	3.03	3.05
0 min A_1 (rel.)	0.02	0.08	0.10	0.44	0.12	0.30
τ_1 [ns]	3	10	21	34	40	46
A_2 (rel.)	0.98	0.92	0.90	0.56	0.88	0.70
τ_2 [ns]	52	79	51	44	100	92
b_2	0.73	0.58	0.44	0.61	0.65	0.63
τ_{Av} [ns]	**89**	**114**	**122**	**52**	**125**	**106**
5 min A_1 (rel.)	0.21	0.31	0.24	0.15	0.07	0.18
τ_1 [ns]	45	27	50	74	27	49
A_2 (rel.)	0.79	0.69	0.76	0.85	0.93	0.82
τ_2 [ns]	247	209	100	91	207	89
b_2	0.79	0.76	0.58	0.63	0.68	0.68
τ_{Av} [ns]	**233**	**179**	**131**	**122**	**251**	**103**
10 min A_1 (rel.)	0.12	0.25	0.10	0.18	0.07	0.22
τ_1 [ns]	37	32	33	87	30	40
A_2 (rel.)	0.88	0.75	0.90	0.82	0.93	0.78
τ_2 [ns]	312	178	123	125	208	95
b_2	0.79	0.73	0.63	0.69	0.72	0.74
τ_{Av} [ns]	**312**	**172**	**161**	**147**	**241**	**97**
20 min A_1 (rel.)	0.04	0.22	0.19	0.16	0.14	0.28
τ_1 [ns]	2	35	38	51	58	41
A_2 (rel.)	0.96	0.78	0.81	0.84	0.86	0.72
τ_2 [ns]	245	174	186	116	196	77
b_2	0.74	0.75	0.71	0.81	0.73	0.72
τ_{Av} [ns]	**285**	**169**	**195**	**118**	**213**	**80**

Table A.2: Fit results using equation 6.3 for the **medium** PL regions (see Figure 6.10). Example fits are shown in Figure A.16. The values for τ_{Av} (equation 6.5) are bolded and plotted in Figure 6.12. Errors are omitted for better readability.

Fit parameters/y		2.97	2.99	3.00	3.01	3.03	3.05
0 min	A_1 (rel.)	0.32	0.34	0.19	0.49	0.41	0.29
	τ_1 [ns]	43	34	36	26	39	48
	A_2 (rel.)	0.68	0.66	0.81	0.51	0.59	0.71
	τ_2 [ns]	45	35	25	23	68	73
	b_2	0.54	0.48	0.43	0.53	0.66	0.65
	τ_{Av} **[ns]**	**68**	**60**	**60**	**34**	**69**	**85**
5 min	A_1 (rel.)	0.23	0.25	0.17	0.24	0.10	0.25
	τ_1 [ns]	55	23	43	50	82	40
	A_2 (rel.)	0.77	0.75	0.83	0.76	0.90	0.75
	τ_2 [ns]	125	144	58	70	115	90
	b_2	0.65	0.74	0.57	0.57	0.63	0.75
	τ_{Av} **[ns]**	**145**	**135**	**86**	**96**	**155**	**90**
10 min	A_1 (rel.)	0.10	0.25	0.15	0.19	0.15	0.28
	τ_1 [ns]	48	29	47	40	86	39
	A_2 (rel.)	0.90	0.75	0.85	0.81	0.85	0.72
	τ_2 [ns]	161	160	81	101	129	89
	b_2	0.64	0.76	0.61	0.69	0.66	0.77
	τ_{Av} **[ns]**	**207**	**149**	**110**	**113**	**160**	**86**
20 min	A_1 (rel.)	0.15	0.27	0.18	0.15	0.12	0.33
	τ_1 [ns]	91	36	51	38	61	37
	A_2 (rel.)	0.85	0.73	0.82	0.85	0.88	0.67
	τ_2 [ns]	229	168	121	94	120	80
	b_2	0.75	0.77	0.68	0.78	0.67	0.77
	τ_{Av} **[ns]**	**247**	**154**	**139**	**98**	**146**	**75**

Table A.3: Fit results using equation 6.3 for the **dark** PL regions (see Figure 6.10). Example fits are shown in Figure A.16. The values for τ_{Av} (equation 6.5) are bolded and plotted in Figure 6.12. Errors are omitted for better readability.

Fit parameters/y	2.97	2.99	3.00	3.01	3.03	3.05
0 min A_1 (rel.)	0.45	0.30	0.24	0.66	0.55	0.40
τ_1 [ns]	26	17	13	17	28	41
A_2 (rel.)	0.55	0.70	0.76	0.34	0.45	0.60
τ_2 [ns]	38	28	29	24	42	60
b_2	0.47	0.42	0.43	0.48	0.55	0.62
$\boldsymbol{\tau_{Av}}$ [ns]	**57**	**62**	**63**	**27**	**45**	**69**
5 min A_1 (rel.)	0.34	0.27	0.22	0.32	0.20	0.33
τ_1 [ns]	46	29	28	26	55	33
A_2 (rel.)	0.66	0.73	0.78	0.68	0.80	0.67
τ_2 [ns]	80	44	37	41	63	65
b_2	0.65	0.55	0.48	0.54	0.55	0.74
$\boldsymbol{\tau_{Av}}$ [ns]	**87**	**64**	**67**	**57**	**96**	**64**
10 min A_1 (rel.)	0.14	0.22	0.18	0.31	0.14	0.35
τ_1 [ns]	66	37	36	33	47	31
A_2 (rel.)	0.86	0.78	0.82	0.69	0.86	0.65
τ_2 [ns]	103	52	48	58	84	68
b_2	0.61	0.58	0.54	0.62	0.62	0.76
$\boldsymbol{\tau_{Av}}$ [ns]	**139**	**72**	**74**	**67**	**111**	**62**
20 min A_1 (rel.)	0.20	0.23	0.17	0.21	0.14	0.37
τ_1 [ns]	73	45	30	37	55	32
A_2 (rel.)	0.80	0.77	0.83	0.79	0.86	0.63
τ_2 [ns]	165	76	70	62	77	59
b_2	0.73	0.65	0.62	0.73	0.60	0.73
$\boldsymbol{\tau_{Av}}$ [ns]	**185**	**90**	**89**	**68**	**10**	**57**

B. Appendix

Modified Williamson-Hall method for microstrain estimation [86]

Broadening and shifts in the XRD peak can be caused by either a reduction in the grain size (Scherrer broadening) and/or non-uniform strain (microstrain). Scherrer broadening will only be significant when the grains are in the range of or less than 100 nm. Strain is the relative change in size of an object with respect to its ideal size (or size before experiencing an external force). The microstrain in a crystalline material is a result of small fluctuations in the lattice spacing, induced by crystal imperfections/structural defects including dislocations, vacancies, stacking faults, interstitials, twinning, and grain boundaries.[1,2,3] By simply considering Braggs law for scattering of light of wavelength λ, $n\lambda = 2d\sin\theta$, it is clear that small fluctuations in d (i.e. Δd) will result in small fluctuations, or broadening, in θ when measuring the X-ray diffraction from the material. We quantify the extent of microstrain in our perovskite crystals by analysing the peak broadening in the diffraction patterns according to the modified Williamson-Hall method.[2,4] The effective observed d-space broadening (Δd_{obs}) determined from the XRD peak width broadening, is a convoluted function of the Gaussian full width half maximum broadening in the 2θ scan due to the instrument response (Δd_{ins}), the grain size (Δd_{size}) and the microstrain (Δd_{ϵ}). These can be de-convoluted from the observed broadening, via,

$$\Delta d_{obs}^2 = \Delta d_{\epsilon}^2 + \Delta d_{ins}^2 + \Delta d_{size}^2 \tag{B.1}$$

where the unit-less microstrain ϵ is defined as $\epsilon = (\Delta d_{\epsilon}/d)$, where d is the mean d-spacing. For single crystals, the size effect induced peak width broadening can be neglected, hence if $\Delta d_{size}^2 \ll \Delta d_{obs}^2$ and we can write:

$$(\Delta d_{obs}^2 - \Delta d_{ins}^2)^{1/2} \approx \epsilon d \tag{B.2}$$

Therefore, the slope of $(\Delta d_{obs}^2 - \Delta d_{ins}^2)^{1/2}$ versus d, gives the magnitude of the microstrain, ϵ, in the crystals.

References:
1. Robinson, I. Harder, R. Coherent X-ray diffraction imaging of strain at the nanoscale. Nat. Mater. 8, 291–8 (2009).
2. A. Pramanick, X. P. Wang, C. Hoffmann, S. O. Diallo, M. R. V. Jørgensen, X.-L. W. Microdomain dynamics in single-crystal BaTiO3 during paraelectric-ferroelectric

phase transition measured with time-of-flight neutron scattering. Phys. Rev. B 92, 174103 (2015). 3. Williamson, G. Hall, W. . X-ray line broadening from filed aluminium and wolfram. Acta Metall. 1, 22–31 (1953).

4. Zhao, Y. Zhang, J. Microstrain and grain-size analysis from diffraction peak width and graphical derivation of high-pressure thermomechanics. J. Appl. Crystallogr. 41, 1095–1108 (2008).

Bibliography

[1] Earth System Research Laboratory - Trends in Atmospheric Carbon Dioxide (accessed September 2018): https://www.esrl.noaa.gov/gmd/ccgg/trends/full.html, 2018.

[2] NASA GISS Surface Temperature Analysis (accessed September 2018): https://data.giss.nasa.gov/gistemp/graphs/.

[3] United Nations Climate Change - The Paris Agreement, https://unfccc.int/process-and-meetings/the-paris-agreement/the-paris-agreement, 2015.

[4] BP Statistical review on world primary energy (accessed September 2018): https://www.bp.com/content/dam/bp/en/corporate/pdf/energy-economics/statistical-review/bp-stats-review-2018-primary-energy.pdf.

[5] Fraunhofer ISE Energy Chart (accessed September 2018): https://www.energy-charts.de/energy_pie.htm.

[6] BP Statistical review on world electricity (accessed September 2018): https://www.bp.com/en/global/corporate/energy-economics/statistical-review-of-world-energy/electricity.html.

[7] MPI für Plasmaphysik: Kernfusion - Stand & Perspektiven (accessed September 2018): https://www.ipp.mpg.de/46293/fusion_d.pdf, 2018.

[8] SolarPowerEurope: Global Market Outlook For Solar Power / 2018 - 2022 (accessed September 2018): http://www.solarpowereurope.org/wp-content/uploads/2018/09/Global-Market-Outlook-2018-2022.pdf, 2018.

[9] World Energy Council: World Energy Scenarios - Composing energy futures to 2050 (accessed September 2018): https://www.worldenergy.org/wp-content/uploads/2013/09/World-Energy-Scenarios_Composing-energy-futures-to-2050_Full-report.pdf, 2013.

[10] B. O'Regan and M. Grätzel, "A low-cost, high-efficiency solar cell based on dye-sensitized colloidal TiO2 films", Nature **353**, 737–740 (1991).

[11] A. Kojima, K. Teshima, Y. Shirai, and T. Miyasaka, "Organometal Halide Perovskites as Visible-Light Sensitizers for Photovoltaic Cells", Journal of the American Chemical Society **131**, 6050–6051 (2009).

[12] H.-S. Kim, C.-R. Lee, J.-H. Im, K.-B. Lee, T. Moehl, A. Marchioro, S.-J. Moon, R. Humphry-Baker, J.-H. Yum, J. E. Moser, M. Grätzel, and N.-G. Park, "Lead Iodide Perovskite Sensitized All-Solid-State Submicron Thin Film Mesoscopic Solar Cell with Efficiency Exceeding 9%", Scientific Reports **2**, 591 (2012).

[13] M. M. Lee, J. Teuscher, T. Miyasaka, T. N. Murakami, and H. J. Snaith, "Efficient Hybrid Solar Cells Based on Meso-Superstructured Organometal Halide Perovskites", Science **338**, 643–647 (2012).

[14] Research Cell Efficiency Records (accessed September 2018): `https://www.nrel.gov/pv/assets/pdfs/pv-efficiencies-07-17-2018.pdf`.

[15] W. S. Yang, B.-W. Park, E. H. Jung, N. J. Jeon, Y. C. Kim, D. U. Lee, S. S. Shin, J. Seo, E. K. Kim, J. H. Noh, and S. I. Seok, "Iodide management in formamidinium-lead-halide – based perovskite layers for efficient solar cells", Science **356**, 1376–1379 (2017).

[16] T. M. Brenner, D. A. Egger, L. Kronik, G. Hodes, and D. Cahen, "Hybrid organic-inorganic perovskites: low-cost semiconductors with intriguing charge-transport properties", Nature Reviews Materials, 16011 (2016).

[17] M. Saliba, J. P. Correa-Baena, M. Grätzel, A. Hagfeldt, and A. Abate, "Perovskite Solar Cells: From the Atomic Level to Film Quality and Device Performance", Angewandte Chemie - International Edition **57**, 2554–2569 (2018).

[18] Z. Li, T. R. Klein, D. H. Kim, M. Yang, J. J. Berry, M. F. Van Hest, and K. Zhu, "Scalable fabrication of perovskite solar cells", Nature Reviews Materials **3**, 1–20 (2018).

[19] F. Di Giacomo, A. Fakharuddin, R. Jose, and T. M. Brown, "Progress, challenges and perspectives in flexible perovskite solar cells", Energy Environ. Sci. **9**, 3007–3035 (2016).

[20] T. Leijtens, K. A. Bush, R. Prasanna, and M. D. McGehee, "Opportunities and challenges for tandem solar cells using metal halide perovskite semiconductors", Nature Energy, 10.1038/s41560–018–0190–4 (2018).

[21] Q. Shan, J. Song, Y. Zou, J. Li, L. Xu, J. Xue, Y. Dong, B. Han, J. Chen, and H. Zeng, "High Performance Metal Halide Perovskite Light-Emitting Diode: From Material Design to Device Optimization", Small **1701770**, 1701770 (2017).

[22] N. K. Kumawat, D. Gupta, and D. Kabra, "Recent Advances in Metal Halide-Based Perovskite Light-Emitting Diodes", Energy Technology **5**, 1734–1749 (2017).

[23] S. D. Stranks, R. L. Z. Hoye, D. Di, R. H. Friend, and F. Deschler, "The Physics of Light Emission in Halide Perovskite Devices", Advanced Materials **Early view**, 1803336 (2018).

[24] W. Tian, H. Zhou, and L. Li, "Hybrid Organic-Inorganic Perovskite Photodetectors", Small **1702107**, 1702107 (2017).

[25] A. R. B. Mohd Yusoff, P. Gao, and M. K. Nazeeruddin, "Recent progress in organohalide lead perovskites for photovoltaic and optoelectronic applications", Coordination Chemistry Reviews (2017) 10.1016/j.ccr.2017.10.021.

[26] Y. Zhang, J. Liu, Z. Wang, Y. Xue, Q. Ou, L. Polavarapu, J. Zheng, X. Qi, and Q. Bao, "Synthesis, properties, and optical applications of low-dimensional perovskites", Chem. Commun. **52**, 13637–13655 (2016).

[27] Y.-H. Lin, P. Pattanasattayavong, and T. D. Anthopoulos, "Metal-Halide Perovskite Transistors for Printed Electronics: Challenges and Opportunities", Advanced Materials **29**, 1702838 (2017).

[28] X. Liu, D. Yu, X. Song, and H. Zeng, "Metal Halide Perovskites: Synthesis, Ion Migration, and Application in Field-Effect Transistors", Small, 1801460 (2018).

[29] J. Choi, J. S. Han, K. Hong, S. Y. Kim, and H. W. Jang, "Organic-Inorganic Hybrid Halide Perovskites for Memories, Transistors, and Artificial Synapses", Advanced Materials, 1704002 (2018).

[30] Oxford PV News: Oxford PV leads consortium to prepare perovskite solar cells for high volume manufacturing (accessed October 2018): https://www.oxfordpv.com/news/oxford-pv-leads-consortium-prepare-perovskite-solar-cells-high-volume-manufacturing.

[31] A. Djurišić, F. Liu, H. Tam, M. Wong, A. Ng, C. Surya, W. Chen, and Z. He, "Perovskite solar cells - An overview of critical issues", Progress in Quantum Electronics **53**, 1–37 (2017).

[32] M. I. H. Ansari, A. Qurashi, and M. K. Nazeeruddin, "Frontiers, opportunities, and challenges in perovskite solar cells: A critical review", Journal of Photochemistry and Photobiology C: Photochemistry Reviews **35**, 1–24 (2018).

[33] A. Senocrate, I. Moudrakovski, G. Y. Kim, T.-Y. Yang, G. Gregori, M. Grätzel, and J. Maier, "The Nature of Ion Conduction in Methylammonium Lead Iodide: A Multimethod Approach", Angewandte Chemie International Edition **56**, 7755–7759 (2017).

[34] G. Y. Kim, A. Senocrate, T.-y. Yang, G. Gregori, M. Grätzel, and J. Maier, "Large tunable photoeffect on ion conduction in halide perovskites and implications for photodecomposition", Nature Materials **17**, 445–450 (2018).

[35] E. L. Unger, E. T. Hoke, C. D. Bailie, W. H. Nguyen, A. R. Bowring, T. Heumüller, M. G. Christoforo, and M. D. McGehee, "Hysteresis and transient behavior in current–voltage measurements of hybrid-perovskite absorber solar cells", Energy Environ. Sci. **7**, 3690–3698 (2014).

[36] Y. Yuan and J. Huang, "Ion Migration in Organometal Trihalide Perovskite and Its Impact on Photovoltaic Efficiency and Stability", Accounts of Chemical Research **49**, 286–293 (2016).

[37] W. Tress, "Metal Halide Perovskites as Mixed Electronic–Ionic Conductors: Challenges and Opportunities—From Hysteresis to Memristivity", The Journal of Physical Chemistry Letters **8**, 3106–3114 (2017).

[38] J. Yang and T. L. Kelly, "Decomposition and Cell Failure Mechanisms in Lead Halide Perovskite Solar Cells", Inorganic Chemistry **56**, 92–101 (2017).

[39] M. I. Asghar, J. Zhang, H. Wang, and P. D. Lund, "Device stability of perovskite solar cells – A review", Renewable and Sustainable Energy Reviews **77**, 131–146 (2017).

[40] K. Brinkmann, J. Zhao, N. Pourdavoud, T. Becker, T. Hu, S. Olthof, K. Meerholz, L. Hoffmann, T. Gahlmann, R. Heiderhoff, M. F. Oszajca, N. A. Luechinger, D. Rogalla, Y. Chen, B. Cheng, and T. Riedl, "Suppressed decomposition of organometal halide perovskites by impermeable electron-extraction layers in inverted solar cells", Nature Communications **8**, 13938 (2017).

[41] J. Huang, S. Tan, P. D. Lund, and H. Zhou, "Impact of H_2O on organic–inorganic hybrid perovskite solar cells", Energy & Environmental Science **10**, 2284–2311 (2017).

[42] N. Aristidou, I. Sanchez-Molina, T. Chotchuangchutchaval, M. Brown, L. Martinez, T. Rath, and S. A. Haque, "The Role of Oxygen in the Degradation of Methylammonium Lead Trihalide Perovskite Photoactive Layers", Angewandte Chemie International Edition **54**, 8208–8212 (2015).

[43] S.-W. Lee, S. Kim, S. Bae, K. Cho, T. Chung, L. E. Mundt, S. Lee, S. Park, H. Park, M. C. Schubert, S. W. Glunz, Y. Ko, Y. Jun, Y. Kang, H.-S. Lee, and D. Kim, "UV Degradation and Recovery of Perovskite Solar Cells", Scientific Reports **6**, 38150 (2016).

[44] S. I. Seok, M. Grätzel, and N.-G. Park, "Methodologies toward Highly Efficient Perovskite Solar Cells", Small **14**, 1704177 (2018).

[45] K. Yan, M. Long, T. Zhang, Z. Wei, H. Chen, S. Yang, and J. Xu, "Hybrid Halide Perovskite Solar Cell Precursors: Colloidal Chemistry and Coordination Engineering behind Device Processing for High Efficiency", Journal of the American Chemical Society **137**, 4460–4468 (2015).

[46] J. Bisquert, *The Physics of Solar Cells* (CRC Press, 2018).

[47] D. Heimfarth, "Exploring zone-casting: A scalable deposition technique for perovskite solar cells", Master's thesis (Heidelberg University, 2018).

[48] D. Leibold, "New Acceptor Molecules for Bulk Heterojunction Organic Solar Cells", Master's thesis (Heidelberg University, 2017).

[49] L. C. Hirst and N. J. Ekins-Daukes, "Fundamental losses in solar cells", Progress in Photovoltaics: Research and Applications **19**, 286–293 (2011).

[50] L. Schmidt-Mende and J. Wecikert, *Organic and Hybrid Solar Cells* (De Gruyter, 2016).

[51] A. Dodabalapur, L. Torsi, H. E. Katz, A. Callegari, and J. M. Shaw, "Organic-Inorganic Hybrid Materials as Semiconductong Channels in Thin-Film Field-Effect Transistors", Science **268**, 270–271 (1995).

[52] J. G. Bednorz and K. A. Mueller, "Possible high Tc superconductivity in the Ba-La-Cu-O system", Zeitschrift fur Physik B Condensed Matter **64**, 189–193 (1986).

[53] D. B. Mitzi, "Templating and structural engineering in organic-inorganic perovskites", Journal of the Chemical Society, Dalton Transactions, 1–12 (2001).

[54] G. Kieslich, S. Sun, and A. K. Cheetham, "Solid-state principles applied to organic–inorganic perovskites: new tricks for an old dog", Chem. Sci. **5**, 4712–4715 (2014).

[55] J. S. Manser, J. A. Christians, and P. V. Kamat, "Intriguing Optoelectronic Properties of Metal Halide Perovskites", Chemical Reviews **116**, 12956–13008 (2016).

[56] W. Travis, E. N. K. Glover, H. Bronstein, D. O. Scanlon, and R. G. Palgrave, "On the application of the tolerance factor to inorganic and hybrid halide perovskites: a revised system", Chemical Science **7**, 4548–4556 (2016).

[57] S. Negele, "Photoluminescence Quantum Efficiency of Organic-Inorganic Lead Halide Perovskite under Different Environmental Influences (Bachelor thesis)", Bachelor's thesis (Heidelberg University, 2016).

[58] M. T. Weller, O. J. Weber, P. F. Henry, A. M. Di Pumpo, and T. C. Hansen, "Complete structure and cation orientation in the perovskite photovoltaic methylammonium lead iodide between 100 and 352 K", Chemical Communications **51**, 4180–4183 (2015).

[59] Z. Xiao and Y. Yan, "Progress in Theoretical Study of Metal Halide Perovskite Solar Cell Materials", Advanced Energy Materials **7**, 1701136 (2017).

[60] P. S. Whitfield, N. Herron, W. E. Guise, K. Page, Y. Q. Cheng, I. Milas, and M. K. Crawford, "Structures, Phase Transitions and Tricritical Behavior of the Hybrid Perovskite Methyl Ammonium Lead Iodide", Scientific Reports **6** (2016) 10.1038/srep35685.

[61] G. Schuck, D. M. Többens, M. Koch-Müller, I. Efthimiopoulos, and S. Schorr, "Infrared Spectroscopic Study of Vibrational Modes across the Orthorhombic–Tetragonal Phase Transition in Methylammonium Lead Halide Single Crystals", The Journal of Physical Chemistry C **122**, 5227–5237 (2018).

[62] S. Singh, C. Li, F. Panzer, K. L. Narasimhan, A. Graeser, T. P. Gujar, A. Köhler, M. Thelakkat, S. Huettner, and D. Kabra, "Effect of Thermal and Structural Disorder on the Electronic Structure of Hybrid Perovskite Semiconductor CH3NH3PbI3", Journal of Physical Chemistry Letters **7**, 3014–3021 (2016).

[63] M. I. Dar, G. Jacopin, S. Meloni, A. Mattoni, N. Arora, A. Boziki, S. M. Zakeeruddin, U. Rothlisberger, and M. Gra tzel, "Origin of unusual bandgap shift and dual emission in organic-inorganic lead halide perovskites", Science Advances **2**, e1601156–e1601156 (2016).

[64] W. Huang, S. Yue, Y. Liu, L. Zhu, P. Jin, Q. Wu, Y. Zhang, Y. Chen, K. Liu, P. Liang, S. Qu, Z. Wang, and Y. Chen, "Observation of Unusual Optical Band Structure of CH3NH3PbI3 Perovskite Single Crystal", ACS Photonics **5**, 1583–1590 (2018).

[65] N. P. Gallop, O. Selig, G. Giubertoni, H. J. Bakker, Y. L. A. Rezus, J. M. Frost, T. L. C. Jansen, R. Lovrincic, and A. A. Bakulin, "Rotational Cation Dynamics in Metal-Halide Perovskites: Effect on Phonons and Material Properties", The Journal of Physical Chemistry Letters, acs.jpclett.8b02227 (2018).

[66] G. P. Nagabhushana, R. Shivaramaiah, and A. Navrotsky, "Direct calorimetric verification of thermodynamic instability of lead halide hybrid perovskites", Proceedings of the National Academy of Sciences **113**, 7717–7721 (2016).

[67] Z. Li, M. Yang, J.-S. Park, S.-H. Wei, J. J. Berry, and K. Zhu, "Stabilizing Perovskite Structures by Tuning Tolerance Factor: Formation of Formamidinium and Cesium Lead Iodide Solid-State Alloys", Chemistry of Materials **28**, 284–292 (2016).

[68] T. Leijtens, K. Bush, R. Cheacharoen, R. Beal, A. Bowring, and M. D. McGehee, "Towards enabling stable lead halide perovskite solar cells; interplay between structural, environmental, and thermal stability", J. Mater. Chem. A **5**, 11483–11500 (2017).

[69] J.-W. Lee, D.-H. Kim, H.-S. Kim, S.-W. Seo, S. M. Cho, and N.-G. Park, "Formamidinium and Cesium Hybridization for Photo- and Moisture-Stable Perovskite Solar Cell", Advanced Energy Materials **5**, 1501310 (2015).

[70] L. Etgar, "The merit of perovskite's dimensionality; can this replace the 3D halide perovskite?", Energy Environ. Sci. **11**, 234–242 (2018).

[71] J. Hu, L. Yan, and W. You, "Two-Dimensional Organic-Inorganic Hybrid Perovskites: A New Platform for Optoelectronic Applications", Advanced Materials **Early view**, 1802041 (2018).

[72] R. E. Brandt, V. Stevanovic, D. S. Ginley, and T. Buonassisi, "Identifying defect-tolerant semiconductors with high minority-carrier lifetimes: Beyond hybrid lead halide perovskites", MRS Communications **5**, 265–275 (2015).

[73] V. Adinolfi, W. Peng, G. Walters, O. M. Bakr, and E. H. Sargent, "The Electrical and Optical Properties of Organometal Halide Perovskites Relevant to Optoelectronic Performance", Advanced Materials **30**, 1700764 (2018).

[74] H. Huang, M. I. Bodnarchuk, S. V. Kershaw, M. V. Kovalenko, and A. L. Rogach, "Lead Halide Perovskite Nanocrystals in the Research Spotlight: Stability and Defect Tolerance", ACS Energy Letters **2**, 2071–2083 (2017).

[75] Z. Yang, A. Surrente, K. Galkowski, N. Bruyant, D. K. Maude, A. A. Haghighirad, H. J. Snaith, P. Plochocka, and R. J. Nicholas, "Unraveling the Exciton Binding Energy and the Dielectric Constant in Single-Crystal Methylammonium Lead Triiodide Perovskite", The Journal of Physical Chemistry Letters **8**, 1851–1855 (2017).

[76] A. Mahboubi Soufiani, Z. Yang, T. Young, A. Miyata, A. Surrente, A. Pascoe, K. Galkowski, M. Abdi-Jalebi, R. Brenes, J. Urban, N. Zhang, V. Bulović, O. Portugall, Y.-B. Cheng, R. J. Nicholas, A. Ho-Baillie, M. A. Green, P. Plochocka, and S. D. Stranks, "Impact of microstructure on the electron–hole interaction in lead halide perovskites", Energy Environ. Sci. **10**, 1358–1366 (2017).

[77] G. Grancini, A. R. Srimath Kandada, J. M. Frost, A. J. Barker, M. De Bastiani, M. Gandini, S. Marras, G. Lanzani, A. Walsh, and A. Petrozza, "Role of microstructure in the electron-hole interaction of hybrid lead halide perovskites", Nature Photonics **9**, 695–701 (2015).

[78] M. E. Ziffer, J. C. Mohammed, and D. S. Ginger, "Electroabsorption Spectroscopy Measurements of the Exciton Binding Energy, Electron–Hole Reduced Effective Mass, and Band Gap in the Perovskite CH3NH3PbI3", ACS Photonics **3**, 1060–1068 (2016).

[79] P. Umari, E. Mosconi, and F. De Angelis, "Infrared Dielectric Screening Determines the Low Exciton Binding Energy of Metal-Halide Perovskites", The Journal of Physical Chemistry Letters **9**, 620–627 (2018).

[80] M. Sendner, P. K. Nayak, D. A. Egger, S. Beck, C. Müller, B. Epding, W. Kowalsky, L. Kronik, H. J. Snaith, A. Pucci, and R. Lovrinčić, "Optical phonons in methylammonium lead halide perovskites and implications for charge transport", Materials Horizons **3**, 613–620 (2016).

[81] K. Galkowski, A. Mitioglu, A. Miyata, P. Plochocka, O. Portugall, G. E. Eperon, J. T.-W. Wang, T. Stergiopoulos, S. D. Stranks, H. J. Snaith, and R. J. Nicholas, "Determination of the exciton binding energy and effective masses for methylammonium and formamidinium lead tri-halide perovskite semiconductors", Energy & Environmental Science **9**, 962–970 (2016).

[82] S. Hunklinger, *Festkörperphysik* (De Gruyter, Berlin, Boston, Dec. 2017).

[83] F. Brivio, K. T. Butler, A. Walsh, and M. van Schilfgaarde, "Relativistic quasiparticle self-consistent electronic structure of hybrid halide perovskite photovoltaic absorbers", Physical Review B **89**, 155204 (2014).

[84] S. De Wolf, J. Holovsky, S.-J. Moon, P. Löper, B. Niesen, M. Ledinsky, F.-J. Haug, J.-H. Yum, and C. Ballif, "Organometallic Halide Perovskites: Sharp Optical Absorption Edge and Its Relation to Photovoltaic Performance", The Journal of Physical Chemistry Letters **5**, 1035–1039 (2014).

[85] S. Shrestha, G. J. Matt, A. Osvet, D. Niesner, R. Hock, and C. J. Brabec, "Assessing Temperature Dependence of Drift Mobility in Methylammonium Lead Iodide Perovskite Single Crystals", The Journal of Physical Chemistry C **122**, 5935–5939 (2018).

[86] J. T.-W. Wang, Z. Wang, S. Pathak, W. Zhang, D. W. DeQuilettes, F. Wisnivesky-Rocca-Rivarola, J. Huang, P. K. Nayak, J. B. Patel, H. A. Mohd Yusof, Y. Vaynzof, R. Zhu, I. Ramirez, J. Zhang, C. Ducati, C. Grovenor, M. B. Johnston, D. S. Ginger, R. J. Nicholas, and H. J. Snaith, "Efficient perovskite solar cells by metal ion doping", Energy Environ. Sci. **9**, 2892–2901 (2016).

[87] M. A. Steiner, J. F. Geisz, I. García, D. J. Friedman, A. Duda, and S. R. Kurtz, "Optical enhancement of the open-circuit voltage in high quality GaAs solar cells", Journal of Applied Physics **113**, 123109 (2013).

[88] J. H. Noh, S. H. Im, J. H. Heo, T. N. Mandal, and S. I. Seok, "Chemical Management for Colorful, Efficient, and Stable Inorganic–Organic Hybrid Nanostructured Solar Cells", Nano Letters **13**, 1764–1769 (2013).

[89] T. Jesper Jacobsson, J.-P. Correa-Baena, M. Pazoki, M. Saliba, K. Schenk, M. Grätzel, and A. Hagfeldt, "Exploration of the compositional space for mixed lead halogen perovskites for high efficiency solar cells", Energy & Environmental Science **9**, 1706–1724 (2016).

[90] R. Prasanna, A. Gold-Parker, T. Leijtens, B. Conings, A. Babayigit, H.-G. Boyen, M. F. Toney, and M. D. McGehee, "Band Gap Tuning via Lattice Contraction and Octahedral Tilting in Perovskite Materials for Photovoltaics", Journal of the American Chemical Society **139**, 11117–11124 (2017).

[91] Z. Xiao, W. Meng, J. Wang, D. B. Mitzi, and Y. Yan, "Searching for promising new perovskite-based photovoltaic absorbers: the importance of electronic dimensionality", Materials Horizons **4**, 206–216 (2017).

[92] S. D. Stranks, S. D. Stranks, G. E. Eperon, G. Grancini, C. Menelaou, M. J. P. Alcocer, T. Leijtens, L. M. Herz, A. Petrozza, and H. J. Snaith, "Electron-Hole Diffusion Lengths Exceeding 1 Micrometer in an Organimetal Trihalide Perovskite Absorber", Science **342**, 341–344 (2014).

[93] Y. Chen, H. T. Yi, X. Wu, R. Haroldson, Y. N. Gartstein, Y. I. Rodionov, K. S. Tikhonov, A. Zakhidov, X. .-.-Y. Zhu, and V. Podzorov, "Extended carrier lifetimes and diffusion in hybrid perovskites revealed by Hall effect and photoconductivity measurements", Nature Communications **7**, 12253 (2016).

[94] Q. Dong, Y. Fang, Y. Shao, P. Mulligan, J. Qiu, L. Cao, and J. Huang, "Electron-hole diffusion lengths > 175 um in solution-grown CH3NH3PbI3 single crystals", Science **347**, 967–970 (2015).

[95] W.-j. Yin, T. Shi, and Y. Yan, "Unusual defect physics in CH3NH3PbI3 perovskite solar cell absorber", Applied Physics Letters **104**, 063903 (2014).

[96] A. Walsh and A. Zunger, "Instilling defect tolerance in new compounds", Nature Materials **16**, 964–967 (2017).

[97] C. Ran, J. Xu, W. Gao, C. Huang, and S. Dou, "Defects in metal triiodide perovskite materials towards high-performance solar cells: origin, impact, characterization, and engineering", Chemical Society Reviews **47**, 4581–4610 (2018).

[98] J. S. Park, S. Kim, Z. Xie, and A. Walsh, "Point defect engineering in thin-film solar cells", Nature Reviews Materials **3**, 194–210 (2018).

[99] B. G. Gribov and K. V. Zinov'ev, "Preparation of High-Purity Silicon for Solar Cells", Inorganic Materials **39**, 653–662 (2003).

[100] G. Coletti, "Sensitivity of state-of-the-art and high efficiency crystalline silicon solar cells to metal impurities", Progress in Photovoltaics: Research and Applications **21**, n/a–n/a (2012).

[101] A. Walsh, D. O. Scanlon, S. Chen, X. G. Gong, and S. H. Wei, "Self-regulation mechanism for charged point defects in hybrid halide perovskites", Angewandte Chemie - International Edition **54**, 1791–1794 (2015).

[102] D. Meggiolaro, S. Motti, E. Mosconi, A. Barker, J. Ball, C. A. R. Perini, F. Deschler, A. Petrozza, and F. De Angelis, "Iodine chemistry determines the defect tolerance of lead-halide perovskites", Energy & Environmental Science **11**, 702–713 (2018).

[103] W. J. Yin, T. Shi, and Y. Yan, "Unique properties of halide perovskites as possible origins of the superior solar cell performance", Advanced Materials **26**, 4653–4658 (2014).

[104] M.-H. Du, "Density Functional Calculations of Native Defects in CH3NH3Pb3: Effects of Spin–Orbit Coupling and Self-Interaction Error", The Journal of Physical Chemistry Letters **6**, 1461–1466 (2015).

[105] A. Buin, P. Pietsch, J. Xu, O. Voznyy, A. H. Ip, R. Comin, and E. H. Sargent, "Materials Processing Routes to Trap-Free Halide Perovskites", Nano Letters **14**, 6281–6286 (2014).

[106] Q. Wang, Y. Shao, H. Xie, L. Lyu, X. Liu, Y. Gao, and J. Huang, "Qualifying composition dependent p and n self-doping in CH3NH3PbI3", Applied Physics Letters **105**, 163508 (2014).

[107] F. De Angelis and A. Petrozza, "Clues from defect photochemistry", Nature Materials **17**, 383–384 (2018).

[108] J. Xu, A. Buin, A. H. Ip, W. Li, O. Voznyy, R. Comin, M. Yuan, S. Jeon, Z. Ning, J. J. McDowell, P. Kanjanaboos, J. P. Sun, X. Lan, L. N. Quan, D. H. Kim, I. G. Hill, P. Maksymovych, and E. H. Sargent, "Perovskite-fullerene hybrid materials suppress hysteresis in planar diodes", Nature Communications **6** (2015) 10.1038/ncomms8081.

[109] J. M. Ball and A. Petrozza, "Defects in perovskite-halides and their effects in solar cells", Nature Energy **1**, 16149 (2016).

[110] H. Tan, F. Che, M. Wei, Y. Zhao, M. I. Saidaminov, P. Todorović, D. Broberg, G. Walters, F. Tan, T. Zhuang, B. Sun, Z. Liang, H. Yuan, E. Fron, J. Kim, Z. Yang, O. Voznyy, M. Asta, and E. H. Sargent, "Dipolar cations confer defect tolerance in wide-bandgap metal halide perovskites", Nature Communications **9**, 3100 (2018).

[111] J. M. Frost, "Calculating polaron mobility in halide perovskites", Physical Review B **96**, 195202 (2017).

[112] A. D. Wright, C. Verdi, R. L. Milot, G. E. Eperon, M. A. Pérez-Osorio, H. J. Snaith, F. Giustino, M. B. Johnston, and L. M. Herz, "Electron–phonon coupling in hybrid lead halide perovskites", Nature Communications **7**, 11755 (2016).

[113] A. M. Leguy, A. R. Goñi, J. M. Frost, J. Skelton, F. Brivio, X. Rodríguez-Martínez, O. J. Weber, A. Pallipurath, M. I. Alonso, M. Campoy-Quiles, M. T. Weller, J. Nelson, A. Walsh, and P. R. Barnes, "Dynamic disorder, phonon lifetimes, and the assignment of modes to the vibrational spectra of methylammonium lead halide perovskites", Physical Chemistry Chemical Physics **18**, 27051–27066 (2016).

[114] H. Zhu, K. Miyata, Y. Fu, J. Wang, P. P. Joshi, D. Niesner, K. W. Williams, S. Jin, and X.-. Y. Zhu, "Screening in crystalline liquids protects energetic carriers in hybrid perovskites", Science **353**, 1409–1413 (2016).

[115] K. Miyata, D. Meggiolaro, M. T. Trinh, P. P. Joshi, E. Mosconi, S. C. Jones, F. De Angelis, and X.-Y. Zhu, "Large polarons in lead halide perovskites", Science Advances **3**, e1701217 (2017).

[116] K. Miyata, T. L. Atallah, and X.-Y. Zhu, "Lead halide perovskites: Crystal-liquid duality, phonon glass electron crystals, and large polaron formation", Science Advances **3**, e1701469 (2017).

[117] F. Ambrosio, J. Wiktor, F. De Angelis, and A. Pasquarello, "Origin of low electron–hole recombination rate in metal halide perovskites", Energy & Environmental Science **11**, 101–105 (2018).

[118] K. Miyata and X.-Y. Zhu, "Ferroelectric large polarons", Nature Materials **17**, 379–381 (2018).

[119] I. Anusca, S. Balčiūnas, P. Gemeiner, Š. Svirskas, M. Sanlialp, G. Lackner, C. Fettkenhauer, J. Belovickis, V. Samulionis, M. Ivanov, B. Dkhil, J. Banys, V. V. Shvartsman, and D. C. Lupascu, "Dielectric Response: Answer to Many Questions in the Methylammonium Lead Halide Solar Cell Absorbers", Advanced Energy Materials **7**, 1700600 (2017).

[120] L. M. Herz, "Charge-Carrier Dynamics in Organic-Inorganic Metal Halide Perovskites", Annual Review of Physical Chemistry **67**, 65–89 (2016).

[121] J. Fu, Q. Xu, G. Han, B. Wu, C. H. A. Huan, M. L. Leek, and T. C. Sum, "Hot carrier cooling mechanisms in halide perovskites", Nature Communications **8**, 1300 (2017).

[122] J. Yang, X. Wen, H. Xia, R. Sheng, Q. Ma, J. Kim, P. Tapping, T. Harada, T. T. W. Kee, F. Huang, Y.-B. Cheng, M. A. Green, A. W. Y. Ho-Baillie, S. Huang, S. Shrestha, R. Patterson, and G. J. Conibeer, "Acoustic-optical phonon up-conversion and hot-phonon bottleneck in lead-halide perovskites", Nature Communications **8**, 14120 (2017).

[123] J. M. Frost, L. D. Whalley, and A. Walsh, "Slow Cooling of Hot Polarons in Halide Perovskite Solar Cells", ACS Energy Letters **2**, 2647–2652 (2017).

[124] S. A. Bretschneider, F. Laquai, and M. Bonn, "Trap-Free Hot Carrier Relaxation in Lead–Halide Perovskite Films", The Journal of Physical Chemistry C **121**, 11201–11206 (2017).

[125] H. Hayashi, H. Inaba, M. Matsuyama, N. Lan, M. Dokiya, and H. Tagawa, "Structural consideration on the ionic conductivity of perovskite-type oxides", Solid State Ionics **122**, 1–15 (1999).

[126] J. M. Frost and A. Walsh, "What Is Moving in Hybrid Halide Perovskite Solar Cells?", Accounts of Chemical Research **49**, 528–535 (2016).

[127] A. Walsh and S. D. Stranks, "Taking Control of Ion Transport in Halide Perovskite Solar Cells", ACS Energy Letters **3**, 1983–1990 (2018).

[128] Z. Xiao, Y. Yuan, Y. Shao, Q. Wang, Q. Dong, C. Bi, P. Sharma, A. Gruverman, and J. Huang, "Giant switchable photovoltaic effect in organometal trihalide perovskite devices", Nature Materials **14**, 193–198 (2015).

[129] D. W. DeQuilettes, W. Zhang, V. M. Burlakov, D. J. Graham, T. Leijtens, A. Osherov, V. Bulović, H. J. Snaith, D. S. Ginger, and S. D. Stranks, "Photo-induced halide redistribution in organic–inorganic perovskite films", Nature Communications **7**, 11683 (2016).

[130] E. T. Hoke, D. J. Slotcavage, E. R. Dohner, A. R. Bowring, H. I. Karunadasa, and M. D. McGehee, "Reversible photo-induced trap formation in mixed-halide hybrid perovskites for photovoltaics", Chemical Science **6**, 613–617 (2015).

[131] C. Eames, J. M. Frost, P. R. Barnes, B. C. O'Regan, A. Walsh, and M. S. Islam, "Ionic transport in hybrid lead iodide perovskite solar cells", Nature Communications **6**, 2–9 (2015).

[132] J. M. Azpiroz, E. Mosconi, J. Bisquert, and F. De Angelis, "Defect migration in methylammonium lead iodide and its role in perovskite solar cell operation", Energy Environ. Sci. **8**, 2118–2127 (2015).

[133] P. Delugas, C. Caddeo, A. Filippetti, and A. Mattoni, "Thermally Activated Point Defect Diffusion in Methylammonium Lead Trihalide: Anisotropic and Ultrahigh Mobility of Iodine", Journal of Physical Chemistry Letters **7**, 2356–2361 (2016).

[134] D. Meggiolaro, E. Mosconi, and F. De Angelis, "Modeling the Interaction of Molecular Iodine with MAPbI3: A Probe of Lead-Halide Perovskites Defect Chemistry", ACS Energy Letters **3**, 447–451 (2018).

[135] D. Barboni and R. A. De Souza, "The thermodynamics and kinetics of iodine vacancies in the hybrid perovskite methylammonium lead iodide", Energy & Environmental Science, doi: 10.1039/C8EE01697F (2018).

[136] T.-Y. Yang, G. Gregori, N. Pellet, M. Grätzel, and J. Maier, "The Significance of Ion Conduction in a Hybrid Organic-Inorganic Lead-Iodide-Based Perovskite Photosensitizer", Angewandte Chemie International Edition **54**, 7905–7910 (2015).

[137] Y. Yuan, J. Chae, Y. Shao, Q. Wang, Z. Xiao, A. Centrone, and J. Huang, "Photovoltaic Switching Mechanism in Lateral Structure Hybrid Perovskite Solar Cells", Advanced Energy Materials 5, 1500615 (2015).

[138] Y.-C. Zhao, W.-K. Zhou, X. Zhou, K.-H. Liu, D.-P. Yu, and Q. Zhao, "Quantification of light-enhanced ionic transport in lead iodide perovskite thin films and its solar cell applications", Light: Science & Applications 6, e16243 (2016).

[139] A. Senocrate, I. Moudrakovski, T. Acartürk, R. Merkle, G. Y. Kim, U. Starke, M. Grätzel, and J. Maier, "Slow CH3NH3+ Diffusion in CH3NH3PbI3 under Light Measured by Solid-State NMR and Tracer Diffusion", The Journal of Physical Chemistry C, acs.jpcc.8b06814 (2018).

[140] D. Walter, A. Fell, Y. Wu, T. Duong, C. Barugkin, N. Wu, T. White, and K. Weber, "Transient Photovoltage in Perovskite Solar Cells: Interaction of Trap-Mediated Recombination and Migration of Multiple Ionic Species", The Journal of Physical Chemistry C 122, 11270–11281 (2018).

[141] O. Hentz, P. Rekemeyer, and S. Gradečak, "Effects of Voltage Biasing on Current Extraction in Perovskite Solar Cells", Advanced Energy Materials 8, 1701378 (2018).

[142] S. N. Habisreutinger, N. K. Noel, and H. J. Snaith, "Hysteresis Index: A Figure without Merit for Quantifying Hysteresis in Perovskite Solar Cells", ACS Energy Letters, 2472–2476 (2018).

[143] E. J. Juarez-Perez, R. S. Sanchez, L. Badia, G. Garcia-Belmonte, Y. S. Kang, I. Mora-Sero, and J. Bisquert, "Photoinduced Giant Dielectric Constant in Lead Halide Perovskite Solar Cells", The Journal of Physical Chemistry Letters 5, 2390–2394 (2014).

[144] B. Chen, M. Yang, S. Priya, and K. Zhu, "Origin of J − V Hysteresis in Perovskite Solar Cells", The Journal of Physical Chemistry Letters 7, 905–917 (2016).

[145] J. Carrillo, A. Guerrero, S. Rahimnejad, O. Almora, I. Zarazua, E. Mas-Marza, J. Bisquert, and G. Garcia-Belmonte, "Ionic Reactivity at Contacts and Aging of Methylammonium Lead Triiodide Perovskite Solar Cells", Advanced Energy Materials 6, 1502246 (2016).

[146] A. Guerrero, A. Bou, G. Matt, O. Almora, T. Heumüller, G. Garcia-Belmonte, J. Bisquert, Y. Hou, and C. Brabec, "Switching Off Hysteresis in Perovskite Solar Cells by Fine-Tuning Energy Levels of Extraction Layers", Advanced Energy Materials 8, 1703376 (2018).

[147] P. Lopez-Varo, J. A. Jiménez-Tejada, M. García-Rosell, J. A. Anta, S. Ravishankar, A. Bou, and J. Bisquert, "Effects of Ion Distributions on Charge Collection in Perovskite Solar Cells", ACS Energy Letters 2, 1450–1453 (2017).

[148] D. A. Jacobs, Y. Wu, H. Shen, C. Barugkin, F. J. Beck, T. P. White, K. Weber, and K. R. Catchpole, "Hysteresis phenomena in perovskite solar cells: the many and varied effects of ionic accumulation", Phys. Chem. Chem. Phys. 19, 3094–3103 (2017).

[149] M. T. Neukom, S. Züfle, E. Knapp, M. Makha, R. Hany, and B. Ruhstaller, "Why perovskite solar cells with high efficiency show small IV-curve hysteresis", Solar Energy Materials and Solar Cells **169**, 159–166 (2017).

[150] S. Weber, I. M. Hermes, S. H. Turren Cruz, C. Gort, V. W. Bergmann, L. Gilson, A. Hagfeldt, M. Grätzel, W. Tress, and R. Berger, "How the Formation of Interfacial Charge Causes Hysteresis in Perovskite Solar Cells", Energy & Environmental Science, Advance Article, DOI: 10.1039/C8EE01447G (2018).

[151] Y. Rong, Y. Hu, S. Ravishankar, H. Liu, X. Hou, Y. Sheng, A. Mei, Q. Wang, D. Li, M. Xu, J. Bisquert, and H. Han, "Tunable hysteresis effect for perovskite solar cells", Energy & Environmental Science **10**, 2383–2391 (2017).

[152] X. Zheng, B. Chen, J. Dai, Y. Fang, Y. Bai, Y. Lin, H. Wei, X. C. Zeng, and J. Huang, "Defect passivation in hybrid perovskite solar cells using quaternary ammonium halide anions and cations", Nature Energy **2**, 17102 (2017).

[153] M. Stolterfoht, C. M. Wolff, J. A. Márquez, S. Zhang, C. J. Hages, D. Rothhardt, S. Albrecht, P. L. Burn, P. Meredith, T. Unold, and D. Neher, "Visualization and suppression of interfacial recombination for high-efficiency large-area pin perovskite solar cells", Nature Energy, doi: 10.1038/s41560–018–0219–8 (2018).

[154] C. Wang, C. Xiao, Y. Yu, D. Zhao, R. A. Awni, C. R. Grice, K. Ghimire, D. Constantinou, W. Liao, A. J. Cimaroli, P. Liu, J. Chen, N. J. Podraza, C. S. Jiang, M. M. Al-Jassim, X. Zhao, and Y. Yan, "Understanding and Eliminating Hysteresis for Highly Efficient Planar Perovskite Solar Cells", Advanced Energy Materials **7**, 1700414 (2017).

[155] J. M. Richter, M. Abdi-Jalebi, A. Sadhanala, M. Tabachnyk, J. P. Rivett, L. M. Pazos-Outón, K. C. Gödel, M. Price, F. Deschler, and R. H. Friend, "Enhancing photoluminescence yields in lead halide perovskites by photon recycling and light out-coupling", Nature Communications **7**, 13941 (2016).

[156] S. P. Senanayak, B. Yang, T. H. Thomas, N. Giesbrecht, W. Huang, E. Gann, B. Nair, K. Goedel, S. Guha, X. Moya, C. R. McNeill, P. Docampo, A. Sadhanala, R. H. Friend, and H. Sirringhaus, "Understanding charge transport in lead iodide perovskite thin-film field-effect transistors", Science Advances **3**, e1601935 (2017).

[157] A. M. Zeidell, C. Tyznik, L. Jennings, C. Zhang, H. Lee, M. Guthold, Z. V. Vardeny, and O. D. Jurchescu, "Enhanced Charge Transport in Hybrid Perovskite Field-Effect Transistors via Microstructure Control", Advanced Electronic Materials, 1800316 (2018).

[158] J. Li, Q. Dong, N. Li, and L. Wang, "Direct Evidence of Ion Diffusion for the Silver-Electrode-Induced Thermal Degradation of Inverted Perovskite Solar Cells", Advanced Energy Materials **7**, 1602922 (2017).

[159] S. Kim, S. Bae, S.-W. Lee, K. Cho, K. D. Lee, H. Kim, S. Park, G. Kwon, S.-W. Ahn, H.-M. Lee, Y. Kang, H.-S. Lee, and D. Kim, "Relationship between ion migration and interfacial degradation of CH3NH3PbI3 perovskite solar cells under thermal conditions", Scientific Reports **7**, 1200 (2017).

[160] D.-Y. Son, S.-G. Kim, J.-Y. Seo, S.-H. Lee, H. Shin, D. Lee, and N.-G. Park, "Universal Approach toward Hysteresis-Free Perovskite Solar Cell via Defect Engineering", Journal of the American Chemical Society **140**, 1358–1364 (2018).

[161] M. Abdi-Jalebi, Z. Andaji-Garmaroudi, S. Cacovich, C. Stavrakas, B. Philippe, J. M. Richter, M. Alsari, E. P. Booker, E. M. Hutter, A. J. Pearson, S. Lilliu, T. J. Savenije, H. Rensmo, G. Divitini, C. Ducati, R. H. Friend, and S. D. Stranks, "Maximizing and stabilizing luminescence from halide perovskites with potassium passivation", Nature **555**, 497 (2018).

[162] J. Cao, S. X. Tao, P. A. Bobbert, C. P. Wong, and N. Zhao, "Interstitial Occupancy by Extrinsic Alkali Cations in Perovskites and Its Impact on Ion Migration", Advanced Materials **30**, 1707350 (2018).

[163] T. Bu, X. Liu, Y. Zhou, J. Yi, X. Huang, L. Luo, J. Xiao, Z. Ku, Y. Peng, F. Huang, Y. B. Cheng, and J. Zhong, "A novel quadruple-cation absorber for universal hysteresis elimination for high efficiency and stable perovskite solar cells", Energy & Environmental Science **10**, 2509–2515 (2017).

[164] A. Polman and H. A. Atwater, "Photonic design principles for ultrahigh-efficiency photovoltaics", Nature Materials **11**, 174–177 (2012).

[165] O. D. Miller, E. Yablonovitch, and S. R. Kurtz, "Strong Internal and External Luminescence as Solar Cells Approach the Shockley–Queisser Limit", IEEE Journal of Photovoltaics **2**, 303–311 (2012).

[166] J. M. Ball, S. D. Stranks, M. T. Hörantner, S. Hüttner, W. Zhang, E. J. W. Crossland, I. Ramirez, M. Riede, M. B. Johnston, R. H. Friend, and H. J. Snaith, "Optical properties and limiting photocurrent of thin-film perovskite solar cells", Energy & Environmental Science **8**, 602–609 (2015).

[167] L. M. Pazos-Outon, M. Szumilo, R. Lamboll, J. M. Richter, M. Crespo-Quesada, M. Abdi-Jalebi, H. J. Beeson, M. Vru ini, M. Alsari, H. J. Snaith, B. Ehrler, R. H. Friend, and F. Deschler, "Photon recycling in lead iodide perovskite solar cells", Science **351**, 1430–1433 (2016).

[168] U. Rau, U. W. Paetzold, and T. Kirchartz, "Thermodynamics of light management in photovoltaic devices", Physical Review B **90**, 035211 (2014).

[169] D. W. Dequilettes, S. Koch, S. Burke, R. K. Paranji, A. J. Shropshire, M. E. Ziffer, and D. S. Ginger, "Photoluminescence Lifetimes Exceeding 8 μs and Quantum Yields Exceeding 30% in Hybrid Perovskite Thin Films by Ligand Passivation", ACS Energy Letters **1**, 438–444 (2016).

[170] D. W. DeQuilettes, S. Jariwala, S. Burke, M. E. Ziffer, J. T. Wang, H. J. Snaith, and D. S. Ginger, "Tracking Photoexcited Carriers in Hybrid Perovskite Semiconductors: Trap-Dominated Spatial Heterogeneity and Diffusion", ACS Nano **11**, 11488–11496 (2017).

[171] S. Draguta, S. Thakur, Y. V. Morozov, Y. Wang, J. S. Manser, P. V. Kamat, and M. Kuno, "Spatially Non-uniform Trap State Densities in Solution-Processed Hybrid Perovskite Thin Films", Journal of Physical Chemistry Letters **7**, 715–721 (2016).

[172] H. Uratani and K. Yamashita, "Charge Carrier Trapping at Surface Defects of Perovskite Solar Cell Absorbers: A First-Principles Study", Journal of Physical Chemistry Letters **8**, 742–746 (2017).

[173] I. L. Braly, D. W. Dequilettes, L. M. Pazos-Outón, S. Burke, M. E. Ziffer, D. S. Ginger, and H. W. Hillhouse, "Hybrid perovskite films approaching the radiative limit with over 90% photoluminescence quantum efficiency", Nature Photonics **12**, 355–361 (2018).

[174] S. D. Stranks, "Nonradiative Losses in Metal Halide Perovskites", ACS Energy Letters **2**, 1515–1525 (2017).

[175] M. Liu, M. B. Johnston, and H. J. Snaith, "Efficient planar heterojunction perovskite solar cells by vapour deposition", Nature **501**, 395–398 (2013).

[176] J.-Y. Jeng, Y.-F. Chiang, M.-H. Lee, S.-R. Peng, T.-F. Guo, P. Chen, and T.-C. Wen, "CH3NH3PbI3 Perovskite/Fullerene Planar-Heterojunction Hybrid Solar Cells", Advanced Materials **25**, 3727–3732 (2013).

[177] P. Docampo, J. M. Ball, M. Darwich, G. E. Eperon, and H. J. Snaith, "Efficient organometal trihalide perovskite planar-heterojunction solar cells on flexible polymer substrates", Nature Communications **4**, 2761 (2013).

[178] Z. Zhao, W. Sun, Y. Li, S. Ye, H. Rao, F. Gu, Z. Liu, Z. Bian, and C. Huang, "Simplification of device structures for low-cost, high-efficiency perovskite solar cells", J. Mater. Chem. A **5**, 4756–4773 (2017).

[179] F. Giordano, A. Abate, J. P. Correa Baena, M. Saliba, T. Matsui, S. H. Im, S. M. Zakeeruddin, M. K. Nazeeruddin, A. Hagfeldt, and M. Graetzel, "Enhanced electronic properties in mesoporous TiO2 via lithium doping for high-efficiency perovskite solar cells", Nature Communications **7**, 10379 (2016).

[180] Q. Jiang, L. Zhang, H. Wang, X. Yang, J. Meng, H. Liu, Z. Yin, J. Wu, X. Zhang, and J. You, "Enhanced electron extraction using SnO2 for high-efficiency planar-structure HC(NH2)2PbI3-based perovskite solar cells", Nature Energy **2**, 16177 (2016).

[181] E. H. Anaraki, A. Kermanpur, L. Steier, K. Domanski, T. Matsui, W. Tress, M. Saliba, A. Abate, M. Grätzel, A. Hagfeldt, and J.-P. Correa-Baena, "Highly efficient and stable planar perovskite solar cells by solution-processed tin oxide", Energy Environ. Sci. **9**, 3128–3134 (2016).

[182] Q. Jiang, X. Zhang, and J. You, "SnO2: A Wonderful Electron Transport Layer for Perovskite Solar Cells", Small **14**, 1801154 (2018).

[183] P. Zhang, J. Wu, T. Zhang, Y. Wang, D. Liu, H. Chen, L. Ji, C. Liu, W. Ahmad, Z. D. Chen, and S. Li, "Perovskite Solar Cells with ZnO Electron-Transporting Materials", Advanced Materials **30**, 1703737 (2018).

[184] Z. Hawash, L. K. Ono, and Y. Qi, "Recent Advances in Spiro-MeOTAD Hole Transport Material and Its Applications in Organic–Inorganic Halide Perovskite Solar Cells", Advanced Materials Interfaces **5**, 1700623 (2018).

[185] M. Saliba, T. Matsui, K. Domanski, J.-Y. Seo, A. Ummadisingu, S. M. Zakeeruddin, J.-P. Correa-Baena, W. R. Tress, A. Abate, A. Hagfeldt, and M. Grätzel, "Incorporation of rubidium cations into perovskite solar cells improves photovoltaic performance", Science **354**, 206–209 (2016).

[186] T. Liu, K. Chen, Q. Hu, R. Zhu, and Q. Gong, "Inverted Perovskite Solar Cells: Progresses and Perspectives", Advanced Energy Materials **6**, 1600457 (2016).

[187] Y. Bai, X. Meng, and S. Yang, "Interface Engineering for Highly Efficient and Stable Planar p-i-n Perovskite Solar Cells", Advanced Energy Materials **8**, 1701883 (2018).

[188] X. Yin, P. Chen, M. Que, Y. Xing, W. Que, C. Niu, and J. Shao, "Highly Efficient Flexible Perovskite Solar Cells Using Solution-Derived NiOx Hole Contacts", ACS Nano **10**, 3630–3636 (2016).

[189] Y. Hou, W. Chen, D. Baran, T. Stubhan, N. A. Luechinger, B. Hartmeier, M. Richter, J. Min, S. Chen, C. O. R. Quiroz, N. Li, H. Zhang, T. Heumueller, G. J. Matt, A. Osvet, K. Forberich, Z. G. Zhang, Y. Li, B. Winter, P. Schweizer, E. Spiecker, and C. J. Brabec, "Overcoming the Interface Losses in Planar Heterojunction Perovskite-Based Solar Cells", Advanced Materials **28**, 5112–5120 (2016).

[190] W. Chen, F. Z. Liu, X. Y. Feng, A. B. Djurišić, W. K. Chan, and Z. B. He, "Cesium Doped NiOx as an Efficient Hole Extraction Layer for Inverted Planar Perovskite Solar Cells", Advanced Energy Materials **7**, 1700722 (2017).

[191] C. Bi, Q. Wang, Y. Shao, Y. Yuan, Z. Xiao, and J. Huang, "Non-wetting surface-driven high-aspect-ratio crystalline grain growth for efficient hybrid perovskite solar cells", Nature Communications **6**, 7747 (2015).

[192] C. M. Wolff, F. Zu, A. Paulke, L. P. Toro, N. Koch, and D. Neher, "Reduced Interface-Mediated Recombination for High Open-Circuit Voltages in CH3NH3PbI3 Solar Cells", Advanced Materials **29**, 1700159 (2017).

[193] M. Stolterfoht, C. M. Wolff, Y. Amir, A. Paulke, L. Perdigon-Toro, P. Caprioglio, D. Neher, L. Perdigón-Toro, P. Caprioglio, and D. Neher, "Approaching the fill factor Shockley-Queisser limit in stable, dopant-free triple cation perovskite solar cells", Energy Environ. Sci. **10**, 1530–1539 (2017).

[194] Q. Zhang, B. Kan, F. Liu, G. Long, X. Wan, X. Chen, Y. Zuo, W. Ni, H. Zhang, M. Li, Z. Hu, F. Huang, Y. Cao, Z. Liang, M. Zhang, T. P. Russell, and Y. Chen, "Small-molecule solar cells with efficiency over 9%", Nature Photonics **9**, 35–41 (2014).

[195] W. Nie, H. Tsai, R. Asadpour, J.-C. Blancon, A. J. Neukirch, G. Gupta, J. J. Crochet, M. Chhowalla, S. Tretiak, M. A. Alam, H.-L. Wang, and A. D. Mohite, "High-efficiency solution-processed perovskite solar cells with millimeter-scale grains", Science **347**, 522–525 (2015).

[196] H. Kim, K.-G. Lim, and T.-W. Lee, "Planar heterojunction organometal halide perovskite solar cells: roles of interfacial layers", Energy Environ. Sci. **9**, 12–30 (2016).

[197] S. Ahn, S. H. Jeong, T. H. Han, and T. W. Lee, "Conducting Polymers as Anode Buffer Materials in Organic and Perovskite Optoelectronics", Advanced Optical Materials **5**, 1600512 (2017).

[198] K. Tvingstedt, L. Gil-Escrig, C. Momblona, P. Rieder, D. Kiermasch, M. Sessolo, A. Baumann, H. J. Bolink, and V. Dyakonov, "Removing Leakage and Surface Recombination in Planar Perovskite Solar Cells", ACS Energy Letters, 424–430 (2017).

[199] T. Liu, F. Jiang, F. Qin, W. Meng, Y. Jiang, S. Xiong, J. Tong, Z. Li, Y. Liu, and Y. Zhou, "Nonreduction-Active Hole-Transporting Layers Enhancing Open-Circuit Voltage and Efficiency of Planar Perovskite Solar Cells", ACS Applied Materials and Interfaces **8**, 33899–33906 (2016).

[200] W. Nie, H. Tsai, J. C. Blancon, F. Liu, C. C. Stoumpos, B. Traore, M. Kepenekian, O. Durand, C. Katan, S. Tretiak, J. Crochet, P. M. Ajayan, M. Kanatzidis, J. Even, and A. D. Mohite, "Critical Role of Interface and Crystallinity on the Performance and Photostability of Perovskite Solar Cell on Nickel Oxide", Advanced Materials **30**, 1703879 (2018).

[201] W. Nie, J. C. Blancon, A. J. Neukirch, K. Appavoo, H. Tsai, M. Chhowalla, M. A. Alam, M. Y. Sfeir, C. Katan, J. Even, S. Tretiak, J. J. Crochet, G. Gupta, and A. D. Mohite, "Light-activated photocurrent degradation and self-healing in perovskite solar cells", Nature Communications **7**, 11574 (2016).

[202] Z. Chuantian and D. Liming, "Modified PEDOT Layer Makes a 1.52 V Voc for Perovskite/PCBM Solar Cells", Advanced Energy Materials **7**, 1601193 (2016).

[203] O. Malinkiewicz, C. Roldán-Carmona, A. Soriano, E. Bandiello, L. Camacho, M. K. Nazeeruddin, and H. J. Bolink, "Metal-Oxide-Free Methylammonium Lead Iodide Perovskite-Based Solar Cells: the Influence of Organic Charge Transport Layers", Advanced Energy Materials **4**, 1400345 (2014).

[204] C. Momblona, O. Malinkiewicz, C. Roldán-Carmona, A. Soriano, L. Gil-Escrig, E. Bandiello, M. Scheepers, E. Edri, and H. J. Bolink, "Efficient methylammonium lead iodide perovskite solar cells with active layers from 300 to 900 nm", APL Materials **2** (2014) 10.1063/1.4890056.

[205] O. Malinkiewicz, A. Yella, Y. H. Lee, G. M. Espallargas, M. Graetzel, M. K. Nazeeruddin, and H. J. Bolink, "Perovskite solar cells employing organic charge-transport layers", Nature Photonics **8**, 128–132 (2014).

[206] D. Zhao, M. Sexton, H. Y. Park, G. Baure, J. C. Nino, and F. So, "High-efficiency solution-processed planar perovskite solar cells with a polymer hole transport layer", Advanced Energy Materials **5**, 1401855 (2015).

[207] Y. Cheng, X. Xu, Y. Xie, H.-W. Li, J. Qing, C. Ma, C.-S. Lee, F. So, and S.-W. Tsang, "18% High-Efficiency Air-Processed Perovskite Solar Cells Made in a Humid Atmosphere of 70% RH", Solar RRL **1700097**, 1700097 (2017).

[208] L. Zhao, J. Gao, Y. L. Lin, Y. W. Yeh, K. M. Lee, N. Yao, Y. L. Loo, and B. P. Rand, "Electrical Stress Influences the Efficiency of CH3NH3PbI3 Perovskite Light Emitting Devices", Advanced Materials **29**, 1605317 (2017).

[209] Z. Xiao, R. A. Kerner, L. Zhao, N. L. Tran, K. M. Lee, T. W. Koh, G. D. Scholes, and B. P. Rand, "Efficient perovskite light-emitting diodes featuring nanometre-sized crystallites", Nature Photonics **11**, 108–115 (2017).

[210] S. Zhang, M. Stolterfoht, A. Armin, Q. Lin, F. Zu, J. Sobus, H. Jin, N. Koch, P. Meredith, P. L. Burn, and D. Neher, "Interface Engineering of Solution-Processed Hybrid Organohalide Perovskite Solar Cells", ACS Applied Materials & Interfaces **10**, 21681–21687 (2018).

[211] X. Xu, C. Ma, Y. Cheng, Y. M. Xie, X. Yi, B. Gautam, S. Chen, H. W. Li, C. S. Lee, F. So, and S. W. Tsang, "Ultraviolet-ozone surface modification for non-wetting hole transport materials based inverted planar perovskite solar cells with efficiency exceeding 18%", Journal of Power Sources **360**, 157–165 (2017).

[212] Z. Yu, L. Zhang, S. Tian, F. Zhang, B. Zhang, F. Niu, P. Zeng, J. Qu, P. N. Rudd, J. Huang, and J. Lian, "Hot-Substrate Deposition of Hole- and Electron-Transport Layers for Enhanced Performance in Perovskite Solar Cells", Advanced Energy Materials **8**, 1701659 (2018).

[213] J. Lee, H. Kang, G. Kim, H. Back, J. Kim, S. Hong, B. Park, E. Lee, and K. Lee, "Achieving Large-Area Planar Perovskite Solar Cells by Introducing an Interfacial Compatibilizer", Advanced Materials **29**, 1606363 (2017).

[214] M. Alsari, A. J. Pearson, J. T.-W. Wang, Z. Wang, A. Montisci, N. C. Greenham, H. J. Snaith, S. Lilliu, and R. H. Friend, "Degradation Kinetics of Inverted Perovskite Solar Cells", Scientific Reports **8**, 5977 (2018).

[215] L. Kegelmann, C. M. Wolff, C. A. Omondi, F. Lang, E. L. Unger, L. Korte, T. Dittrich, D. Neher, B. Rech, and S. Albrecht, "It takes two to tango – double-layer selective contacts in perovskite solar cells for improved device performance and reduced hysteresis", ACS Applied Materials & Interfaces, acsami.7b00900 (2017).

[216] Y. Shao, Z. Xiao, C. Bi, Y. Yuan, and J. Huang, "Origin and elimination of photocurrent hysteresis by fullerene passivation in CH3NH3PbI3 planar heterojunction solar cells", Nature Communications **5**, 5784 (2014).

[217] J. H. Heo, H. J. Han, D. Kim, T. K. Ahn, and S. H. Im, "Hysteresis-less inverted CH3NH3PbI3 planar perovskite hybrid solar cells with 18.1% power conversion efficiency", Energy Environ. Sci. **8**, 1602–1608 (2015).

[218] Y. Zhao, W. Zhou, W. Ma, S. Meng, H. Li, J. Wei, R. Fu, K. Liu, D. Yu, and Q. Zhao, "Correlations between Immobilizing Ions and Suppressing Hysteresis in Perovskite Solar Cells", ACS Energy Letters **1**, 266–272 (2016).

[219] M. De Bastiani, G. Dell'Erba, M. Gandini, V. D'Innocenzo, S. Neutzner, A. R. S. Kandada, G. Grancini, M. Binda, M. Prato, J. M. Ball, M. Caironi, and A. Petrozza, "Ion Migration and the Role of Preconditioning Cycles in the Stabilization of the J-V Characteristics of Inverted Hybrid Perovskite Solar Cells", Advanced Energy Materials **6**, 1501453 (2016).

[220] C. Park, H. Ko, D. H. Sin, K. C. Song, and K. Cho, "Organometal Halide Perovskite Solar Cells with Improved Thermal Stability via Grain Boundary Passivation Using a Molecular Additive", Advanced Functional Materials **27**, 1703546 (2017).

[221] C.-T. Lin, S. Pont, J. Kim, T. Du, S. Xu, X. Li, D. Bryant, M. A. Mclachlan, and J. R. Durrant, "Passivation against oxygen and light induced degradation by the PCBM electron transport layer in planar perovskite solar cells", Sustainable Energy & Fuels **Advance Ar** (2018) 10.1039/C8SE00095F.

[222] F. Huang, A. R. Pascoe, W. Q. Wu, Z. Ku, Y. Peng, J. Zhong, R. A. Caruso, and Y. B. Cheng, "Effect of the Microstructure of the Functional Layers on the Efficiency of Perovskite Solar Cells", Advanced Materials **29**, 1601715 (2017).

[223] F. Mathies, H. Eggers, B. S. Richards, G. Hernandez-Sosa, U. Lemmer, and U. W. Paetzold, "Inkjet-Printed Triple Cation Perovskite Solar Cells", ACS Applied Energy Materials **1**, 1834–1839 (2018).

[224] Y. Deng, X. Zheng, Y. Bai, Q. Wang, J. Zhao, and J. Huang, "Surfactant-controlled ink drying enables high-speed deposition of perovskite films for efficient photovoltaic modules", Nature Energy **3**, 560–566 (2018).

[225] K. Hwang, Y. S. Jung, Y. J. Heo, F. H. Scholes, S. E. Watkins, J. Subbiah, D. J. Jones, D. Y. Kim, and D. Vak, "Toward large scale roll-to-roll production of fully printed perovskite solar cells", Advanced Materials **27**, 1241–1247 (2015).

[226] J. Ávila, C. Momblona, P. P. Boix, M. Sessolo, and H. J. Bolink, "Vapor-Deposited Perovskites: The Route to High-Performance Solar Cell Production?", Joule **1**, 431–442 (2017).

[227] Y. Chen, M. He, J. Peng, Y. Sun, and Z. Liang, "Structure and Growth Control of Organic-Inorganic Halide Perovskites for Optoelectronics: From Polycrystalline Films to Single Crystals", Advanced Science **3**, 1500392 (2016).

[228] J.-H. Im, I.-H. Jang, N. Pellet, M. Grätzel, and N.-G. Park, "Growth of CH3NH3PbI3 cuboids with controlled size for high-efficiency perovskite solar cells", Nature Nanotechnology **9**, 927–932 (2014).

[229] N. J. Jeon, J. H. Noh, Y. C. Kim, W. S. Yang, S. Ryu, and S. I. Seok, "Solvent engineering for high-performance inorganic-organic hybrid perovskite solar cells", Nature Materials **13**, 897–903 (2014).

[230] R. J. Stewart, C. Grieco, A. V. Larsen, G. S. Doucette, and J. B. Asbury, "Molecular Origins of Defects in Organohalide Perovskites and Their Influence on Charge Carrier Dynamics", Journal of Physical Chemistry C **120**, 12392–12402 (2016).

[231] D. P. McMeekin, Z. Wang, W. Rehman, F. Pulvirenti, J. B. Patel, N. K. Noel, M. B. Johnston, S. R. Marder, L. M. Herz, and H. J. Snaith, "Crystallization Kinetics and Morphology Control of Formamidinium-Cesium Mixed-Cation Lead Mixed-Halide Perovskite via Tunability of the Colloidal Precursor Solution", Advanced Materials **29**, 1607039 (2017).

[232] F. K. Aldibaja, L. Badia, E. Mas-Marzá, R. S. Sánchez, E. M. Barea, and I. Mora-Sero, "Effect of different lead precursors on perovskite solar cell performance and stability", Journal of Materials Chemistry A **3**, 9194–9200 (2015).

[233] D. P. Nenon, J. A. Christians, L. M. Wheeler, J. L. Blackburn, E. M. Sanehira, B. Dou, M. L. Olsen, K. Zhu, J. J. Berry, and J. M. Luther, "Structural and chemical evolution of methylammonium lead halide perovskites during thermal processing from solution", Energy Environ. Sci. **9**, 2072–2082 (2016).

[234] D. T. Moore, H. Sai, K. W. Tan, D. M. Smilgies, W. Zhang, H. J. Snaith, U. Wiesner, and L. A. Estroff, "Crystallization kinetics of organic-inorganic trihalide perovskites and the role of the lead anion in crystal growth", Journal of the American Chemical Society **137**, 2350–2358 (2015).

[235] Q. Hu, L. Zhao, J. Wu, K. Gao, D. Luo, Y. Jiang, Z. Zhang, C. Zhu, E. Schaible, A. Hexemer, C. Wang, Y. Liu, W. Zhang, M. Grätzel, F. Liu, T. P. Russell, R. Zhu, and Q. Gong, "In situ dynamic observations of perovskite crystallisation and microstructure evolution intermediated from [PbI6]4- cage nanoparticles", Nature Communications **8**, 15688 (2017).

[236] A. A. Petrov, I. P. Sokolova, N. A. Belich, G. S. Peters, P. V. Dorovatovskii, Y. V. Zubavichus, V. N. Khrustalev, A. V. Petrov, M. Grätzel, E. A. Goodilin, and A. B. Tarasov, "Crystal Structure of DMF-Intermediate Phases Uncovers the Link between CH3NH3PbI3 Morphology and Precursor Stoichiometry", Journal of Physical Chemistry C **121**, 20739–20743 (2017).

[237] H. Yu, F. Wang, F. Xie, W. Li, J. Chen, and N. Zhao, "The Role of Chlorine in the Formation Process of "CH 3 NH 3 PbI 3-x Cl x " Perovskite", Advanced Functional Materials **24**, 7102–7108 (2014).

[238] W. Zhang, M. Saliba, D. T. Moore, S. K. Pathak, M. T. Hörantner, T. Stergiopoulos, S. D. Stranks, G. E. Eperon, J. A. Alexander-Webber, A. Abate, A. Sadhanala, S. Yao, Y. Chen, R. H. Friend, L. A. Estroff, U. Wiesner, and H. J. Snaith, "Ultrasmooth organic–inorganic perovskite thin-film formation and crystallization for efficient planar heterojunction solar cells", Nature Communications **6**, 6142 (2015).

[239] A. Sharenko, C. Mackeen, L. Jewell, F. Bridges, and M. F. Toney, "Evolution of Iodoplumbate Complexes in Methylammonium Lead Iodide Perovskite Precursor Solutions", Chemistry of Materials **29**, 1315–1320 (2017).

[240] H. J. Hyuck, S. D. Ho, H. H. Ji, K. S. Yeon, K. J. Ho, K. Dasom, S. H. Won, A. T. Kyu, W. Christoph, L. Tae-Woo, and I. S. Hyuk, "Planar CH3NH3PbI3 Perovskite Solar Cells with Constant 17.2% Average Power Conversion Efficiency Irrespective of the Scan Rate", Advanced Materials **27**, 3424–3430 (2015).

[241] H. Yu, H. Lu, F. Xie, S. Zhou, and N. Zhao, "Native Defect-Induced Hysteresis Behavior in Organolead Iodide Perovskite Solar Cells", Advanced Functional Materials **26**, 1411–1419 (2016).

[242] G. Li, T. Zhang, and Y. Zhao, "Hydrochloric acid accelerated formation of planar CH3NH3PbI3 perovskite with high humidity tolerance", Journal of Materials Chemistry A **3**, 19674–19678 (2015).

[243] Y. Yu, C. Wang, C. R. Grice, N. Shrestha, J. Chen, D. Zhao, W. Liao, A. J. Cimaroli, P. J. Roland, R. J. Ellingson, and Y. Yan, "Improving the Performance of Formamidinium and Cesium Lead Triiodide Perovskite Solar Cells using Lead Thiocyanate Additives", ChemSusChem **9**, 3288–3297 (2016).

[244] W. Ke, C. Xiao, C. Wang, B. Saparov, H. S. Duan, D. Zhao, Z. Xiao, P. Schulz, S. P. Harvey, W. Liao, W. Meng, Y. Yu, A. J. Cimaroli, C. S. Jiang, K. Zhu, M. Al-Jassim, G. Fang, D. B. Mitzi, and Y. Yan, "Employing Lead Thiocyanate Additive to Reduce the Hysteresis and Boost the Fill Factor of Planar Perovskite Solar Cells", Advanced Materials **28**, 5214–5221 (2016).

[245] Y. Sun, J. Peng, Y. Chen, Y. Yao, and Z. Liang, "Triple-cation mixed-halide perovskites: Towards efficient, annealing-free and air-stable solar cells enabled by Pb(SCN) 2 additive", Scientific Reports **7** (2017) 10.1038/srep46193.

[246] C. Wang, D. Zhao, Y. Yu, N. Shrestha, C. R. Grice, W. Liao, A. J. Cimaroli, J. Chen, R. J. Ellingson, X. Zhao, and Y. Yan, "Compositional and morphological engineering of mixed cation perovskite films for highly efficient planar and flexible solar cells with reduced hysteresis", Nano Energy **35**, 223–232 (2017).

[247] Y. Yu, C. Wang, C. R. Grice, N. Shrestha, D. Zhao, W. Liao, L. Guan, R. A. Awni, W. Meng, A. J. Cimaroli, K. Zhu, R. J. Ellingson, and Y. Yan, "Synergistic Effects of Lead Thiocyanate Additive and Solvent Annealing on the Performance of Wide-Bandgap Perovskite Solar Cells", ACS Energy Letters, 1177–1182 (2017).

[248] N. K. Noel, M. Johnston, N. K. Noel, M. Congiu, A. J. Ramadan, S. Fearn, P. David, J. B. Patel, M. B. Johnston, B. Wenger, and H. J. Snaith, "Unveiling the Influence of pH on the Crystallization of Hybrid Perovskite, Delivering Low Voltage Loss Photovoltaics", Joule **1**, 328–343 (2017).

[249] M. Ralaiarisoa, Y. Busby, J. Frisch, I. Salzmann, J.-J. Pireaux, and N. Koch, "Correlation of annealing time with crystal structure, composition, and electronic properties of CH3NH3PbI3-xClx mixed-halide perovskite films", Phys. Chem. Chem. Phys. Phys. Chem. Chem. Phys **19**, 828–836 (2017).

[250] K. H. Stone, A. Gold-Parker, V. L. Pool, E. L. Unger, A. R. Bowring, M. D. McGehee, M. F. Toney, and C. J. Tassone, "Transformation from crystalline precursor to perovskite in PbCl2-derived MAPbI3", Nature Communications **9**, 3458 (2018).

[251] J. Qing, H. T. Chandran, Y. H. Cheng, X. K. Liu, H. W. Li, S. W. Tsang, M. F. Lo, and C. S. Lee, "Chlorine Incorporation for Enhanced Performance of Planar Perovskite Solar Cell Based on Lead Acetate Precursor", ACS Applied Materials and Interfaces 7, 23110–23116 (2015).

[252] H. C. Liao, P. Guo, C. P. Hsu, M. Lin, B. Wang, L. Zeng, W. Huang, C. M. M. Soe, W. F. Su, M. J. Bedzyk, M. R. Wasielewski, A. Facchetti, R. P. Chang, M. G. Kanatzidis, and T. J. Marks, "Enhanced Efficiency of Hot-Cast Large-Area Planar Perovskite Solar Cells/Modules Having Controlled Chloride Incorporation", Advanced Energy Materials 7, 1601660 (2017).

[253] C. Quarti, E. Mosconi, P. Umari, and F. De Angelis, "Chlorine Incorporation in the CH3NH3PbI3 Perovskite: Small Concentration, Big Effect", Inorganic Chemistry 56, 74–83 (2017).

[254] G. Nan, X. Zhang, M. Abdi-Jalebi, Z. Andaji-Garmaroudi, S. D. Stranks, G. Lu, and D. Beljonne, "How Methylammonium Cations and Chlorine Dopants Heal Defects in Lead Iodide Perovskites", Advanced Energy Materials 8, 1702754 (2018).

[255] N. Sakai, Z. Wang, V. M. Burlakov, J. Lim, D. McMeekin, S. Pathak, and H. J. Snaith, "Controlling Nucleation and Growth of Metal Halide Perovskite Thin Films for High-Efficiency Perovskite Solar Cells", Small 13 (2017) 10.1002/smll.201602808.

[256] W. Zhang, S. Pathak, N. Sakai, T. Stergiopoulos, P. K. Nayak, N. K. Noel, A. A. Haghighirad, V. M. Burlakov, D. W. Dequilettes, A. Sadhanala, W. Li, L. Wang, D. S. Ginger, R. H. Friend, and H. J. Snaith, "Enhanced optoelectronic quality of perovskite thin films with hypophosphorous acid for planar heterojunction solar cells", Nature Communications 6, 10030 (2015).

[257] I. Levchuk, Y. Hou, M. Gruber, M. Brandl, P. Herre, X. Tang, F. Hoegl, M. Batentschuk, A. Osvet, R. Hock, W. Peukert, R. R. Tykwinski, and C. J. Brabec, "Deciphering the Role of Impurities in Methylammonium Iodide and Their Impact on the Performance of Perovskite Solar Cells", Advanced Materials Interfaces 3, 1600593 (2016).

[258] S. Bai, N. Sakai, W. Zhang, Z. Wang, J. T.-W. Wang, F. Gao, and H. J. Snaith, "Reproducible Planar Heterojunction Solar Cells Based on One-Step Solution-Processed Methylammonium Lead Halide Perovskites", Chemistry of Materials 29, 462–473 (2017).

[259] J. Seo, S. Park, Y. Chan Kim, N. J. Jeon, J. H. Noh, S. C. Yoon, and S. I. Seok, "Benefits of very thin PCBM and LiF layers for solution-processed p–i–n perovskite solar cells", Energy Environ. Sci. 7, 2642–2646 (2014).

[260] S. Paek, P. Schouwink, E. N. Athanasopoulou, K. T. Cho, G. Grancini, Y. Lee, Y. Zhang, F. Stellacci, M. K. Nazeeruddin, and P. Gao, "From Nano- to Micrometer Scale: The Role of Antisolvent Treatment on High Performance Perovskite Solar Cells", Chemistry of Materials 29, 3490–3498 (2017).

[261] M. Konstantakou, D. Perganti, P. Falaras, and T. Stergiopoulos, "Anti-Solvent Crystallization Strategies for Highly Efficient Perovskite Solar Cells", Crystals **7**, 291 (2017).

[262] P. Gratia, I. Zimmermann, P. Schouwink, J. H. Yum, J. N. Audinot, K. Sivula, T. Wirtz, and M. K. Nazeeruddin, "The Many Faces of Mixed Ion Perovskites: Unraveling and Understanding the Crystallization Process", ACS Energy Letters **2**, 2686–2693 (2017).

[263] K. Bruening and C. J. Tassone, "Antisolvent processing of lead halide perovskite thin films studied by in situ X-ray diffraction", Journal of Materials Chemistry A (2018) 10.1039/C8TA06025H.

[264] N. Pellet, P. Gao, G. Gregori, T.-Y. Yang, M. K. Nazeeruddin, J. Maier, and M. Grätzel, "Mixed-Organic-Cation Perovskite Photovoltaics for Enhanced Solar-Light Harvesting", Angewandte Chemie **126**, 3215–3221 (2014).

[265] D. Bi, W. Tress, M. I. Dar, P. Gao, J. Luo, C. Renevier, K. Schenk, A. Abate, F. Giordano, J.-P. Correa Baena, J.-D. Decoppet, S. M. Zakeeruddin, M. K. Nazeeruddin, M. Grätzel, and A. Hagfeldt, "Efficient luminescent solar cells based on tailored mixed-cation perovskites", Science Advances **2**, e1501170 (2016).

[266] M. Saliba, T. Matsui, J.-Y. Seo, K. Domanski, J.-P. Correa-Baena, M. K. Nazeeruddin, S. M. Zakeeruddin, W. Tress, A. Abate, A. Hagfeldt, and M. Grätzel, "Cesium-containing triple cation perovskite solar cells: improved stability, reproducibility and high efficiency", Energy Environ. Sci. **9**, 1989–1997 (2016).

[267] O. A. Syzgantseva, M. Saliba, M. Grätzel, and U. Rothlisberger, "Stabilization of the Perovskite Phase of Formamidinium Lead Triiodide by Methylammonium, Cs, and/or Rb Doping", Journal of Physical Chemistry Letters **8**, 1191–1196 (2017).

[268] T. Duong, H. K. Mulmudi, H. Shen, Y. L. Wu, C. Barugkin, Y. O. Mayon, H. T. Nguyen, D. Macdonald, J. Peng, M. Lockrey, W. Li, Y. B. Cheng, T. P. White, K. Weber, and K. Catchpole, "Structural engineering using rubidium iodide as a dopant under excess lead iodide conditions for high efficiency and stable perovskites", Nano Energy **30**, 330–340 (2016).

[269] Z. Tang, T. Bessho, F. Awai, T. Kinoshita, M. M. Maitani, R. Jono, T. N. Murakami, H. Wang, T. Kubo, S. Uchida, and H. Segawa, "Hysteresis-free perovskite solar cells made of potassium-doped organometal halide perovskite", Scientific Reports **7**, 12183 (2017).

[270] D. J. Kubicki, D. Prochowicz, A. Hofstetter, P. Péchy, S. M. Zakeeruddin, M. Grätzel, and L. Emsley, "Cation Dynamics in Mixed-Cation (MA)x(FA)1-xPbI3 Hybrid Perovskites from Solid-State NMR", Journal of the American Chemical Society **139**, 10055–10061 (2017).

[271] D. J. Kubicki, D. Prochowicz, A. Hofstetter, S. M. Zakeeruddin, M. Grätzel, and L. Emsley, "Phase Segregation in Potassium-Doped Lead Halide Perovskites from 39 K Solid-State NMR at 21.1 T", Journal of the American Chemical Society **140**, 7232–7238 (2018).

[272] J.-P. Correa-Baena, Y. Luo, T. M. Brenner, J. Snaider, S. Sun, X. Li, M. A. Jensen, L. Nienhaus, S. Wieghold, J. R. Poindexter, S. Wang, Y. S. Meng, T. Wang, B. Lai, M. G. Bawendi, L. Huang, D. P. Fenning, and T. Buonassisi, "Homogenization of Halide Distribution and Carrier Dynamics in Alloyed Organic-Inorganic Perovskites", aRXIV, arXiv:1804.08722v2 (2018).

[273] J. Burschka, N. Pellet, S. J. Moon, R. Humphry-Baker, P. Gao, M. K. Nazeeruddin, and M. Grätzel, "Sequential deposition as a route to high-performance perovskite-sensitized solar cells", Nature **499**, 316–319 (2013).

[274] J.-H. Im, I.-H. Jang, N. Pellet, M. Grätzel, and N.-G. Park, "Growth of CH3NH3PbI3 cuboids with controlled size for high-efficiency perovskite solar cells", Nature Nanotechnology **9**, 927–932 (2014).

[275] Q. Chen, H. Zhou, Z. Hong, S. Luo, H.-s. Duan, H.-h. Wang, Y. Liu, G. Li, and Y. Yang, "Planar Heterojunction Perovskite Solar Cells via Vapor-Assisted Solution Process", Journal of the American Chemical Society **136**, 622–625 (2014).

[276] H. Chen, "Two-Step Sequential Deposition of Organometal Halide Perovskite for Photovoltaic Application", Advanced Functional Materials **27**, 1605654 (2017).

[277] Q. Jiang, Z. Chu, P. Wang, X. Yang, H. Liu, Y. Wang, Z. Yin, J. Wu, X. Zhang, and J. You, "Planar-Structure Perovskite Solar Cells with Efficiency beyond 21%", Advanced Materials **29**, 1703852 (2017).

[278] C. Müller, T. Glaser, M. Plogmeyer, M. Sendner, S. Döring, A. A. Bakulin, C. Brzuska, R. Scheer, M. S. Pshenichnikov, W. Kowalsky, A. Pucci, and R. Lovrinčić, "Water Infiltration in Methylammonium Lead Iodide Perovskite: Fast and Inconspicuous", Chemistry of Materials **27**, 7835–7841 (2015).

[279] G. Rajendra Kumar, A. Dennyson Savariraj, S. N. Karthick, S. Selvam, B. Balamuralitharan, H.-J. Kim, K. K. Viswanathan, M. Vijaykumar, and K. Prabakar, "Phase transition kinetics and surface binding states of methylammonium lead iodide perovskite", Physical Chemistry Chemical Physics **18**, 7284–7292 (2016).

[280] G. E. Eperon, S. N. Habisreutinger, T. Leijtens, B. J. Bruijnaers, J. J. van Franeker, D. W. DeQuilettes, S. Pathak, R. J. Sutton, G. Grancini, and D. S. Ginger, "The importance of moisture in hybrid lead halide perovskite thin film fabrication", ACS nano **9**, 851–9380 (2015).

[281] S. N. Habisreutinger, T. Leijtens, G. E. Eperon, S. D. Stranks, R. J. Nicholas, and H. J. Snaith, "Carbon nanotube/polymer composites as a highly stable hole collection layer in perovskite solar cells", Nano Letters **14**, 5561–5568 (2014).

[282] Z. Hawash, L. K. Ono, and Y. Qi, "Moisture and Oxygen Enhance Conductivity of LiTFSI-Doped Spiro-MeOTAD Hole Transport Layer in Perovskite Solar Cells", Advanced Materials Interfaces **3**, 1600117 (2016).

[283] J. Luo, C. Jia, Z. Wan, F. Han, B. Zhao, and R. Wang, "The novel dopant for hole-transporting material opens a new processing route to efficiently reduce hysteresis and improve stability of planar perovskite solar cells", Journal of Power Sources **342**, 886–895 (2017).

[284] T. Leijtens, T. Giovenzana, S. N. Habisreutinger, J. S. Tinkham, N. K. Noel, B. A. Kamino, G. Sadoughi, A. Sellinger, and H. J. Snaith, "Hydrophobic Organic Hole Transporters for Improved Moisture Resistance in Metal Halide Perovskite Solar Cells", ACS Applied Materials and Interfaces **8**, 5981–5989 (2016).

[285] J. A. Christians, P. Schulz, J. S. Tinkham, T. H. Schloemer, S. P. Harvey, B. J. T. de Villers, A. Sellinger, J. J. Berry, and J. M. Luther, "Tailored interfaces of unencapsulated perovskite solar cells for >1,000 hour operational stability", Nature Energy **3**, 68–74 (2018).

[286] U.-G. Jong, C.-J. Yu, G.-C. Ri, A. P. McMahon, N. M. Harrison, P. R. F. Barnes, and A. Walsh, "Influence of water intercalation and hydration on chemical decomposition and ion transport in methylammonium lead halide perovskites", Journal of Materials Chemistry A **6**, 1067–1074 (2018).

[287] J. A. Christians, P. A. Miranda Herrera, and P. V. Kamat, "Transformation of the excited state and photovoltaic efficiency of CH3NH3PbI3 perovskite upon controlled exposure to humidified air", Journal of the American Chemical Society **137**, 1530–1538 (2015).

[288] J. Yang, B. D. Siempelkamp, D. Liu, and T. L. Kelly, "Investigation of CH3NH3PbI3 degradation rates and mechanisms in controlled humidity environments using in situ techniques", ACS Nano **9**, 1955–1963 (2015).

[289] A. M. Leguy, Y. Hu, M. Campoy-Quiles, M. I. Alonso, O. J. Weber, P. Azarhoosh, M. Van Schilfgaarde, M. T. Weller, T. Bein, J. Nelson, P. Docampo, and P. R. Barnes, "Reversible hydration of CH3NH3PbI3 in films, single crystals, and solar cells", Chemistry of Materials **27**, 3397–3407 (2015).

[290] D. Li, S. A. Bretschneider, V. W. Bergmann, I. M. Hermes, J. Mars, A. Klasen, H. Lu, W. Tremel, M. Mezger, H. J. Butt, S. A. Weber, and R. Berger, "Humidity-Induced Grain Boundaries in MAPbI3 Perovskite Films", Journal of Physical Chemistry C **120**, 6363–6368 (2016).

[291] Z. Song, A. Abate, S. C. Watthage, G. K. Liyanage, A. B. Phillips, U. Steiner, M. Grätzel, and M. J. Heben, "Perovskite Solar Cell Stability in Humid Air: Partially Reversible Phase Transitions in the PbI2-CH3NH3I-H2O System", Advanced Energy Materials **6**, 1600846 (2016).

[292] E. Mosconi, J. M. Azpiroz, and F. De Angelis, "Ab Initio Molecular Dynamics Simulations of Methylammonium Lead Iodide Perovskite Degradation by Water", Chemistry of Materials **27**, 4885–4892 (2015).

[293] J. Schlipf, L. Bießmann, L. Oesinghaus, E. Berger, E. Metwalli, J. A. Lercher, L. Porcar, and P. Müller-Buschbaum, "In Situ Monitoring the Uptake of Moisture into Hybrid Perovskite Thin Films", The Journal of Physical Chemistry Letters 9, 2015–2021 (2018).

[294] Z. Zhu, V. G. Hadjiev, Y. Rong, R. Guo, B. Cao, Z. Tang, F. Qin, Y. Li, Y. Wang, F. Hao, S. Venkatesan, W. Li, S. Baldelli, A. M. Guloy, H. Fang, Y. Hu, Y. Yao, Z. Wang, and J. Bao, "Interaction of Organic Cation with Water Molecule in Perovskite MAPbI3: From Dynamic Orientational Disorder to Hydrogen Bonding", Chemistry of Materials 28, 7385–7393 (2016).

[295] Q. Wang, B. Chen, Y. Liu, Y. Deng, Y. Bai, Q. Dong, and J. Huang, "Scaling behavior of moisture-induced grain degradation in polycrystalline hybrid perovskite thin films", Energy Environ. Sci. 10, 516–522 (2017).

[296] L. Zhao, R. A. Kerner, Z. Xiao, Y. L. Lin, K. M. Lee, J. Schwartz, and B. P. Rand, "Redox Chemistry Dominates the Degradation and Decomposition of Metal Halide Perovskite Optoelectronic Devices", ACS Energy Letters 1, 595–602 (2016).

[297] C. Ma, D. Shen, J. Qing, H. Thachoth Chandran, M.-F. Lo, and C.-S. Lee, "Effects of Small Polar Molecules (MA+ and H2O) on Degradation Processes of Perovskite Solar Cells", ACS Applied Materials & Interfaces 9, 14960–14966 (2017).

[298] D. Bryant, N. Aristidou, S. Pont, I. Sanchez-Molina, T. Chotchunangatchaval, S. Wheeler, J. R. Durrant, and S. A. Haque, "Light and oxygen induced degradation limits the operational stability of methylammonium lead triiodide perovskite solar cells", Energy & Environmental Science 9, 1655–1660 (2016).

[299] A. J. Pearson, G. E. Eperon, P. E. Hopkinson, S. N. Habisreutinger, J. T.-W. Wang, H. J. Snaith, and N. C. Greenham, "Oxygen Degradation in Mesoporous Al 2 O 3 /CH 3 NH 3 PbI 3- x Cl x Perovskite Solar Cells: Kinetics and Mechanisms", Advanced Energy Materials 6, 1600014 (2016).

[300] E. T. Hoke, I. T. Sachs-Quintana, M. T. Lloyd, I. Kauvar, W. R. Mateker, A. M. Nardes, C. H. Peters, N. Kopidakis, and M. D. McGehee, "The Role of Electron Affinity in Determining Whether Fullerenes Catalyze or Inhibit Photooxidation of Polymers for Solar Cells", Advanced Energy Materials 2, 1351–1357 (2012).

[301] B. Rivkin, P. Fassl, Q. Sun, A. D. Taylor, Z. Chen, and Y. Vaynzof, "Effect of Ion Migration-Induced Electrode Degradation on the Operational Stability of Perovskite Solar Cells", ACS Omega 3, 10042–10047 (2018).

[302] N. Aristidou, C. Eames, I. Sanchez-molina, X. Bu, J. Kosco, M. S. Islam, and S. A. Haque, "Fast oxygen diffusion and iodide defects mediate oxygen-induced degradation of perovskite solar cells", Nature Communications 8, 15218 (2017).

[303] A. Senocrate, T. Acartürk, G. Y. Kim, R. Merkle, U. Starke, M. Grätzel, and J. Maier, "Interaction of oxygen with halide perovskites", Journal of Materials Chemistry A 6, 10847–10855 (2018).

[304] N. Aristidou, C. Eames, M. S. Islam, and S. A. Haque, "Insights into the increased degradation rate of CH3NH3PbI3 solar cells in combined water and O2 environments", Journal of Materials Chemistry A **5**, 25469–25475 (2017).

[305] L. Zhang and P. H.-L. H.-L. Sit, "Ab initio study of the role of oxygen and excess electrons in the degradation of CHNH3PbI3", J. Mater. Chem. A **5**, 9042–9049 (2017).

[306] D. Meggiolaro, E. Mosconi, and F. De Angelis, "Mechanism of Reversible Trap Passivation by Molecular Oxygen in Lead-Halide Perovskites", ACS Energy Letters **1**, 2794–2798 (2017).

[307] Q. Chen, H. Zhou, T.-b. Song, S. Luo, and Z. Hong, "Controllable self-induced passivation of hybrid lead iodide perovskites toward high performance solar cells", Nano Letters **14**, 4158–4163 (2014).

[308] D. H. Cao, C. C. Stoumpos, C. D. Malliakas, M. J. Katz, O. K. Farha, J. T. Hupp, and M. G. Kanatzidis, "Remnant PbI2, an unforeseen necessity in high-efficiency hybrid perovskite-based solar cells?", APL Materials **2**, 091101 (2014).

[309] L. Wang, C. Mccleese, A. Kovalsky, Y. Zhao, and C. Burda, "Femtosecond Time-Resolved Transient Absorption Spectroscopy of CH3NH3PbI3 Perovskite Films: Evidence for Passivation Effect of PbI2", Journal of the American Chemical Society **35**, 12205–12208 (2014).

[310] S. Wang, W. Dong, X. Fang, Q. Zhang, S. Zhou, Z. Deng, R. Tao, J. Shao, R. Xia, C. Song, L. Hu, and J. Zhu, "Credible evidence for the passivation effect of remnant PbI3 in CH3NH3PbI3 films in improving the performance of perovskite solar cells", Nanoscale **8**, 6600–6608 (2016).

[311] U. Thakur, U. Kwon, M. M. Hasan, W. Yin, D. Kim, N. Y. Ha, S. Lee, T. K. Ahn, and H. J. Park, "Investigation into the Advantages of Pure Perovskite Film without PbI2 for High Performance Solar Cell", Scientific Reports **6**, 35994 (2016).

[312] F. Liu, Q. Dong, M. K. Wong, A. B. Djurišić, A. Ng, Z. Ren, Q. Shen, C. Surya, W. K. Chan, J. Wang, A. M. C. Ng, C. Liao, H. Li, K. Shih, C. Wei, H. Su, and J. Dai, "Is Excess PbI2 Beneficial for Perovskite Solar Cell Performance?", Advanced Energy Materials **6**, 1502206 (2016).

[313] C. Roldán-Carmona, P. Gratia, I. Zimmermann, G. Grancini, P. Gao, M. Grätzel, and M. K. Nazeeruddin, "High efficiency methylammonium lead triiodide perovskite solar cells: the relevance of non-stoichiometric precursors", Energy Environ. Sci. **8**, 3550–3556 (2015).

[314] Y. C. Kim, N. J. Jeon, J. H. Noh, W. S. Yang, J. Seo, J. S. Yun, A. Ho-Baillie, S. Huang, M. A. Green, J. Seidel, T. K. Ahn, and S. I. Seok, "Beneficial Effects of PbI2 Incorporated in Organo-Lead Halide Perovskite Solar Cells", Advanced Energy Materials **6**, 1502104 (2016).

[315] J. Chang, H. Zhu, J. Xiao, F. H. Isikgor, Z. Lin, Y. Hao, K. Zeng, Q.-H. Xu, and J. Ouyang, "Enhancing the planar heterojunction perovskite solar cell performance through tuning the precursor ratio", J. Mater. Chem. A **4**, 7943–7949 (2016).

[316] M. Jahandar, N. Khan, H. K. Lee, S. K. Lee, W. S. Shin, J. C. Lee, C. E. Song, and S. J. Moon, "High-Performance CH3NH3PbI3-Inverted Planar Perovskite Solar Cells with Fill Factor over 83% via Excess Organic/Inorganic Halide", ACS Applied Materials and Interfaces **9**, 35871–35879 (2017).

[317] D.-Y. Son, J.-W. Lee, Y. J. Choi, I.-H. Jang, S. Lee, P. J. Yoo, H. Shin, N. Ahn, M. Choi, D. Kim, and N.-G. Park, "Self-formed grain boundary healing layer for highly efficient CH3NH3PbI3 perovskite solar cells", Nature Energy **1**, 16081 (2016).

[318] H. Y. Hsu, L. Ji, M. Du, J. Zhao, E. T. Yu, and A. J. Bard, "Optimization of PbI2/MAPbI3 Perovskite Composites by Scanning Electrochemical Microscopy", Journal of Physical Chemistry C **120**, 19890–19895 (2016).

[319] T. Du, C. H. Burgess, J. Kim, J. Zhang, J. R. Durrant, and M. A. McLachlan, "Formation, location and beneficial role of PbI2 in lead halide perovskite solar cells", Sustainable Energy Fuels **1**, 119–126 (2017).

[320] S. Berweger, G. A. MacDonald, M. Yang, K. J. Coakley, J. J. Berry, K. Zhu, F. W. DelRio, T. M. Wallis, and P. Kabos, "Electronic and Morphological Inhomogeneities in Pristine and Deteriorated Perovskite Photovoltaic Films", Nano Letters **17**, 1796–1801 (2017).

[321] G. Zheng, C. Zhu, Y. Chen, J. Zhang, Q. Chen, X. Gao, and H. Zhou, "Microstructure variations induced by excessive PbX2 or AX within perovskite thin films", Chemical Communications **53**, 12966–12969 (2017).

[322] G. Zheng, C. Zhu, J. Ma, X. Zhang, G. Tang, R. Li, Y. Chen, L. Li, J. Hu, J. Hong, Q. Chen, X. Gao, and H. Zhou, "Manipulation of facet orientation in hybrid perovskite polycrystalline films by cation cascade", Nature Communications **9**, 2793 (2018).

[323] M. L. Petrus, Y. Hu, D. Moia, P. Calado, A. M. A. Leguy, P. R. F. Barnes, and P. Docampo, "The Influence of Water Vapor on the Stability and Processing of Hybrid Perovskite Solar Cells Made from Non-Stoichiometric Precursor Mixtures", ChemSusChem **9**, 2699–2707 (2016).

[324] J. Emara, T. Schnier, N. Pourdavoud, T. Riedl, K. Meerholz, and S. Olthof, "Impact of Film Stoichiometry on the Ionization Energy and Electronic Structure of CH3NH3PbI3 Perovskites", Advanced Materials **28**, 553–559 (2016).

[325] Y. Sevinchan, "Analysis of the Effects of Caesium Doping on the Properties of Zinc Oxide Layers and Inverted Hybrid Photovoltaic Devices", Bachelor's thesis (Heidelberg University, 2015).

[326] J. J. Friel, *X-ray and image analysis in electron microscopy* (Princeton Gamma-Tech All, 2003).

[327] H. Demers, N. Poirier-Demers, A. R. Couture, D. Joly, M. Guilmain, N. de Jonge, and D. Drouin, "Three-dimensional electron microscopy simulation with the CASINO Monte Carlo software", Scanning **33**, 135–146 (2011).

[328] howstuffworks: Scanning Electron Microscope (accessed October 2018): `https://s.hswstatic.com/gif/scanning-elecron-microscope-illustration.jpg`.

[329] Wikimemia: Electron Interaction with Matter (accessed October 2018): `https://commons.wikimedia.org/wiki/File:Electron_Interaction_with_Matter.svg`.

[330] J. C. de Mello, H. F. Wittmann, and R. H. Friend, "An improved experimental determination of external photoluminescence quantum efficiency", Advanced Materials **9**, 230–232 (1997).

[331] D. Becker-Koch, "Exploring sub-bandgap states in organic and hybrid photovoltaic materials using photothermal deflection spectroscopy", Master's thesis (Heidelberg University, 2017), Master thesis.

[332] A. Bausch, "Optical Properties Of Organo-Metallic Perovskites", Master's thesis (Heidelberg University, 2017).

[333] A. Weu, "Mechanisms, Identifying Degradation Cells, in P3HT:PCBM Organic Solar", Master's thesis (Heidelberg University, 2016).

[334] Q. Sun, P. Fassl, D. Becker-Koch, A. Bausch, B. Rivkin, S. Bai, P. E. Hopkinson, H. J. Snaith, and Y. Vaynzof, "Role of Microstructure in Oxygen Induced Photodegradation of Methylammonium Lead Triiodide Perovskite Films", Advanced Energy Materials **7**, 1700977 (2017).

[335] Y. Yang, M. Yang, D. T. Moore, Y. Yan, E. M. Miller, K. Zhu, and M. C. Beard, "Top and bottom surfaces limit carrier lifetime in lead iodide perovskite film", Nature Energy **2**, 1–7 (2017).

[336] J. S. Yun, A. Ho-Baillie, S. Huang, S. H. Woo, Y. Heo, J. Seidel, F. Huang, Y. B. Cheng, and M. A. Green, "Benefit of grain boundaries in organic-inorganic halide planar perovskite solar cells", Journal of Physical Chemistry Letters **6**, 875–880 (2015).

[337] Z. Chu, M. Yang, P. Schulz, D. Wu, X. Ma, E. Seifert, L. Sun, X. Li, K. Zhu, and K. Lai, "Impact of grain boundaries on efficiency and stability of organic-inorganic trihalide perovskites", Nature Communications **8**, 2230 (2017).

[338] N. Cho, F. Li, B. Turedi, L. Sinatra, S. P. Sarmah, M. R. Parida, M. I. Saidaminov, B. Murali, V. M. Burlakov, A. Goriely, O. F. Mohammed, T. Wu, and O. M. Bakr, "Pure crystal orientation and anisotropic charge transport in large-area hybrid perovskite films", Nature Communications **7**, 13407 (2016).

[339] S. Y. Leblebici, L. Leppert, Y. Li, S. E. Reyes-Lillo, S. Wickenburg, E. Wong, J. Lee, M. Melli, D. Ziegler, D. K. Angell, D. F. Ogletree, P. D. Ashby, F. M. Toma, J. B. Neaton, I. D. Sharp, and A. Weber-Bargioni, "Facet-dependent photovoltaic efficiency variations in single grains of hybrid halide perovskite", Nature Energy **1**, 16093 (2016).

[340] G. Abdelmageed, L. Jewell, K. Hellier, L. Seymour, B. Luo, F. Bridges, J. Z. Zhang, and S. Carter, "Mechanisms for light induced degradation in MAPbI 3 perovskite thin films and solar cells", Applied Physics Letters **109**, 233905 (2016).

[341] X. Tang, M. Brandl, B. May, I. Levchuk, Y. Hou, M. Richter, H. Chen, S. Chen, S. Kahmann, A. Osvet, F. Maier, H. P. Steinrück, R. Hock, G. J. Matt, and C. J. Brabec, "Photoinduced degradation of methylammonium lead triiodide perovskite semiconductors", Journal of Materials Chemistry A **4**, 15896–15903 (2016).

[342] C. Stavrakas, A. A. Zhumekenov, R. Brenes, M. Abdi-Jalebi, V. Bulović, O. M. Bakr, E. S. Barnard, and S. D. Stranks, "Probing buried recombination pathways in perovskite structures using 3D photoluminescence tomography", Energy & Environmental Science **11**, 2846–2852 (2018).

[343] P. Fassl, V. Lami, A. Bausch, W. Zhiping, M. T. Klug, H. J. Snaith, and Y. Vaynzof, "Fractional deviations in precursor stoichiometry dictate the properties, performance and stability of perovskite photovoltaic devices", Energy & Environmental Science, DOI: 10.1039/c8ee01136b (2018).

[344] M. L. Petrus, J. Schlipf, C. Li, T. P. Gujar, N. Giesbrecht, P. Müller-Buschbaum, M. Thelakkat, T. Bein, S. Hüttner, and P. Docampo, "Capturing the Sun: A Review of the Challenges and Perspectives of Perovskite Solar Cells", Advanced Energy Materials **8**, 1700264 (2018).

[345] Y. Luo, S. Aharon, M. Stuckelberger, E. Magaña, B. Lai, M. I. Bertoni, L. Etgar, and D. P. Fenning, "The Relationship between Chemical Flexibility and Nanoscale Charge Collection in Hybrid Halide Perovskites", Advanced Functional Materials **28**, 1706995 (2018).

[346] M. Saliba, J.-P. Correa-Baena, C. M. Wolff, M. Stolterfoht, N. Phung, S. Albrecht, D. Neher, and A. Abate, "How to make over 20% efficient perovskite solar cells in regular (n-i-p) and inverted (p-i-n) architectures", Chemistry of Materials **30**, 4193–4201 (2018).

[347] Q. Sun, P. Fassl, and Y. Vaynzof, "Large-Scale Compositional and Electronic Inhomogeneities in CH3NH3PbI3 Perovskites and Their Effect on Device Performance", ACS Applied Energy Materials **1**, 2410–2416 (2018).

[348] L. Zhao, D. Luo, J. Wu, Q. Hu, W. Zhang, K. Chen, T. Liu, Y. Liu, Y. Zhang, F. Liu, T. P. Russell, H. J. Snaith, R. Zhu, and Q. Gong, "High-Performance Inverted Planar Heterojunction Perovskite Solar Cells Based on Lead Acetate Precursor with Efficiency Exceeding 18%", Advanced Functional Materials **26**, 3508–3514 (2016).

[349] M. Ahmadi, T. Wu, and B. Hu, "A Review on Organic-Inorganic Halide Perovskite Photodetectors: Device Engineering and Fundamental Physics", Advanced Materials **29**, 1605242 (2017).

[350] S. Olthof and K. Meerholz, "Substrate-dependent electronic structure and film formation of MAPbI3 perovskites", Scientific Reports **7**, 40267 (2017).

[351] T. J. Jacobsson, J. P. Correa-Baena, E. Halvani Anaraki, B. Philippe, S. D. Stranks, M. E. Bouduban, W. Tress, K. Schenk, J. Teuscher, J. E. Moser, H. Rensmo, and A. Hagfeldt, "Unreacted PbI2 as a Double-Edged Sword for Enhancing the Performance of Perovskite Solar Cells", Journal of the American Chemical Society **138**, 10331–10343 (2016).

[352] B. Philippe, M. Saliba, J. P. Correa-Baena, U. B. Cappel, S. H. Turren-Cruz, M. Grätzel, A. Hagfeldt, and H. Rensmo, "Chemical Distribution of Multiple Cation (Rb+, Cs+, MA+, and FA+) Perovskite Materials by Photoelectron Spectroscopy", Chemistry of Materials **29**, 3589–3596 (2017).

[353] C. G. Bischak, E. M. Sanehira, J. T. Precht, J. M. Luther, and N. S. Ginsberg, "Heterogeneous Charge Carrier Dynamics in Organic-Inorganic Hybrid Materials: Nanoscale Lateral and Depth-Dependent Variation of Recombination Rates in Methylammonium Lead Halide Perovskite Thin Films", Nano Letters **15**, 4799–4807 (2015).

[354] N. Klein-Kedem, D. Cahen, and G. Hodes, "Effects of Light and Electron Beam Irradiation on Halide Perovskites and Their Solar Cells", Accounts of Chemical Research **49**, 347–354 (2016).

[355] A. Thompson, "X-ray data booklet", Journal of Synchrotron Radiation **8**, 1125–1125 (2001).

[356] C. C. Stoumpos, C. D. Malliakas, and M. G. Kanatzidis, "Semiconducting Tin and Lead Iodide Perovskites with Organic Cations: Phase Transitions, High Mobilities, and Near-Infrared Photoluminescent Properties", Inorganic Chemistry **52**, 9019–9038 (2013).

[357] N. Tessler, "Adding 0.2 V to the open circuit voltage of organic solar cells by enhancing the built-in potential", Journal of Applied Physics **118**, 215501 (2015).

[358] O. Magen and N. Tessler, "On electrode pinning and charge blocking layers in organic solar cells", Journal of Applied Physics **121** (2017) 10.1063/1.4983298.

[359] Z. Hawash, S. R. Raga, D. Y. Son, L. K. Ono, N. G. Park, and Y. Qi, "Interfacial Modification of Perovskite Solar Cells Using an Ultrathin MAI Layer Leads to Enhanced Energy Level Alignment, Efficiencies, and Reproducibility", Journal of Physical Chemistry Letters **8**, 3947–3953 (2017).

[360] U. Rau, "Reciprocity relation between photovoltaic quantum efficiency and electroluminescent emission of solar cells", Physical Review B **76**, 85303 (2007).

[361] W. Tress, M. Yavari, K. Domanski, P. K. Yadav, B. Niesen, J.-P. Correa-Baena, A. Hagfeldt, and M. Grätzel, "Interpretation and Evolution of Open-Circuit Voltage, Recombination, Ideality Factor and Subgap Defect States during Reversible Light-Soaking and Irreversible Degradation of Perovskite Solar Cells", Energy Environ. Sci. **11**, 151–165 (2018).

[362] K. Tvingstedt, O. Malinkiewicz, A. Baumann, C. Deibel, H. J. Snaith, V. Dyakonov, and H. J. Bolink, "Radiative efficiency of lead iodide based perovskite solar cells", Scientific Reports **4**, 6071 (2015).

[363] W. Tress, "Perovskite Solar Cells on the Way to Their Radiative Efficiency Limit - Insights Into a Success Story of High Open-Circuit Voltage and Low Recombination", Advanced Energy Materials **7**, 1602358 (2017).

[364] L.-M. Chen, Z. Hong, G. Li, and Y. Yang, "Recent Progress in Polymer Solar Cells: Manipulation of Polymer:Fullerene Morphology and the Formation of Efficient Inverted Polymer Solar Cells", Advanced Materials **21**, 1434–1449 (2009).

[365] H. Choi, C.-K. Mai, H.-B. Kim, J. Jeong, S. Song, G. C. Bazan, J. Y. Kim, and A. J. Heeger, "Conjugated polyelectrolyte hole transport layer for inverted-type perovskite solar cells", Nature Communications **6**, 7348 (2015).

[366] J. C. Yu, J. A. Hong, E. D. Jung, D. B. Kim, S. M. Baek, S. Lee, S. Cho, S. S. Park, K. J. Choi, and M. H. Song, "Highly efficient and stable inverted perovskite solar cell employing PEDOT:GO composite layer as a hole transport layer", Scientific Reports **8**, 1070 (2018).

[367] Z. Ahmad, M. A. Najeeb, R. A. Shakoor, A. Alashraf, S. A. Al-Muhtaseb, A. Soliman, and M. K. Nazeeruddin, "Instability in CH3NH3PbI3 perovskite solar cells due to elemental migration and chemical composition changes", Scientific Reports **7**, 15406 (2017).

[368] K. Domanski, J.-P. Correa-Baena, N. Mine, M. K. Nazeeruddin, A. Abate, M. Saliba, W. Tress, A. Hagfeldt, and M. Grätzel, "Not All That Glitters Is Gold: Metal-Migration-Induced Degradation in Perovskite Solar Cells", ACS Nano **10**, 6306–6314 (2016).

[369] W. Ming, D. Yang, T. Li, L. Zhang, and M. H. Du, "Formation and Diffusion of Metal Impurities in Perovskite Solar Cell Material CH3NH3PbI3: Implications on Solar Cell Degradation and Choice of Electrode", Advanced Science **5**, 1700662 (2018).

[370] J. M. Frost, K. T. Butler, F. Brivio, C. H. Hendon, M. Van Schilfgaarde, and A. Walsh, "Atomistic origins of high-performance in hybrid halide perovskite solar cells", Nano Letters **14**, 2584–2590 (2014).

[371] L. Zhang and P. H.-L. Sit, "Ab Initio Study of Interaction of Water, Hydroxyl Radicals, and Hydroxide Ions with CH3NH3PbI3 and CH3NH3PbBr3 Surfaces", The Journal of Physical Chemistry C **119**, 22370–22378 (2015).

[372] N. Z. Koocher, D. Saldana-Greco, F. Wang, S. Liu, and A. M. Rappe, "Polarization Dependence of Water Adsorption to CH3NH3PbI3 (001) Surfaces", The Journal of Physical Chemistry Letters **6**, 4371–4378 (2015).

[373] W. Hao, X. Chen, and S. Li, "Synergistic Effects of Water and Oxygen Molecule Co-adsorption on (001) Surfaces of Tetragonal CH3NH3PbI3: A First-Principles Study", Journal of Physical Chemistry C **120**, 28448–28455 (2016).

[374] L. Zhang, M.-G. Ju, and W. Liang, "The effect of moisture on the structures and properties of lead halide perovskites: a first-principles theoretical investigation", Physical Chemistry Chemical Physics **18**, 23174–23183 (2016).

[375] T. Oku, "Crystal Structures of CH3NH3PbI3 and Related Perovskite Compounds Used for Solar Cells", in *Solar cells - new approaches and reviews* (InTech, Oct. 2015).

[376] Z. Song, S. C. Watthage, A. B. Phillips, B. L. Tompkins, R. J. Ellingson, and M. J. Heben, "Impact of Processing Temperature and Composition on the Formation of Methylammonium Lead Iodide Perovskites", Chemistry of Materials **27**, 4612–4619 (2015).

[377] J. R. Klein, O. Flender, M. Scholz, K. Oum, and T. Lenzer, "Charge carrier dynamics of methylammonium lead iodide: from PbI2 -rich to low-dimensional broadly emitting perovskites", Phys. Chem. Chem. Phys. **18**, 10800–10808 (2016).

[378] J. Zhao, Y. Deng, H. Wei, X. Zheng, Z. Yu, Y. Shao, J. E. Shield, and J. Huang, "Strained hybrid perovskite thin films and their impact on the intrinsic stability of perovskite solar cells", Science Advances **3**, eaao5616 (2017).

[379] A. Pramanick, X. P. Wang, C. Hoffmann, S. O. Diallo, M. R. V. Jørgensen, and X.-L. Wang, "Microdomain dynamics in single-crystal BaTiO3 during paraelectric-ferroelectric phase transition measured with time-of-flight neutron scattering", Physical Review B **92**, 174103 (2015).

[380] S. John, C. Soukoulis, M. H. Cohen, and E. N. Economou, "Theory of electron band tails and the urbach optical-absorption edge", Physical Review Letters **57**, 1777–1780 (1986).

[381] A. D. Wright, R. L. Milot, G. E. Eperon, H. J. Snaith, M. B. Johnston, and L. M. Herz, "Band-Tail Recombination in Hybrid Lead Iodide Perovskite", Advanced Functional Materials **27**, 1700860 (2017).

[382] J. L. Minns, P. Zajdel, D. Chernyshov, W. Van Beek, and M. A. Green, "Structure and interstitial iodide migration in hybrid perovskite methylammonium lead iodide", Nature Communications **8**, 15152 (2017).

[383] Y. Tian, M. Peter, E. Unger, M. Abdellah, K. Zheng, T. Pullerits, A. Yartsev, V. Sundström, and I. G. Scheblykin, "Mechanistic insights into perovskite photoluminescence enhancement: light curing with oxygen can boost yield thousandfold", Phys. Chem. Chem. Phys. **17**, 24978–24987 (2015).

[384] J. F. Galisteo-López, M. Anaya, M. E. Calvo, and H. Míguez, "Environmental Effects on the Photophysics of Organic–Inorganic Halide Perovskites", The Journal of Physical Chemistry Letters **6**, 2200–2205 (2015).

[385] X. Feng, H. Su, Y. Wu, H. Wu, J. Xie, X. Liu, J. Fan, J. Dai, and Z. HE, "Photon-generated Carriers Excited Superoxide Species Inducing Long-term Photoluminescence Enhancement of MAPbI3 Perovskite Single Crystals", J. Mater. Chem. A **5**, 12048–12053 (2017).

[386] R. Brenes, D. Guo, A. Osherov, N. K. Noel, C. Eames, E. M. Hutter, S. K. Pathak, F. Niroui, R. H. Friend, M. S. Islam, H. J. Snaith, V. Bulović, T. J. Savenije, and S. D. Stranks, "Metal Halide Perovskite Polycrystalline Films Exhibiting Properties of Single Crystals", Joule **1**, 155–167 (2017).

[387] R. Brenes, C. Eames, V. Bulovi, S. Islam, and S. D. Stranks, "The Impact of Atmosphere on the Local Luminescence Properties of Metal Halide Perovskite Grains", Advanced Materials **30**, 1706208 (2018).

[388] Y. Yamada, T. Yamada, A. Shimazaki, A. Wakamiya, and Y. Kanemitsu, "Interfacial Charge-Carrier Trapping in CH3NH3PbI3-Based Heterolayered Structures Revealed by Time-Resolved Photoluminescence Spectroscopy", Journal of Physical Chemistry Letters **7**, 1972–1977 (2016).

[389] T. W. Jones, A. Osherov, M. Alsari, M. Sponseller, B. C. Duck, Y.-K. Jung, C. Settens, F. Niroui, R. Brenes, C. V. Stan, Y. Li, M. Abdi-Jalebi, N. Tamura, J. E. Macdonald, M. Burghammer, V. Bulović, A. Walsh, G. J. Wilson, S. Lilliu, and S. D. Stranks, "Local Strain Heterogeneity Influences the Optoelectronic Properties of Halide Perovskites", aRXIV, arXiv:1803.01192 (2018).

[390] C. P. Lindsey and G. D. Patterson, "Detailed comparison of the Williams–Watts and Cole–Davidson functions", The Journal of Chemical Physics **73**, 3348–3357 (1980).

[391] D. W. de Quilettes, S. M. Vorpahl, S. D. Stranks, H. Nagaoka, G. E. Eperon, M. E. Ziffer, H. J. Snaith, and D. S. Ginger, "Impact of microstructure on local carrier lifetime in perovskite solar cells", Science **348**, 683–686 (2015).

[392] T. S. Sherkar, C. Momblona, L. Gil-Escrig, J. Ávila, M. Sessolo, H. J. Bolink, and L. J. A. Koster, "Recombination in Perovskite Solar Cells: Significance of Grain Boundaries, Interface Traps, and Defect Ions", ACS Energy Letters **2**, 1214–1222 (2017).

[393] V. Sarritzu, N. Sestu, D. Marongiu, X. Chang, S. Masi, A. Rizzo, S. Colella, F. Quochi, M. Saba, A. Mura, and G. Bongiovanni, "Optical determination of Shockley-Read-Hall and interface recombination currents in hybrid perovskites", Scientific Reports **7**, 44629 (2017).

List of Publications

Publications Used in This Thesis

[1] **P. Fassl,** A. Taylor, Y. Zakharko, J. Zaumseil, Y. Vaynzof, "Effect of Density of Defects on Photoluminescence Properties in MAPbI3 Perovskite", Journal of Material Chemistry C (in preparation) (2018).

[2] **P. Fassl,** V. Lami, A. Bausch, W. Zhiping, M. T. Klug, H. J. Snaith, Y. Vaynzof, "Fractional deviations in precursor stoichiometry dictate the properties, performance and stability of perovskite photovoltaic devices", Energy & Environmental Science, DOI: 10.1039/c8ee01136b (2018).

[3] Q. Sun*, **P. Fassl*,** D. Becker-Koch, A. Bausch, B. Rivkin, S. Bai, P. E. Hopkinson, H. J. Snaith, Y. Vaynzof, "Role of Microstructure in Oxygen Induced Photodegradation of Methylammonium Lead Triiodide Perovskite Films", Advanced Energy Materials **7**, 1700977. *These Authors contributed equally. (2017).

Additional Publications

[1] **P. Fassl,** S. Ternes, V. Lami, Y. Zakharko, D. Heimfarth, P. E. Hopkinson, F. Paulus, A. Taylor, J. Zaumseil, Y. Vaynzof, "The effect of crystal grain orientation on the rate of ionic transport in perovskite polycrystalline thin films", ACS Applied Materials & Interfaces (submitted) (2018).

[2] B. Rivkin, **P. Fassl,** Q. Sun, A. D. Taylor, Z. Chen, Y. Vaynzof, "Effect of Ion Migration-Induced Electrode Degradation on the Operational Stability of Perovskite Solar Cells", ACS Omega **3**, 10042–10047 (2018).

[3] Q. Sun, **P. Fassl,** Y. Vaynzof, "Large-Scale Compositional and Electronic Inhomogeneities in CH3NH3PbI3 Perovskites and Their Effect on Device Performance", ACS Applied Energy Materials **1**, 2410–2416 (2018).

[4] Q. An, **P. Fassl,** Y. J. Hofstetter, D. Becker-Koch, A. Bausch, P. E. Hopkinson, Y. Vaynzof, "High performance planar perovskite solar cells by ZnO electron transport layer engineering", Nano Energy **39**, 400–408 (2017).

[5] V. Lami, D. Leibold, **P. Fassl,** Y. Hofstetter, D. Becker-Koch, P. Biegger, F. Paulus, P. E. Hopkinson, M. Adams, U. H. F. Bunz, S. Huettner, I. Howard, A. A. Bakulin, Y. Vaynzof, "N-Heteroacenes as a New Class of Non-Fullerene Electron Acceptors for Organic Bulk-Heterojunction Photovoltaic Devices", Solar RRL **1**, 1700053 (2017).

List of Conference Presentations

[1] **P. Fassl,** V. Lami, A. Bausch, Z. Wang, H. J. Snaith, Y. Vaynzof, "Fractional Deviations in Precursor Stoichiometry Dictate the Properties and Stability of Perovskite Photovoltaic Devices", Poster - GRC Conference 2018, Hongkong.

[2] **P. Fassl,** V. Lami, A. Bausch, Z. Wang, H. J. Snaith, Y. Vaynzof, "Effect of Varying the Density of Defects on the Properties of Organometal Halide Perovskites", Oral presentation - DPG Spring Meeting 2018, Berlin, Germany.

[3] **P. Fassl,** Q. Sun, D. Becker-Koch, A. Bausch, B. Rivkin, S. Bai, P. E. Hopkinson, H. J. Snaith, Y. Vaynzof, "Role of Microstructure in Oxygen Induced Photodegradation of Methylammonium Lead Triiodide Perovskite Films", Oral presentation- DPG Spring Meeting 2017, Dresden, Germany.

[4] **P. Fassl,** Q. Sun, D. Becker-Koch, P. E. Hopkinson, Y. Vaynzof, "Degradation Studies of Methylammonium Lead Iodide under Controlled Exposure to Oxygen and Light", Poster- PSCO 2016, Genoa, Italy.

Danksagung/Acknowledgements

und witzigsten Büro-Kollegen überhaupt. Aber auch DBK, David L., Andi, Joshua, Daniel, Simon, Boris, Alexandra und Lukas danke ich für die tolle gemeinsame Zeit und erfolgreiche Zusammenarbeit.

Ich danke allen meinen tollen Freunden in und um Heidelberg herum, welche die Ph.D. Zeit zu etwas Besonderem gemacht haben. Hier seien insbesondere Joscha, Jorina, Kristian und Freya erwähnt, die immer für mich da waren auch in schwereren Zeiten. Schön dass es euch gibt!

Bedanken möchte ich mich auch bei MEINEN ELTERN, die mich in jeder Phase meines Studiums und meiner Doktorarbeit unterstützt haben, und mir immer die Freiheit gegeben haben, meinen Interessen nachzugehen. Danke, dass ihr immer für mich da seid!